University of Trento

Giuseppe Abbiati (Ph.D. Student)

DYNAMIC SUBSTRUCTURING OF COMPLEX HYBRID SYSTEMS BASED ON TIME-INTEGRATION, MODEL REDUCTION AND MODEL IDENTIFICATION TECHNIQUES

Prof. Oreste S. Bursi (Tutor)

April, 2014

University of Trento

Doctorate in Engineering of Civil and Mechanical Structural Systems - Cycle XXVI

Board of examiners:

Prof. Dionisio P. Bernal

Prof. Michel Destrade

Prof. Oreste S. Bursi

Prof. Andrea G. Calogero

Prof. Paola Falugi

ABSTRACT

Hybrid Simulation with Dynamic Substructuring (HSDS) is a mixed numerical/-experimental simulation techniques. In detail, HSDS combines a Physical Substructure (PS) -the most critical subpart- with a Numerical Substructure (NS), and a compliant time integration process calculates the overall dynamic response of the emulated system. With the objective to circumvent three among major limitations of HSDS, the present thesis offers methodological procedures and algorithms aimed at: i) emulating a consistent degradation between PSs and NSs via model updating techniques; ii) handling PSs characterized by several internal DoFs with a reduced number of interface actuation points; iii) improving the computational efficiency in the case of complex NSs via partitioned time integrators. An old reinforced concrete bridge and a steel piping network for industrial plants are introduced as full-scale structural case studies.

Part of significant results were published on referee journals and proceedings of international conferences. Part of developed tools was uploaded to the *NEESHub* web repository that is a United States web platform for research, collaboration and education powered by the George E. Brown, Jr. Network for Earthquake Engineering Simulation (NEES).

ACKNOLEDGEMENTS

First and foremost, I must thank my family and my girlfriend Gemma for their love and patience.

To my supervisor, Prof. Oreste Salvatore Bursi, who drove me throughout the invaluable experience of the doctorate.

To Prof. Rosario Ceravolo, who always stimulated me through constructive discussions.

To Dr. Pierre Pegon, Dr. Francisco Javier Molina and all the guys of the ELSA Laboratory of Joint Research Centre of Ispra, for their support and hints.

To the RETRO team and in particular to Dr. Fabrizio Paolacci and Dr. Luigi Di Sarno, for their precious cooperation.

To the University of Trento for granting me the Ph.D. fellowship to commence this thesis and to carry out the inherent work.

To the Laboratory and Structures and Material of the University of Trento that allowed for conducting a significant part of developed experimental activities.

To my colleagues and students, all friends of mine, go finally my thanks.

PUBLICATIONS

As a result of the work conducted in this thesis, the following publications have been produced:

Journal publications

- Ceravolo R., **Abbiati G.**, 2012. Time Domain Identification Of Structures: A Comparative Analysis Of Output-Only Methods - International Journal of Engineering Mechanics, 139(4).

- Bursi O.S., **Abbiati G.**, Reza Md.S., 2013. A Novel Hybrid Testing Approach for Piping Systems of Industrial Plants. Special Issue of Smart Structures and Systems on "Recent Advances in Real-time Hybrid Simulation" (RTHS) - *In publication*.

- Reza Md.S., **Abbiati G.**, Bursi O.S., Paolacci F., 2013. Seismic performance evaluation of a full-scale industrial piping system at serviceability and ultimate limit states. Journal of Loss Prevention - *Submitted*.

- **Abbiati G.**, Ceravolo R., Surace C., 2013. Unbiased time-dependent estimators for on-line monitoring of full-scale structures under ambient excitation. Mechanical Systems and Signal Processing - *Under review*.

- **Abbiati G.**, Bursi O.S., Di Sarno L., Molina F.J., Paolacci F., Pegon P., 2014. Hybrid simulations of a multi-span RC viaduct with plain bars and sliding bearings - *In preparation*.

SCOPUS indexed publications

- Reza M.S., **Abbiati G.**, Bonelli A., Bursi O.S., 2013. "Pseudo-dynamic testing of a piping system based on model reduction techniques". SERIES Concluding Workshop joint with NEES-US Earthquake Engineering Research Infrastructures. JRC Ispra, May 28-30.

- **Abbiati G.**, Bursi O.S., Cazzador E., Mei Z., Paolacci F., Pegon P., 2013. "Pseudo-dynamic testing with non-linear substructuring of a reinforced concrete bridge". SERIES Concluding Workshop joint with NEES-US Earthquake Engineering Research Infrastructures JRC Ispra, May 28-30.

- Paolacci F., Di Sarno L., Pegon P., Molina F. J., Poljansek M., Bursi O.S., **Abbiati G.**, Ceravolo R., Erdik M., Deisi R., Mohamad A, 2013. "Assessment of the seismic behaviour of a retrofitted old R.C. highway bridge through PsD testing". SERIES Concluding Workshop joint with NEES-US Earthquake Engineering Research Infrastructures JRC Ispra, May 28-30.

- Paolacci F., Di Sarno L., De Risi R., **Abbiati G.**, Mohamad A., Malena M., Corritore D. 2013. "Refined and simplified numerical models of an isolated old highway bridge for PsD testing". SERIES Concluding Workshop joint with NEES-US Earthquake Engineering Research Infrastructures JRC Ispra, May 28-30.

NEESHub uploads

Following developed software has been uploaded to the NEESHub (`https://nees.org/`) where is available as open source code:

- *simlsrt2* - id #209: Simulink implementation of the LSRT-2 time integration algorithm.

- *stftnlidtool* - id #208: Matlab system identification tool based on the Short Time Fourier Transform (STFT).

- *simmgalpha* - id #210: Simulink implementations of the Modified Generalized-α time integration.

CONTENTS

LIST OF FIGURES

LIST OF TABLES

CHAPTER 1

INTRODUCTION

1.1 Hybrid Simulation with dynamic substructuring

Hybrid Simulation with Simulation Substructuring (HSDS) is an experimental techniques in which the overall dynamic response of a system -structure- is evaluated by combining the experimental response of a Physical Substructure (PS), which is the most critical part, with the numerical response of a Numerical Substructure (NS) (Bursi, 2008). The term *hybrid* entails an approach that part of a structural or mechanical system is analytically modeled while the rest is physically tested. Dynamic substructuring plays a significant role in the field of structural dynamics and can be seen as a special class of domain decomposition. Such paradigm originates from the desire to analyze complex problems by considering separately the problem of its components and the problem of finding the interface solution (Klerk et al., 2008). It allows for the simulation of a complex dynamic system by combining its discretised, analytical and experimental parts. While coupling two or more substructures, two conditions must hold at interface Degrees-of-Freedom (DoFs): i) compatibility on kinematic quantities and ii) force balance. Therefore, the so called transfer system, i.e. actuators and relevant feedback sensors managed by real-time computers, must reproduce such conditions. At the same time, a numerical simulation environment solves the NS and the time integration of coupled equations of motion advances. As a result, dynamics of both substructures are accurately reproduced, as well as their mutual interactions. HSDS does integrate cutting-edge research obtained from the fields of numerical analysis, i.e. linear/nonlinear dynamics, multibody dynamics, digital control and

system modeling. When the PS shows a rate independent behavior, HSDS can be conducted at extended time scales, typically $50 - 200$ times slower than the actual earthquake time. This is the case of Pseudo-Dynamic Testing (PDT). Accordingly, inertial and damping components of restoring forces are numerically simulated. Conversely, when rate dependent effects are significant, a Real-time Testing (RT) strategy must be selected to obtain reliable simulations. Since experimental set-ups are restricted to PSs, HSDS facilitates the simulation of full-scale structural systems. As a result, costs and efforts required to conduct a shake table test on the entire system are significantly reduced.

1.2 Original scientific contributions of the thesis

HSDS is a powerful and costs saving tool for testing complex and large dynamic systems. Within its the scope, the performed research activity focused on three main objectives: i) the modeling of tunable nonlinear NSs for the purpose of the hybrid simulation of the Rio Torto Bridge, where a consistent degradation all piers, i.e. physical and numerical, was needed; ii) the implementation of hybrid simulations of an industrial piping system characterized by a twisted and branched PSs with a reduced number of actuators; iii) the development of hybrid compatible partitioned time integration algorithms tailored to first order systems and prone to parallel implementations. Different branches of numerical analysis were involved; in particular, model updating, model reduction and time integration. Experimental case studies corroborated all numerical advances. Major scientific contributions are summarized herein for all the aforementioned topics.

The need for assessing the seismic performance of an old reinforced concrete bridge characterized by nonlinear hysteretic piers and isolators motivated the development of reduced nonlinear NSs for the purpose of hybrid simulation. Characterized by a total span of $400m$ and plain steel bar reinforcements, the Rio Torto Bridge was underdesigned with respect to seismic requirements dictated by both Italian and European codes. The installation of a pair -one per column- of Friction Pendulum Bearing (FPB) isolation devices interposed between the deck and the cap beam of each pier portal frame was proposed as seismic retrofitting. In order to simulate the dynamic response of one of the two independent roadways, a comprehensive set of hybrid simulations was conceived for both the isolated and the

non isolated cases. Since preliminary numerical simulations highlighted the hysteretic response of piers already at serviceability limit state (Paolacci and Giannini, 2012), nonlinear NSs were deemed necessary to conduct realistic hybrid simulations. Entailing parameters were tuned according to the fiber-based OpenSEES FE Reference Model (RM) of the bridge. As a result, hybrid simulations of the Rio Torto Bridge were successfully implemented at the ELSA Laboratory of the Joint Research Centre of Ispra (VA), Italy. The PM method (Pegon and Magonette, 2002), which embeds subcycling capabilities, allowed for the implementation of the continuous PDT method. In order to simulate a consisted degradation of physical and numerical piers, a novel testing procedure was developed. It was based on recursive model identification of PSs and updating of NSs.

In the case of simple structural topologies, i.e., shear type frames, inverted pendulum systems, chain like systems, etc., few actuators handling the totality of physical DoFs can efficiently reproduce the response path of tested specimens; and the system of equations of motion can be solved through suitable time integrators. Nonetheless, this approach is not suitable for dealing with complex Physical Substructures (PSs) subjected to distributed inertia forces, where a plenty of physical DoFs come on stage; and this is the case of typical piping networks subjected to seismic loading. The need for assessing dynamic responses of typical industrial piping systems motivated the application of model reduction techniques to experimental dynamic substructuring. Therefore, RTs and PDTs of the piping system were successfully implemented. In particular, the LSRT2 time integration algorithm (Bursi, 2011) was applied in both the two cases. The delay compensation strategy proposed by Wu (2013) and based on the over prediction of the actuator command was selected to conduct RTs.

Todays state of the art servo-hydraulic control systems run at sampling times Δt of the order of $1 msec$ and below. With regard to the continuous PDT method, this means that new displacement values are required at very short and deterministic time intervals for the signal generation of actuator commands. On the other hand, the numerical integration of the equation of motion can be very time consuming in the case of complex NSs. Hence, both the computational driver and the control system run at different time rates (Schellenberg, 2009). In order to achieve

greater computational efficiency, one must be able to solve numerical and physical subdomains separately with different time steps and then couple their solutions together. Therefore, parallel partitioned time integration algorithms, which allow for the concurrent solution of involved subdomains, represent a suitable approach. Since numerical models of both NSs and PSs can be profitably used for dynamic identification, model-based control and model order reduction, a unique representation of the system is preferable. As a result, the most flexible state space form is a reasonable choice. From this perspective three partitioned hybrid compatible time integration algorithms were developed for first order systems. They inherited the favorable user controlled algorithmic damping feature of the Generalized-α method after Jansen et al. (2000).

1.3 Structure of the thesis

This thesis summarizes research activities performed by the author. Developments of novel methodological approaches and algorithms are presented and the validated throughout realistic case studies. The remainder of the thesis is divided in six chapters:

- **Chapter 2**: The reference literature involved in the present research activity was summarized. In detail, open challenges in HSDS were emphasized through a review of more recent developments and case studies.

- **Chapter 3**: First, the Rio Torto Case Study was introduced and both the as-built and the retrofitted configurations were discussed. Then, the OpenSEES RM was presented to support the implementation of hybrid simulations. Results of time history analyses of the OpenSEES RM justified the selected substructuring scheme. In greater detail, the Guyan method (Guyan, 1965) was applied to each pier portal frame to obtain reduced linear stiffness and mass. Resulting S-DoF reduced models were extended to the nonlinear range by means of nonlinear springs capable of reproducing displacement responses of OpenSEES piers. With regard to FPB isolation devices, suitable S-DoF reduced models were tailored according to the state space bilinear model of Mostaghel (1999). Validations of reduced models of the Rio Torto Bridge based on substructured components followed. Finally, conclu-

sions were drawn.

- **Chapter 4**: First, substructuring schemes and entailing experimental set-ups tailored to the Rio Torto Case Study were discussed. Then, the scaling of specimens was described. A novel testing procedure aimed at simulating a consistent degradation among physical and numerical piers, i.e. PSs and NSs, was presented and applied to the Rio Torto Bridge. It was based on off-line sessions of model identification of PSs and updating of NSs. Accordingly, a tool for the identification of parameters of OpenSEES FE models was implemented in the Matlab environment. As a result, physical piers were characterized after each test where damage was observed. The OpenSEES RM model of the Rio Torto Bridge was updated accordingly and took as reference for the updating of reduced S-DoF piers, i.e. NSs. As a result, a consistent degradation of physical and numerical piers was simulated in both non isolated and isolated conditions. Finally, results of hybrid simulations were discussed.

- **Chapter 5**: Before introducing any reduction strategy, a clear insight into the dynamic response of the industrial piping system was provided from a PS perspective. In detail, the Principal Component Analysis (PCA) was exploited. Accordingly and complying with experimental limitations of each testing strategy, consistent reduction bases were defined for both PDT and RT techniques in the case of an elastic response of the PS. Successively, a Modified version of the System Equivalent Reduction-Expansion Process (M-SEREP) (OCallahan and Riemer, 1989) and Craig-Bampton reduction methods (Bampton, 1968) were employed for the reduction of both the PS and distributed earthquake forces. This allowed for an effective experimental testing of the actual system. Two further reduction bases were investigated from a numerical perspective only. Finally and in view of validation, relevant implementations and experimental results were shown.

- **Chapter 6**: First, the monolithic MG-α algorithm was introduced for the uncoupled case. Its stability, accuracy and spectral properties were investigated from both analytical and numerical viewpoints. A careful description of both

the GC-MG-α and the PM-MG-α partitioned time integration procedures followed. The former, which consists of a staggered scheme, was proposed as starting procedure of the latter, which is a parallel scheme not self starting, within the same implementation. Then, the parallel partitioned GCbis-MG-α method was introduced as an alternative approach. Features of both strategies were analyzed on numerical case studies. Finally, experimental validations were discussed.

- **Chapter 7** Conclusions were summarized and outlooks on future perspectives were given.

CHAPTER 2

HYBRID SIMULATION WITH DYNAMIC SUBSTRUCTURING: STATE-OF-ART OPEN CHALLENGES

Hybrid Simulation (HS) with Dynamic Substructuring (DS) is an experimental technique that combines the experimental response of a Physical Substructure (PS), which is the most critical part of the emulated system, with the numerical response of a Numerical Substructure (NS). A standard computer solves the equation of motion of the hybrid system by means of a compatible time integrator and the interaction between NS and PS can be simulated. In detail, at each time step, actuators impose calculated displacements to specimens through a set of interface Degrees-of-Freedom (DoFs). Then, measured feedback forces enter the dynamic balance equation of the entire emulated system and the integration loop advances (Bursi, 2008).

2.1 Model updating in HSDS

Since the PS gathers components lacking of predictive numerical models, the application of hybrid simulation is not ideal for structures characterized by complex nonlinearities distributed to the overall emulated system. As a matter of example, this is the case of multi-pier bridges. In fact, due to the high cost for providing an experimental testing environment for a single specimen, hybrid simulation of such systems normally involve at most one or a few experimental piers. The remainder are reasonably replaced by their numerical counterparts. As a result, it is very likely that combined PSs and NSs show incompatible structural responses, despite their similar prototypes. As far as the demand for more and more realistic hybrid simulations increases, the need for implementing consistent PSs and NSs

becomes the imperative. From this perspective, the measured response of the experimental specimen could supply information to calibrate numerical parts and the accuracy of hybrid simulation would benefit from improved models. By reducing the discrepancies between the response of the mathematical model and that of the actual system, model updating represents a suitable approach aimed at identifying system parameters. Over the last two decades, model updating and system identification techniques were extensively applied to improve the prediction of numerical models by identifying related parameters on the actual structural response.

Finite element (FE) model updating has been around for more than two decades. Most of the established FE model updating techniques exploits linear models (Mottershead and Friswell, 1993; Mottershead et al., 2011). However, since the simulation of complex structural systems characterized by critical subparts represents the strong point of hybrid simulation, typically, responses experienced by tested specimens span the nonlinear range. Therefore, nonlinear models are amenable to hybrid applications where a damage process involving hysteresis is often investigated (Bursi, 2012). Modeling and identification of nonlinear systems of structural elements in extreme loading conditions is challenging, and particular care must be devoted to check the well-posedness and the well-conditioning of the associated optimization problem. Moreover, one is forced to admit that there is no general analysis method that can be applied to all systems in all instances. The reason is that the functional, which maps the input to the output, is not known beforehand (Kerschen et al., 2006). Since in post-experiment parameter identification there are usually no constraints on computational and data processing times, model updating is typically performed offline. With recent significant advances in embedded systems and their real-time computing capabilities, online updating can be performed. In this particular case, algorithms must converge smoothly and rapidly to proper parameter values in order to capture parameter changes as time progresses. In recent years, many techniques were developed for this purpose, including least squares estimation (Smyth et al., 1999), the Extended Kalman Filter (EKF), the Unscented Kalman filter (UKF) and the Particle Filter (PF) (Chatzi and Smyth, 2009). Time-frequency domain approaches relying on the Short Time Fourier Transform (STFT) are prone to online implementations as well (Ceravolo

et al., 2013). With reference to the hybrid simulation framework, Kwon and Kammula (2013) developed an online model updating scheme based on several alternative numerical models, formulated encompassing the possible variation in the hysteretic behavior of the tested specimen. In detail, an online optimization procedure provided instantaneous estimations of a set of weighting factors, which allowed for reproducing the measured response as a weighted combination of the responses of a bunch of models. Therefore, if one of the implemented models exactly matches the specimen, the weighting factor for that model tends to one, whilst the remainder goes to zero. Song and Dyke (2013) developed a cyber-physical experimental platform based on the UKF to conduct real-time model updating of nonlinear dynamic systems. The objective was to perform the updating computation in hard real-time, so that an updated model evolves during and is available immediately after the dynamic input ends. Yang (2012) proposes an online procedure for the purpose of hybrid simulation of a bridge with multiple identical piers. During a hybrid simulation, the set of identified parameters that matches the experimental data measured from the physical specimen was identified and identical NSs were contemporary updated. Two variant were presented, and they were based on the Nelder-Mead Simplex method and the UKF, respectively.

According to the need for being updated during the experimental simulation, Hashemi et al. (2014) proposed a straightforward classification of NSs: i) NSs with properties similar to tested PSs and experiencing very similar loading histories; ii) NSs with properties similar to tested PSs and experiencing different loading histories; and iii) remainder NSs that are no similar to tested PSs. For the first category of NSs, the experimental response could be used directly to update NSs parameters. With regard to the second category of NSs, numerical parameters can be updated with some conversion or modification. Discussed state-of-art case studies fall within first two categories and exploit online implementations. In the author's knowledge, there is a lack of publications concerning the third, and most challenging, category where completely different NSs and PSs are of concern. Moreover, so far, nobody investigated the interaction between estimator and emulated system dynamics, which can jeopardize the hybrid simulation process.

2.2 HSDS of PSs characterized by a complex geometry

Since the introduction of the HSDS technique to evaluate seismic performance of structures, simple structural schemes of PSs and NSs confined its applicability range. In fact, shear type frames, inverted pendulum and chain-like systems were traditionally tested as PSs. Nevertheless, such approach fails in the case of complex specimens characterized by a number of DoFs greater than the actuator provision. In the author's knowledge, very few attempts were done to overcome this limitation. Hashemi and Mosqueda (2014) developed an innovative HSDS technique for multistory building and based on subdomain overlapping. Additional sensing of internal member forces in experimental columns were used within the feedback loop for the HSDS. One assumption used in the past was a pin at the likely inflection point of beams and columns. The pin simplifies the interface between numerical and experimental substructures and conveniently does not require control of rotations and moments at the boundaries. However, except first story columns, the remainder usually displays a random distribution of its position.

Since typical industrial plants are characterize by complex geometries, they are not prone to classic HSDS implementations, where PS matrices are condensed at few interface DoFs. Nonetheless, piping systems play a highly important role in many industries, such as petrochemical, oil and gas and nuclear plants, and a single failure can trigger serious accidental chains. Therefore, a special attention to evaluate their safety represents an imperative requirement. In fact, such systems, elbows, Tee joints and flange joints as well as support structures suffered significant damages during recent earthquakes causing severe losses both to human lives and to environment (Krausmann et al., 2010; Paolacci et al., 2013). This led researchers to carry out considerable studies on the seismic safety assessment of piping systems and their components (Touboul, 2006; Reza, 2013). However, so far only few experimental investigations -mainly through shaking table tests- have been performed on such structures at full-scale under realistic seismic loading (De-Grassi and Hofmayer, 2008; Otani and Shiratori, 2011). The need for applying the hybrid simulation technique to typical industrial plant components in a realistic context of a branched and twisted piping network subjected to realistic seismic loading

represents an impelling need.

A lot of effort was devoted to couple numerical and physical substructures in the context of linear system theory (Rixen and van der Valk, 2013; Voormeeren and Rixen, 2012), where frequency- and impulse-response-based approaches are allowed. Although HSDS offers a powerful framework for combining physical and numerical subsystems, there is still a lack of effective and flexible methods that enable the implementation of geometrically complex PSs.

2.3 Partitioned time integrators for continuous testing

While coupling two or more substructures, two conditions must hold at interface DoFs: i) compatibility on kinematic quantities and ii) force balance. Therefore, the so called transfer system, i.e. actuators and relevant feedback sensors managed by real-time operating systems, must reproduce such conditions. Concurrently, the computational driver provided with the numerical simulation environment solves the NS and integrates the coupled equations of motion. When PSs show a rate independent behaviour, extended experimental time scales can relax testing limitations owing to control accuracy and actuator capacity. Typical time scales λ range between 50 and 200, and this is the case of Pseudo-Dynamic Testing (PDT), where inertial and damping components of physical restoring forces are numerically simulated. Conversely, when rate dependent effects are significant, no extended time scales can be exploited and Real-time Testing (RT) strategy must be selected, i.e. $\lambda = 1$. For the sake of simplicity, HSDS refers to the PDT case in the present paper. As far as complexity of emulated structural systems increases, the role of time integration becomes more and more crucial. In fact, todays state-of-the-art servo-hydraulic control systems run at sampling times Δt of the order of 1 ms and below. This means that new displacement values are required at very short and deterministic time intervals for the signal generation of smooth actuator commands, which preserve the optimum signal/noise ratio of the continuous testing method. On the other hand, the computational driver can take much more time to solve complex NSs and to integrate the equation of motion. Necessarily, numerical and physical sides run at different rates and the need for a synchronization of the two time integration processes arises.

From this perspective, parallel partitioned time integration algorithms, which al-

low for the concurrent solution of involved subdomains with different time steps, represent a very attractive approach. In fact, they maintains the smoothness of the displacement trajectory avoiding any extrapolation/interpolation assumption. In particular, the Finite Element Tearing and Interconnecting (FETI) method emerged as one of the most powerful domain decomposition method for quasi-static mechanical problems (Farhat and Roux, 1991); later, the FETI was extended to transient problems (Farhat et al., 1995). In order to couple involved subdomains, Lagrange multipliers impose continuity conditions at the shared interface nodes. Gravouil (2001) proved that velocity continuity at the interface leads to a stable algorithm. In particular, they conceived a multi-time-step coupling method, labelled as the GC method, able to couple arbitrary Newmark schemes with different time steps in different subdomains. In this context, they proved that the GC method is unconditionally stable as long as all individual subdomains satisfy their own stability requirements. Unfortunately, the GC is a sequential staggered algorithm where the tasks in different subdomains are not concurrent. In order to solve this problem, Pegon and Magonette (2002) developed and implemented an enhanced parallel partitioned algorithm, the PM method; it was based on the GC method, but the NS and the PS states advance simultaneously and continuously, as proved in the laboratory on several structural hybrid systems. The PM method was deeply investigated by Bonelli et al. (2008), who proved its convergence and stability characteristics. Energy dissipation at the interface and the loose of one order of accuracy in the case with subcycling were pointed out as major drawbacks. Bursi (2010) proposed an extension of the PM method that enables arbitrary Generalized-α schemes to be coupled with different time steps in each subdomain, i.e. the PM method. The Generalized-α method is well known for its favorable user controlled algorithmic damping feature that allows for filtering out spurious high-frequency components but preserving low-frequency components. Prakash and Hjelmstad (2004) developed a variant of the GC method, the so-called PH method, achieving energy preservation by eliminating the calculation of interface reactions at the fine time step. Nonetheless, the PH method remains a staggered procedure. In fact, residuals of the interpolated balance equation of the free problem related to the coarse time grid subdomain must be accounted for as interface loading for the solution of

the free problem related to the fine grid subdomain. As a result, the PH method preserves second order accuracy in the case with subcycling but negates for the implementation of continuous HSDS. The GCbis method developed by Mahjoubi (2010) overcame such strict limitation. In particular, the same interpolation setting of the GC method was applied to free kinematic quantities, whilst interface reactions were calculated at coarse time steps as for the PH method. Hence, interpolated Lagrange multipliers entered the balance equation of the subdomain characterized by the finer time step in place of aforementioned residual interface forces. As a result, no information exchange between subdomains was required and parallel implementations were enabled. Moreover, the self-starting capability of the GCbis method, which paves the way for simpler implementations, makes it very attractive for the purpose of HSDS despite it is not yet considered.

All partitioned time integration algorithms described so far apply to the Euler-Lagrange form of the equation of motion. Within the framework of partitioned time integrators applied to the Hamilton form of equations of motion, Nakshatrala et al. (2008) proposed a FETI-based staggered method capable of accommodating different time integrators and time steps in diverse subdomains. This was made possible by using a differentiated kinematic constraint and by rendering explicit the calculation of interface Lagrange multipliers. The proposed method was non A-stable and stabilization techniques depending on arbitrary constants where required to reduced drift-off effects on interface quantities. Along the same line, Bursi et al. (2012) developed two partitioned schemes with subcycling capabilities but prone to parallel implementations. Both coupling schemes were conceived to combine a pair of Linearly Stable Real-Time (LSRT-2) compatible monolithic time integrators of the Rosenbrock type (Bursi et al., 2008). Both the primal, labelled as Parallel LSRT-2 (PLSRT-2), and its improved version, denoted as IPLSRT-2, operate with differentiated kinematic constraints applied to interface accelerations; therefore, first they explicitly solve the interface problem by means of Lagrange multipliers and then, they advance the solution in all the subdomains. Since both the PLSRT-2 and the IPLSRT-2 were not endowed with self-starting capabilities, modified staggered implementations were implemented as initialization procedures. Therefore, experimental validations were conducted on a 2-DoF system.

CHAPTER 3

DYNAMIC SUBSTRUCTURING OF THE FIBER-BASED FINITE ELEMENT MODEL OF THE RIO TORTO BRIDGE FOR HYBRID SIMULATION PURPOSES

3.1 Introduction

The assessment of seismic performances of an old concrete bridge was conceived within the RETRO transnational activity funded by the SERIES European project (Fardis, 2009). The aim of the research study was twofold: i) to investigate the nonlinear response of reinforced concrete pier portal frames provided with plain steel reinforcement bars; ii) to estimate the effectiveness of seismic isolation systems applied to this class of structures. In particular, the Rio Torto Bridge was selected as case study. Characterized by $400m$ of total span and plain steel bar reinforcements, it was underdesigned with respect to seismic requirements dictated by both Italian and European actual codes (NTC-2008, 2008; EUROCODE-8, 2004). The installation of a pair -one per column- of Friction Pendulum Bearing (FPB) isolation devices interposed between the deck and the cap beam of each pier portal frame was proposed as seismic retrofitting. In order to simulate the dynamic response of one of the two independent roadways, a comprehensive set of hybrid simulations was conceived for both the isolated and the non isolated cases. Since piers exhibited hysteretic responses already at serviceability limit state, nonlinear NSs were deemed necessary to conduct realistic simulations. Entailing parameters were tuned according to the fiber-based OpenSEES FE Reference Model (RM) of the bridge. First, the Rio Torto case study is introduced and both the as-built and the retrofitted configurations are discussed. Then, the OpenSEES RM

(a)

(b) (c)

Figure 3.1: **a** View of the Rio Torto viaduct, **b** Detail of portal piers, **c** Detail of the deck

is presented to support the implementation of all NSs. Results of time history analyses of the OpenSEES RM justified the selected substructuring scheme. In greater detail, the Guyan method (Guyan, 1965) was applied to each pier portal frame to obtain reduced linear stiffness and mass. Resulting S-DoF reduced models were extended to the nonlinear range by means of nonlinear springs capable of reproducing the displacement responses of OpenSEES piers. With regard to FPB isolation devices, suitable S-DoF reduced models were based on a bilinear state space model (Mostaghel, 1999). Validations of reduced models of the Rio Torto Bridge based on substructured components follow. Finally, conclusions are drawn.

3.2 Description of the case study

The Rio Torto Bridge is characterized by two independent roadways. Twelve portal piers support each thirteen-span deck. Extreme spans measure $29m$, whilst internal span $33m$. Figure 3.1 collects views of viaduct portal piers and concrete deck. Figure 3.2 depicts the structural scheme of the single roadway. Each pier

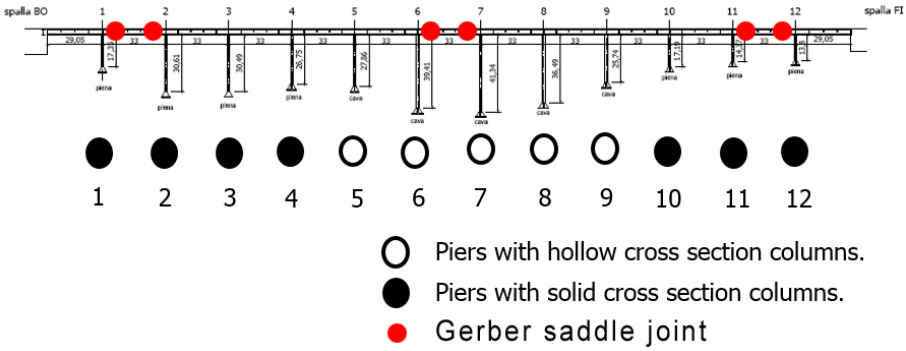

Figure 3.2: Structural scheme of the Rio Torto Bridge

Pier	Height [m]	Pier	Height [m]	Pier	Height [m]
1	17.35	5	27.86	9	25.74
2	30.61	6	39.41	10	17.19
3	30.49	7	41.34	11	14.37
4	26.75	8	36.49	12	13.80

Table 3.1: Heights of piers of the Rio Torto Bridge

portal frame is composed by two solid or hollow circular columns of variable diameter, 1200mm and 1600mm, respectively. They are connected by a cap-beam at the top and by one or more transverse beams of rectangular section at intermediate levels. Table 3.1 summarizes heights of piers. As can be appreciated in Figure 3.2, six Gerber saddles are placed in the middle of the bridge and close to both abutments. Figure 3.3 reports a close-up view of one of the Gerber saddles. As highlighted by Figure 3.4, which depicts the cross section of the deck, two vertical dowels constraint the deck to each pier. Conversely, abutment bearings are realized with fixed devices. Geometrical properties of the cross section of the deck are reported in Table 3.2. The calculation of the linear weight of the deck is summarized in Table 3.3. In order to achieve seismic performance requirements of EUROCODE-8 (2004), the removal of Gerber saddles and the installation of a pair of FPB isolators -one per column of each pier- were proposed as seismic retrofitting. The isolation system was designed according to the di-

Figure 3.3: Detail of one Gerber saddle

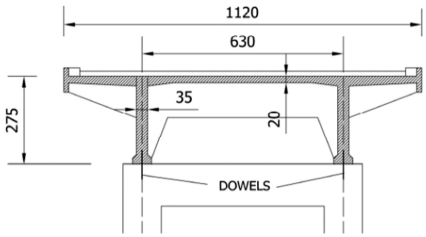

Figure 3.4: Cross section of the deck

Area [m^2]	I_x [m^4]	I_z [m^4]	J [m^4]
4.63	3.45	51.90	0.1027

Table 3.2: Deck cross section properties

Element	Linear weight [kN/m]
RC deck	112
Slab	6
Stiffners	10
Alphalt	30
Guard rail	2
Waterproof	1
Parapet	5
Total	166

Table 3.3: Calculation of the linear weight of the deck

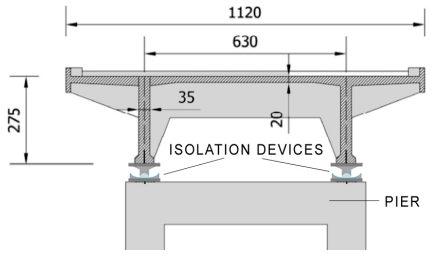

Figure 3.5: Layout of isolation devices on a generic piers

rect displacement-based procedure proposed by Priestley (2007). It focused on two objectives: i) to keep pier responses in the elastic range; ii) to minimize the displacement demand at abutment expansion joints. The design of the isolation system for the Rio Torto viaduct can be found in De Risi and Taucer (2011). According to Figure 3.5, each pair of FPB devices were interposed between the cap beam of the relevant pier portal frame and the deck. In greater detail, isolators with one spherical sliding surface with an height of articulated slider of 90mm were considered to seismically isolate the Rio Torto bridge. As shown in Figure 3.6, the basic elements of the single-surface FPB device are: the upper anchor plate (1), the sliding surface (2), the sliding material interface (3), the rotation element (4), the rotation sliding surface (5) and the lower anchor plate (6). As can be appreciated in Figure 3.6(b), employed FPB devices provided regular hysteretic loops. In

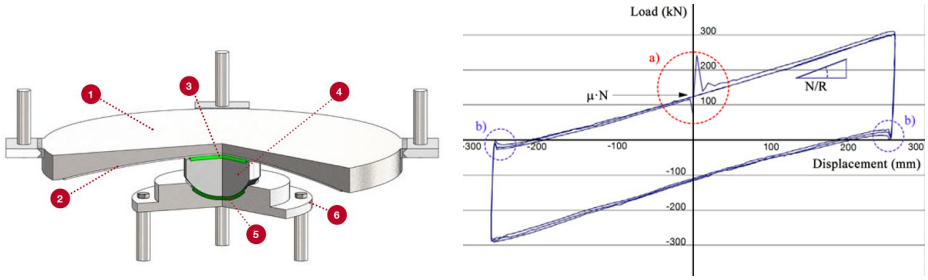

(a) (b)

Figure 3.6: **a** scheme of a single-surface FPB device and its **b** typical shear hysteretic loop

greater detail their beahviour can be expressed by the bilinear force displacement relationship of Eq. 3.1.

$$V_{FPB} = \mu_f N + \frac{N}{R}\Delta_{iso} \tag{3.1}$$

where: V_{FPB} is the shear restoring force, μ_f is the friction coefficient, N is the vertical load, R is the curvature radius of the device and Δ_{iso} is the sliding displacement in the isolator. With reference to full-scale dimensions, the radius R of the FPB used for the seismic retrofitting of the Rio Torto was $3.00m$ and a 4.00% friction coefficient μ_f was assumed. The initial yield displacement of devices was 0.5mm. Since each pier portal frame bears a vertical load varying between $5600kN$ and $5300kN$, the vertical load N acting of the single device varies between $2800kN$ and $2650kN$. The threshold shear force was 7500kN. The E-W and the N-S components of the Emilia earthquake of 2012 were considered as Serviceability Limit State (SLS) and Ultimate Limit State (ULS) seismic actions, respectively. Figure 3.7 depicts both accelerograms. The SLS accelerogram was characterized by $2.56m/s^2$ PGA, whilst the ULS accelerogram by $2.67m/s^2$ PGA. Relevant acceleration and displacement response spectra are compared in Figure 3.8. With regard to Figure 3.8, dash lines correspond to first four fundamental periods of the bridge obtained from the modal analysis of the OpenSEES RM presented in the next section. Though PGAs are very close, corresponding displacement and acceleration spectral responses at ULS double SLS values.

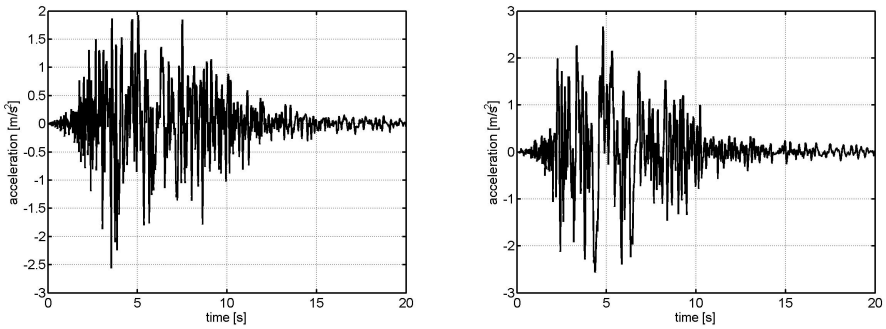

(a) (b)

Figure 3.7: **a** SLS and **b** ULS accelerograms

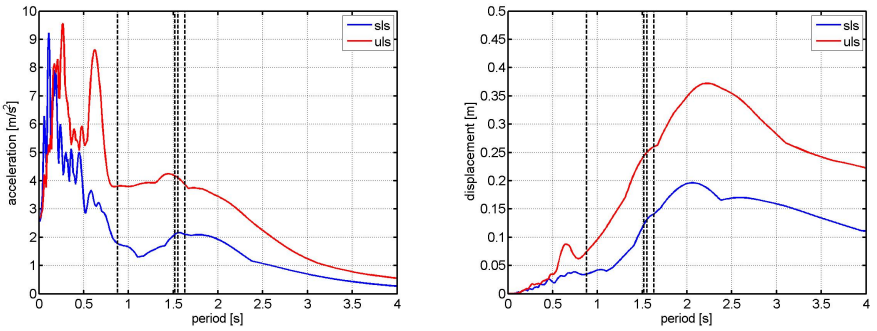

(a) (b)

Figure 3.8: **a** Acceleration and **b** displacement response spectra of both SLS and ULS accelerograms

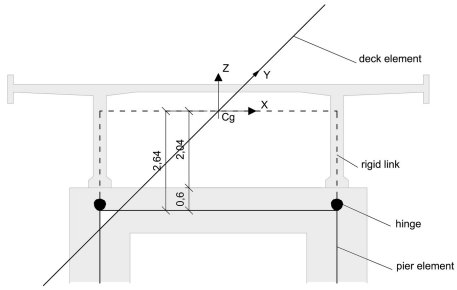

Figure 3.9: Details of the FE model of the pier-deck connection (dimensions in m)

3.3 The OpenSEES FE Reference Model

In order to support the design of hybrid simulations, a refined OpenSEES fiber-based FE RM able to simulate the hysteretic behavior of piers was set (Paolacci and Giannini, 2012). Piers were considered clamped at the base; translational DoFs of both abutments were fixed whilst rotations released. To take into account the offset distance between the center of gravity of the deck cross section and the cap beam axis, each pier was connected to the deck through a rigid link. In detail, each rigid link was considered fixed to the deck and hinged to the relevant pier, as shown in Figure 3.9. Gerber saddles were modeled as hinges allowing for longitudinal and transversal shear transfer. Linear beam elements were adopted to model the deck. Piers were discretized with nonlinear beam elements. In greater detail, fibers elements were considered. They allowed for an accurate discretisation of cross sections, reproducing the exact position and dimension of reinforcing bars and concrete with relevant constitutive laws. Figure 3.10 depicts the OpenSEES fiber based FE model of Pier #12 characterized by solid cross section columns. According to previous experimental tests, the contribution of the concrete tensile strength may be neglected in the case of plain steel bars and poor seismic details (Alessandri, 2013). As a consequence, the Kent-Scott-Park model was employed to simulate the concrete behavior (Kent and Park, 1971) that is implemented in the *Concrete*01 OpenSEES material. According to Figure 3.11, which depicts the constitutive law of the *Concrete*01 material, a first parabolic branch reaches the maximum compressive strength f_{pc}, which was assumed equal to 26MPa; the corresponding compressive yielding strain $*epsc*0 was assumed equal to 0.25%.

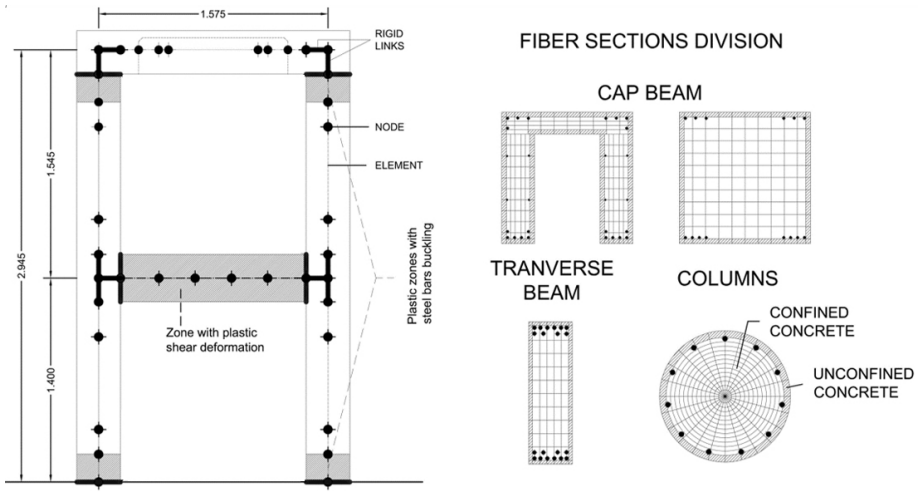

Figure 3.10: Scheme of the OpenSEES fiber-based FE model of Pier #12

Then a decreasing linear branch connects the maximum compressive strength $f_{pc} and the ultimate compressive strength $f_{pcu}, which was assumed equal to 22MPa with a corresponding ultimate strain $epsU of 0.6%. Reinforcing steel bars were modeled according to the Menegotto-Pinto constitutive law (Menegotto M., 1973), which is implemented in the *Steel*02 OpenSEES material. Figure 3.12 depicts the relevant constitutive law. The yielding stress f_y was assumed equal to 360MPa, along with a Young modulus of 205000MPa; the hardening parameter was set equal to 0.025. A phenomenological shear-strain hysteretic relationship was assumed for the shear nonlinear behavior of the transverse beam in the presence of plain longitudinal bars. It consisted of a trilinear envelope curve. The influence of axial forces was neglected. It was implemented by means of the OpenSEES *hysteretic* material whose force-deformation relationship is depicted in Figure 3.13. In particular, forces were obtained according to the formulation proposed by Priestley et al. (1994), based on the Modified Compression Field theory (Vecchio, 1988). The total shear strength V_t is the sum of concrete and reinforcement contributions, i.e.

$$V_t = V_c + V_s \tag{3.2}$$

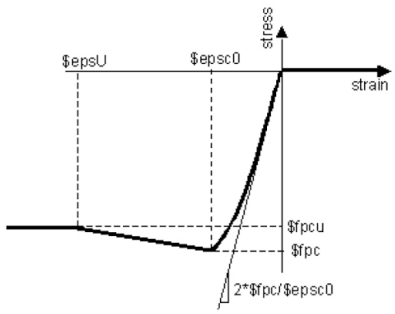

(a)

Figure 3.11: Constitutive laws of *concrete01* OpenSEES materials

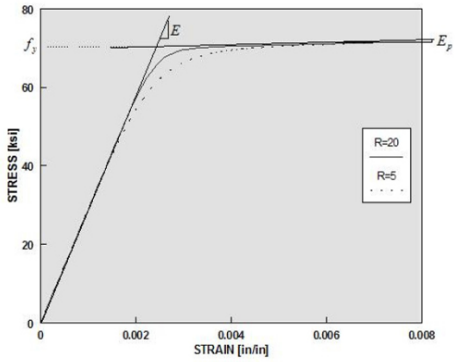

(a)

Figure 3.12: Constitutive laws of *steel02* OpenSEES materials

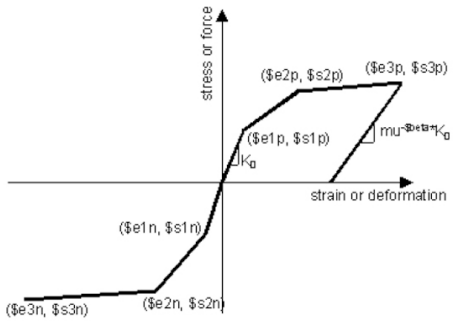

(a)

Figure 3.13: Constitutive laws of *hysteretic* OpenSEES materials

with:

$$V_c = 0.8 k_d \sqrt{f_c} A_c \tag{3.3}$$

$$V_s = A_{sw}/s_s f_y D \cot(\theta) + (\sin(\beta) A_{sp})/s_p f_y D(\cot(\theta) + \cot(\beta)) \tag{3.4}$$

where: f_c is the compressive concrete strength and f_y is the steel yield strength. Same parameters assumed to define fiber materials were considered. In particular, f_c was set equal to 26MPa, whilst f_y was assumed equal to 360MPa. A_c is the cross section area, A_{sw} and A_{sp} are stirrups and inclined rebars (with angle β) areas; relevant spacing are s_s and s_p, respectively. D is the cross section depth. For the calculation of V_c, the curvature ductility-dependent coefficient k_d was set to 0.20. According to Figure 3.13, $\$s1p$ was assumed equal to V_c, whilst both $\$s2p$ and $\$s3p$ were assumed equal to V_t. Corresponding shear deformations $\$e1p$, $\$e2p$ and $\$e3p$ were assumed equal to $3.5e-4$, $1e-3$ and $1e-2$, respectively. They were characterized on previous cyclic tests on the mock-up 1/4 scale specimen of Pier #12 (Paolacci and Giannini, 2012). The hysteretic shear material was coupled to the flexural behavior by using the *section aggregator* OpenSEES command; as a result, balance equations accounted for both shear and flexural behaviors, even though their mechanical formulations were uncoupled. In order to simulated the Rio Torto Bridge in the isolated case, the OpenSEES RM was modified according to the foreseen seismic retrofitting. According to the arrangement depicted in Figure 3.5, a pair of *Single Friction Pendulum Bearing* OpenSEES elements were interposed between each portal pier frame and the rigid link element supporting the deck. Figure 3.14 depicts the scheme of such elements. With regard to Figure 3.14, the *iNode* represents the concave sliding surface and the *jNode* represents the articulated slider. Isolators were implemented considering the effective element depth. In order to reproduce the uplift behavior of FPBs, a zero tensile strength *UniaxialMaterial* was specified in the axial direction. P-Delta moments were entirely transferred to the concave sliding surface at *iNode*. It is important to note that rotations of the concave sliding surface at *iNode* affect the shear response. A comprehensive set of time history analyses of the resulting OpenSEES RM was carried out to estimate the dynamic response of the bridge

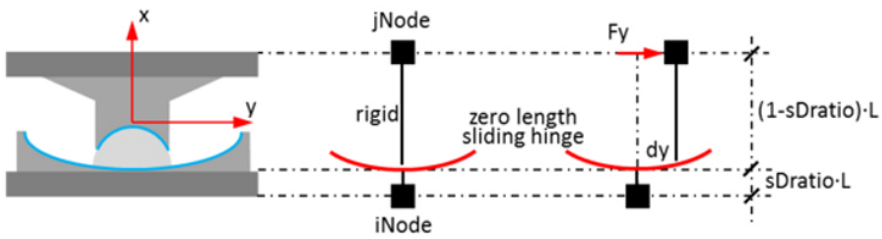

Figure 3.14: Scheme of the *Single Friction Pendulum Bearing* OpenSEES element

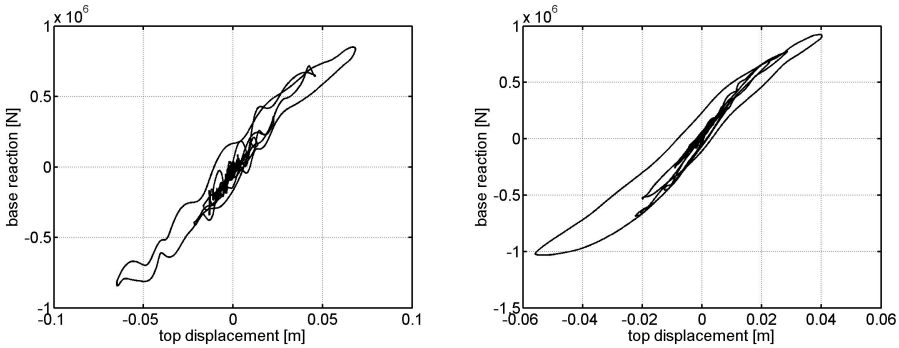

(a) (b)

Figure 3.15: Cap beam displacement vs. base reaction force plots relevant to transversal responses of: **a** Pier #9; and **b** Pier #11 at SLS in the non isolated case

at both the Serviceability Limit State (SLS) and Ultimate Limit State (ULS). Figure 3.15 reports hysteretic loops relevant to Piers #9 and #11 (PSs) for both limit states in the non isolated case. Displacement were measured at the cap beam level of each pier; forces refer to relevant base transversal reactions along the same X direction. As can be appreciated in Figure 3.15(b), Pier #11 shows a slight hysteretic response already at SLS. Figure 3.16 depicts hysteretic loops of same piers at ULS. In principle, hysteretic loops of tall piers, such as Pier #9, are more jagged than those of short piers, such as Pier #11. Time history analyses were conducted in the isolated case and they proved that piers remained essentially in the linear range. Figure 3.17 shows hysteretic loops of same Piers #9 and #11 subjected to

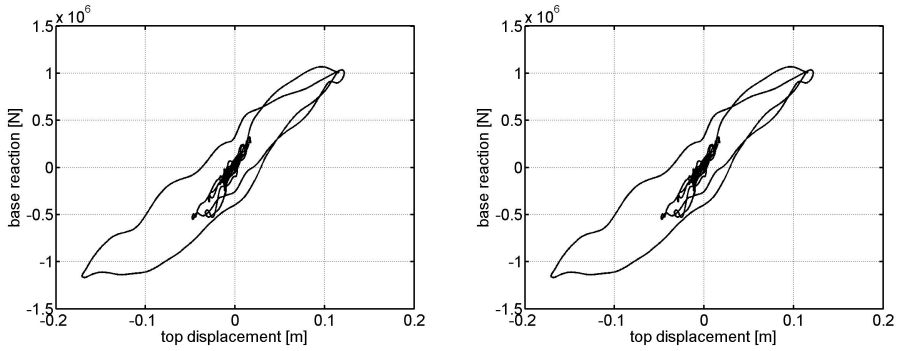

Figure 3.16: Cap beam displacement vs. base reaction force plots relevant to transversal responses of :**a** Pier #9; and **b** Pier #11 at ULS in the non isolated case

the SLS accelerogram in the isolated case. As can be appreciated by Figure 3.17, narrow loops confirm that piers remained in the linear range. According to Figure 3.18, same considerations can be drawn for the ULS. Dynamic responses of relevant isolator pairs confirm that FPB devices carry the most of the hysteretic energy dissipation. Figures 3.19 and 3.20 depict dynamic responses of right isolators of Piers #9 and #11 at SLS and ULS respectively. In detail, displacements refer to slip movements within devices. According to Figures 3.19 and 3.20, FPB devices play a fundamental role at both limit states; they entail high levels of hysteretic energy dissipation and keep responses of piers in the linear range.

3.4 Dynamic substructuring of the Rio Torto Bridge for the purpose of hybrid simulation

Todays state of the art servo-hydraulic control systems run at sampling times Δt of the order of $1 msec$ and below. With regard to the continuous time hybrid simulation technique, this means that new displacement values are required at very short, deterministic time intervals for the signal generation of the actuator commands. On the other hand, the numerical integration of the system of equations of motion, which is performed in the finite element analysis software, can be very time consuming. In addition, the computation times required to advance the numerical

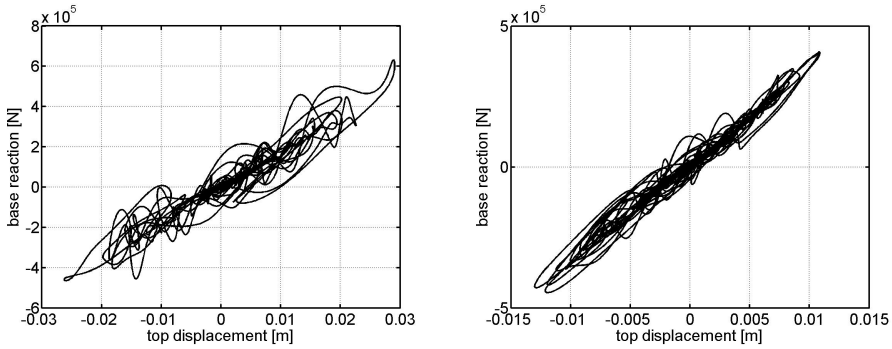

(a) (b)

Figure 3.17: Cap beam displacement vs. base reaction force plots relevant to transversal responses of: **a** Pier #9; and **b** Pier #11 at SLS in the isolated case

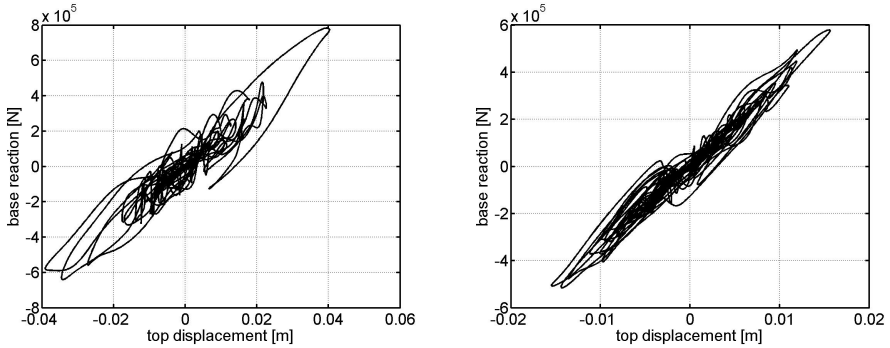

(a) (b)

Figure 3.18: Cap beam displacement vs. base reaction force plots relevant to transversal responses of: **a** Pier #9; and **b** Pier #11 at ULS in the isolated case

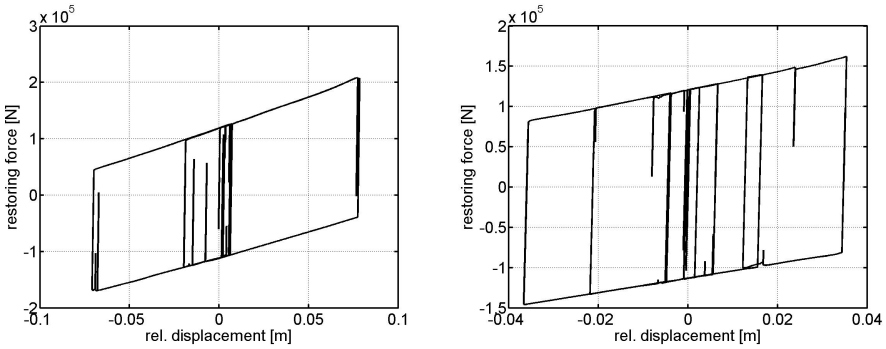

Figure 3.19: Relative displacement vs. restoring force relevant to right FPB devices installed on: **a** Pier #9; and **b** Pier #11 at SLS

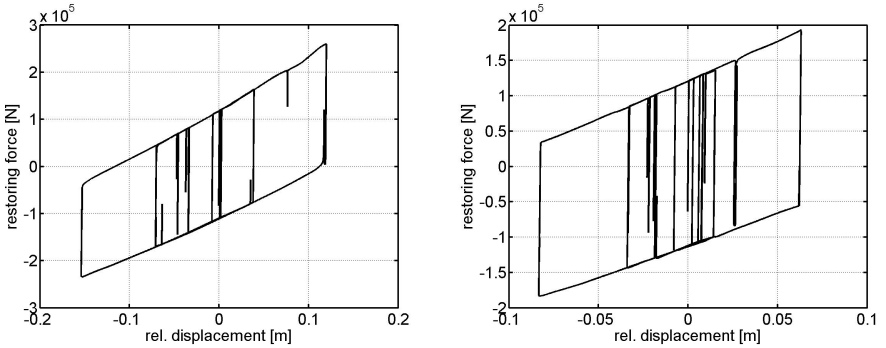

Figure 3.20: Relative displacement vs. restoring force relevant to right FPB devices installed on: **a** Pier #9; and **b** Pier #11 at ULS

solutions to the next step are generally nondeterministic when iterative solver are selected. Hence, the computational driver and the servo- hydraulic control system run at different time rates, where the former is nondeterministic and the latter is deterministic. However, it is possible to synchronize these two processes; different algorithms were successfully implemented (Schellenberg, 2009) and adopted for the HSDS of full-scale bridges (Terzic and Stojadinovic, 2013). The parallel partitioned time integration scheme developed by Pegon and Magonette (2002), i.e. the PM method, represents a valuable alternative and was used for the hybrid simulation of the Rio Torto Bridge, . Since it allows for subcycling, the time integration of the NS advances at a coarse time step Δt_A, whilst a smallest time integration step $\Delta t_B = \Delta t_A / n$ is considered for the PS; n defines the subcycling. Since a PDT is performed at an extended time scale λ, typically 50-200 times slower than the actual earthquake time, the following relationship holds:

$$\Delta t_B = \frac{\Delta t}{\lambda} \tag{3.5}$$

As a consequence, the subcycling parameter n can be expressed as,

$$n = \frac{\Delta t_A}{\Delta t} \lambda \tag{3.6}$$

The upper bound of the available solving time for the calculation of NS response is $n\Delta t$. Since the controller time step Δt is fixed, n must be increased to allow longer solving times. Nonetheless, large time scales λ entail structural relaxation issues and thus are not recommended. Moreover, large Δt_A degrade the numerical solution of the NS. As a consequence, subcycling allows for increasing the available solving time of the NS but it must be limited to preserve the quality of the experimental test. In this particular case, a time scale factor λ equal to 200 was considered; the coarse time step Δt_A was set equal to $0.0025s$, whilst the controller time step was $0.002s$. The resulting subcycling $n = 250$ entailed a solving time of $0.5s$. The PM method was implemented on a real-time computer at the ELSA laboratory of JRC (Ispra (VA), Italy). Conversely, the CAST3M FE code running on a Windows based system solved the nonlinear NS. Controller and CAST3M machine interacted through a Gigabit Ethernet network. Communication times further reduced the effective solving time available. From this perspective, a rational

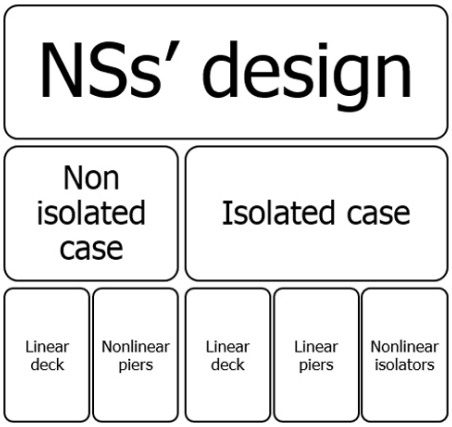

Figure 3.21: Substructuring scheme for the reduction of the OpenSEES RM of the Rio Torto Bridge

reduction of the aforementioned OpenSEES RM was devised for hybrid simulation purposes. The dynamic substructuring approach was selected (Klerk et al., 2008). In greater detail, the deck, each single pier and each single pair of isolation devices were considered as subparts of the global emulated system. Since two of the twelve piers with relevant isolation devices were replaced by their physical counterparts, such component wise approach was preferable. Moreover, simple models characterized by a few DoFs and localized nonlinearities can be easily reproduced regardless the available experimental equipment is. The substructuring scheme adopted for the reduction of the bridge model is reported in Figure 3.21. According to the OpenSEES RM, the substructured deck of the reduced model of the Rio Torto Bridge was considered as linear. In detail, linear beam elements with a consistent mass matrix formulation were adopted. As highlighted by Paolacci and Giannini (2012), during the seismic event most of the damage was concentrated within piers, which carry the most of the hysteretic energy dissipation. In order to quantify such energy dissipation, time history analyses of the OpenSEES RM in both the isolated and the non isolated cases. Histograms depicted in Figure 3.22 reports obtained values. Clearly, piers experience greater dissipation at ULS where the bridge is much more excited. Small energy dissipation characterize piers in the isolated case confirming the effectiveness of the proposed retrofitting

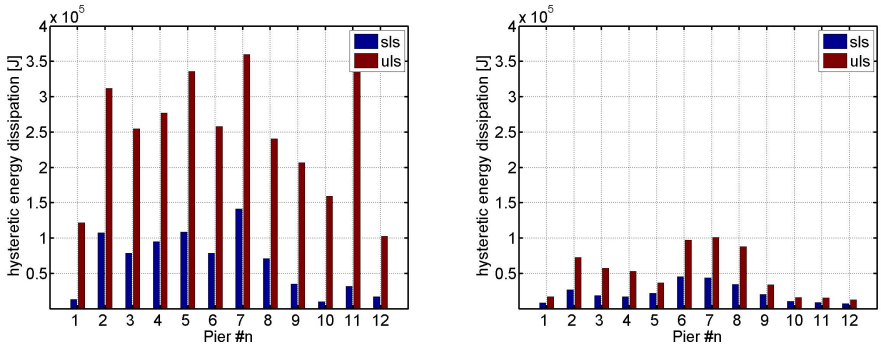

Figure 3.22: Hysteretic energy dissipation of piers in the: **a** non isolated case; **b** isolated case

scheme. In particular, Figure 3.23 shows the distribution of the dissipated energy among piers and relevant FPB pairs. According to Figure 3.23, isolators dissipate the most of the hysteretic energy in the isolated case. As a consequence, linear substructured piers were considered for the reduced model of the isolated bridge; in greater detail, parameters of Table 3.7 were kept and nonlinearities were confined to substructured FPB pairs. This additional assumption allows for the simplification of the reduced model of the bridge in the isolated case.

3.4.1 ANSYS linear models of bridge

In order to provide linear stiffness and mass matrices, an 832-DoFs ANSYS Reference Model (RM) of the bridge was implemented. With respect to the linear range, the same constraint conditions, cross sections, material properties and equivalent viscous damping of the OpenSEES RM were considered. In detail, a 5% Rayleigh equivalent viscous damping was applied considering eigenmodes carrying the most of the modal mass, i.e. Mode #2 and #4. To avoid matrix ill-conditioned cases, a consistent formulation was adopted for the ANSYS based models, whilst OpenSEES allows for lumped mass matrices. Table 3.4 summarizes modal characteristics of the ANSYS RM. Modal mass fractions and their cumulative values refer to the seismic loading direction, i.e. the *X* direction, which is transversal to be deck axis. With regard to Table 3.4,the following relationship holds:

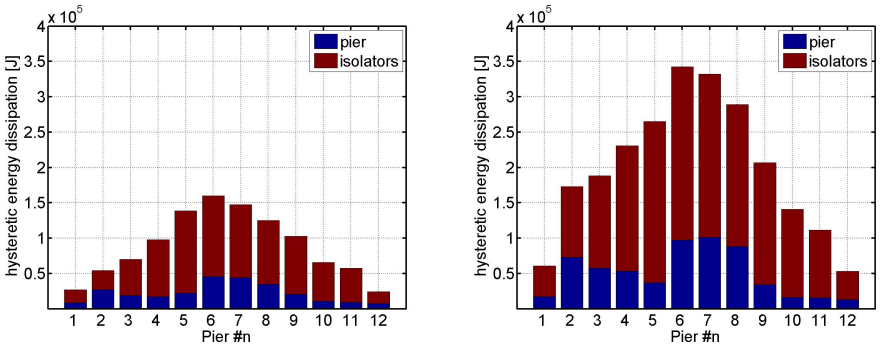

Figure 3.23: Distributions of hysteretic energy dissipation between piers and relevant isolator pairs at: **a** SLS; and **b** ULS

Mode	Frequency [Hz]	m_k	M_k
1	0.6254	0.0269	0.0269
2	0.6452	0.4912	0.5181
3	0.7017	0.1167	0.6348
4	1.1023	0.2069	0.8417
5	1.2183	0.0457	0.8874
6	1.2429	0.0003	0.8877
7	1.2453	0.0000	0.8877
8	1.2460	0.0039	0.8916
9	1.3757	0.0018	0.8934
10	1.3917	0.0484	0.9418

Table 3.4: Modal characteristics of the ANSYS RM

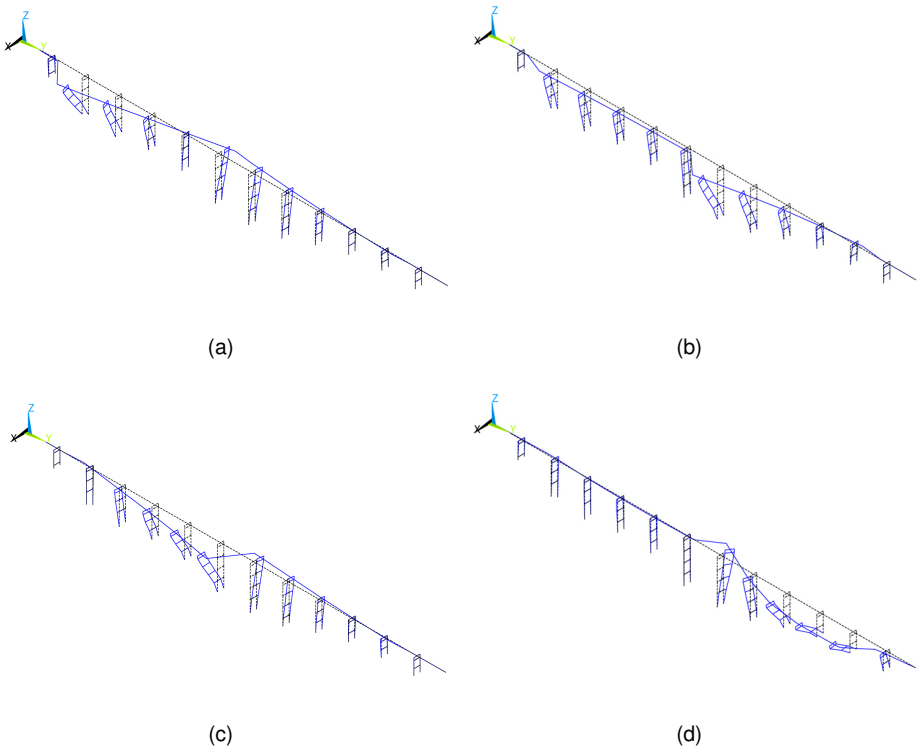

Figure 3.24: Eigenmodes of the ANSYS RM of the Rio Torto Bridge in the non-isolated case: **a** #1; **b** #2; **c** #3; and **d** #4

$$M_k = \sum_{i}^{k} m_i \tag{3.7}$$

where m_i is the modal mass fraction calculated by the ANSYS FE code with respect to X translational inertial loads. As can be appreciated, first four eigenmodes carry up to the 84% of the modal mass in the seismic loading direction. They are depicted in Figure 3.24. They synthesize the transversal response of the deck and govern the dynamic response of the bridge subjected to the foreseen seismic action. Time history analyses conducted on the aforementioned ANSYS RM highlighted that piers experience mainly in-plane deformations; as a result, a significant simplification of the internal constraint setting was allowed. In detail, a further ANSYS Simplified Model (SM) characterized by 808-DoFs was introduced. According to Figure 3.25, out-of-plane displacements of piers were fixed, whilst relative rota-

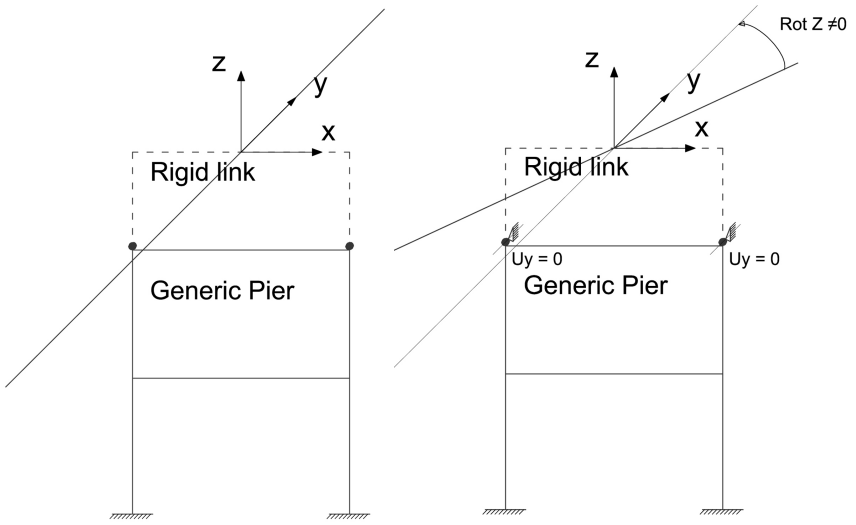

Figure 3.25: Deck-pier constraint setting of the **a** ANSYS RM and the **b** ANSYS SM

tions among the deck and piers were released. First four eigenfrequencies of the ANSYS RM, the ANSYS SM and the OpenSEES RM are compared in Table 3.5: Both ANSYS linear models well agree with the OpenSEES RM. With regard to deformed mode shapes, the Modal Assurance Criterion (MAC) was considered. The MAC score is a coefficient analogous to the correlation coefficient in statistics or coherence in signal processing. It compares pair of mode shapes providing a unit

Mode	OpenSEES	ANSYS RM	ANSYS SM
1	0.6137	0.6254	0.6227
2	0.6432	0.6452	0.6433
3	0.6576	0.7017	0.7004
4	1.1383	1.1023	1.1007

Table 3.5: Comparison of modal frequencies of the models of teh Rio Torto Bridge

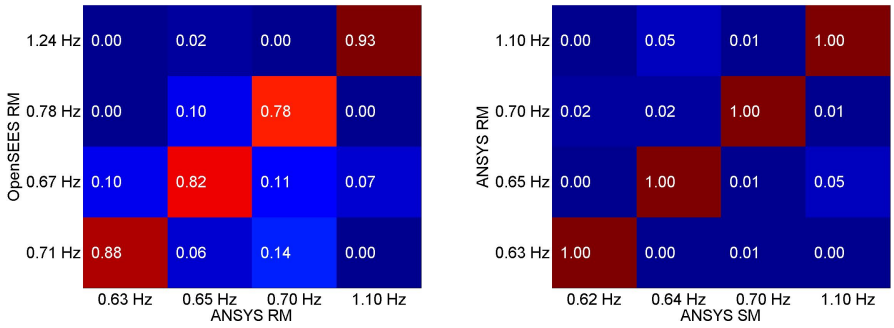

(a) (b)

Figure 3.26: MAC matrices between **a** OpenSEES RM and ANSYS RM and **b** ANSYS RM and ANSYS SM models

value for perfect correlation and a zero value for uncorrelated orthogonal modes.

$$MAC(\Phi_1, \Phi_2) = \frac{(\Phi_1^T \Phi_2)^2}{(\Phi_1^T \Phi_1)(\Phi_2^T \Phi_2)} \tag{3.8}$$

where Φ_1 and Φ_2 are a pair of mode shape vectors from models being compared. The MAC matrix depicted in Figure 3.26(a) compares deformed mode shape vectors of the OpenSEES RM and the ANSYS RM. The MAC matrix of Figure 3.26(b) compares deformed mode shape vectors of the ANSYS RM and the ANSYS SM. As can be appreciated in Figure 3.26(a), the OpenSEES RM well agrees with the ANSYS RM. The most of the discrepancy was due to different mass matrix formulations employed. The OpenSEES RM was characterized by a lumped mass matrix, whilst both ANSYS models were characterized by a consistent mass matrix. As can be appreciated in Figure 3.26(b), the modified constraint setting of the ANSYS SM did not affect low frequency modal characteristics of the ANSYS RM. Figure 3.27 compare deformed shapes of first four eigenmodes from ANSYS and OpenSEES FE models. Time history analyses were conducted on both OpenSEES and ANSYS models in the linear range. The SLS accelerogram scaled to $0.05g$ of PGA was considered as seismic input. A comparison in term of Normalized Root Mean Square Errors (NRMSEs) on transversal displacement, velocity and acceleration responses of piers measured at cap beam levels are presented as validation of ANSYS linear models of the bridge. In greater detail, NRMSE

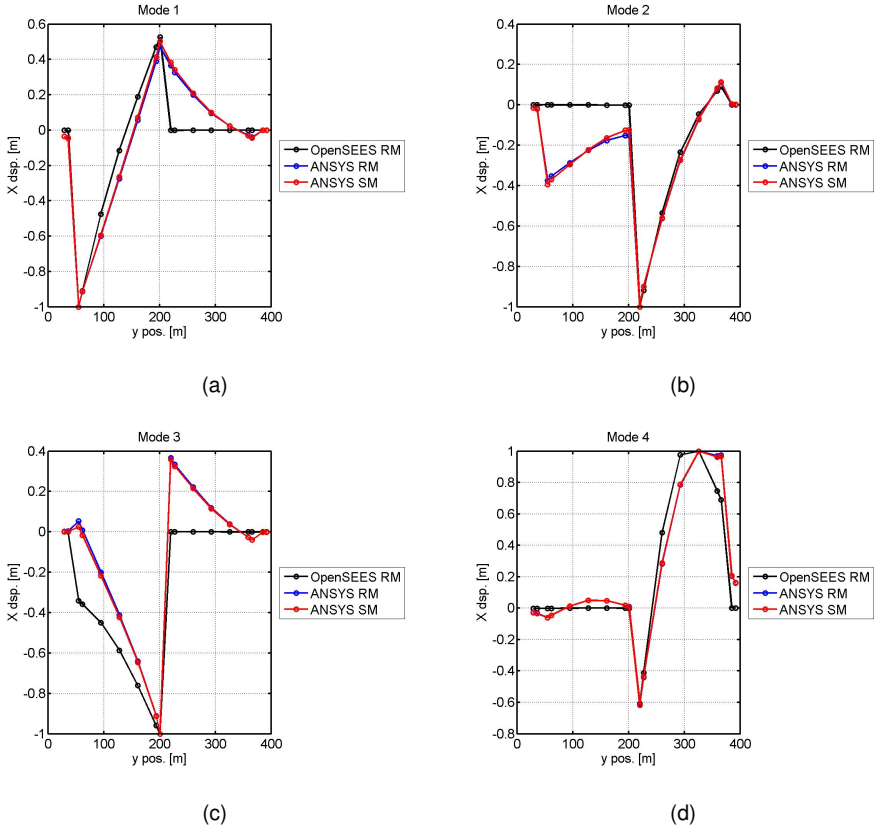

Figure 3.27: To view of deformed shapes of Modes **a** #1; **b** #2; **c** #3; and **d** #4

	ANSYS RM			ANSYS SM		
Mode	dis.	vel.	acc.	dis.	vel.	acc.
1	0.04	0.04	0.03	0.04	0.04	0.03
2	0.07	0.07	0.05	0.07	0.07	0.05
3	0.04	0.03	0.02	0.04	0.03	0.02
4	0.04	0.04	0.02	0.04	0.04	0.02
5	0.11	0.10	0.05	0.11	0.11	0.06
6	0.19	0.18	0.10	0.19	0.18	0.10
7	0.17	0.16	0.11	0.17	0.16	0.11
8	0.18	0.15	0.09	0.17	0.15	0.09
9	0.16	0.11	0.06	0.16	0.11	0.06
10	0.08	0.05	0.02	0.08	0.05	0.02
11	0.08	0.05	0.02	0.08	0.05	0.02
12	0.03	0.03	0.03	0.04	0.04	0.03

Table 3.6: NRMSE between linear responses of piers of OpenSEES RM and ANSYS models subjected to the SLS accelerogram scaled to 0.05 PGA.

reads,

$$\text{NRMSE}(\mathbf{y}_{ref}, \mathbf{y}_{red}) = \frac{\sqrt{\frac{1}{n}\sum_{i=1}^{n}(y_{red,i} - y_{ref,i})^2}}{y_{ref,\max} - y_{ref,\min}} \tag{3.9}$$

where subscript *red* stands for reduced, whilst subscript *ref* for reference, and y is a generic time history quantity, i.e. x,$\dot{x}$, $\ddot{x}$ and r. The NRMSE score is not sensitive to the amplitude -PGA value- of the seismic input in the linear range. Tables 3.6 summarizes NRMSE scores between ANSYS and OpenSEES models. As can be appreciated in Figure 3.28, both the ANSYS RM and the ANSYS SM were capable of reproducing the behavior of the OpenSEES RM in the linear range. Moreover, the ANSYS SM lent itself for an effective reduction of piers as plane superelements. As a result, it was considered as basis for the development of a reduced model of the bridge complying with the computational resources of the experimental equipment.

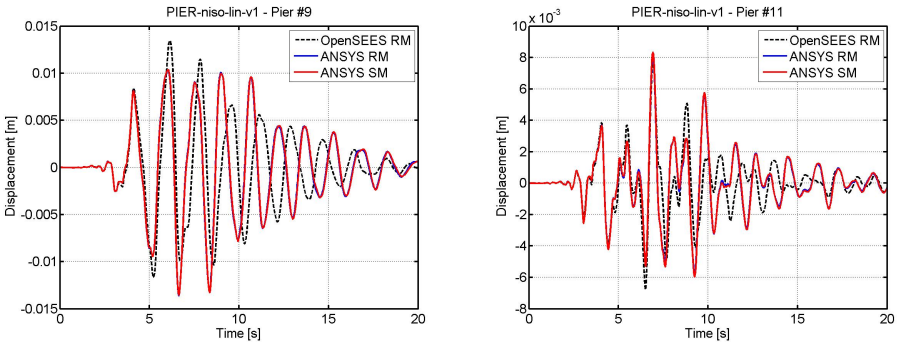

(a) (b)

Figure 3.28: Comparison of transversal displacement responses of: **a** Pier #9; and **b** Pier #11 measured at cap beam levels. The SLS accelerogram scaled to 0.05g of PGA was considered as seismic input.

3.4.2 Dynamic substructuring of piers

As anticipated, the ANSYS SM lend itself for the substructuring of piers as plane superelements. Since the seismic load excites mainly the four lowest global eigenmodes of the bridge, piers are substantially pulled along the *X* transversal direction indicated in Figure 3.24. In greater detail, local eigenmodes of piers were not excited. As a result, the so called Guyan reduction method (Guyan, 1965) was found to be very effective for the condensation of pier matrices. In detail the top transversal displacement DoF of each pier was considered as master, i.e. $\mathbf{u}_r$, whilst the remainder as slaves, i.e. $\mathbf{u}_l$. For the sake of clarity the entailing algebraic formulation is reported herein:

$$\mathbf{u} = \begin{bmatrix} \mathbf{u}_r \\ \mathbf{u}_l \end{bmatrix} = \begin{bmatrix} \mathbf{T} \end{bmatrix} \mathbf{u}_r \tag{3.10}$$

where:

- $\mathbf{u}_r$: master DoFs
- $\mathbf{u}_l$: slave DoFs
- $\mathbf{T}$: condensation matrix

Pier	$\bar{K}$ [N/m]	$\bar{M}$ [kg]	$\bar{F}$ [kg]
1	32211638	35106	45034
2	9934273	75300	103715
3	8834668	80397	108883
4	11947669	67167	90580
5	18401015	69616	96933
6	9468336	92891	132832
7	8426304	99025	140808
8	11186607	85172	122064
9	23560981	62955	88393
10	22920098	42569	56426
11	38140390	39013	50693
12	42660613	37068	48389

Table 3.7: Linear parameters of reduced S-DoF piers

According to the original formulation, linear parameters of reduced S-DoF piers read:

$$\bar{K} = \mathbf{T}^T \mathbf{K} \mathbf{T} \tag{3.11}$$

$$\bar{M} = \mathbf{T}^T \mathbf{M} \mathbf{T} \tag{3.12}$$

$$\bar{F} = \mathbf{T}^T \mathbf{M} \mathbf{L} \tag{3.13}$$

where, **K** and **M** are stiffness and mass matrices, respectively; **L** is a Boolean vector that projects the seismic inertial acceleration to X translational DoFs. Table 3.7 summarizes linear parameters of reduced S-DoF piers. The resulting 88-DoFs reduced model of the Rio Torto Bridge provided with reduced S-DoF linear piers, the ANSYS Guyan Model (GM) hereinafter, is depicted in Figure 3.29. The modal analysis of the ANSYS GM proved the effectiveness of the proposed substructuring

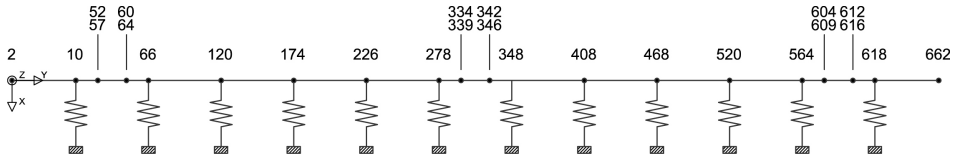

Figure 3.29: Plan view of the reduced linear ANSYS GM of the Rio Torto Bridge in the non-isolated case. Reduced S-DoF piers provide transversal stiffness to the deck.

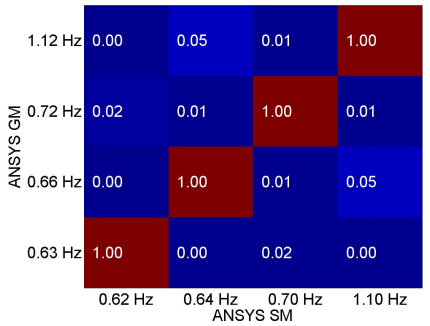

Figure 3.30: MAC matrices between ANSYS GM and ANSYS SM models

scheme. Figure 3.30 reports the MAC matrices relevant to first four modes of the ANSYS SM and the ANSYS GM Since no local eigenmodes of piers were excited, the proposed reduction resulted to be almost exact in the linear range. In the case of non negligible excitations of local modes, a further refinement of the reduction could be based on the Craig-Bampton method (Bampton, 1968). According to the following relationship, the proposed reduced S-DoF piers lent themselves to a natural extension to the nonlinear range by replacing elastic stiffnesses with nonlinear springs,

$$\bar{K}x + \bar{C}\dot{x} + \bar{M}\ddot{x} \Rightarrow r + \bar{C}\dot{x} + \bar{M}\ddot{x} = f(t) - \bar{F}a_g(t) \tag{3.14}$$

In order to reproduce the hysteretic behavior of fiber based OpenSEES piers nonlinear restoring forces r were defined as further state variables entailing memory:

$$\dot{r} = g(x, \dot{x}, r, \theta) \tag{3.15}$$

where θ is the parameter vector. Since rate independent OpenSEES materials were considered, nonlinear restoring forces r must satisfy:

$$k\dot{r} = g(x, k\dot{x}, r, \theta), \forall k \in \mathbb{N} \tag{3.16}$$

A nonlinear springs based on a modified version of the well-known Bouc-Wen was devised (Smyth et al., 1999). It allowed for substructuring piers at both limit states with few parameters. Linear parameters of reduced S-DoF piers were assumed as basis for the formulation of nonlinear restoring force models capable of reproducing the reference behavior. Regardless the restoring force model, each substructured pier was considered as a stand-alone Single-Input-Single-Output (SISO) system for the purpose of the identification of nonlinear parameters. Internal forces recorded at the cap beam level from time history analyses of the Open-SEES RM were considered as input applied to each substructured pier, whilst the cap beam level displacement response was considered as output. A penalty function was set in terms of NRMSE between displacement response histories of the reduced S-DoF pier and the OpenSEES RM.

$$\hat{\theta} = \min_{\theta} \text{NRMSE}(x_{ref}, x_{red}(\theta)) \tag{3.17}$$

At each iteration of the optimization loop, the displacement response of the reduced nonlinear pier $x_{red}(\theta)$ was calculated by integrating Eq. (3.14) with the *ode15s* Matlab solver for stiff ODEs. The differential model of the modified Bouc-Wen spring proposed for the nonlinear substructuring of Rio Torto piers recalls the work of Smyth et al. (1999). In order to replicate the softening behavior of OpenSEES piers inherited from material constitutive laws, the term $1/(1 + \alpha x^2)$ was introduced.

$$\dot{f} = \left(\frac{\rho A}{1 + \alpha x^2} - (\beta sgn(\dot{x} f) + \gamma)|f|^n \right) \dot{x} \tag{3.18}$$

where A, β, γ and n are parameters of the Bouc-Wen model. A was assumed equal to the reduced linear stiffness $\bar{K}$, whilst ρ was introduced to represents its average degradation. In order to decrease the computational burden of resulting identification problems, γ was set equal to zero and n to one. As a result, the effective component of the elastic tangent stiffness decrease as the squared displacement x

	SLS			ULS		
Pier	ρ	α	β	ρ	α	β
1	1.00	1987.15	0.00	0.83	1942.26	0.10
2	0.67	32.50	1.17	0.50	0.19	2.13
3	0.81	108.82	1.32	0.96	215.65	2.19
4	0.66	125.55	2.51	0.50	24.98	3.93
5	0.63	248.94	1.90	0.68	338.44	0.60
6	0.79	161.51	1.25	0.50	8.66	1.44
7	0.50	7.94	1.05	0.50	8.34	1.94
8	0.59	44.75	0.58	0.50	29.30	1.25
9	0.73	338.32	0.84	0.95	1005.93	0.36
10	1.00	1151.93	0.00	0.59	387.69	1.58
11	0.79	919.21	1.84	0.50	490.84	1.31
12	0.99	1997.13	0.01	0.72	1090.46	3.10

Table 3.8: Non-linear parameters of S-DoF reduced piers based on modified Bouc-Wen springs

increases according to the rate α. According to Bursi (2012), the proposed model is rate independent. Proposed reduced nonlinear springs characterized by few parameters were not capable of reproducing piers' behavior at their full operating range. As a consequence, different nonlinear parameter sets were identified at different limit states. Table 3.8 summarizes parameters sets for both the SLS and the ULS, respectively. According to Table 3.8, an appreciable stiffness degradation at ULS is evident. Moreover β parameters, which are responsible of the hysteretic energy dissipation, increased. NRMSEs between time history responses of stand-alone reduced piers and the OpenSEES RM were calculated as matching scores. They are collected in Table 3.9 for both the SLS and the ULS. Figures 3.31 and 3.32 compare displacement responses of reduced S-DoF models of Piers #9 and #11 in the transversal direction to the OpenSEES reference solution at both limit states. Matching scores reported in Table 3.9 and plots of Figures 3.31, 3.32, prove that the proposed nonlinear spring is suitable for the dynamic substructuring

	SLS			ULS		
Pier	dsp.	vel.	for.	dsp.	vel.	for.
1	0.03	0.04	0.03	0.03	0.05	0.05
2	0.06	0.07	0.04	0.07	0.09	0.06
3	0.03	0.05	0.04	0.07	0.08	0.07
4	0.06	0.05	0.03	0.08	0.08	0.05
5	0.05	0.06	0.04	0.06	0.09	0.08
6	0.03	0.05	0.05	0.07	0.06	0.05
7	0.05	0.06	0.04	0.09	0.06	0.06
8	0.03	0.05	0.04	0.04	0.06	0.05
9	0.02	0.06	0.03	0.05	0.07	0.08
10	0.02	0.05	0.03	0.04	0.06	0.05
11	0.02	0.04	0.02	0.07	0.07	0.06
12	0.02	0.03	0.02	0.04	0.04	0.03

Table 3.9: NRMSEs on displacements, velocities and restoring forces of S-DoF reduced piers with respect to the OpenSEES RM.

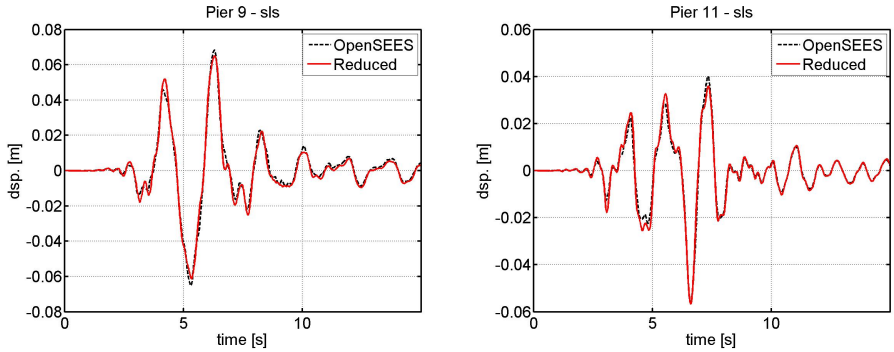

(a) (b)

Figure 3.31: Displacement response of reduced S-DoF Piers: **a** #9; and **b** #11 at SLS.

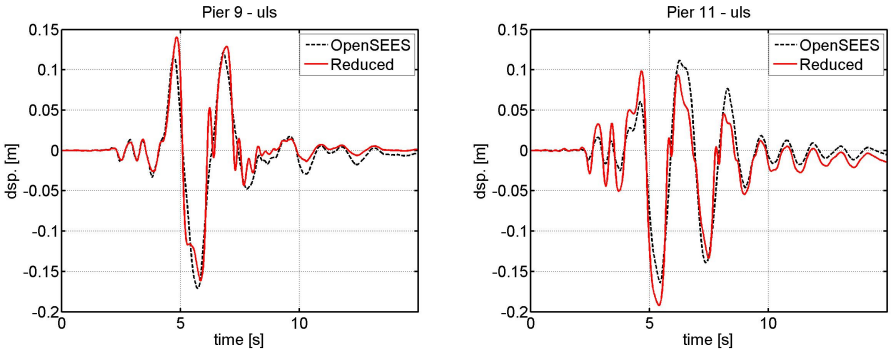

(a) (b)

Figure 3.32: Displacement response of reduced S-DoF Piers: **a** #9; and **b** #11 at ULS.

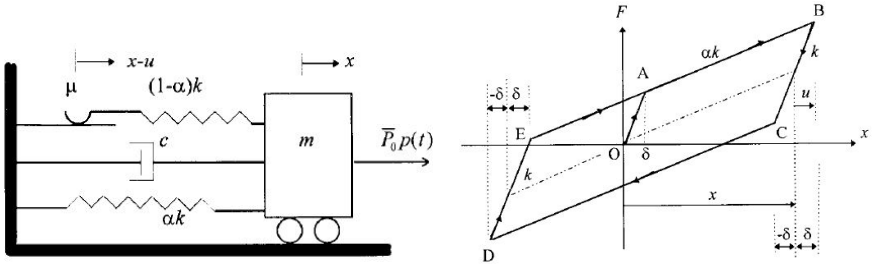

(a) (b)

Figure 3.33: **a** Hysteretic S-DoF oscillator with entailing **b** bilinear hysteretic loop

of the hysteretic piers of the Rio Torto Bridge.

3.4.3 Dynamic substructuring of isolators

OpenSEES isolator elements are characterized by a physical model which replicates the slip mechanism of FPB devices. Resulting hysteretic loops are characterized by bilinear shapes. Accordingly, the proposed model for substructuring of isolator elements was based on the bilinear model proposed by Mostaghel (1999). Figure 3.33 shows both the hysteretic S-DoF oscillator and the entailing bilinear hysteretic loop. The aforementioned bilinear model was able to reproduce the nonlinear behavior of the two-node *single friction pendulum bearing* element imple-

mented in the OpenSEES RM. The ODE set that characterizes the bilinear system of Figure 3.33 reads:

$$m\ddot{x} + c\dot{x} + \alpha kx + (1-\alpha)ku = \bar{P}_0 p(t) \tag{3.19}$$

$$\dot{u} = (\bar{N}(\dot{x})\bar{M}(u-\delta) + M(\dot{x})N(u+\delta))\dot{x} \tag{3.20}$$

Since N, M, $\bar{N}$ and $\bar{M}$ are defined as polynomials based on the *sign* function, the proposed model is clearly rate independent. In detail, they read:

$$N(w) = 0.5(1 + sign(w))(1 + (1 - sign(w))) \tag{3.21}$$

$$M(w) = 0.5(1 - sign(w))(1 - (1 + sign(w))) \tag{3.22}$$

$$\bar{N}(w) = 0.5(1 + sign(w))(1 - (1 - sign(w))) \tag{3.23}$$

$$\bar{M}(w) = 0.5(1 - sign(w))(1 + (1 + sign(w))) \tag{3.24}$$

The state space variable u stores the memory of the hysteretic system as slip displacement. The time integration of Eqs. 3.19 and 3.20 defines the response of any nondegenerating hysteretic bilinear system under a given load history $\bar{P}_0 p(t)$. In the present case, mass and damping contributions of isolators were neglected. A penalty function was defined as the NRMSE between reference and reduced restoring forces relevant to one isolator element:

$$\{\hat{k}, \hat{\alpha}, \hat{\delta}\} = \min_{k,\alpha,\delta} \text{NRMSE}\ (\mathbf{r}_{ref}, \mathbf{r}_{red}(k, \alpha, \delta)) \tag{3.25}$$

where:

$$r_{red,i} = \alpha k x_{ref,i} + (1-\alpha)ku_i \tag{3.26}$$

$$u_i = \sum_{j=1}^{i} \dot{x}_{ref,j}(\bar{N}(\dot{x}_{ref,j})\bar{M}(u_j - \delta) + M(\dot{x}_{ref,j})N(u_j + \delta))dt \tag{3.27}$$

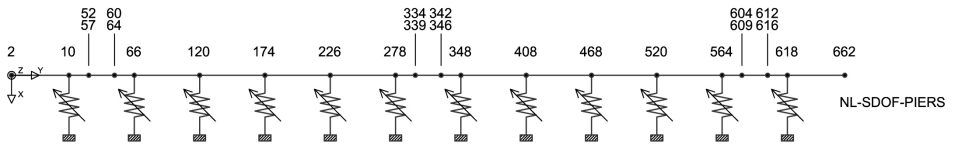

Figure 3.34: Plan view of the reduced nonlinear model of the Rio Torto Viaduct in the non-isolated case

In detail, $\mathbf{r}_{ref}$ is the restoring force history of the single OpenSEES isolator elements; $\mathbf{x}_{ref}$ and $\dot{\mathbf{x}}_{ref}$ are the corresponding relative displacement and velocity histories, respectively. Eq. 3.25 defines the penalty function for the estimation of nonlinear parameters, which are reported below:

$$k = 2.03e8N/m \ , \ \alpha = 0.0046 \ , \ \delta = 0.00050m \tag{3.28}$$

The penalty function of Eq. 3.25 was minimized through the Matlab *pattern search* algorithm. Same parameters were validated for all isolators. Although the effect of variable vertical loads was neglected, simplified bilinear models well reproduced the complex behavior of OpenSEES isolator elements and were implemented in view of the hybrid simulation of the Rio Torto Bridge.

3.5 Validation of the reduced model of the Rio Torto Bridge in the non-isolated case

In order to validate the effectiveness of substructured components for the purpose of the hybrid simulation of the Rio Torto Bridge, a reduced model of the structure was assembled. Figure 3.34 depicts the scheme of the resulting model of the Rio Torto Bridge in the non-isolated case with node numbering. In detail, deck matrices were imported from the ANSYS GM and based on *BEAM44* elements. Nonlinear S-DoF piers acted as transversal springs. Table 3.10 summarizes external constraint conditions. Gerber saddles were implemented by means of Constraint Equations (CEs) defined on internal DoFs. Table 3.11 summarizes the aforementioned CEs. NRMSEs were calculated on displacement, velocity and acceleration responses of piers measured at cap beam levels with respect to the OpenSEES reference solution. Table 3.12 summarizes obtained NRMSE values considering nonlinear reduced S-DoF piers at SLS and ULS. According to Tables 3.12 pro-

Node selection	Constraint setting
2,662	Ux,Uy,Uz,Roty = 0
10,66,120,174,226,278,348,408,468,520,564,618	Uy,Uz,Roty = 0

Table 3.10: External constraints of the reduced model of the Rio Torto Bridge in the non-isolated case

Node selection	Coupled DoFs
52,57	Ux,Uy,Uz,Roty
60,64	Ux,Uy,Uz,Roty
334,339	Ux,Uy,Uz,Roty
342,346	Ux,Uy,Uz,Roty
604,609	Ux,Uy,Uz,Roty
612,616	Ux,Uy,Uz,Roty

Table 3.11: CEs aimed at implementing Gerber saddles

posed models well reproduced the dynamic response of the OpenSEES RM at SLS and ULS in the non-isolated case. Figures 3.35 and 3.36 report displacement responses of Pier #9 and #11 of the reduced model of the Rio Torto Bridge in the non-isolated case at SLS and ULS, respectively. According to Tables 3.12 and Figures 3.35 and 3.36, the proposed reduced model of the bridge based on modified Bouc-Wen springs well reproduced the dynamic response of the OpenSEES RM at both SLS and ULS.

3.6 Validation of the reduced model of the Rio Torto Bridge in the isolated case

In order to validate the effectiveness of substructured components for the purpose of the hybrid simulation of the Rio Torto Bridge in the isolated case, a reduced model of the structure was assembled. Since FPB devices carried the most of the hysteretic energy dissipation, piers were supposed to remain in the linear regime, see Figure 3.21 in this respect. Thus nonlinearities were confined within

	SLS			ULS		
Pier	dsp.	vel.	acc.	dsp.	vel.	acc.
1	0.04	0.03	0.02	0.07	0.06	0.07
2	0.06	0.07	0.04	0.06	0.04	0.03
3	0.05	0.05	0.03	0.05	0.04	0.03
4	0.04	0.04	0.02	0.04	0.03	0.03
5	0.03	0.03	0.02	0.04	0.03	0.02
6	0.04	0.04	0.02	0.04	0.04	0.03
7	0.05	0.05	0.03	0.05	0.03	0.04
8	0.05	0.05	0.03	0.04	0.04	0.03
9	0.05	0.05	0.02	0.05	0.07	0.05
10	0.04	0.03	0.02	0.08	0.09	0.07
11	0.03	0.03	0.02	0.09	0.09	0.09
12	0.02	0.02	0.02	0.05	0.04	0.04

Table 3.12: Reduced model of the Rio Torto Bridge in the non isolated case: NRMSEs on transversal kinematic histories measured at cap beam levels of piers based on modified Bouc-Wen springs at SLS and ULS.

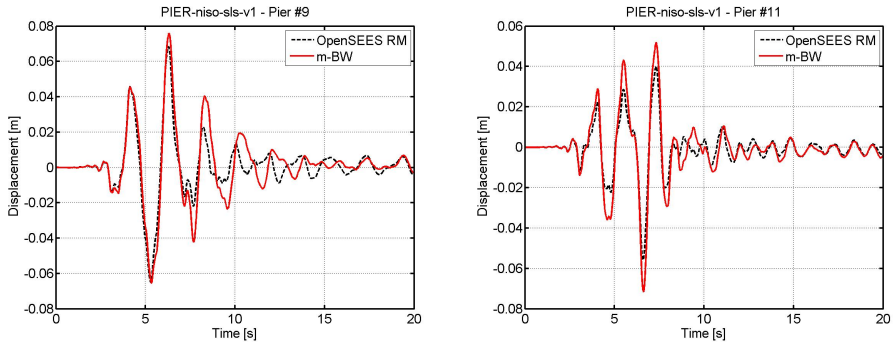

(a) (b)

Figure 3.35: Displacement responses of Piers #9 and #11 at SLS in the non isolated case

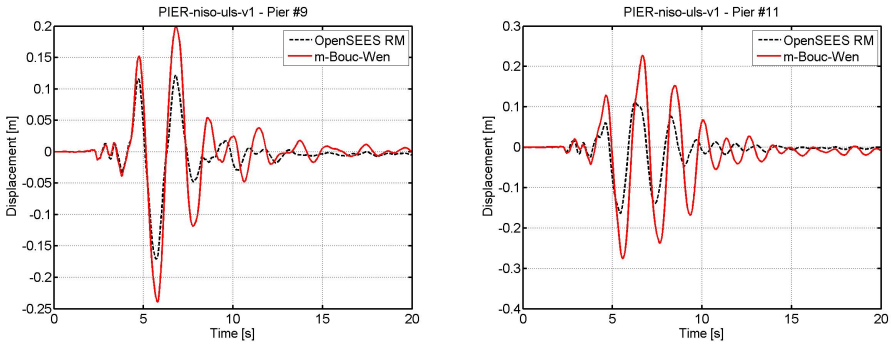

(a) (b)

Figure 3.36: Displacement responses of Piers #9 and #11 at ULS in the non isolated case

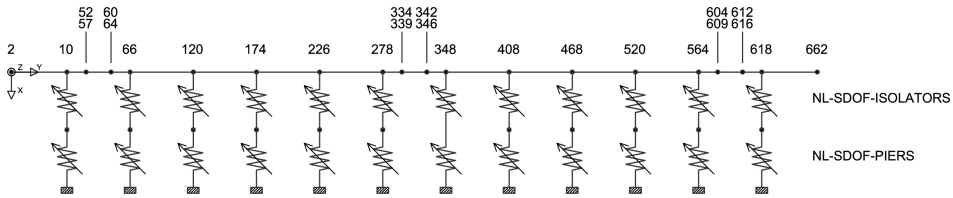

Figure 3.37: Plan view of the reduced nonlinear model of the Rio Torto Viaduct in the isolated case

substructured isolators. Figure 3.37 depicts the scheme of the resulting model of the Rio Torto Bridge in the isolated case with node numbering. The external constraint setting remained unchanged with respect to the non isolated case, see Table 3.10 in this respect. According to the foreseen retrofitting scheme, Gerber saddles were removed. Table 3.13 summarizes modified CEs. NRMSEs were calculated on displacement, velocity and acceleration responses of piers measured at cap beam levels with respect to the OpenSEES reference solution. Table 3.14 summarizes obtained values at both the SLS and the ULS. Figures 3.38 and 3.39 depicts displacement responses of Pier #9 and #11 of the reduced model of the Rio Torto Bridge in the isolated case at SLS and ULS, respectively. Figures 3.38 and 3.39 confirm scores collected by Table 3.14, which emphasizes a slight degradation of the solution quality in the isolate case. The different mass matrix

Node selection	Coupled DoFs
52,57	Ux,Uy,Uz,Rotx,Roty,Rotz
60,64	Ux,Uy,Uz,Rotx,Roty,Rotz
334,339	Ux,Uy,Uz,Rotx,Roty,Rotz
342,346	Ux,Uy,Uz,Rotx,Roty,Rotz
604,609	Ux,Uy,Uz,Rotx,Roty,Rotz
612,616	Ux,Uy,Uz,Rotx,Roty,Rotz

Table 3.13: CEs aimed at removing Gerber saddles

	SLS			ULS		
Pier	dsp.	vel.	acc.	dsp.	vel.	acc.
1	0.12	0.07	0.08	0.09	0.09	0.08
2	0.07	0.06	0.11	0.05	0.05	0.08
3	0.07	0.05	0.13	0.10	0.06	0.07
4	0.10	0.09	0.13	0.10	0.09	0.08
5	0.13	0.11	0.13	0.12	0.11	0.09
6	0.09	0.08	0.11	0.09	0.08	0.08
7	0.09	0.09	0.12	0.10	0.08	0.07
8	0.09	0.07	0.09	0.08	0.08	0.09
9	0.14	0.10	0.09	0.11	0.12	0.10
10	0.11	0.09	0.09	0.08	0.06	0.08
11	0.13	0.09	0.07	0.10	0.09	0.08
12	0.10	0.09	0.09	0.08	0.08	0.06

Table 3.14: Reduced model of the Rio Torto Bridge in the isolated case: NRMSEs on transversal kinematic histories measured at cap beam levels of piers at SLS and ULS

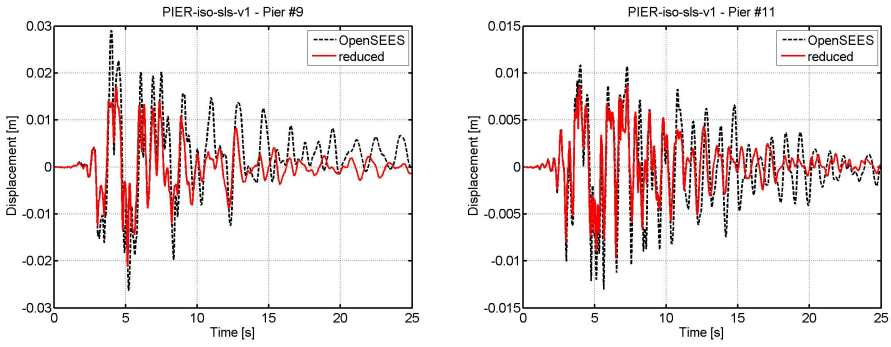

(a) (b)

Figure 3.38: Displacement responses of Piers #9 and #11 at SLS in the isolated case

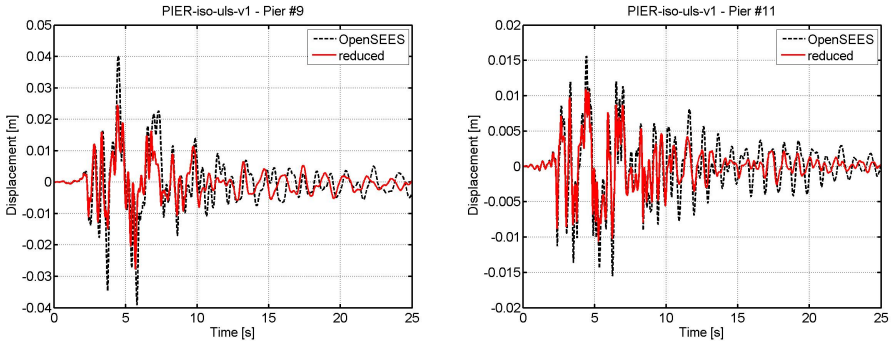

(a) (b)

Figure 3.39: Displacement responses of Piers #9 and #11 at ULS in the isolated case

	SLS		ULS	
Pier	dsp.	for.	dsp.	for.
1	0.04	0.22	0.02	0.12
2	0.10	0.15	0.02	0.09
3	0.06	0.16	0.03	0.10
4	0.03	0.17	0.04	0.11
5	0.03	0.17	0.03	0.11
6	0.04	0.15	0.03	0.09
7	0.04	0.16	0.03	0.08
8	0.05	0.13	0.03	0.11
9	0.07	0.12	0.04	0.09
10	0.07	0.14	0.04	0.08
11	0.07	0.18	0.04	0.12
12	0.10	0.14	0.04	0.12

Table 3.15: Reduced model of the Rio Torto Bridge in the isolated case: NRMSEs on relative displacement and restoring force histories of right isolators at SLS and ULS.

formulations of the OpenSEES and the ANSYS based reduced models can justify this phenomenon. In fact, to avoid matrix ill-conditioning, a consistent formulation was adopted, whilst OpenSEES allows for lumped mass matrices only. Since hysteretic damping does not occurs in the linear range, the dynamic response of higher eigenmodes, sensitive to small mass changes, deteriorate kinematic matching. Same NRMSE matching scores were calculated on reduced isolator response histories. In detail, relative displacements and restoring forces were considered. Table 3.15 summarizes NRMSEs on relative displacements and restoring forces of right isolators for all piers between the OpenSEES RM and the reduced model of the isolated bridge at both limit states. Figures 3.40 and 3.41 compare hystertic loops of right isolators of Piers #9 and #11 of the OpenSEES RM and the reduced models at SLS and ULS, respectively. Table 3.15 and both Figures 3.40 and 3.41 confirm that proposed substructured model well agree with the OpenSEES RM

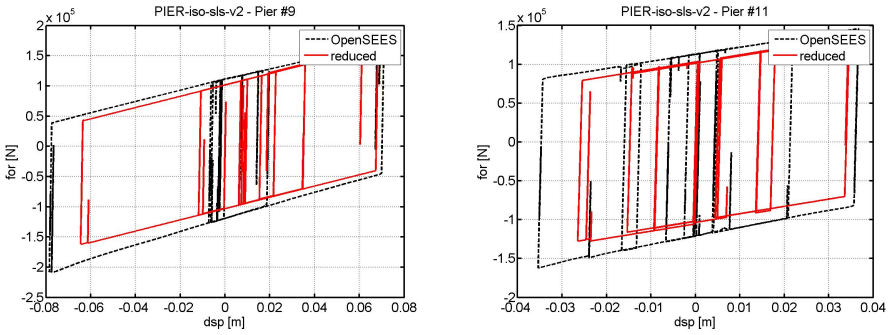

(a) (b)

Figure 3.40: Hysteretic loops of right isolators of Piers #9 and #11 at SLS from OpenSEES RM and reduced model

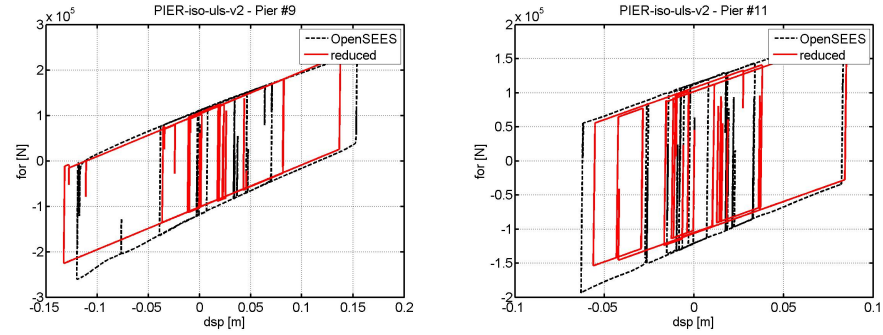

(a) (b)

Figure 3.41: Hysteretic loops of right isolators of Piers #9 and #11 at ULS from OpenSEES RM and reduced model

also in the isolated case.

3.7 Conclusions

The assessment of the seismic performances of the Rio Torto Bridge was conceived within the RETRO transnational activity funded by the SERIES research project. The OpenSEES RM of this bridge was implemented to support the development of the experimental campaign. In greater detail, a comprehensive set of hybrid simulations covered both the as-built and the retrofitted conditions. Since computational resources denied the implementation of NSs based on fiber elements, the nonlinear dynamic substructuring of the OpenSEES RM of the Rio Torto Bridge was devised. In detail, deck, piers and relevant FPB isolator pairs were considered as subparts. In this chapter, the additional ANSYS RM of the bridge was implemented to provide linear mass and stiffness matrices for the purpose of dynamic substructuring. Then, internal constraint setting of the ANSYS RM was deeply investigated and small variations were introduced. The resulting ANSYS SM facilitated the substructuring of piers as S-DoF elements preserving global eigenproperties. Reduced S-DoF piers were extended to the nonlinear range by means of modified Bouc-Wen springs (Smyth et al., 1999). OpenSEES FPB isolator elements were replaced by S-DoF state space models capable of replicating their characteristic bilinear hysteretic loop (Mostaghel, 1999). Time history responses of the OpenSEES RM were taken as reference for the identification of nonlinear parameters of each single substructured component treated as SISO system. Substructured elements were assembled and resulting reduced models of the Rio Torto Bridge were validated with respect to OpenSEES RMs. As a result, tailored NSs were successfully implemented for the purpose of the hybrid simulation of the Rio Torto Bridge at the ELSA facility.

CHAPTER 4

HYBRID SIMULATION OF THE RIO TORTO BRIDGE

4.1 Introduction

A comprehensive set of hybrid simulations was conceived to estimate the seismic performance of the Rio Torto Bridge presented in Chapter 3 in both the non isolated and the isolated conditions. Therefore, 1:2.5 scale mock-up models of Piers #9 and #11 together with relevant FPB isolators were coupled to the remainder part of the bridge implemented in the CAST3M FE code (Cast3M, 2003) at the ELSA Laboratory of the Joint Research Centre of Ispra (VA), Italy. The PM method (Pegon and Magonette, 2002), which embeds subcycling capabilities, allowed for the implementation of the continuous PDT method. First, substructuring schemes and entailing experimental set-ups were presented. Then, the scaling of specimens was described. A novel testing procedure aimed at simulating a consistent degradation among physical and numerical piers, i.e. Physical and Numerical Substructures (PSs and NSs) was presented and applied to the Rio Torto Bridge. It was based on off-line sessions of model identification of PSs and updating of NSs. Accordingly, a tool for the identification of parameters of OpenSEES FE models was implemented in the Matlab environment. As a result, physical piers were characterized after each test where damage was observed. The OpenSEES RM model of the Rio Torto Bridge was updated accordingly and took as reference for the updating of reduced S-DoF piers, i.e. NSs. As a result, a consistent degradation of physical and numerical piers was simulated in both the non isolated and the isolated conditions. Experimental results of hybrid simulations are then discussed. Finally, conclusions are drawn.

4.2 Substructuring scheme

A couple of piers and relevant isolators of the Rio Torto Bridge were experimentally substructured at the ELSA Laboratory of the Joint Research Centre of Ispra (VA), Italy. In greater detail, Piers #9 and #11 with relevant isolator pairs PSs were loaded through dynamic actuators, whilst remaining ten piers, relevant isolator pairs and the deck, i.e. NSs, were numerically modeled and solved by the *CAST3M* FE code. Figures 4.1 and 4.2 depict substructuring schemes adopted for the non isolated and the isolated bridge, respectively.

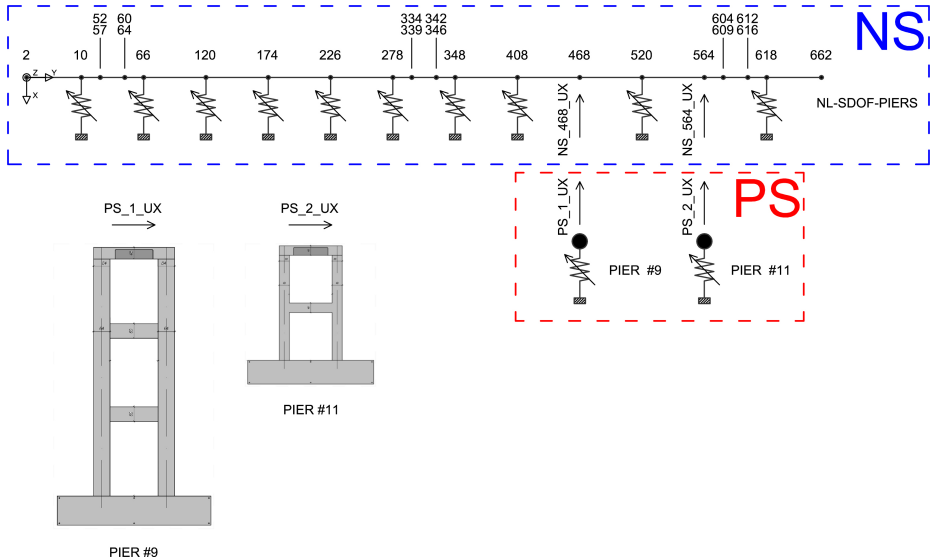

Figure 4.1: Substructuring scheme of the Rio Torto Bridge in the non isolated case

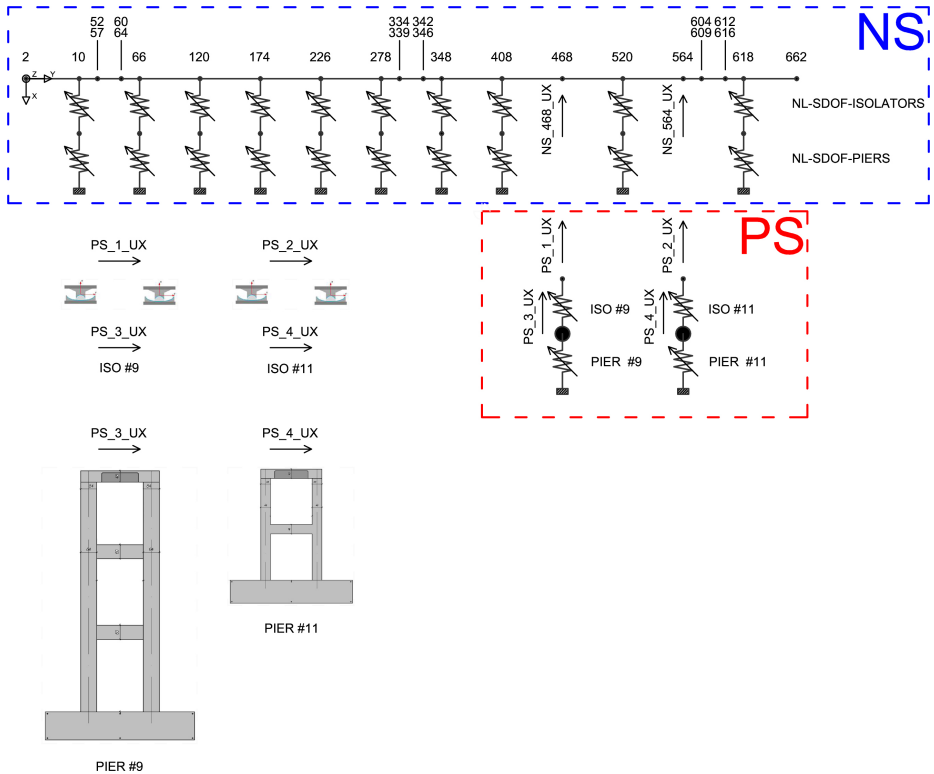

Figure 4.2: Substructuring scheme of the Rio Torto Bridge in the isolated case

According to Figures 4.1 and 4.2, the coupling setting reads:

$$NS\_468\_UX = PS\_1\_UX \tag{4.1}$$

$$NS\_564\_UX = PS\_2\_UX \tag{4.2}$$

As can be appreciated in Figure 4.1, a 2-DoFs PS was considered for the non isolated bridge; according to Figure 4.2, a 4-DoFs PS resulted for the isolated bridge, where isolation devices were interposed among deck and piers. In both the isolated and the non isolated cases, substructured deck, piers and isolators devised in Chapter 3 were assembled to produce the remainder numerical part of the Rio Torto Bridge, i.e. the NS. Hybrid simulations of simpler 2-DoFs coupled systems were conducted for the purpose of the validation of the experimental implementation; they combined a single num./exp. pier with relevant num./exp. FPB isolator pairs. Since rate independent PSs were considered, the PDT approach was selected to conduct hybrid simulations of the entire bridge. Due to the complexity of the nonlinear NS of the Rio Torto Bridge, the computational driver and the servo-hydraulic control system ran at different time rates. The parallel partitioned time integration scheme developed by Pegon and Magonette (2002), i.e. the PM method, synchronized these two processes and the equation of motion was successfully integrated. In greater detail, a coarse time step Δt_A was selected for the computational driver whereby the NS was solved, whilst a smaller time step $\Delta t_B = \Delta t_A / n$, was selected for the integration of the PS, where n defined the subcycling. As a result, displacement commands were provided to the transfer system at the controller sampling time $\Delta t = 0.002ms$; smooth trajectories of actuators were obtained and the continuous time PDT method was successfully implemented. A lot of effort was devoted to the development of the continuous time PDT method at the ELSA laboratory (Pegon and Magonette, 2002, 2005; Bonelli et al., 2008). In fact, the removal of the hold period in the specimen loading phase avoids relaxation issues and increases the signal/noise ratio. An improvement of the quality of results follows. Moreover, a considerable reduction of the simulation time can be achieved. Relationships among sampling times involved by the time integration

setting read,

$$\Delta t_B = \frac{\Delta t}{\lambda} \tag{4.3}$$

$$n = \frac{\Delta t_A}{\Delta t}\lambda \tag{4.4}$$

where λ is the extended time scale characterizing the pseudodynamic hybrid simulation. For the purpose of hybrid simulation of the Rio Torto Bridge the PM method, was implemented considering a time scale $\lambda = 200$ and a subcycling parameter $n = 250$. As result, the coarse time step $\Delta t_A = 2.5msec$ was assumed for NSs, whilst a fine time step $\Delta t_B = 0.01msec$ was selected for the PS. As can be appreciated, subcycling is the key feature for the implementation of the continuous time PDT method. Parallel partitioned time integrations enable subcycling avoiding any interpolation/extrapolation of actuator commands at the controller sampling time Δt. Thus, no spurious dynamics affects the response of the specimen. From the implementation perspective, the last improvement of the ELSA controller consisted on a TCP/IP interface to the CAST3M FE code. It allowed for the implementation of the nonlinear model of the Rio Torto Bridge presented in Chapter 3 as NS for the purpose of hybrid simulation.

4.3 Description of scaled physical substructures

Due to limited size and capacity of the experimental facility, scaled specimens were tested rather than full-scale structures. In detail, 1:2.5 scale mock-up models of Piers #9 and #11 with relevant FPB isolator pairs were considered for the hybrid simulation of the Rio Torto Bridge. Reduced specimens allowed for saving costs and reducing loads below the maximum capacity of actuators. For typical dynamic problems, three are the fundamental dimensional characteristics, namely, mass M, length L and time T; accordingly, three independent scale factors may be potentially selected for a rigorous scaling. The solution of the entailing dimensional problem is governed by the well-known Buckingham Theorem. Since gravity loads play an important role, mass was of concern. Thus only the scale factor of S^3 was of interest for mass, being the density the same. Accordingly, a force scale S^2 was assumed to preserve experimental stress quantities. As a result, target dis-

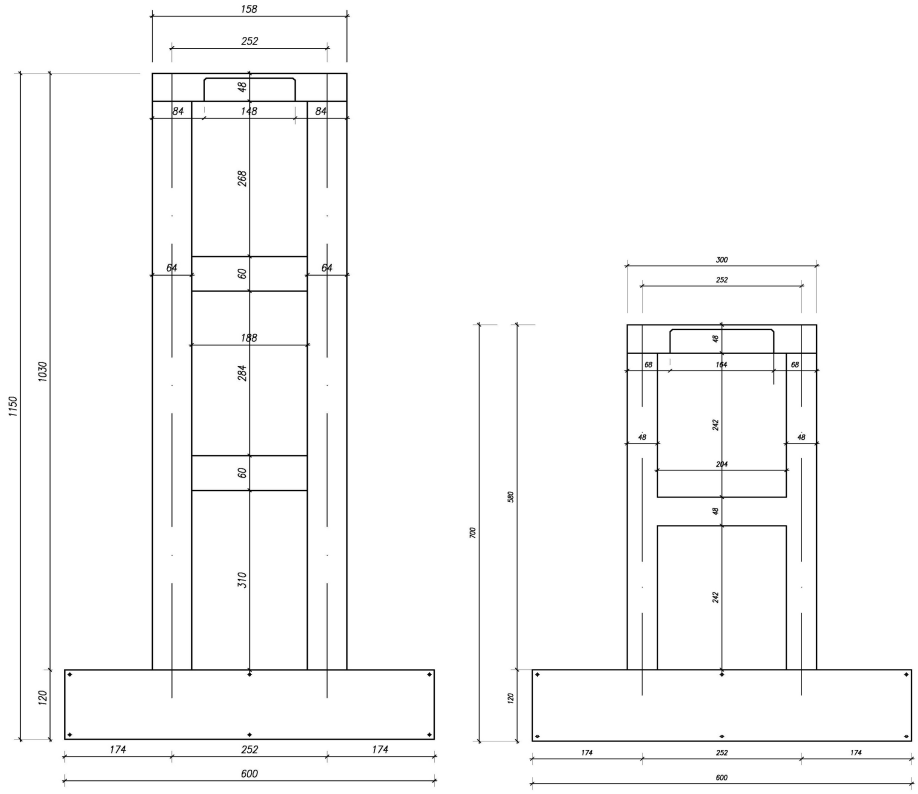

(a) (b)

Figure 4.3: Mock-up 1:2.5 scale models of **a** Pier #9 and **b** Pier #11. Dimensions in cm.

placements obtained from the numerical integration of the equation of motion were divided by S and applied to specimens, whilst restoring forces measured by actuator load cells were multiplied by S^2 and fed back to the time integration algorithm, where $S = 2.5$.

4.3.1 Scaling of physical piers

According to Figure 4.3(a), the specimen of Pier #9 was characterized by 3 levels and total height of 11.50m; as can be appreciated from Figure 4.3(b), the specimen of Pier #11 was characterized by 2 levels and 7.00m of total height. Both specimen were provided with a 6.00m x 2.80m x 1.20m block foundation. A rigorous scaling of geometrical characteristics including reinforcement diameters

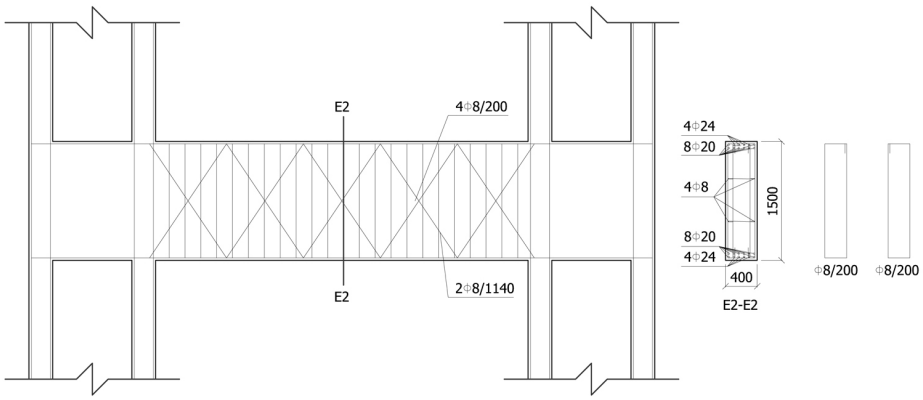

Figure 4.4: Transverse element of Pier #11 with reinforcements

and positions was realized. With regard to columns of Pier #9 and #11, plain steel rebars of diameter of 8 and 10mm replaced full-scale diameters of 24 and 20mm, respectively. Therefore, a small approximation occurred for the 24mm diameter. Particular care was devoted to the shear strength for the consistent scaling of transverse elements. As can be appreciated in Figure 4.4, which depicts the transverse element of Pier #11, both diameters and spacings of stirrups and inclined rebars must be scaled to reproduce the correct confinement effect. Hence, 3mm diameter rebars replaced the full scale reinforcement based on stirrups and inclined rebars characterized by 8mm diameter. Rounding errors entailed by available diameters denied a perfect geometrical scaling of shear reinforcements of transverse elements. Nonetheless, resulting errors were estimated through the formulation of Priestley et al. (1994). Table 4.1 reports shear strength estimations of lower transverse elements of Piers #9 and #11 in the full-, exact- and actual-scale cases.

	Pier #9			Pier #11				
	full	exact	actual	full	exact	actual	unit	Description
b	400	160	160	400	160	160	mm	cross sec. width
h	1500	600	600	1200	480	480	mm	cross sec. depth
D	1350	540	540	1080	432	432	mm	cross sec. eff. depth
A	600000	96000	96000	480000	76800	76800	mm^2	cross sec. area
A_c	480000	76800	76800	384000	61440	61440	mm^2	cross sec. eff. area
ϕ_{sw}	8	3,2	3	8	3,2	3	mm	stir. diameter
n_{sw}	4	4	4	2	2	2	n	stir. braces
A_{sw}	201	32	28	101	16	14	mm^2	stir. area
s_{sw}	200	80	80	200	80	80	mm	stir. spacing
ϕ_{sp}	8	3,2	3	8	3,2	3	mm	inc. reb. diameter
n_{sp}	2	2	2	2	2	2	n	inc. reb. braces
A_{sp}	101	16	14	101	16	14	mm^2	inc. reb. area
s_{sp}	1140	456	456	1140	456	456	mm	inc. reb. spcing
V_c	391605	62657	62657	313284	50125	50125	N	concrete shear strength
V_s	549191	87871	77230	243920	39027	34301	N	reinf. shear strength
V_t	940795	150527	139887	557204	89153	84427	N	tot. shear strength

Table 4.1: Estimations of shear strengths of full-scale and scaled mid cross sections of transverse elements

The exact-scale case considers scaled rebars without rounding errors owing to available commercial diameters. The actual-scale case refers to realized specimens, where rounding errors affected scaled diameters of rebars. In greater detail, V_c, V_s and V_t reported in Table 4.1 are calculated according to Eqs. 3.2, 3.3 and 3.4 and refer to the formulation of Priestley et al. (1994) reported in Chapter 3. The compressive yielding strength f_c of concrete was set to 26MPa, whilst the yielding strength of steel rebars f_y to 360MPa. Since rectangular cross sections were considered, the effective area A_c was set equal to $0.8A$, whilst the effective depth D was set to $0.9h$. A curvature ductility-dependent coefficient k_d of 0.20 was assumed. Both angles of concrete struts θ and inclined rebars β were set to 45°. According to Table 4.1, actual-scaled transverse elements of Pier #9 and #11 underestimated shear strengths of their exact-scaled counterparts of 7% and 5%, respectively. Therefore, approximations were considered acceptable. With regard to bond performances between concrete and plain steel rebars, previous experimental campaign proved that scaling affects propagation of cracks and slip effect (Ichinose et al., 2004; Pinto, 2009). Nonetheless, the anchorage strength provided by hooks prevails (Fabbrocino, 2005). Accordingly, the simple geometrical scaling was considered for the present case study (Paolacci and Giannini, 2012).

4.3.2 Scaling of physical FPB isolators

According to the geometrical scaling strategy, mock-up scale 1:2.5 model of FPB isolators were manufactured by ALGA s.p.a. The foreseen full-scale radius of the concave sliding surface was reduced to 1200mm, whilst the same friction coefficient equal to 4% characterized reduced devices. Drawings of the reduced FPB isolator are depicted in Figure 4.6. Each single FPB isolator depicted in Figure 4.7 was designed to support a scaled vertical load of $2800/2.5^2 = 448kN$.

4.4 Description of the experimental set-up

In order to perform the experimental campaign, eighteen hydraulic actuators were employed at the ELSA facility. Short actuators of the type depicted in Figure 4.8(a) applied vertical loads to both piers and FPB isolators. Long actuators of the type depicted in Figure 4.8(b) applied horizontal displacements to all PSs according to substructuring schemes presented. Each actuator was provided with

Figure 4.5: Mock-up 1:2.5 scale specimens of Piers #9 and #11

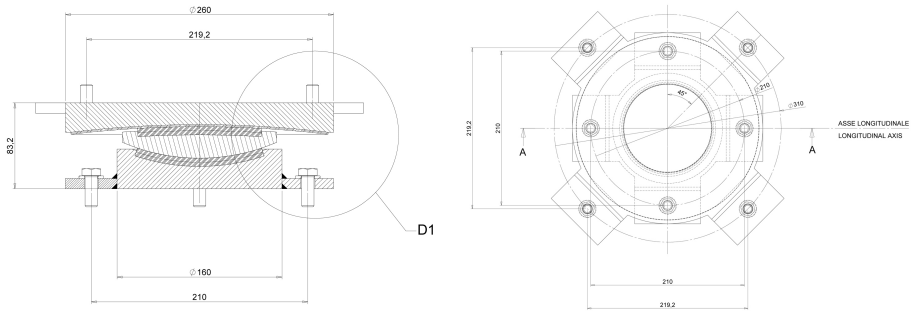

(a) (b)

Figure 4.6: Scaled FPB device: **a** section; **b** top view. Dimension in mm.

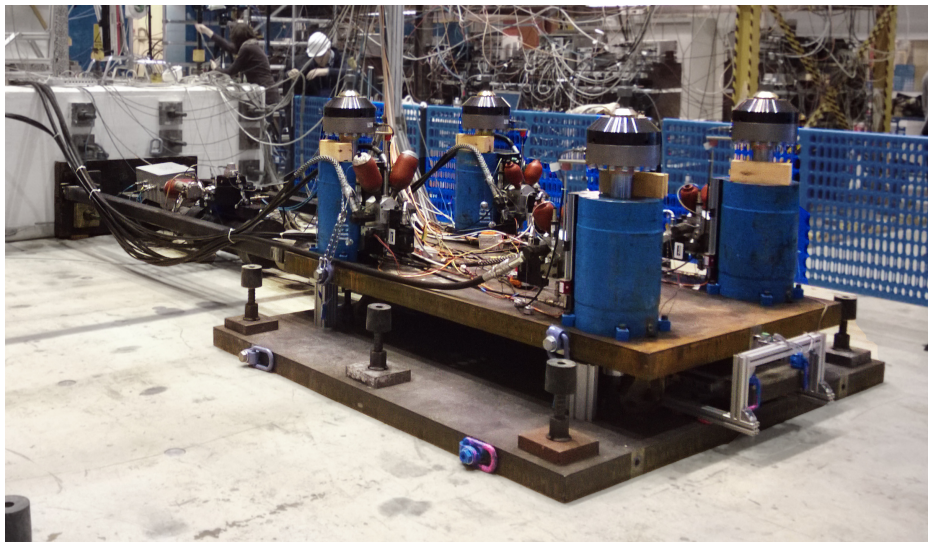

Figure 4.7: Experimental set-up conceived for FPB isolation devices of Pier #11

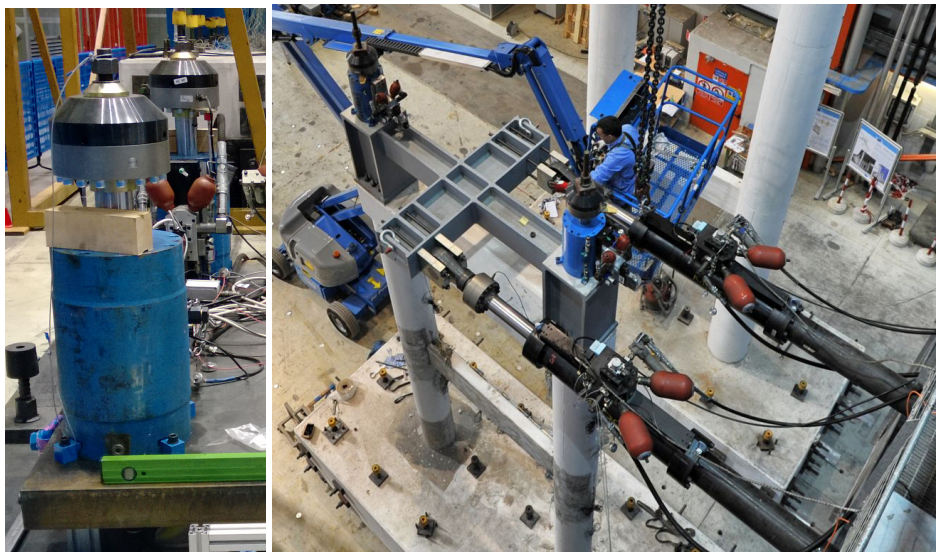

(a) (b)

Figure 4.8: **a** short actuators for vertical loads; **b** long actuators for horizontal displacements.

Pier	Type	Purpose
1E,2E,3E,4E	short	vertical load on FPB isolators of Pier #9
1D,2D,3D,4D	short	vertical load on FPB isolators of Pier #11
1C,2C	short	vertical load on Pier #9
1B,2B	short	vertical load on Pier #11
2A,3C	long	horizontal displacement of Pier #9
1A,3B	long	horizontal displacement of Pier #11
4A	long	horizontal displacement of FPB isolators of Pier #9
3A	long	horizontal displacement of FPB isolators of Pier #11

Table 4.2: List of actuators, types and purposes.

a *TEMPOSONICS* displacement transducer, which measures the actuator stroke, and a load cell measuring the entailing axial force; further sensors provided data regarding the oil pressure within the servo-valve as well as its spool displacement. Table 4.2 summarizes label and purpose of each hydraulic actuator adopted: With regard to horizontal actuators, i.e. $2A$, $3C$, $1A$, $3B$, $3A$ and $4A$, additional feedback *HEIDENHAIN* displacement transducers were used for control purpose; they measured specimen displacements with respect to a fixed reference frame resting on the reaction floor. Each single actuator and relevant measurements were managed by a dedicated SLAVE controller with the same label and running the specific PID displacement/force control algorithm. Figures 4.9 and 4.10 depict schematic views of displacement and force measurement channels, respectively.

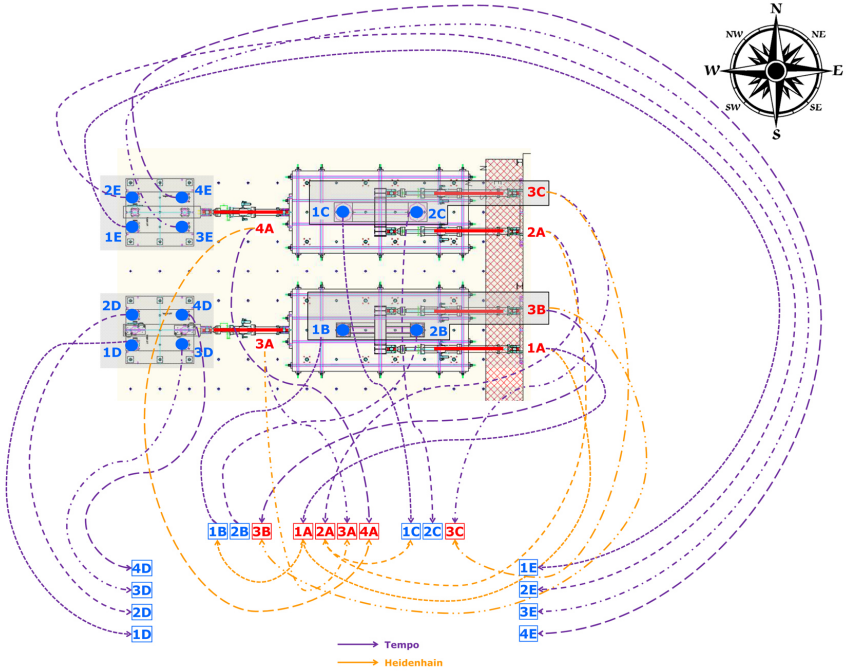

Figure 4.9: Displacement measurement channels relevant to *HEIDENHAIN* and *TEMPOSONICS* transducers

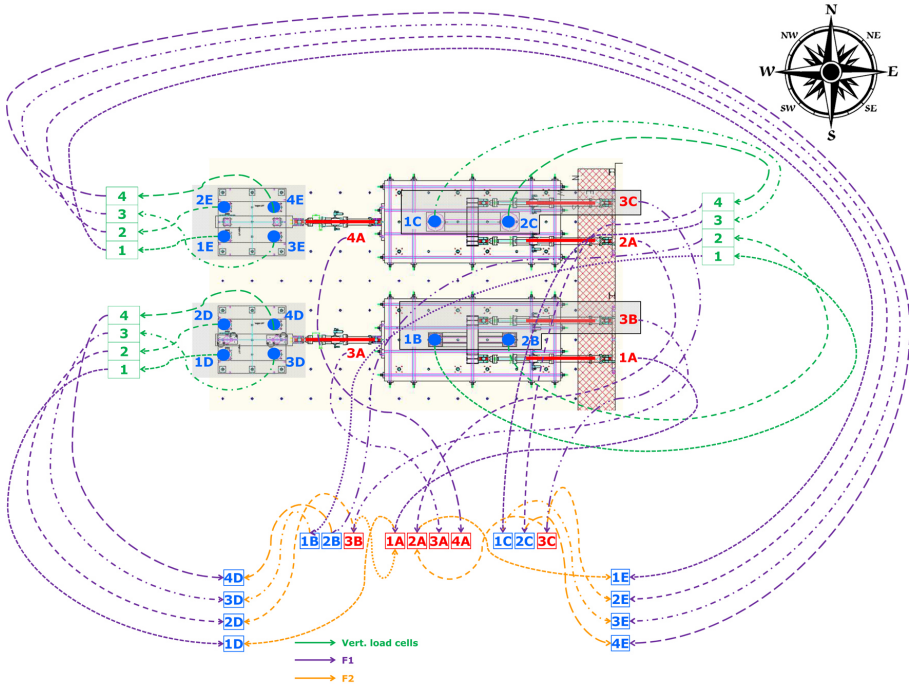

Figure 4.10: Force measurement channels relevant to actuator load cells

As a result, nonlinear NSs were implemented and solved exploiting the huge element library of the CAST3M FE code as well as its nonlinear solver. Figure 4.11 shows the complete set-up installed at the ELSA experimental facility. As can be appreciated in Figure 4.11, the yellow reference steel frame resting on the reaction floor supports *HEIDENHAIN* displacement transducers. Experimental set-ups of piers and FPB isolators are carefully described in following sections. For the sake of clarity, the following notation is introduced and refers to FPB isolators:

- $Fv_{Iso\#9,West} = F_{1E} + F_{2E}$: Vertical force applied to West FPB isolator of Pier #9
- $Fv_{Iso\#9,East} = F_{3E} + F_{4E}$: Vertical force applied to East FPB isolator of Pier #9
- $Fv_{Iso\#11,West} = F_{1D} + F_{2D}$: Vertical force applied to West FPB isolator of Pier #11
- $Fv_{Iso\#11,East} = F_{3D} + F_{4D}$: Vertical force applied to East FPB isolator of Pier #11
- $Fh_{Iso\#9} = F_{4A}/2$: Horizontal force applied to FPB isolators of Pier #9
- $Fh_{Iso\#11} = F_{3A}/2$: Horizontal force applied to FPB isolators of Pier #11
- $Dh_{Iso\#9} = D_{4A}$: Horizontal displacement of FPB isolators of Pier #9
- $Dh_{Iso\#11} = D_{3A}$: Horizontal displacement of FPB isolators of Pier #11

Accordingly, the following notation refers to piers:

- $Fv_{Pier\#9,West} = F_{1C}$: Vertical force applied to West column of Pier #9
- $Fv_{Pier\#9,East} = F_{2C}$: Vertical force applied to East column of Pier #9
- $Fv_{Pier\#11,West} = F_{1B}$: Vertical force applied to West column of Pier #11
- $Fv_{Pier\#11,East} = F_{2B}$: Vertical force applied to East column of Pier #11
- $Fh_{Pier\#9} = F_{2A} + F_{3C}$: Horizontal force applied to Pier #9
- $Fh_{Pier\#11} = F_{1A} + F_{3B}$: Horizontal force applied to Pier #11

Figure 4.11: Mock-up 1:2.5 scale specimens of Piers #9 and #11 with relevant FPB isolator pairs

- $Dh_{Pier\#9} = (D_{2A} + D_{3C})/2$: Horizontal displacement of Pier #9
- $Dh_{Pier\#11} = (D_{1A} + D_{3B})/2$: Horizontal displacement of Pier #11

where, $F_{(\bullet)}$ and $D_{(\bullet)}$ are restoring force and displacement measured on actuator $(\bullet)$, respectively.

4.4.1 Experimental set-up of piers

In order to avoid torsional rotations, a pairs of actuators applied the horizontal displacement to each physical pier. In detail, MASTER A151, which ran the PDT procedure, sent displacement targets to both $1A$ and $2A$ actuators of Piers #9 and #11, respectively throughout relevant SLAVE controllers. Feedback displacement measurements from *HEIDENHAIN* transducers were sent back to MASTER C189 and MASTER B150 as displacement targets for North horizontal actuators $3C$ and $3B$ of Piers #9 and #11, respectively, throughout relevant SLAVE controllers. Feedback forces from both actuator pairs entered the integration loop of the equation of motion solved by the MASTER A151's DLL. For each pier, displacements of both horizontal actuators were averaged. Figure 4.12 depicts the experimental set-up of both Pier #9 and #11. As can be appreciated in Figure 4.12, in order to take into account offset distances between cap beams and the center of gravity of the deck cross section, two rigid steel frames provide 0.80m lever arms to horizontal actuators. They were secured to concrete beams with anchored bolts and supported vertical actuators. According to reduced models of the Rio Torto Bridge presented in Chapter 3, vertical DoFs were removed from substructured components. Nonetheless, corresponding gravity loads were crucial for simulating the dynamic response of physical piers and isolators. As a consequence, they were applied to all specimens by means of force controlled actuators according to nominal values implemented in the OpenSEES RM. In greater detail, two pairs of vertical actuators of the type depicted in Figure 4.8(a) applied $2800/2.5^2 = 448kN$ to each column of both piers through tensioned DYWIDAG bar anchored at pier supports. In greater detail, actuators $1C$ and $2C$ managed by the MASTER controller C189 held constant vertical loads on Pier #9, whilst actuators $1B$ and $2B$ managed by the MASTER controller B150 held constant vertical loads on Pier #11. In order to apply nominal values of vertical loads, reduced target forces compensated self-

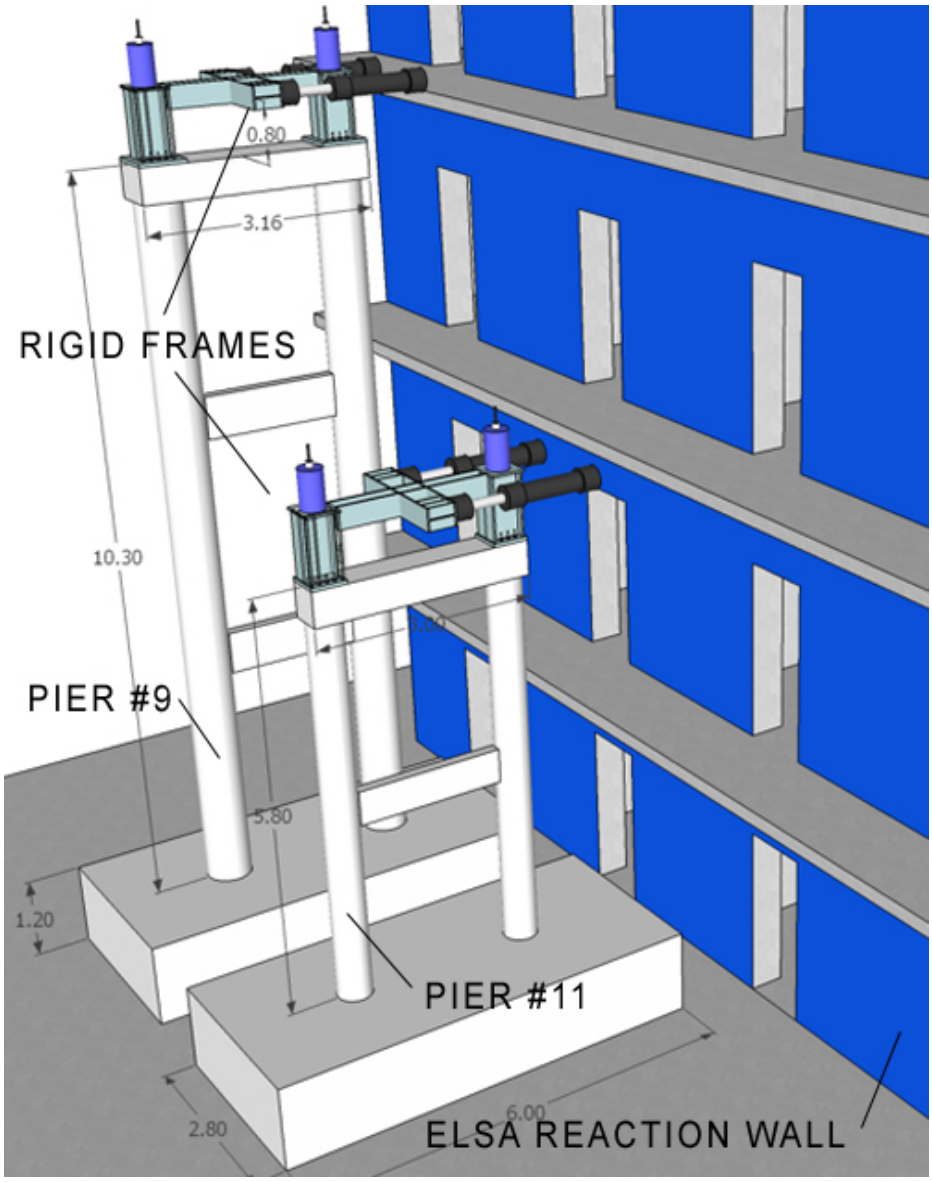

Figure 4.12: Experimental set-up of piers.

		Weight [kN]	
	Quantity	Pier #9	Pier #11
Rigid steel frame	1	18.42	17.02
Vertical actuators	2	5.52	5.52
Horizontal actuators	0.5*x*2	10.97	10.97
Load Cells	2	1.27	1.27
	Total	**36.18**	**34.78**

Table 4.3: Self weights of set-up elements

	SPECIMEN SCALE		PROTOTYPE SCALE	
	Pier #11	Pier #9	Pier #11	Pier #9
Height h [m]	8	12.5	20	31.25
Total vertical load V [kN]	900.00	900.00	5625.00	5625.00
Geometric stiffness V/h [kN/m]	-112.50	-72.00	-281.25	-180.00
Linear tangent stiffness K_{geo} [kN/m]	15256.00	9424.40	38140.00	23561.00

Table 4.4: Geometric stiffness of piers

weights of rigid steel frames and actuators reported in Table 4.3. Vertical loads were applied as increasing ramps before each hybrid simulations. Assuming actuator pairs infinitely stiff compared to relevant piers, the $P-\Delta$ effect of vertical loads causes appreciable increases of horizontal restoring forces during tests characterized by large displacements. Accordingly, for each pier, the restoring force r fed back to the time integrator was calculated as follows:

$$r = r_{mes} + K_{geo} x_{mes} \tag{4.5}$$

where r_{mes} is the measured restoring force vector, x_{mes} the relevant displacement vector and K_{geo} the negative geometric stiffness calculated according to the $P-\Delta$ model. Table 4.4 summarizes geometric stiffness of Piers #9 and #11 for both the specimen -reduced- and the prototype -full- scales. Linear tangent stiffnesses of Table 4.4 must be intended as upper bounds; in fact, they refer to undamaged

piers in the linear range. A strong stiffness degradation was observed at ULS on both piers. Moreover, their softening behavior at large displacements made contributions of geometric stiffness more and more significant. Eq. 4.5 and negative geometric stiffness of Table 4.4 were implemented in the A151 MASTER controller.

4.4.1.1 Displacement measurements

In order to calculate average curvature, shear and axial deformations of cross sections, a plenty of sensors were distributed on specimens. In grater detail, 2 load cells, 3 wires -one per level- and 73 LVDT displacement transducers were installed on Pier #9; 2 load cells, 2 wires and 48 LVDT displacement transducers were installed on Pier #11. Figures 4.13 and 4.14 depict sensor set-ups installed on piers. As can be appreciated in these figures, triangular lattices of LVTD displacement transducers were set to capture the cross sectional behavior of transverse beams. Wire displacement transducers measured total horizontal translations at transverse levels. Figure 4.15 depicts close-up views of LVDT displacement transducers mounted on transverse elements and column bases. Positions of nodes of each deformed LVDT lattice can be easily calculated. The solution of a system of nonlinear equations where lengths of deformed sensors are expressed in terms of nodal coordinates provided such measurements. According to Figure 4.16, which depicts a schematic view of a generic transverse beam LVDT lattice, interpolations of nodal displacements Ux_i and Uy_i can provide continuous displacement vector fields $Ux(x, y)$ and $Uy(x, y)$. Averaged section quantities such as rotation $\theta(x)$ and curvature $\chi(x)$ can be obtained as follows:

$$\theta(x) = \frac{\partial Uy(x, y)}{\partial x} \tag{4.6}$$

$$\chi(x) = r(x)^{-1} = \frac{\partial^2 Uy(x, y)}{\partial x^2} \left(1 + \left(\frac{\partial Uy(x, y)}{\partial x}\right)^2\right)^{-3/2} \tag{4.7}$$

Aforementioned average quantities were directly compared to OpenSEES simulations, which supported the interpretation of the huge data amount acquired.

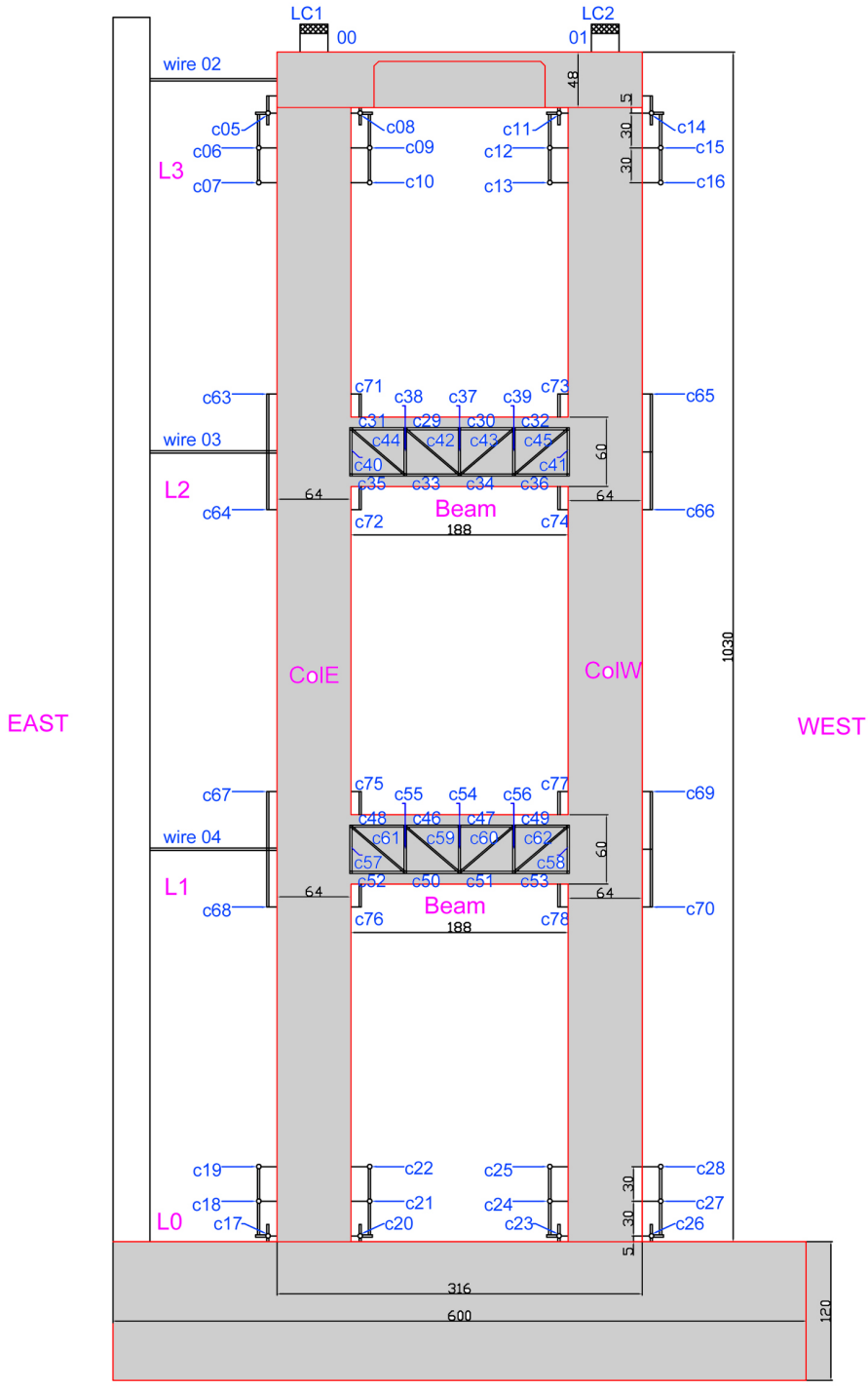

Figure 4.13: Sensor set-up of Pier #9.

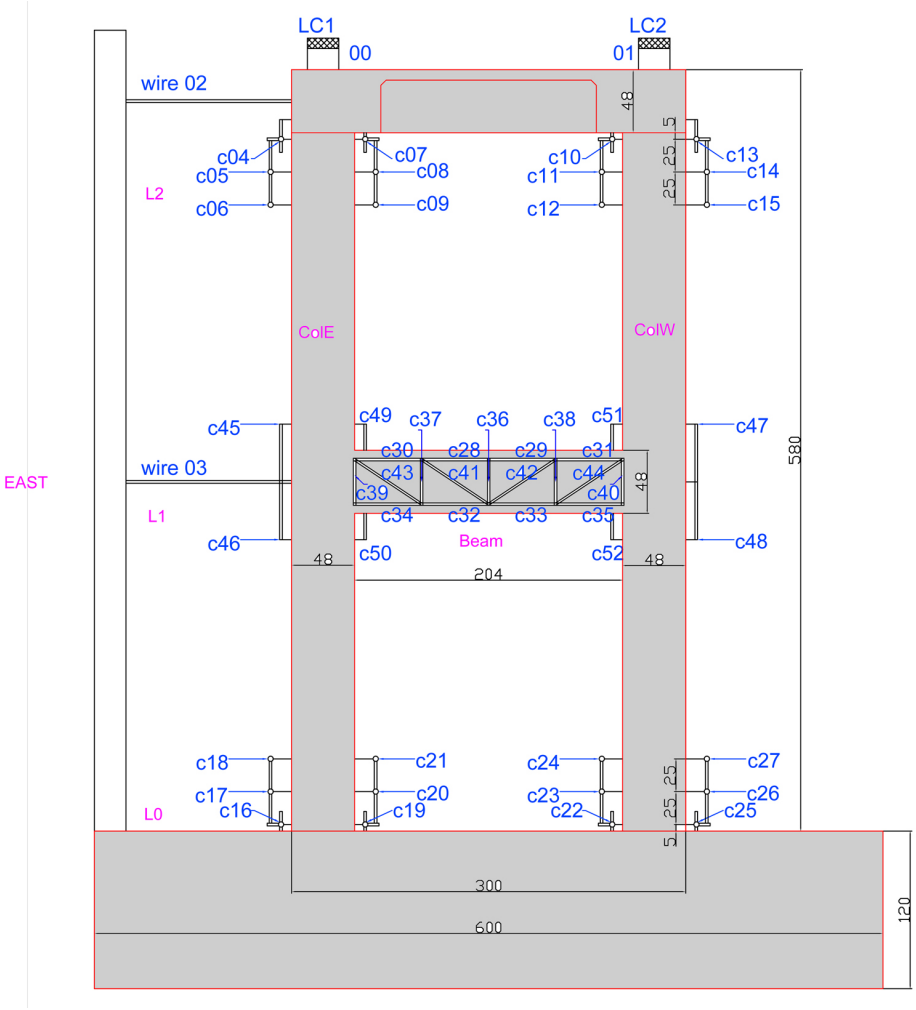

Figure 4.14: Sensor set-up of Pier #11.

(a) (b)

Figure 4.15: Close-up views of: **a** column base LVDT sensor; **b** LVDT lattice of a transverse beam.

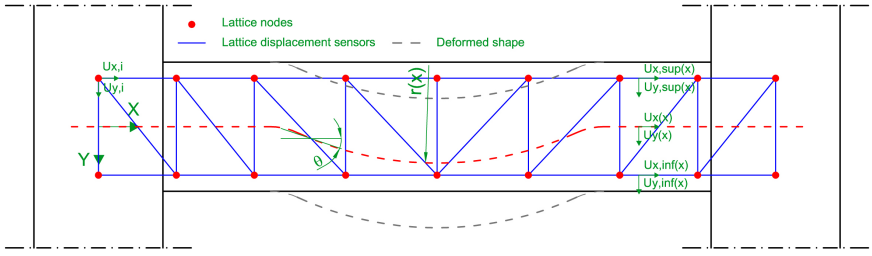

Figure 4.16: Layout of the LVDT lattice installed on transverse beams.

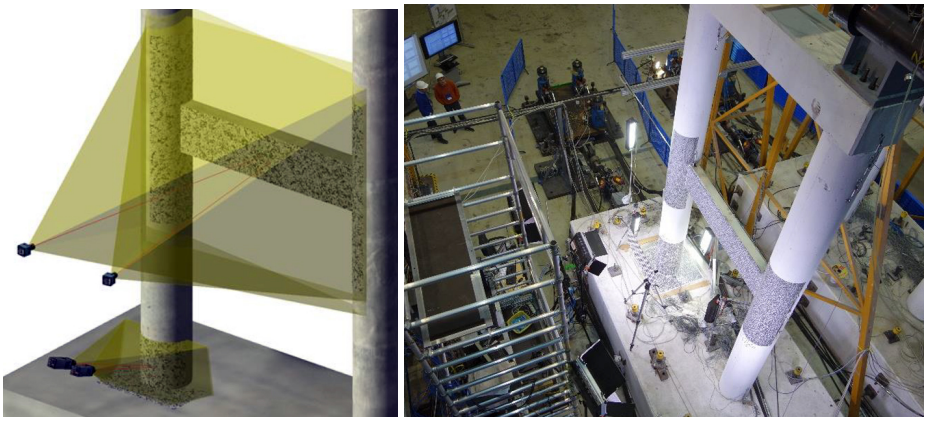

(a) (b)

Figure 4.17: **a** Schematic view of the foreseen arrangement of cameras; **b** installed acquisition equipment.

4.4.1.2 Photogrammetric measurements

An additional optical stereoscopic image acquisition system was foreseen for Pier #11. In detail, two pairs of *PCO.Edge* high resolution cameras pointed the West column base joint and the lower transverse element where a strong nonlinear response was expected. It allowed for capturing the displacement field by means of image processing algorithms. Figure 4.17 depicts the acquisition set-up with a detail of the arrangement of cameras. In order to capture the complete base joint, two astronomical mirrors were installed behind the column. Thus the back side of the joint was recorded avoiding further cameras. Figure 4.18 depicts both top and side views of the foreseen stereo photogrammetry set-up. Random speckled patterns textured joint and transverse surfaces improving the pattern recognition in the data processing phase. Each pair of cameras provided plane displacement fields of monitored surfaces. They were synchronized with the input accelerogram.

4.4.2 Experimental set-up of FPB isolators

According to Figures 4.19 and 4.20, which depict both plan and side views of the experimental set-up foreseen for each group of FPB isolators, four short actuators of the type depicted in Figure 4.8(a) applied vertical loads, whilst a long

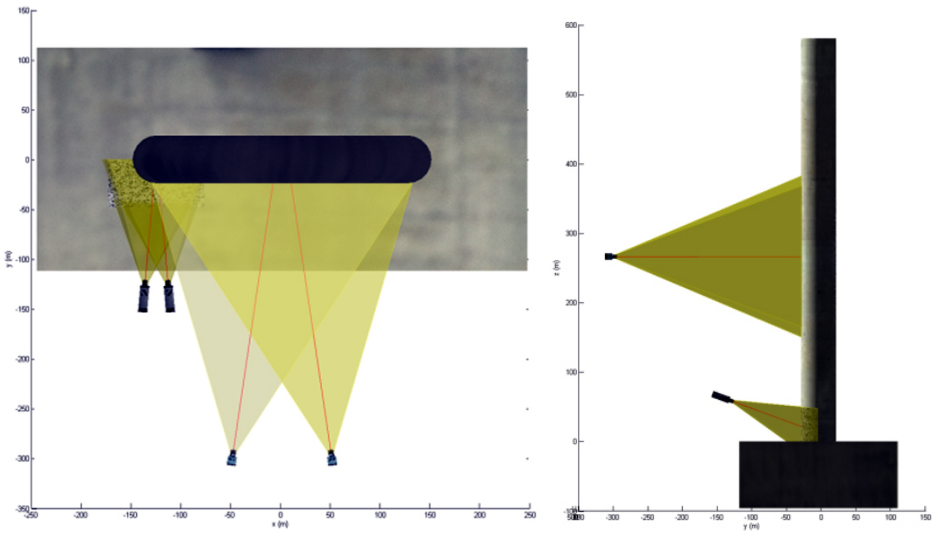

(a) (b)

Figure 4.18: Acquisition set-up for photogrammetric measurements: **a** top and **b** side views.

actuator of the type depicted in Figure 4.8(b) applied the horizontal displacement. Basically, the set-up was based on three plates: i) the lower plate that was fixed at the reaction floor; ii) the mid plate that was hinged to the horizontal actuator; in order to follow the configuration of FPB isolators, it was free to translate and rotate; iii) the upper plate that bore vertical actuators; it can rotate and translate in the vertical direction but in-plane rotation and translations were not allowed. According to Figure 4.21, which depicts the structural scheme of the experimental set-up of one block of FPB isolators, four FPB isolators were employed for each pier. Figure 4.21 highlights in red sliding surfaces; with regard to the lower FPB isolator pair, it was oriented downward; conversely, the upper pair was oriented upward. The lower FPB isolator pair was introduced to support the mid plate avoiding roller bearings. They would have biased the measurement of the horizontal restoring force by introducing spurious friction forces. According to the kinematic behavior of the proposed set-up, both FPB isolator pairs translate of the same quantity. Moreover West and East FPB isolators experienced same vertical loads $Fv_{Iso\#i,West}$ and $Fv_{Iso\#i,East}$. As a result, the clean measure of the horizontal restoring force

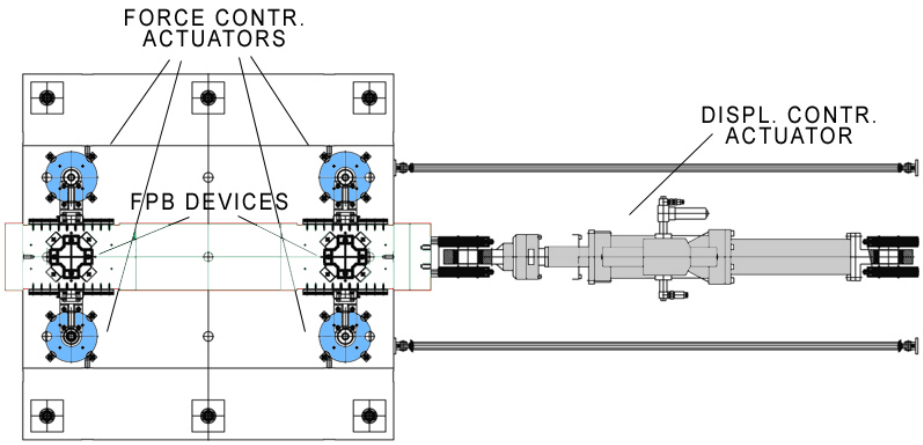

Figure 4.19: Plan view of the experimental set-up of the FPB device pair

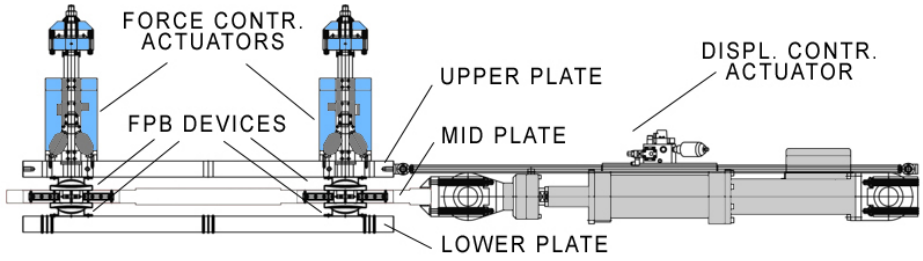

Figure 4.20: Side view of the experimental set-up of the FPB device pair

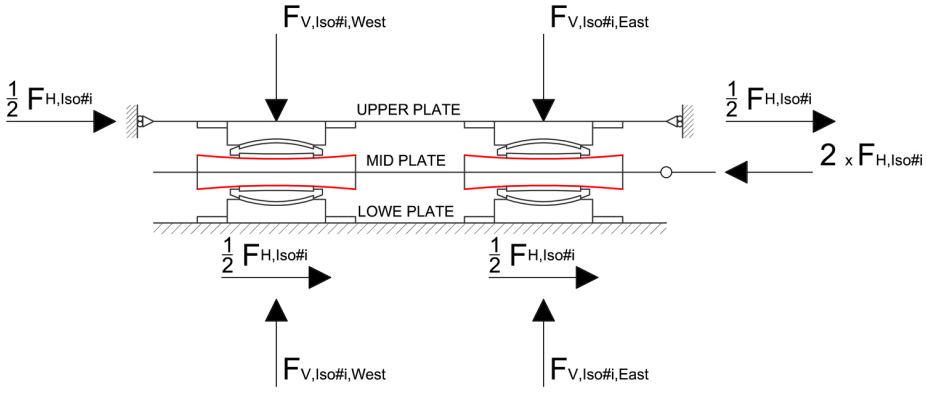

Figure 4.21: Structural scheme of the experimental set-up conceived for each single isolator block

	Quantity	Weight [kN]
Middle plate	1	7.6
Top plate	1	22.6
Vertical actuators	4	10.83
Load cells	4	2.75
Horizontal actuators	0.5	4.5
	Total	**48.2**

Table 4.5: Self weights of set-up elements

relevant to the single FPB isolator pair, i.e. $Fh_{Iso\#i}$ was obtained by halving the restoring force of the horizontal actuator.

MASTER controller A151 managed horizontal actuators $4A$ and $3A$, which applied horizontal displacements to mid plates of isolator groups of Pier #9 and #11, respectively; MASTER controller E152 and D149 handled two relevant groups of vertical actuators. According to Figure 4.20, vertical loads were applied by pulling *DYWIDAG* bars fixed to the lower plate. A vertical load equal to $2800/2.5^2 = 448kN$ was applied to West and East FPB isolators. Permanent weights of set-up elements, which are summarized in Table 4.5, were compensated. According to Figure 4.22, the overturning moment due to lever arm L of horizontal load F_H generated vertical reaction forces $\pm\Delta F_V = \pm F_H L/B$ at the base of the rigid steel frame. They were summed to constant gravity loads and applied to both West and East FPB isolators. With regard to Pier #9, Eqs. 4.8 and 4.9 express vertical forces acting on West and East FPB isolators:

$$Fv_{Iso\#9,West} = 448kN + Fh_{Pier\#9}\frac{B}{L} \tag{4.8}$$

$$Fv_{Iso\#9,East} = 448kN - Fh_{Pier\#9}\frac{B}{L} \tag{4.9}$$

For this purpose, horizontal restoring forces $Fh_{Pier\#9}$ was sent from MASTER A151 controller to MASTER E159 controller handling vertical actuators of isolators of Pier #9. The control strategy implemented for the four vertical actuators applied to

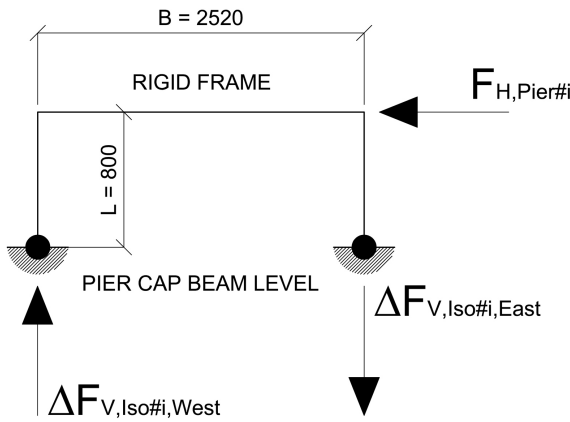

Figure 4.22: Structural scheme and vertical reactions of the rigid steel frame

FPB isolators of Pier #9, i.e. $1E$, $2E$, $3E$ and $4E$, reads:

$$F_{1E} = Fv_{Iso\#9,West} - F_{2E} \tag{4.10}$$

$$F_{3E} = Fv_{Iso\#9,East} - F_{4E} \tag{4.11}$$

Two further constraints were imposed: i) null warping moment of vertical forces and ii) null rolling rotation of the middle. Thus, the target force F_{2E} was expressed as:

$$F_{2E} = F_{1E} - F_{3E} + F_{4E} \tag{4.12}$$

and the target displacement D_{4E} was calculated as:

$$D_{4E} = D_{1E} - D_{2E} + D_{3E} \tag{4.13}$$

For the sake of completeness, vertical loads on FPB isolators of Pier #11 read,

$$Fv_{Iso\#11,West} = 450kN + Fh_{Pier\#11}\frac{B}{L} \tag{4.14}$$

$$Fv_{Iso\#11,East} = 450kN - Fh_{Pier\#11}\frac{B}{L} \tag{4.15}$$

Accordingly, the control strategy of vertical actuators applied to FPB isolators of Pier #11 follows:

$$F_{1D} = Fv_{Iso\#11,West} - F_{2D} \tag{4.16}$$

$$F_{3D} = Fv_{Iso\#11,East} - F_{4D} \tag{4.17}$$

$$F_{2D} = F_{1D} - F_{3D} + F_{4D} \tag{4.18}$$

$$D_{4D} = D_{1D} - D_{2D} + D_{3D} \tag{4.19}$$

Both horizontal restoring forces $Fh_{Iso\#9}$ and $Fh_{Iso\#11}$ were sent to MASTER A151 controller for the purpose of the time integration of the equation of motion of the hybrid system.

4.5 Scheduling of experiments and model updating testing procedure

A total of sixty-four tests were executed during the five months long RETRO testing campaign. Basically, they can be classified as follows:

- characterization of isolators
- characterization of undamaged piers
- hybrid simulations of the Rio Torto Bridge

All test types are carefully described and relevant tests are listed in following subsections.

4.5.1 Characterization of FPB isolators

According to the item list above, the first test type was aimed at characterizing the behavior of FPB isolators of both piers. In particular, harmonic, monotonic and random horizontal displacement histories were applied to specimens. The full operating range was investigated considering different amplitudes, frequencies

Label	Description	Vertical Load [kN]	Date
d01	2 waves, ampl. 10...50mm	450kN	13/09/2013
d02	2 waves, ampl. 30mm	450kN	17/09/2013
d03	Cyclic, ampl. 50,40,30,20,10mm	450kN	17/09/2013
d04	Cyclic, ampl. 50,40,30,20,10mm	450kN	30/09/2013

Table 4.6: Characterization tests of FPB isolators of Pier #9.

Label	Description	Vertical Load [kN]	Date
b06	Cyclic, ampl. 10mm	450kN	16/07/2013
b07	Cyclic, ampl. 10mm	450kN	17/07/2013
b08	Cyclic, ampl. 4mm	450kN	18/07/2013
b09	Cyclic, ampl. 5mm	450kN	18/07/2013
b10	Cyclic, ampl. 5mm	450kN	19/07/2013
b11	Cyclic, ampl. 10,30,50,40mm	100kN	24/07/2013
b12	Cyclic, ampl. 40,50,30mm	100,450kN	24/07/2013
b13	Cyclic, ampl. 30,40,50mm	550,450,350kN	25/07/2013
b14	Cyclic, ampl. 6mm	450kN	26/07/2013
b15	Sweep sine 0.001-1.5Hz, ampl. 10mm	450kN	29/07/2013
b16	Cyclic, ampl. 50,40,30,20,10mm	450kN	30/07/2013
b17	Random Pattern, ampl. -30,+7mm	470kN	31/07/2013
b18	Random Pattern, ampl. -30,+7mm	470kN	02/08/2013
b19	Sweep sine .001-1.5Hz, ampl. 10,20	450kN	07/08/2013
b20	Sweep sine 0.001-1.5Hz, ampl. 10,20	450kN	08/08/2013
b21	Random pattern, ampl. -30,+7mm,	470kN	08/08/2013
b22	2 waves, ampl. 30mm	450kN	13/08/2013
b23	Random pattern, ampl. -30,+7mm	470kN	13/08/2013

Table 4.7: Characterization tests of FPB isolators of Pier #11.

Label	Description	Vertical Load [kN]	Date
f02	Cyclic, ampl. 1.5mm	450kN	08/10/2013
f03	Cyclic, ampl. 1.5mm	450kN	08/10/2013

Table 4.8: Characterization tests of Pier #11.

Label	Description	Vertical Load [kN]	Date
f04	Cyclic, ampl. 2.0mm	450kN	09/10/2013

Table 4.9: Characterization tests of Pier #9.

and axial forces. Tables 4.6 and 4.7 report the complete lists of characterization tests of both FPB isolator groups of Pier #9 and #11, respectively. Vertical loads reported in Tables 4.6 and 4.7 refer to axial forces applied to each single FPB isolators according to the foreseen experimental set-up.

4.5.2 Characterization of piers

The second test type focused on piers; its purpose was twofold: i) to tune PID gains to achieve an optimal performance of the control system; ii) to characterize undamaged specimens. Tables 4.9 and 4.8 report lists of tests. Essentially, static cyclic displacement histories were applied at the top of each pier. Vertical loads reported in Tables 4.9 and 4.8 were held constant and applied to both West and East columns to reproduce scaled deck gravity loads.

4.5.3 Hybrid simulation of the Rio Torto Bridge

Finally, the fourth test type is introduced. According to the aims of the RETRO research project, the testing program included hybrid simulations of the Rio Torto Bridge in both the non isolated and the isolated cases. Table 4.10 reports the list of hybrid simulations of the bridge.

Label	Time integrator	PS	NS	Seismic input	Date
k04	Partitioned	Piers #9 and #11	non-isol bridge	0.1 SLS 12.5s	05/11/2013
k05	Partitioned	Piers #9 and #11	non-isol bridge	0.1 SLS 25s	06/11/2013
k06	Partitioned	Piers #9 and #11	non-isol bridge	0.1 SLS 12.5s	08/11/2013
k07	Partitioned	Piers #9 and #11	non-isol bridge	1.0 SLS 6.6s	08/11/2013
l01	Partitioned	Piers #9 and #11	isol bridge	1.0 SLS	12/11/2013
l02	Partitioned	Piers #9 and #11	isol bridge	1.0 ULS	13/11/2013
n01	Partitioned	Iso. #9 and #11	isol bridge	1.0 SLS	14/11/2013
p01	Partitioned	Piers #9 and #11 + Iso. #9 and #11	isol bridge	1.0 SLS	15/11/2013
p02	Partitioned	Piers #9 and #11 + Iso. #9 and #11	isol bridge	0.7 ULS	15/11/2013
q01	Partitioned	Pier #9 + Iso. #9	isol bridge	1.0 SLS	18/11/2013
q02	Partitioned	Pier #9 + Iso. #9	isol bridge	0.65 ULS	18/11/2013
q03	Partitioned	Pier #9 + Iso. #9	isol bridge	0.65 ULS	18/11/2013
k09	Partitioned	Piers #9 and #11	non isol bridge	1.0 ULS	19/11/2013
k10	Partitioned	Piers #9 and #11	non isol bridge	1.0 ULS	21/11/2013
k12	Partitioned	Piers #9 and #11	non isol bridge	2.0 ULS	21/11/2013
r01	Partitioned	Iso. #9	isol bridge	0.65 ULS	20/11/2013
r02	Partitioned	Iso. #9	isol bridge	0.80 ULS	20/11/2013
r03	Partitioned	Iso. #9	isol bridge	0.90 ULS	20/11/2013

Table 4.10: RETRO tests: hybrid simulations of the Rio Torto Bridge

Tests *k*04 to *k*06 were aimed at simulating the dynamic response of the non isolated bridge in the linear range; in fact, the SLS accelerogram was applied with a PGA reduced to 10% of its original value. The purpose of Test *k*07 was to reproduce the damage state of the real bridge on pier specimens. The SLS seismic input was applied to the non isolated bridge, which induced slight damage to piers. Then, the effectiveness of the proposed seismic retrofitting was estimated through Tests *l*01 and *l*02 on the isolated bridge at SLS and ULS, respectively. Since characterization tests on FPB isolation devices highlighted a friction coefficient μ = 7% greater than the designed μ = 4%, numerical isolators were considered also for physical piers during Tests *l*01 and *l*02. Further hybrid simulations *n*01, *p*01, *p*02, *q*01, *q*02 and *q*03 of the isolated bridge were executed considering physical isolators. Nonetheless, reduced vertical loads were applied in order to compensate unexpected higher values of friction coefficients. Moreover, reduced PGA values were considered at ULS to preserve corresponding physical piers from damage. According to Table 4.10, Tests *r*01, *r*02 and *r*03 were further conducted; isolators of Pier #9 were physically substructured and the applied ULS accelogram was reduced to 65%, 80% and 90% of its PGA value. In these cases, full vertical loads were applied to physical specimens. Finally, hybrid simulations of the Rio Torto Bridge were conducted in the non isolated case in order to estimate its seismic vulnerability at ULS. In greater detail, Test *k*09 simulated the dynamic response of the bridge at ULS. In order simulate an aftershock event on the damaged bridge, the same ULS accelerogram was repeated during Test *k*10. The last Test *k*12 was aimed at simulating a seismic even beyond design conditions; hence, the ULS accelerogram was applied with a 200% magnified PGA value.

4.5.4 The model updating testing procedure

As highlighted by Paolacci and Giannini (2012), the Rio Torto Bridge in the non isolated condition accumulates damage within piers during the seismic event, whilst the deck remains in the linear regime. In order to account for such damage accumulation on both numerical an physical piers, a novel model updating testing procedure was conceived and applied. In the author's knowledge, few attempts aimed at simulating a consistent degradation of PSs and NSs were made until today (Kwon and Kammula, 2013; Yang, 2012). They are based on on-line param-

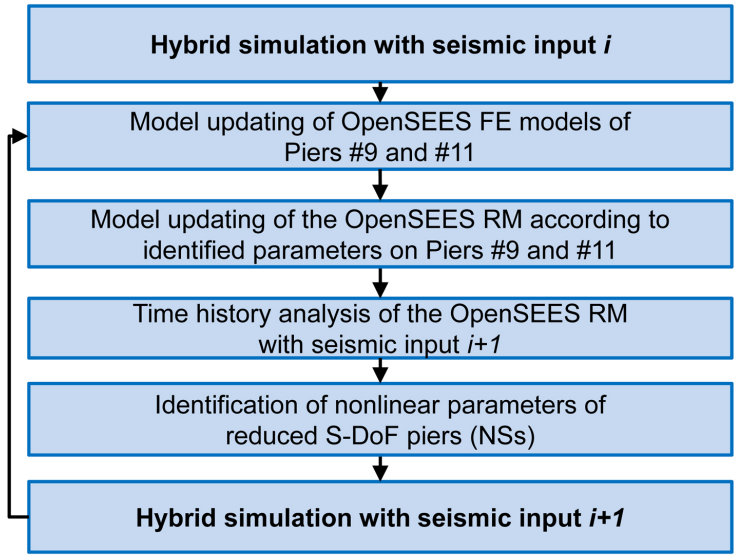

Figure 4.23: Flowchart of the testing procedure applied to the Rio Torto Bridge

eter estimators but application case studies are restricted to simple benchmark structures. In the proposed offline approach hybrid simulations are conducted at increasing PGA levels. In order to replicate damage experienced by PSs up to the latest test, NSs are updated off-line before the incoming hybrid simulation. In detail, FE models of PSs are set; then, their parameters are identified after each test. Parameters of a FE model of the global emulated system are upgraded accordingly. A time history of this model is conducted considering the seismic input of the incoming test. In order to reproduce the dynamic response of the updated global FE model, nonlinear parameters of reduced NSs are updated and implemented. The flowchart of Figure 4.23 summarizes the testing procedure applied to the Rio Torto Bridge. With regard to the Rio Torto case study, 2D OpenSEES FE models of Piers #9 and #11 were set to quantify damage experienced by corresponding specimens after a generic hybrid simulation *i*. The maximum compressive strength of *concrete01* OpenSEES material was considered as updating parameters. Identified values on Pier #9 and #11 were applied to remaining hollow and solid cross section columns, respectively, of the OpenSEES RM presented in Chapter 3. Then, a time history analysis of the updated OpenSEES RM was conducted assuming

the seismic input of the incoming hybrid simulation. In order to reproduce calculated dynamic responses, nonlinear parameters of reduced S-DoF piers presented in Chapter 3 were updated and implemented for the hybrid simulation $i+1$. As can be appreciated, the quick characterization of physical piers between subsequent hybrid simulations was crucial for the purpose of damage propagation in remaining piers. To this end, a numerical tool for the updating of OpenSEES FE models was implemented in the Matlab environment and carefully described in the next section.

4.6 Nonlinear identification of physical substructures

In order to characterize physical piers and FPB isolators, relevant OpenSEES FE models were taken as reference. In this respect, a model updating tool was devised. It operates between Matlab and OpenSEES environments allowing for the identification of parameters of OpenSEES FE models. In greater detail, it was based on a Matlab interface to OpenSEES; given a generic displacement history and a set of parameters, such interface generates the updated *tcl* code of the OpenSEES model and then runs the OpenSEES analysis. In order to simulate the quasi-static loading procedure characterizing the hybrid simulation technique, OpenSEES nonlinear static analyses with imposed displacement histories were considered. Finally, the interface function provides OpenSEES recorded restoring forces as output arguments. The Matlab code of the interface function is reported herein.

```
1   function [FOR] = pier_9/pier_11/iso(k,DSP)
2
3   % CALCULATION OF THE INCREMENTAL DISPLACEMENT VECTOR
4   CMD = diff(DSP);
5   save CMD.txt CMD -ascii;
6
7   % UPDATING OF THE TCL CODE WITH PARAMETER k
8   FID_out = fopen('pila_9_mu.tcl/pila_11_mu.tcl/iso_mu.tcl','wt');
9   fprintf(FID_out,'%s;\n','wipe');
10  fprintf(FID_out,'set k %f;\n',k);
11  FID_inp = fopen('pila_9.tcl/pila_11.tcl/iso.tcl','rt');
12  LIN_inp = fgetl(FID_inp);
13  while ischar(LIN_inp)
```

```
14          fprintf(FID_out,'%s \n',LIN_inp);
15          LIN_inp = fgetl(FID_inp);
16      end
17      fclose(FID_out);
18
19      % OPENSEES SOLVER
20      dos('OpenSees.exe ...
            pila_9_mu.tcl/pila_11_mu.tcl/iso_mu.tcl','-echo');
21
22      % READING OPENSEES RECORDERS
23      FOR = importdata('DATA\FOR.txt');
24
25      end
```

With regard to the proposed code, Row #20 is crucial for the effectiveness of the interface. In fact, it lets Matlab to wait until the OpenSEES solver closes. As a result, it can be efficiently called within the model updating loop. In order to identify nonlinear parameters of FE models of each specimen, a penalty function was defined; it was conceived as the NRMSE between measured and simulated restoring forces given the measured displacement history.

$$\hat{\theta} = \min_{\theta} \text{NRMSE}(\mathbf{r}_{mes}, \mathbf{r}_{num}(\mathbf{x}_{mes}, \theta)) \tag{4.20}$$

where:

- $\mathbf{x}_{mes}$: measured displacement history;
- $\mathbf{r}_{mes}$: measured restoring force history;
- $\mathbf{r}_{num}$: numerical restoring force history calculated via OpenSEES;
- θ : vector of OpenSEES nonlinear parameters;

In order to avoid gradient estimations, the derivative-free Matlab *patter search* algorithm was adopted to solve each optimization problem defined by (4.20). Since each iteration entails a 30000 steps OpenSEES nonlinear static analysis, the maximum number of function evaluations was set to 50. Full-scale FE model of substructured components were considered; accordingly, measured histories on specimens were magnified according to relevant scaling factors, i.e. 2.5 for displacements and $2.5^2 = 6.25$ for forces.

Label	Test type	Date
f03	Cyclic on Pier #11	08/10/2013
f04	Cyclic on Pier #9	09/10/2013
k05	Hybrid sim. of the non-isol. bridge at 0.1 SLS	06/11/2013
k07	Hybrid sim. of the non-isol. bridge at 1.0 SLS	08/11/2013
k09	Hybrid sim. of the non-isol. bridge at 1.0 ULS	19/11/2013
k10	Hybrid sim. of the non-isol. bridge at 1.0 ULS	21/11/2013
k12	Hybrid sim. of the non-isol. bridge at 2.0 ULS	21/11/2013

Table 4.11: List of tests followed by characterizations of physical piers, i.e. model identification of PSs

4.6.1 Characterization of piers

As anticipated, fiber-based OpenSEES FE models of both Piers #9 and #11 were taken as reference for the characterization of relevant specimens. Since each model updating session entailed many OpenSEES runs, 3D fiber based FE models of piers belonging to the OpenSEES RM presented in Chapter 3 were replaced by their 2D counterparts with reduced numbers of DoFs. Same geometries, constraint conditions, material constitutive laws and cross sections were considered. Figure 4.24 depicts schemes of both 2D FE models of Piers #9 and #11 with relevant node numbering. With respect to Figure 4.24, measured displacement histories $\mathbf{x}_{mes}$ were applied to highlighted DoFs through the interface function as input arguments; relevant numerical restoring force histories $\mathbf{r}_{num}$ calculated via OpenSEES were fed back as output arguments to the Matlab environment. A penalty function was defined according to Eq. (4.20) and the maximum compressive strength f_{pc} of the *concrete01* OpenSEES material was considered as updating variable θ. In order to avoid ill-conditioning problems, a sensitivity analysis confirmed the effectiveness of the parameter selection. Since no damage was expected on piers in the isolated case, specimens were characterized after preliminary cyclic tests and each hybrid simulation of the non isolated bridge; see Table 4.11 in this respect. Figure 4.25 summarizes identified values and emphasizes monotonic de-

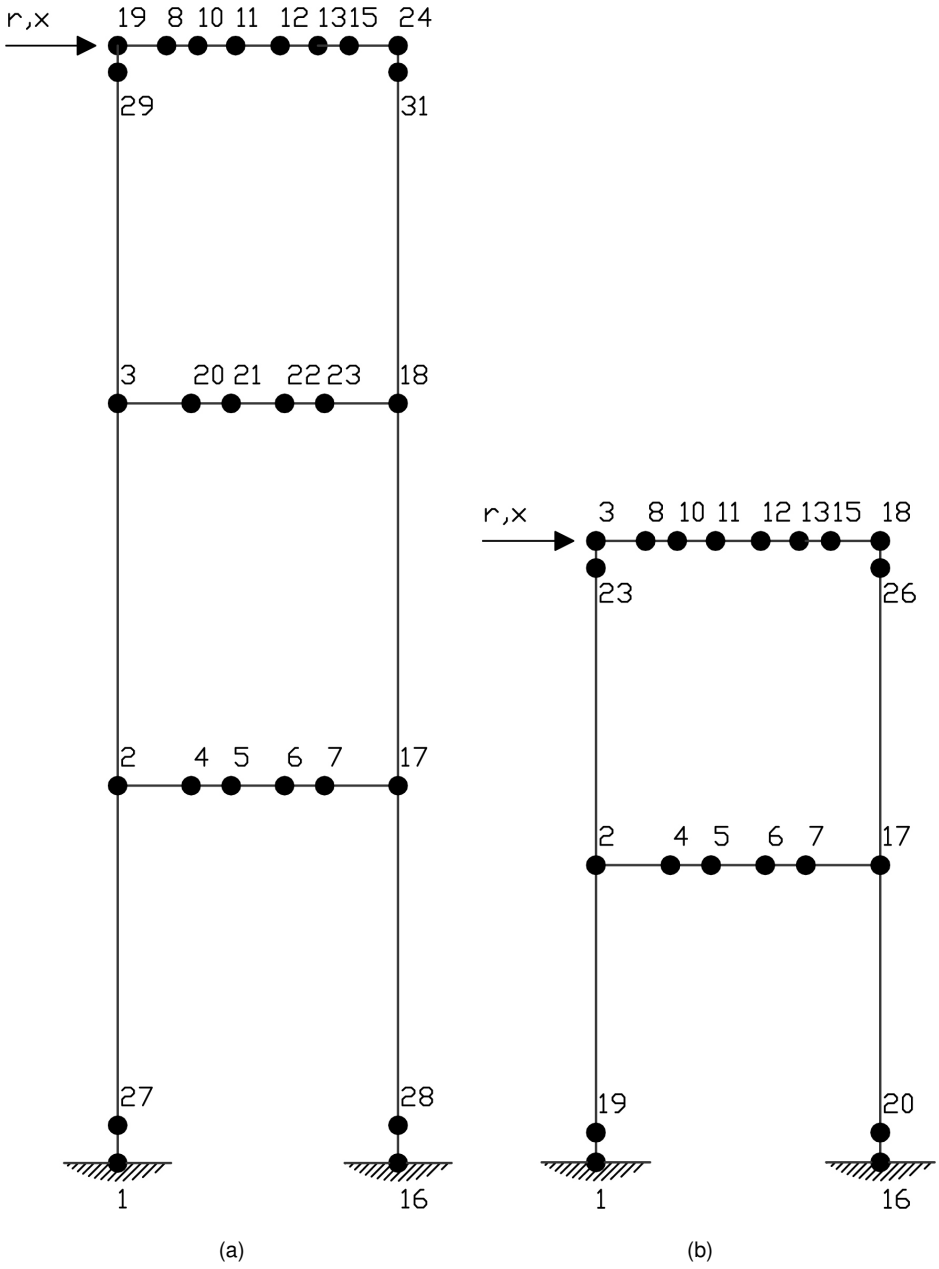

Figure 4.24: Fiber-based OpenSEES 2D FE model of **a** Pier #9; and **b** Pier #11 with relevant node numbering.

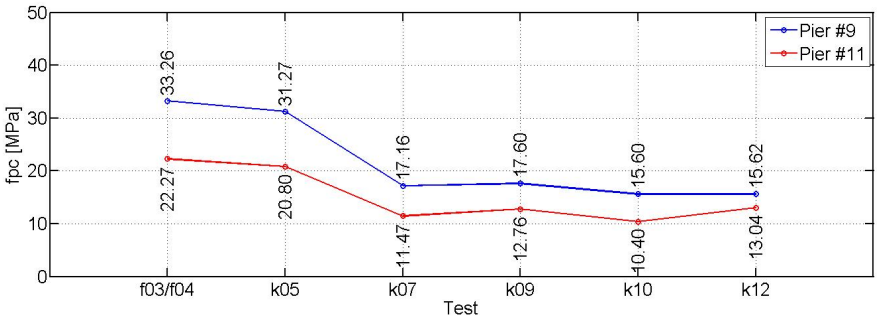

Figure 4.25: Identified values of maximum compressive strength f_{pc} of OpenSEES *concrete01* material

creasing trends of identified parameters. As can be appreciated in Figure 4.25, first estimations showed an appreciable difference. In fact, maximum compressive strengths of 22.27MPa and 33.26MPa were identified on Piers #9 and #11, respectively. Nonetheless, OpenSEES 2D FE models did not account for cracking as well as for shrinkage that can induce localized damage patterns. Moreover, different types of cross sections can amplify parameter discrepancies. In fact, columns of Pier #11 were characterized by solid cross sections, whilst columns of Pier #9 by hollow cross sections. A sudden drop of concrete compressive strength was observed on both piers at Test $k07$. Figure 4.26 compares identified hysteretic loops to experimental measurements on Piers #9 and #11during Test $k09$. As can be appreciated in Figure 4.26, OpenSEES models well reproduced hysteretic loops of physical specimens.

4.6.2 Characterization of FPB isolators

As done for piers, an OpenSEES model of a single FPB isolators at the prototype scale was implemented for the purpose of the identification of the friction parameter μ . According to Lomiento et al. (2013) the friction parameter μ is mainly affected by:

- vertical load: μ diminishes with an applied vertical load
- velocity: μ increases at higher velocities
- cycling: μ decreases at temperature rises

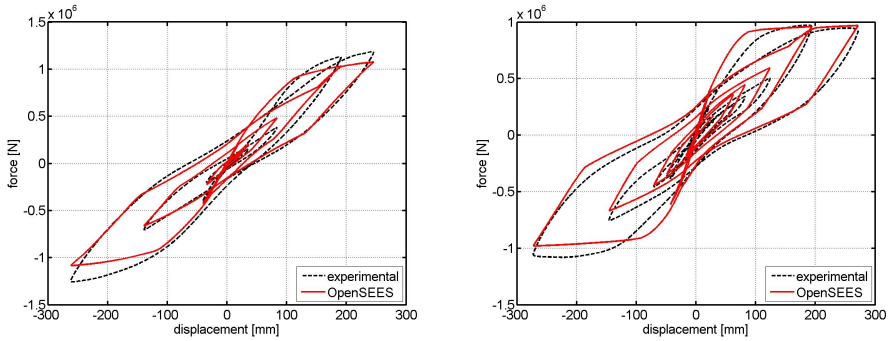

Figure 4.26: Comparison between experimental and numerical hysteretic loops of **a** Pier #9; and **b** Pier #11 during Test *k*09.

- breakaway: peak values of μ occur at null velocities (dynamic to static friction)

This last effect does not affect much the energy dissipation of the force-displacement cycle, but may dangerously modify the force demand on the isolated structure. As a consequence, a testing protocol based on cyclic tests characterized by two wave displacement patterns with variable frequency, amplitude and vertical load was conceived. Experiments were carried out within the expected operating range of FPB isolators foreseen by numerical simulations. Five minutes stops were interposed between subsequent patterns to avoid overheating. The preliminary characterization of the friction coefficient μ focused on Tests *d*02, *d*03, *b*16 and *b*22. According to foreseen gravity forces, they were characterized by a constant vertical load of 450kN applied to each FPB isolator, see Tables 4.6 and 4.7 in this respect. Tests *b*16 and *d*03 were characterized by five cycles at constant frequency of 1/100Hz and decreasing amplitudes of 50, 40, 30, 20 and 10mm. As a result, velocity peaks ranged between 3.14 and 0.63mm/s in the specimen -reduced- scale. Figure 4.27 reports experimental and identified hysteretic loops on FPB isolators of Piers #9 and #11 during Tests *d*03 and *b*16, respectively. Hysteretic loops of Figure 4.27 refer to the response of a single pair of FPB isolators magnified to the prototype -full- scale. Conversely, Tests *b*22 and *d*02 were characterized by a variable frequency ranging between 1/500 and 1/30Hz and a constant amplitude

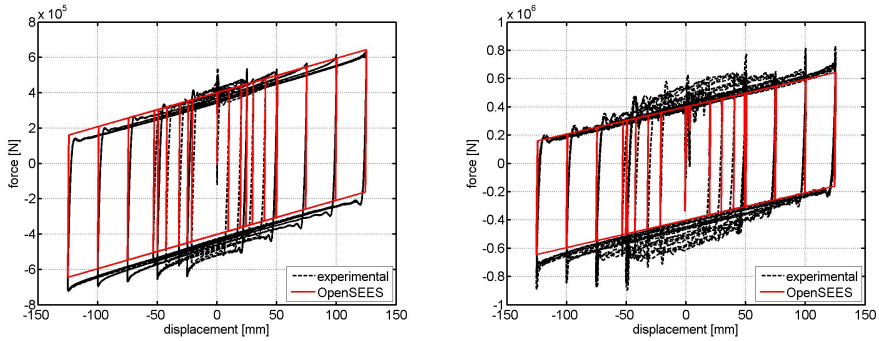

(a) (b)

Figure 4.27: Hysteretic loops of FPB isolation devices of: **a** Pier #9 during Test *d*03; and **b** Pier #11 during Test *b*16.

	Iso. #9		Iso. #11	
Test	d02	d03	b16	b22
Friction parameter μ	0.069	0.071	0.071	0.069

Table 4.12: Friction parameter μ of OpenSEES *single FP bearing* elements identified of physical isolators

of 30mm. The velocity peaks ranged from 0.63 to 37.7mm/sec in the specimen -reduced- scale. Figure 4.28 reports experimental and identified hysteretic loops on FPB isolator of Piers #9 and #11 during Tests *d*02 and *b*22, respectively, and magnified to the prototype -full- scale. Hysteretic loops of Figure 4.28 refer to the response of a single pair of FPB isolators magnified to the prototype scale. As can be appreciated in Figures 4.27 and 4.28, the effect of cycling was not appreciated at tested velocities. The breakaway effect was quite small above 6.3mm/s; it became stronger at slower speeds even though it remained limited. Table 4.12 summarizes identified values of the OpenSEES friction parameter μ. As can be appreciated in Table 4.12, FPB isolation devices installed on both Piers #9 and #11 showed friction values almost twice than the design value, which was set to 0.04. In order to preserve specimens of piers, only numerical isolators were implemented for the purpose of the hybrid simulation of the Rio Torto Bridge in the

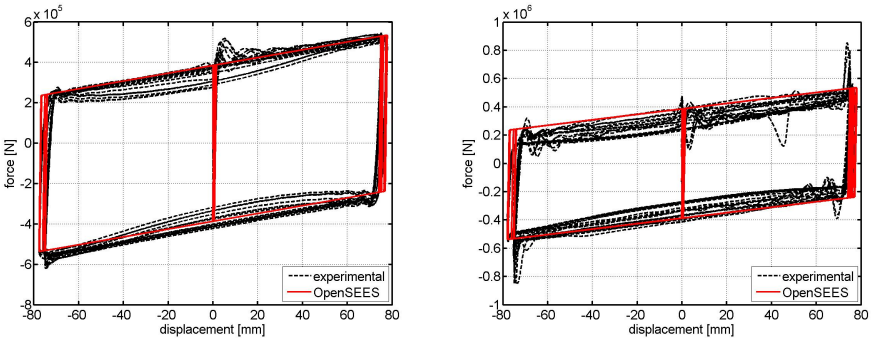

(a) (b)

Figure 4.28: Hysteretic loops of FPB isolation devices of: **a** Pier #9 during Test *d*02; and **b** Pier #11 during Test *b*22.

isolated case at ULS. Further tests with physical FPB isolators were executed with reduced vertical loads to compensate unexpected higher friction values. Reduced PGA values were considered at ULS in these cases.

4.7 Model updating of numerical substructures

According to the novel model updating testing procedure, the OpenSEES RM developed in Chapter 3 was updated after each characterization of physical piers. Identified values of OpenSEES *concrete01* material parameters summarized in Figure 4.25 were applied to numerical piers. In greater detail, the maximum compressive strength f_{pc} identified on Pier #9 was applied to all piers provided with hollow section columns, i.e. #5,#6,#7,#8 and #9, whilst the maximum compressive strength f_{pc} identified on Pier #11 was applied to all piers provided with solid cross section columns, i.e. #1, #2, #3, #4, #10, #11 and #12. Since characterizations of piers were done after tests where damage was experienced, a predictive OpenSEES RM of the bridge was always available before each hybrid simulation. In order to predict dynamic responses of piers at the following test, a time history analysis of the updated OpenSEES RM was conducted assuming the target seismic input. Nonlinear parameters of reduced S-DoF piers, i.e. NSs, were updated accordingly as shown in Chapter 3 and implemented as NSs for the incoming hybrid simulation. Table 4.13 summarizes dependencies between nonlinear identi-

fication and model updating sessions aimed at propagating damage from physical to numerical piers.

Nonlinear id. of PSs		Model updating of NSs		
Test	Description	Test	Description	Parameter set
d03/d04:	cyclic tests	**k05**	non iso. at 10% SLS	#1
k05:	non iso. at 10% SLS	**k07**	non iso. at 100% SLS	#2
k07	non iso. at 100% SLS	**l01**,p01,q01	iso. at 100% SLS	#3
		l02,n01,p02,q02,q03	iso. at 100,100,70,65 and 65% ULS	#4
		r1,r2,r3	iso. at 65,80 and 90% ULS	#5
		k09,k10	non iso. at 100% ULS	#6
		k12	non iso. at 200% ULS	#7

Table 4.13: Dependencies between nonlinear identification and model updating sessions.

As reported in Table 4.13, a parameter set was defined for each model updating session. It consisted of ρ, α and β matrices of parameters of reduced S-DoF piers implemented as NSs. With regard to bold highlighted tests, Tables 4.14 and 4.15 report identified nonlinear parameters of reduced models of piers.

	Test k05			Test k07			Test k09			Test k12		
Pier	α	β	ρ	α	β	ρ	α	β	ρ	α	β	ρ
1	0.00	0.00	0.80	1208.99	0.19	0.68	1.468	1.900	0.113	312.170	0.653	0.166
2	0.00	0.00	0.95	169.74	0.06	0.75	124.914	0.561	0.617	15.824	1.229	0.338
3	0.00	0.00	0.95	76.08	1.14	0.66	162.437	0.024	0.674	7.984	1.192	0.314
4	0.00	0.00	0.73	85.71	0.93	0.51	20.307	0.875	0.293	1.000	0.750	0.176
5	0.00	0.00	0.80	87.58	1.88	0.50	1.907	1.333	0.255	0.002	0.703	0.165
6	0.00	0.00	0.84	32.50	1.18	0.60	7.669	1.172	0.394	1.000	0.811	0.334
7	0.00	0.00	0.85	6.43	2.00	0.50	0.992	1.500	0.375	252.398	0.648	0.898
8	0.00	0.00	0.84	61.66	0.69	0.61	21.388	1.176	0.404	9.500	0.500	0.304
9	0.00	0.00	0.83	252.93	0.80	0.67	3.775	2.176	0.248	246.743	0.650	0.458
10	0.00	0.00	0.83	596.65	0.00	0.71	28.914	2.597	0.219	1.884	1.842	0.107
11	0.00	0.00	0.83	490.83	1.82	0.57	0.246	3.455	0.135	27.837	1.631	0.106
12	0.00	0.00	0.83	1010.25	0.42	0.70	157.200	2.652	0.254	29.293	2.292	0.116

Table 4.14: Hybrid simulations of the non isolated bridge: nonlinear parameters of S-DoF reduced piers.

Tables 4.16 and 4.17 summarize entailing errors with respect to OpenSEES RMs in both the non isolated and the isolated conditions. In detail, NRMSE on displacement, velocity and acceleration responses measured at the cap beam level of each pier of the reduced bridge were calculated.

	Test /01			Test /02		
Pier	α	β	ρ	α	β	ρ
1	0.00	0.00	0.45	989.73	0.03	0.42
2	0.00	0.00	0.70	289.11	0.03	0.63
3	0.00	0.00	0.60	67.34	0.57	0.54
4	0.00	0.00	0.45	48.68	1.81	0.39
5	0.00	0.00	0.51	133.30	0.22	0.51
6	0.00	0.00	0.51	0.97	0.88	0.45
7	0.00	0.00	0.51	0.69	0.00	0.47
8	0.00	0.00	0.51	10.83	1.44	0.44
9	0.00	0.00	0.49	736.95	0.01	0.59
10	0.00	0.00	0.45	534.75	0.01	0.49
11	0.00	0.00	0.50	549.39	0.14	0.52
12	0.00	0.00	0.51	987.34	1.28	0.53

Table 4.15: Hybrid simulations of the isolated bridge: nonlinear parameters of S-DoF reduced piers.

	Test $k05$			Test $k07$			Test $k09$			Test $k12$		
Pier	dsp	vel	acc	dsp	vel	acc	dsp	vel	acc	dsp	vel	acc
1	0.03	0.02	0.01	0.02	0.02	0.01	0.08	0.06	0.04	0.08	0.05	0.03
2	0.11	0.09	0.06	0.05	0.05	0.03	0.06	0.05	0.04	0.07	0.04	0.02
3	0.09	0.08	0.05	0.04	0.04	0.03	0.05	0.04	0.03	0.07	0.04	0.02
4	0.08	0.07	0.04	0.04	0.04	0.02	0.05	0.04	0.02	0.07	0.04	0.02
5	0.06	0.05	0.04	0.04	0.04	0.02	0.06	0.04	0.02	0.07	0.04	0.02
6	0.06	0.05	0.03	0.05	0.04	0.03	0.07	0.05	0.03	0.07	0.05	0.02
7	0.09	0.08	0.06	0.04	0.04	0.02	0.06	0.04	0.02	0.05	0.04	0.02
8	0.10	0.08	0.05	0.04	0.04	0.02	0.06	0.03	0.02	0.05	0.04	0.02
9	0.09	0.06	0.04	0.04	0.03	0.01	0.06	0.04	0.03	0.06	0.04	0.02
10	0.06	0.05	0.03	0.04	0.03	0.02	0.07	0.05	0.03	0.07	0.05	0.03
11	0.05	0.05	0.03	0.04	0.04	0.02	0.09	0.07	0.04	0.09	0.06	0.03
12	0.02	0.01	0.01	0.02	0.02	0.01	0.07	0.07	0.05	0.12	0.05	0.03

Table 4.16: Hybrid simulations of the non isolated bridge: NRMSEs on displacement, velocity and acceleration responses of reduced S-DoF piers.

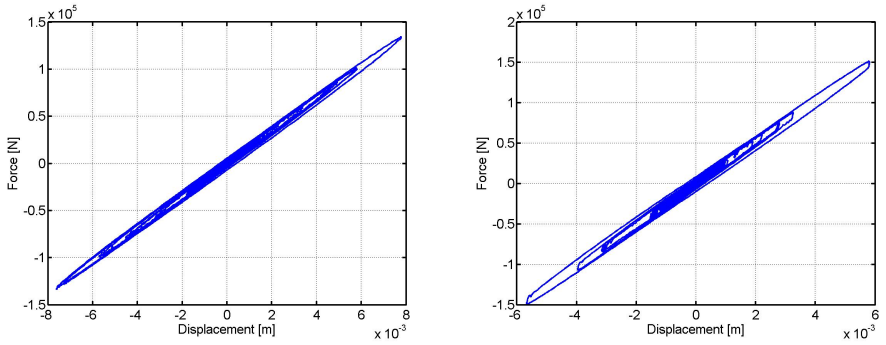

Figure 4.29: Hysteretic loops of top restoring forces of: **a** Pier #9; and **b** Pier #11 relevant to Test $k05$, i.e. non-isolated bridge at SLS 10%

According to reported NRMSE matching scores, S-DoF nonlinear piers always entailed satisfying results.

4.8 Results of hybrid simulations

Experimental results of hybrid simulations reported in the present section concern main tests carried out in both the non isolated and the isolated case. Since physical FPB isolators were characterized by friction parameters twice than design values, tests with numerical FPB isolators were considered to estimated the effectiveness of the proposed retrofitting. Table 4.18 summarizes NRMSE scores calculated on displacement responses of both piers with respect to the reduced and the OpenSEES RM models of the Rio Torto Bridge. According to NRMSE scores reported in Table 4.18, experimental responses of Pier #9 and #11 agree with time history analyses of both the reduced and the OpenSEES models.

4.8.1 The non isolated Rio Torto Bridge

In order to estimate the dynamic response of the bridge in the linear range, Test $k05$ was conducted assuming the SLS accelerogram scaled to 10% of its PGA. Figure 4.29 depicts narrow hysteretic loops characterizing both specimens. Displacements and forces refer to measurements of horizontal actuators magnified to the prototype scale. Test $k07$ was aimed at inducing the damage state of

	Test *l*01			Test *l*02		
Pier	dsp	vel	acc	dsp	vel	acc
1	0.05	0.06	0.09	0.04	0.06	0.11
2	0.07	0.06	0.14	0.03	0.04	0.11
3	0.04	0.05	0.15	0.02	0.03	0.09
4	0.05	0.05	0.14	0.02	0.03	0.13
5	0.06	0.05	0.11	0.03	0.04	0.12
6	0.05	0.04	0.10	0.02	0.04	0.09
7	0.05	0.05	0.12	0.04	0.04	0.10
8	0.05	0.04	0.08	0.05	0.03	0.06
9	0.04	0.04	0.06	0.04	0.05	0.06
10	0.04	0.04	0.08	0.04	0.04	0.06
11	0.06	0.06	0.09	0.07	0.06	0.06
12	0.06	0.08	0.09	0.07	0.08	0.08

Table 4.17: Hybrid simulations of the isolated bridge: NRMSEs on displacement, velocity and acceleration responses of reduced S-DoF piers.

Pier	Test *k*05	Test *k*07	Test *l*01	Test *l*02	Test *k*09	Test *k*10	Test *k*12
9	0.04	0.05	0.31	0.22	0.21	0.25	0.23
11	0.07	0.12	0.31	0.32	0.25	0.29	0.25

Table 4.18: NRMSE scores on experimental responses of Piers #9 and #11 with respect to reduced models of the bridge.

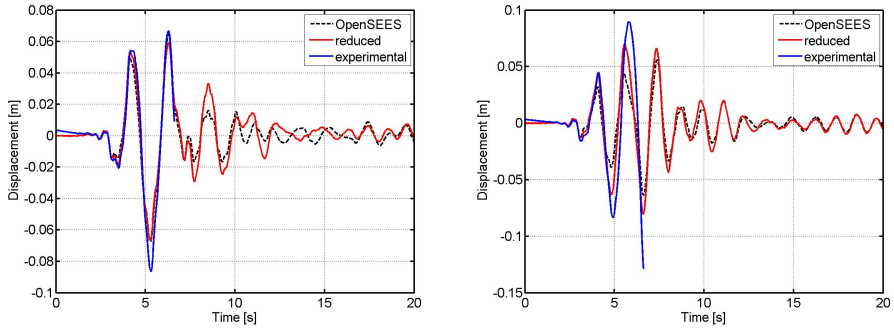

Figure 4.30: Comparison between numerical and experimental responses of: **a** Pier #9; and **b** Pier #11 during Test *k*07, i.e. non-isolated bridge at SLS.

real piers to specimens. As a result, the SLS accelerogram was applied. As can be appreciated in Figure 4.25, both piers experienced a sudden drop of concrete compressive strength, which assumed the asymptotic value on each specimen. Accordingly, displacement responses exceeded numerical predictions and the test was stopped after 6.6s only. The slight nonlinear response of both specimens can be appreciated also in Figure 4.29, which depicts force-deflection loops of both Piers #9 and #11. Limited hairline cracks were observed on transverse beams of Piers #9 and #11. Figure 4.32 depicts four frames of the axial strain field acquired by means of the photogrammetric technique on the transverse element of Pier #11. A combined flexural-shear damage mechanism triggered hairline cracks, which propagated from end sections to the middle of the transverse beam. In fact, assuming a bending moment with linear variation and a constant shear force along the element length, end sections were characterized by higher deviatoric stresses. Pier #11 experienced a drift ratio of about 0.6%. According to Figure 4.33, the transverse element experienced a maximum shear deformation γ of about 1e-3 during Test *k*07. According to Figure 4.33 the geometry of the LVDT transducer lattice, the average shear deformation γ was calculated was follows:

$$\gamma = \frac{\Delta\alpha + \Delta\beta}{2} \tag{4.21}$$

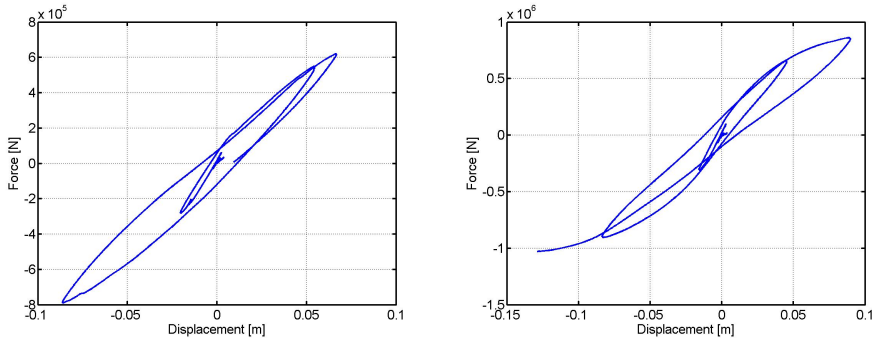

(a) (b)

Figure 4.31: Hysteretic loops of top restoring forces of **a** Pier #9 and **b** Pier #11 during Test *k*07, i.e. non-isolated bridge at SLS.

with,

$$\Delta\alpha = \alpha_0 - (\alpha_2 + \alpha_1) \tag{4.22}$$

$$\Delta\theta = \theta_0 - (\theta_2 + \theta_1) \tag{4.23}$$

where $\alpha = \alpha_2 + \alpha_1$, $\theta = \theta_2 + \theta_1$, while α_0 and β_0 depend on the initial configuration sensors. Limited cracks owing to bond slip effects were observed at bottom sections of columns of both Piers #9 and #11. Test *k*09 was aimed at simulating the dynamic response of the non isolated bridge at ULS. Significant shear crack patterns were observed on transverse beams of both piers. Minor cracks opened also on cap beams and column joints. In order to simulat an aftershock event, the seismic input of Test *k*09 was repeated during Test *k*10. Figure 4.35 compares hysteretic loops of Pier #9 and #11 obtained from Tests *k*09 and *k*10. As can be appreciated in Figure 4.35, increasing column fix-end rotations owing to higher slippage of rebars shrunk hysteretic loops of piers at the second shock. Nonetheless and according to Figure 4.36, displacement responses of both piers remained almost unchanged. In order to simulate a seismic event beyond design conditions, the same ULS accelerogram was applied with a PGA magnified to the 200% of its original value. According to Figure 4.37, which compares hysteretic loops of both

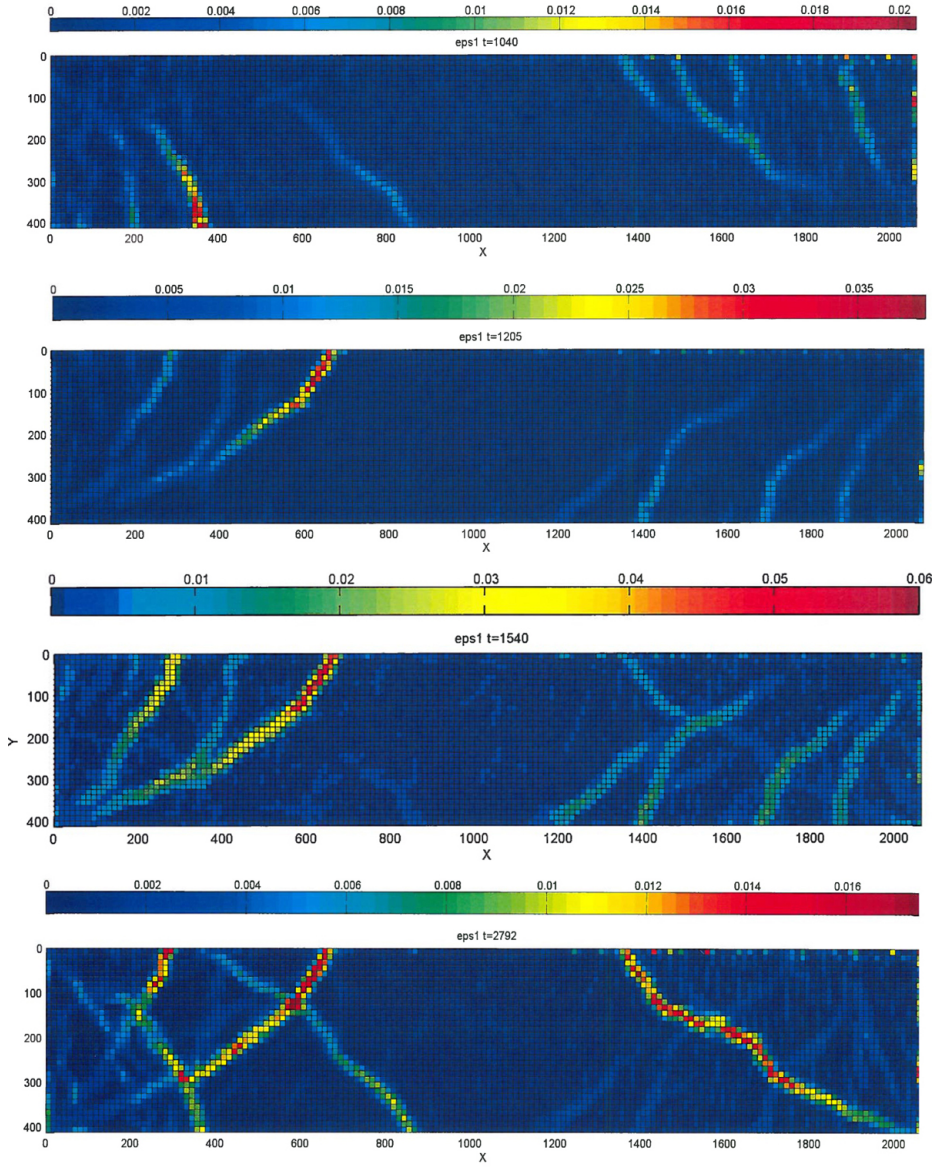

Figure 4.32: Countour plots of axial strain fields at different times of Test *k*07, i.e. non-isolated bridge at SLS.

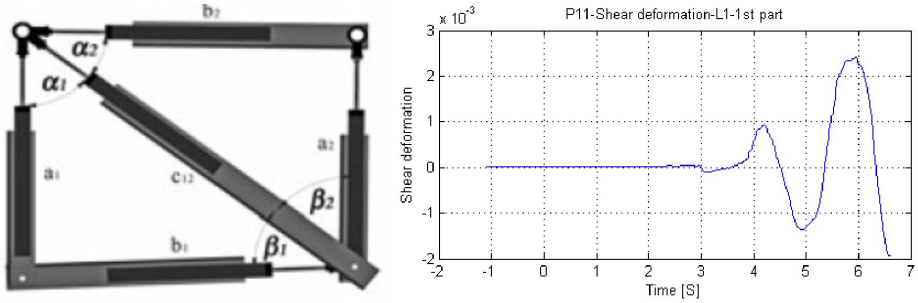

(a) (b)

Figure 4.33: **a** Geometric characteristics of the LVDT lattice; **b** average shear deformation history of transverse beam of Pier #11 relevant to Test *k*07, i.e. non-isolated bridge at SLS.

(a) (b)

Figure 4.34: Close-up views of Pier #11: **a** transverse beam and **b** left column, after Test *k*09, i.e. non isolated bridge at ULS.

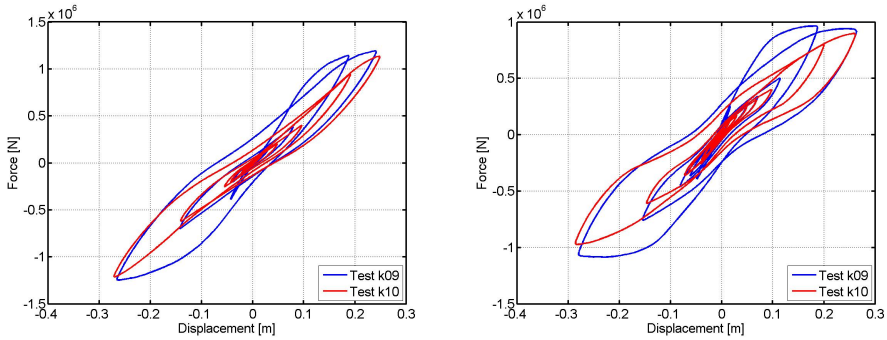

(a) (b)

Figure 4.35: Comparison of hysteretic loops of top restoring forces of: **a** Pier #9; and **b** Pier #11 relevant to Tests $k09$ and $k10$, i.e. non isolated bridge at ULS and ULS aftershock, respectively.

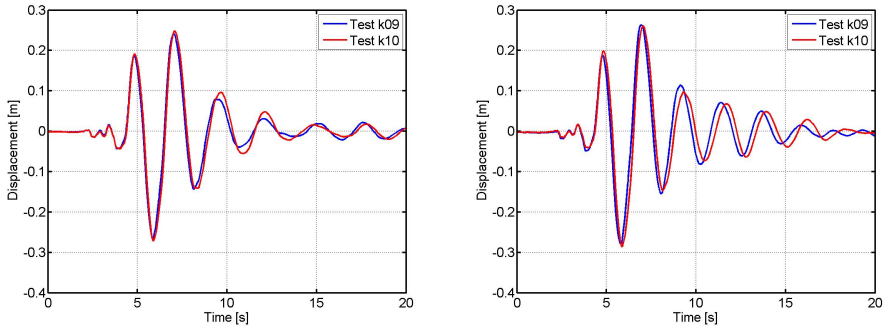

(a) (b)

Figure 4.36: Comparison of displacement responses of **a** Pier #9 and **b** Pier #11 relevant to Tests $k09$ and $k10$, i.e. non isolated bridge at ULS and ULS aftershock, respectively.

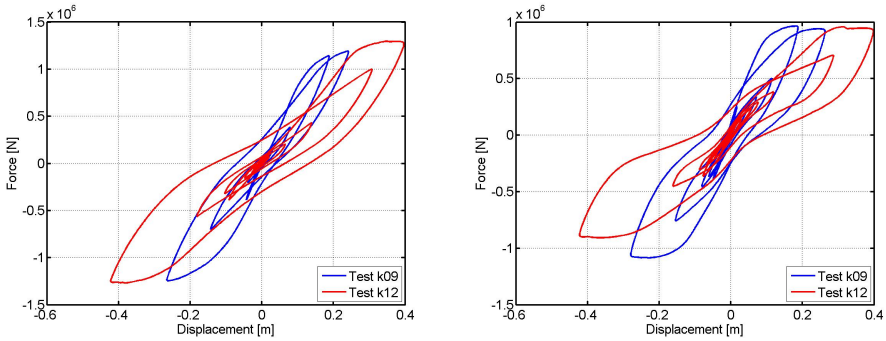

Figure 4.37: Comparison of hysteretic loops of top restoring forces of **a** Pier #9 and **b** Pier #11 relevant to Tests $k09$ and $k12$, i.e. non isolated bridge at ULS and ULS 200%, respectively.

Piers #9 and #11 of Tests $k09$ and $k12$, threshold restoring forces experienced during the former were not exceeded. Nonetheless, during Test $k12$ both specimens experienced maximum displacements twice times higher than peaks characterizing Test $k09$. Numerical analyses of the OpenSEES RM highlighted a 2% threshold drift ratio for the shear failure of the transverse beam (Alessandri, 2013). A 2.4% drift ratio was observed on Pier #11 during Test $k12$ and the shear failure of the transverse beam occurred. Figures 4.39 and 4.40 depict damaged columns and transverse beams of both piers. Degradation was more pronounced on Pier #11. In particular, large shear cracks affected the transverse beam. Expulsion of the concrete cover and buckling of steel rebars were observed on the same element. A less severe damage scenario was observed on Pier #9. A smaller total drift ratio of 1.2%, which was far from ultimate conditions, was measured. Characterizations of pier specimens during tests highlighted an appreciable degradation of stiffness and strength characteristics. Damage conditions were effectively propagated to numerical piers by means of the novel testing procedure based on off-line model identification and updating sessions. As a result, all piers experienced a consisted degradation, which was confirmed by trends of modal frequencies of updated models reported in Table 4.19. Damage caused by simulated seismic events halved frequencies of main Modes #2 and #4, which characterized the displacement re-

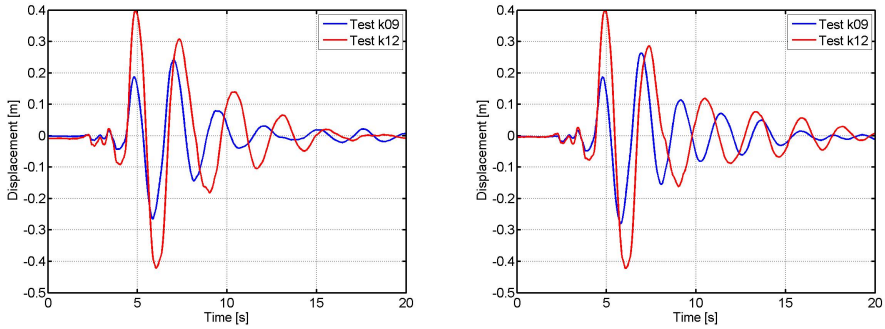

(a) (b)

Figure 4.38: Comparison displacement responses of **a** Pier #9 and **b** Pier #11 during Tests $k09$ and $k12$, i.e. non isolated bridge at ULS and ULS 200%, respectively.

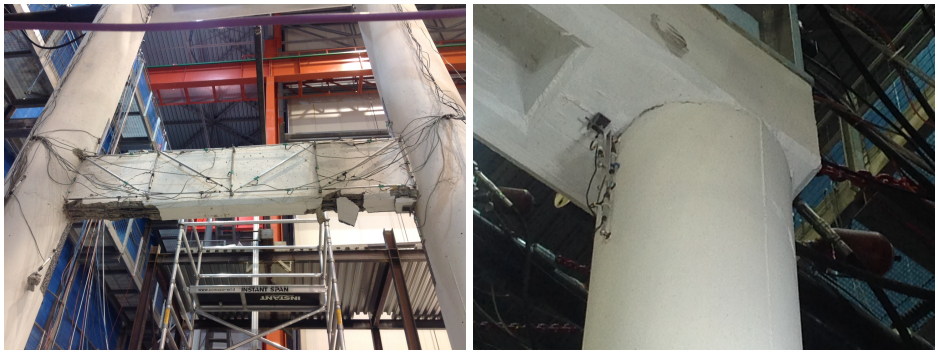

(a) (b)

Figure 4.39: Close-up views of Pier #11: **a** transverse beam and **b** column top after Test $k12$, i.e. non isolated bridge at ULS 200%.

(a) (b)

Figure 4.40: **a** Expulsion of the concrete cover on transverse beam of Pier #11; **b** crack pattern of the lower transverse beam of Pier #9 after Test *k*12, i.e. non isolated bridge at ULS 200%.

	Frequency [Hz]				
Mode	Test k05	Test k07	Test k09	Test k10	Test k12
1	0.60	0.49	0.38	0.38	0.34
2	0.61	0.53	0.40	0.40	0.36
3	0.64	0.53	0.41	0.41	0.42
4	1.02	0.90	0.47	0.47	0.49

Table 4.19: Modal frequencies of the bridge at different tests

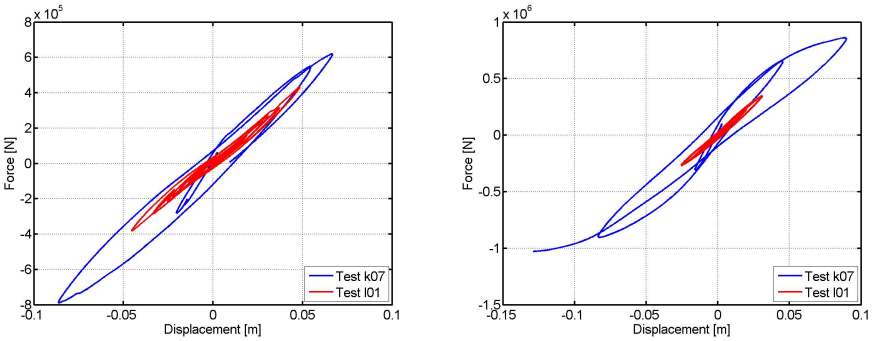

(a) (b)

Figure 4.41: Comparison of hysteretic loops of top restoring forces of **a** Pier #9 **b** Pier #11 relevant Test *I*01 and Test *k*07, i.e. isolated and non isolated bridge at SLS, respectively

sponse of the Rio Torto Bridge.

4.8.2 The isolated Rio Torto Bridge

Since the characterization of FPB isolators highlighted friction coefficients higher than design values, i.e. μ = 7% $>$ 4%, most significant hybrid simulations of the isolated bridge were conducted considering numerical isolators. In greater detail, Test *I*01 and *I*02 proved the effectiveness of the proposed seismic retrofitting at SLS and ULS, respectively. Figure 4.41 compares hysteretic loops of Piers #9 and #11 at SLS in the isolated -Test *I*01- and the non isolated -Test *k*07- cases. As can be appreciated in Figure 4.41, both piers remained in the linear range during Test *I*01. As a result, piers were preserved from crack opening and propagation. Displacement responses depicted in Figures 4.42 confirm the effectiveness of the proposed retrofitting which considerably reduced maximum peaks on both piers at SLS. Test *I*02 proved the effectiveness of the isolation system at ULS. In detail, Figure 4.43 compares hysteretic loops of both piers in the isolated -Test *I*02- and the non isolate cases -Test *k*09-. According to Figure 4.43, hysteretic dissipation of piers was almost completely removed in the isolated case at ULS. As can be appreciated in Figure 4.44, which compares displacement responses of both piers in the isolated and the non isolated cases, the proposed retrofitting entailed a no-

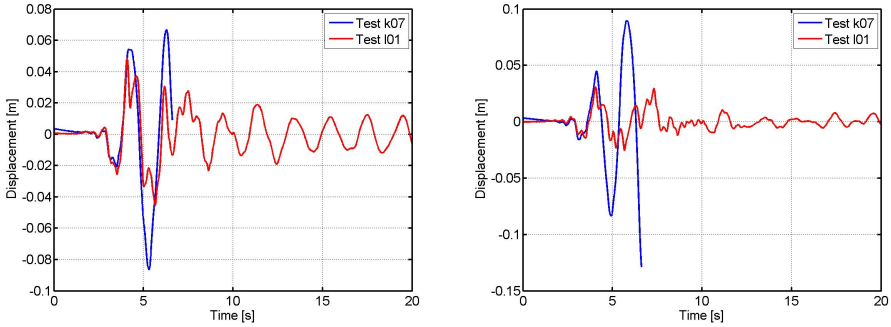

(a) (b)

Figure 4.42: Comparison of displacement responses of **a** Pier #9 and **b** Pier #11 relevant Test *l*01 and Test *k*07, i.e. isolated and non isolated bridge at SLS, respectively

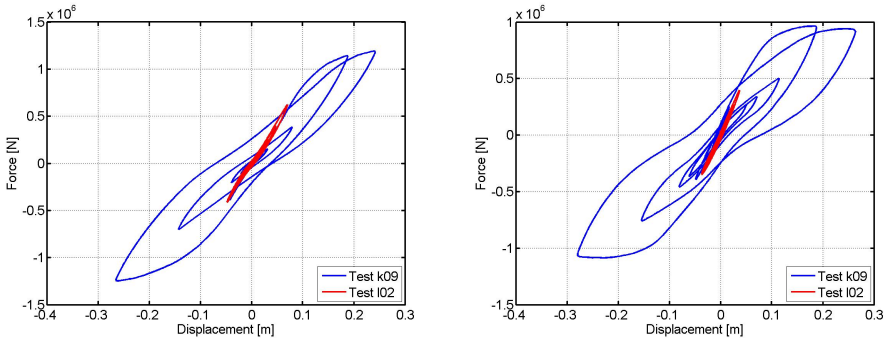

(a) (b)

Figure 4.43: Comparison of hysteretic loops of top restoring forces of **a** Pier #9 **b** Pier #11 relevant Test *l*02 and Test *k*09, i.e. isolated and non isolated bridge at ULS, respectively

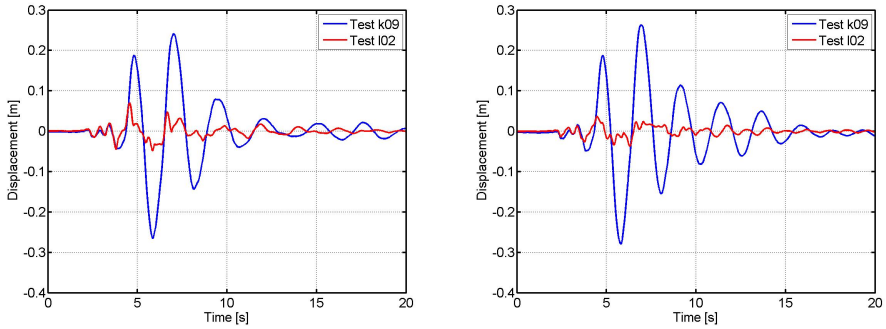

(a) (b)

Figure 4.44: Comparison of displacement responses of **a** Pier #9 and **b** Pier #11 relevant Test *l*02 and Test *k*09, i.e. isolated and non isolated bridge at ULS, respectively.

ticeable drop of peak amplitudes. Piers did not accumulate damage both during Tests *l*01 and *l*02. Further hybrid simulations of the isolated bridge were conducted considering physical piers and FPB isolators. Test *p*01 was aimed at simulating the SLS. Since FPB isolators of Pier #11 exhibited a jagged force response, the ULS accelerogram was reduced to the 70% of its PGA value and applied through Test *p*02. In order to reproduce the design friction coefficient μ = 4%, reduced vertical forces were applied to physical FPB isolators. Figure 4.45 compares hysteretic loops of both piers obtained from Test *l*01 and *p*01, i.e. with numerical and physical FPB isolators respectively. Figure 4.46 compares displacement responses of both piers obtained from same Test *l*01 and *p*01. According to Figures 4.45 and 4.46, Test *l*01 and *p*01 entailed consistent responses, which remained in the linear range. According to Figure 4.47, a slight nonlinear response of piers was observed on Test *p*02. As a consequence, hybrid simulations of the isolated bridge at ULS were conducted considering numerical FPB isolators only.

4.9 Conclusions

A comprehensive set of hybrid simulations was conceived to estimate the seismic performance of the Rio Torto Bridge in both the isolated and the non isolated conditions. In detail, 1:2.5 scale mock-up models of Piers #9 and #11 together with

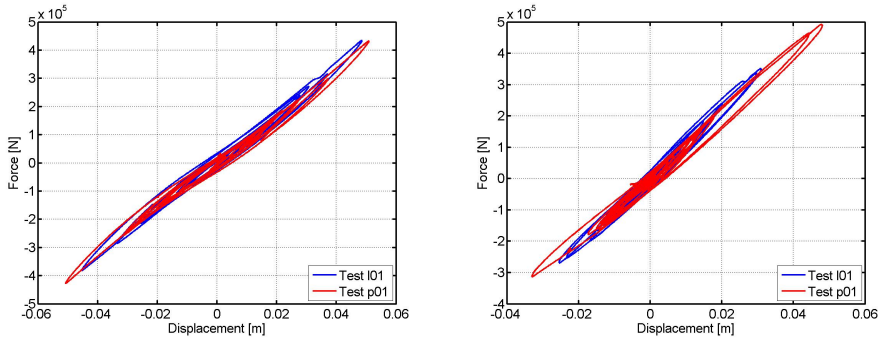

Figure 4.45: Comparison of hysteretic loops of top restoring forces of **a** Pier #9 and **b** Pier #11 relevant Test *l*01 and Test *p*01, i.e. SLS with numerical and physical FPB isolators, respectively.

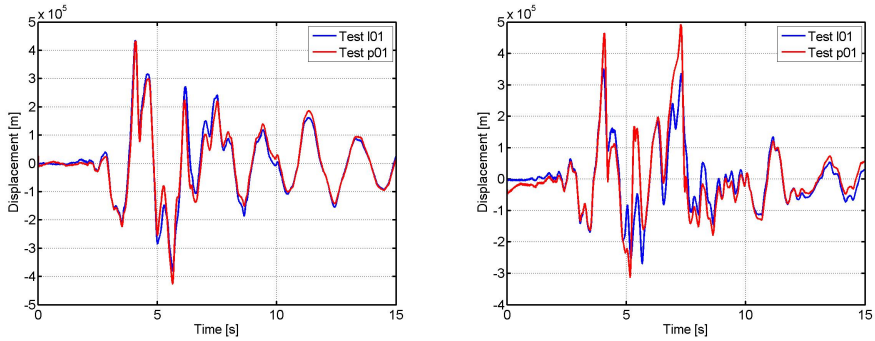

Figure 4.46: Comparison of displacement responses of **a** Pier #9 and **b** Pier #11 relevant Test *l*01 and Test *p*01, i.e. SLS with numerical and physical FPB isolators, respectively.

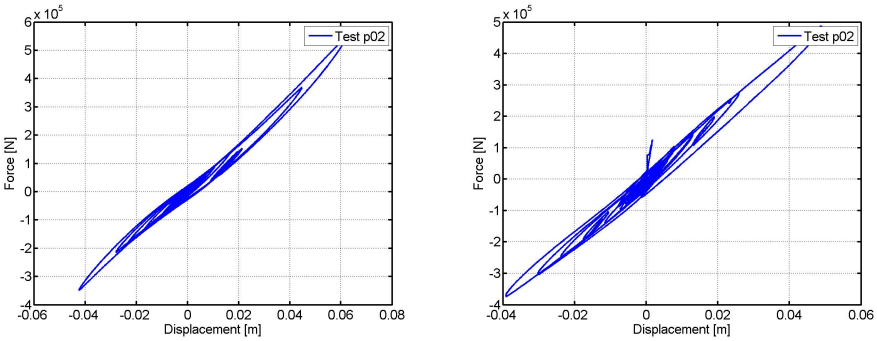

Figure 4.47: Hysteretic loops of top restoring forces of **a** Pier #9 and **b** Pier #11 relevant to Test *p*02, i.e. ULS 70% with physical FPB isolators.

relevant FPB isolation devices were coupled to the remainder part of the bridge implemented in the CAST3M FE code (Cast3M, 2003). The PM method (Pegon and Magonette, 2002; Bonelli et al., 2008), which embeds subcycling capabilities, allowed for the implementation of the continuous PDT method. First, substructuring schemes and relevant experimental set-ups were presented. Then, the scaling of specimens was described. A novel testing procedure aimed at simulating a consistent degradation among physical and numerical piers was presented and applied to the Rio Torto Bridge. It was based on off-line sessions of model identification of PSs and updating of NSs. Accordingly, a tool for the identification of parameters of OpenSEES FE models was implemented in the Matlab environment. As a result, physical piers were characterized after each test, where damage could be observed. The OpenSEES RM model of the Rio Torto Bridge was updated accordingly and took as reference for the updating of reduced S-DoF piers, i.e. NSs. As a result, a consistent degradation of physical and numerical piers was simulated in both the non isolated and the isolated conditions. The characterization of piers highlighted an appreciable degradation of stiffness and strength characteristics after non isolated tests. Crack opening and failure of transverse beams characterized the ULS damage patterns. Accordingly, modal frequencies of the non isolated bridge showed decreasing values. Since the characterization of FPB isolators highlighted friction coefficients higher than design values, i.e. $\mu = 7\% > 4\%$,

most significant hybrid simulations of the isolated bridge were conducted considering numerical isolators. Since pier responses were kept in the linear range at both limit states, the effectiveness of the proposed retrofitting was proved. Further hybrid simulations of the isolated bridge were conducted considering physical piers and FPB isolators. In order to reproduce the design friction coefficient μ = 4%, reduced vertical forces were applied to physical FPB isolators. Moreover, the ULS accelerogram was applied with reduced PGA values. Hybrid simulations of the isolated bridge at SLS with numerical and physical isolators showed consistent results. Therefore, the proposed testing procedure is of general validity and allows for simulating a consistent degradation of PSs and NSs.

CHAPTER 5

HYBRID SIMULATION OF AN INDUSTRIAL PIPING SYSTEM BASED ON MODEL REDUCTION

5.1 Introduction

In the case of simple structural topologies, i.e., shear type frames, inverted pendulum systems, chain like systems, etc., few actuators handling the totality of physical Degrees of Freedom (DoFs) can efficiently reproduce the response path of tested specimens; and the system of equations of motion can be solved through suitable time integrators. Nonetheless, this approach is not suitable for dealing with complex Physical Substructures (PSs) subjected to distributed inertia forces, where a plenty of physical DoFs come on stage; and this is the case of typical piping networks. The need for assessing dynamic responses of typical industrial piping systems subjected to seismic loading motivated the authors to apply model reduction techniques to experimental dynamic substructuring. Before introducing any reduction strategy, a clear insight into the dynamic response of the emulated system from the PS perspective was provided. Accordingly and complying with experimental limitations of each testing strategy, consistent reduction bases were defined for both Pseudo Dynamic Testing (PDT) and Real-time Testing (RT) techniques in the case of an elastic response of the PS. Successively, a Modified version of the System Equivalent Reduction-Expansion Process (M-SEREP) (OCallahan and Riemer, 1989) and Craig-Bampton reduction methods (Bampton, 1968) were employed for the reduction of both the PS and distributed earthquake forces. This allowed for an effective experimental testing of the actual system. Two further reduction bases were investigated from a numerical perspective only. With regard

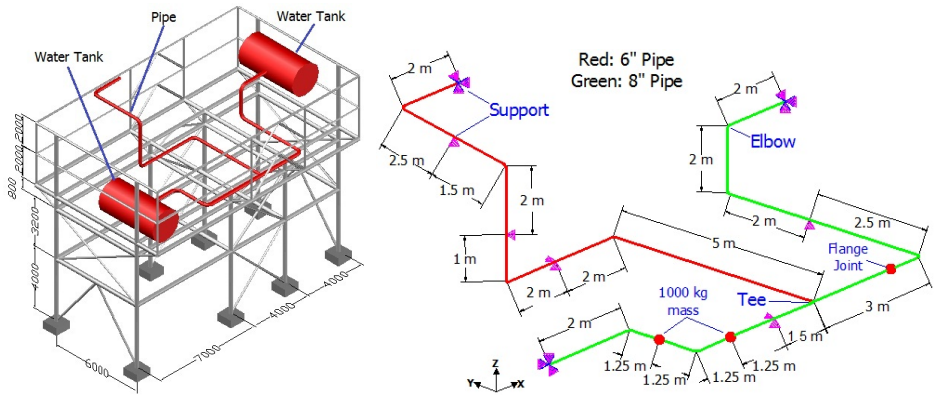

Figure 5.1: **a** 3D model of the piping system placed on the support structure; **b** specifications and dimensions of the piping system after DeGrassi and Hofmayer (2008). Dimensions are in mm

to time integration, the L-Stable Real Time compatible (LSRT2) (Bursi, 2011) was employed, together with an effective delay compensation method (Wu, 2013). Successively, relevant implementations and experimental results were shown. Finally, conclusions were drawn.

5.2 A distributed parameters piping system

5.2.1 Main characteristics and dimensions

A typical full-scale industrial piping system placed on a steel support structure, as illustrated in Figure 5.1(a), was investigated within this study; its general dimensions and other geometrical properties depicted in Figure 5.1(b) were taken after DeGrassi and Hofmayer (2008). The piping network contained $8''$ (outer dia: 219.08mm; thickness: 8.18mm) and $6''$ (outer dia: 168.28mm; thickness: 7.11mm) schedule 40 straight pipes and several critical components, i.e. elbows, a Tee joint and an EN 1092-1 standard PN 40 weld-neck bolted flange joint. The pipes were of API 5L Gr. X52 material (nominal f_y and f_u equal to 418MPa and 554MPa, respectively) and were filled with water at an internal pressure of 3.2MPa, corresponding to 80% of the maximum allowable pressure of the piping network.

Limit States			PGA [m/s^2]	PGA [g]
Serviceability Limit states	SLO	Operational limit state	0.77	0.08
	SLD	Damage limit state	1.10	0.11
Ultimate Limit States	SLV	Safe life limit state	4.13	0.42
	SLC	Collapse limit state	5.88	0.60

Table 5.1: PGAs corresponding to Serviceability and Ultimate Limit States of support structure

5.2.2 Selection of input earthquake loading

The piping network was placed on a steel support structure shown in Figure 5.1(a) that typically acts as a dynamic filter; it causes amplifications of input earthquakes at different structure locations. Therefore, to select realistic earthquake input loadings, earthquake accelerations were generated on elevated floors of the support structure through time history analyses carried out by means of an FE model of the structure subjected to a base input, i.e. a natural accelerogram taken from the European Strong-motion Database (`http://www.isesd.hi.is/ESD_Local/frameset.htm`). A reference floor accelerogram was thus chosen; it was the most severe floor accelerogram in terms of amplitude and resonance frequency of the piping network with a relevant PGA at about $4.13 m/s^2$. To comply with performance-based earthquake engineering Italian Standards (NTC-2008, 2008), its PGA was magnified corresponding to both serviceability (operational-SLO, damage SLD) and ultimate limit states (safe life SLV, collapse -SLC) of the support structure as listed in Table 5.1. Figure 5.2 shows both the reference floor accelerogram and its relevant acceleration response spectrum magnified to the SLC PGA. As can be appreciated in Figure 5.2(b), the period T at maximum amplification was around 0.2s, which was close to the natural frequency of the piping system.

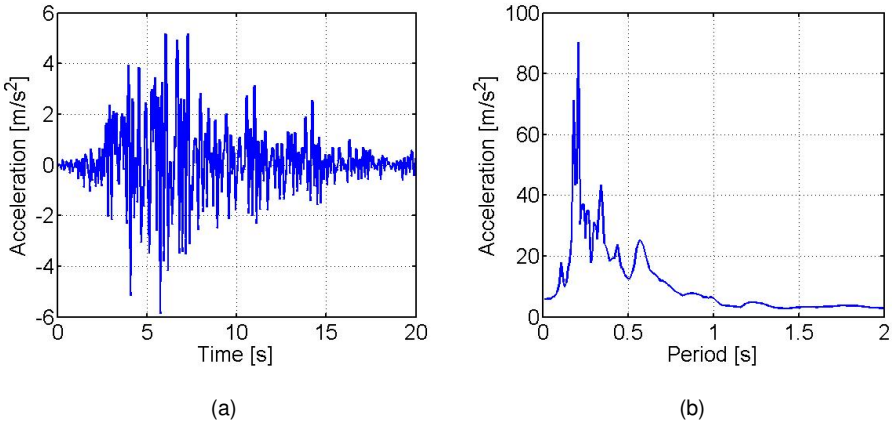

Figure 5.2: **a** SLC reference floor accelerogram; **b** relevant acceleration response spectrum for 0.5% equivalent viscous damping

5.2.3 Characterization of approximated elbow elements

In order to perform preliminary numerical analyses and to extract system matrices for hybrid simulations, a 3D FE model of the piping system was developed in ANSYS (ANSYS, 2007). All pipes including elbows were modeled using straight beam elements with pipe sections. Two 1000 kg masses, employed to take into account valves, etc., were connected to two relevant joints through MASS21 elements. Pipe material density was increased to take into account water mass. Flexible elbow components represent potential critical locations in a piping network where stresses are intensified owing to their geometrical irregularity; see, in this respect, Figure 5.4 where unsymmetrical cyclic responses of pipe elbows obtained from tests carried out by Varelis (2013) are depicted. To consider their elastic behavior in the FE model, flexibilities of straight elbow elements (EN13480-3, 2002) were adjusted according to an ABAQUS-based FE SHELL model (ABAQUS, 2003). In greater detail, original curved elbow elements were modeled in ABAQUS software and 3D FE analyses under axial, shear and bending loading were performed; see in this respect Figure 5.3, where in-plane and out-of-plane moment-rotation curves of an elbow element obtained from FE analyses are presented. Thus, an equivalence between ABAQUS shell FE curved and ANSYS straight elas-

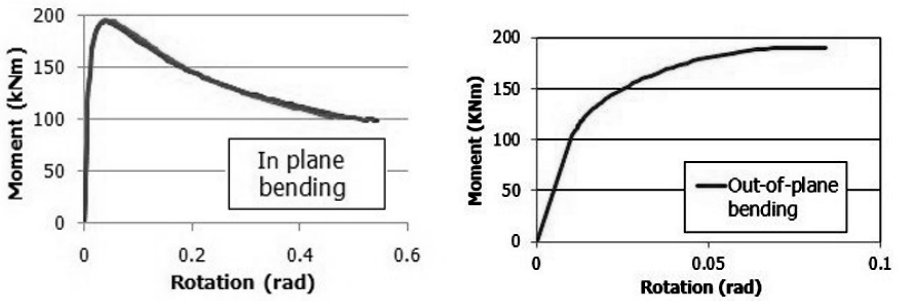

(a) (b)

Figure 5.3: Bending moment-rotation relationships of an elbow under bending loading from ABAQUS FE analyses: **a** in-plane; and **b** out-of-plane bending.

tic elements was established. Each elbow had a radius R equal to 1.5 times the outer diameter d_{out} of connecting pipes; moreover, the flexibility effect of an elbow was considered to spread across a distance equal to two times the mean diameter of the pipe; the equivalent straight elbow element consisted of a curved and two straight parts; their individual flexibilities were added to obtain the overall flexibility of the straight element. In this view, elastic stiffness matrices of equivalent straight elbows were developed according to the Euler-Bernoulli (EB) beam theory. In particular, the stiffness matrix of a straight elbow element based on the EB theory can be expressed in the following form:

$$\begin{bmatrix} k_{11} & 0 & 0 & k_{14} & 0 & 0 \\ 0 & k_{22} & k_{23} & 0 & k_{25} & k_{26} \\ 0 & k_{32} & k_{33} & 0 & k_{35} & k_{36} \\ k_{41} & 0 & 0 & k_{44} & 0 & 0 \\ 0 & k_{52} & k_{53} & 0 & k_{55} & k_{56} \\ 0 & k_{62} & k_{63} & 0 & k_{65} & k_{66} \end{bmatrix} \begin{bmatrix} u_1 \\ v_1 \\ \varphi_1 \\ u_4 \\ v_4 \\ \varphi_4 \end{bmatrix} = \begin{bmatrix} H_1 \\ F_1 \\ M_1 \\ F_4 \\ H_4 \\ M_4 \end{bmatrix} \tag{5.1}$$

where:

$$k_{11} = k_{44} = -k_{14} = -k_{41} = K_{ax} \tag{5.2}$$

$$k_{22} = k_{55} = -k_{25} = -k_{52} = K_{sh} \tag{5.3}$$

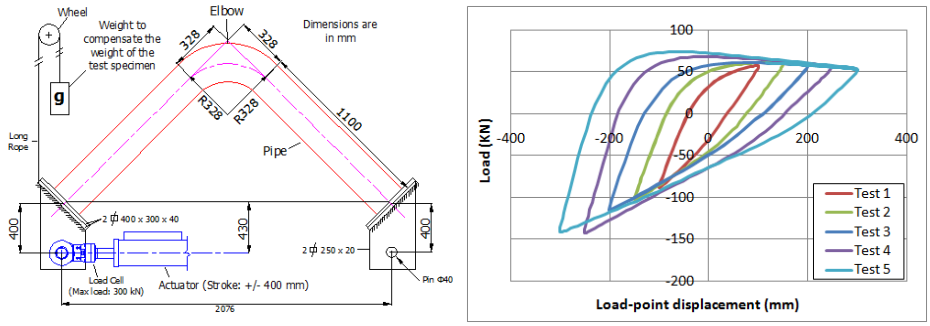

(a) (b)

Figure 5.4: Experiments on pipe elbows performed by Varelis et al. (2012): **a** test set-up; **b** cyclic response

$$k_{33} = k_{66} = K_{bg} \tag{5.4}$$

$$k_{36} = k_{63} = (1-\omega)\frac{1}{6}k_{sh}l^2 + \omega\frac{1}{2}K_{bg} \tag{5.5}$$

$$-k_{23} = -k_{32} = -k_{26} = k_{35} = k_{53} = -k_{62} = k_{56} = k_{65} = (1-\omega)\frac{1}{2}k_{sh}l + \omega\frac{3}{2}\frac{K_{bg}}{l} \tag{5.6}$$

where only in-plane contributions are shown for simplicity. In Eq. (5.1), u and v are displacements; φ is rotation; H and F are forces; M is moment; K_{ax}, K_{sh} and K_{bg} are axial, shear and bending stiffness coefficients, respectively. By varying the elbow thickness, the elastic stiffness of each straight elbow was fitted with those found from the above-mentioned analyses. The adjusted geometry and properties of modified straight elbow elements are reported in Table 5.2. An optimal value of $\omega = 0.89$ was found and out of plane bending and shear were also considered in these analyses.

5.3 Substructuring and FE modelling

For substructuring purposes, the piping system was divided into two parts: (i) a PS, which was physically built in the lab and loaded through actuators; (ii) a

Property	8″ Elbow		6″ Elbow	
	Original	Modified	Original	Modified
Outer diameter [mm]	219.08	219.08	168.28	168.28
Thickness, e_n [mm]	8.18	6.61	7.11	4.35
Flexibility factor, k_B	6.84	1.35	5.97	2.46
Moment of inertia, J [mm^4]	3.02 x 1e7	2.49 x 1e7	1.17 x 1e7	7.53 x 1e6

Table 5.2: Elbow properties considered in the piping system model with straight elements

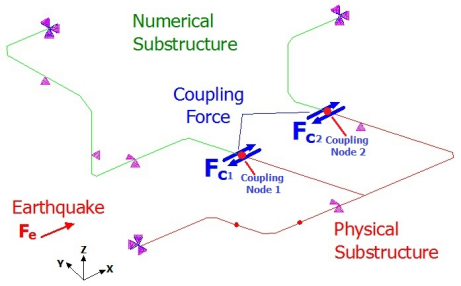

(a)

Figure 5.5: PS, NS and relevant coupling DoFs.

Numerical Substructure (NS) that was solved via software; the two substructures exchanged information through coupling DoFs they mutually shared. Since physical excitation of rotational DoFs is very difficult to accomplish (Klerk et al., 2008), coupling nodes with bending moment close to zero in the xy plane -most of the pipes run in this plane- were selected; see Figure 5.5 in this respect. Accordingly, two MOOG actuators were attached to those nodes and were oriented in x direction. In detail, the following coupling conditions were forced for translational and rotational DoFs, respectively:

$$u_x^N = u_x^P \ , \ u_y^N = u_y^P = 0 \ , \ u_z^N = u_z^P = 0 \tag{5.7}$$

$$\theta_x^N \neq \theta_x^P \ , \ \theta_y^N \neq \theta_y^P \ , \ \theta_z^N \neq \theta_z^P \tag{5.8}$$

where, u and θ represents displacements and rotations, respectively; N and P refers to the NS and PS, respectively. Eqs. (5.7) and (5.8) show that the two coupling nodes were constrained to move in the x direction, thus satisfying compatibility conditions. Rotations were kept free while movements along y and z were constrained. Therefore, hybrid tests were conducted by means of two hydraulic actuators which imposed displacement commands in the x direction of the PS.

5.3.1 ANSYS FE models of the piping system for PDT

In order to validate dynamic substructuring, an additional ANSYS FE model embedding the actual coupling conditions of Eqs. (5.7) and (5.8), was developed. This model, defined as the ANSYS Reference Model (RM), was assumed as the reference for validating model reduction techniques, time-integration algorithms as well as the experimental set-up. The RM in which both substructures PS and NS were embedded was compared with the ANSYS FE model of the actual piping system, referred herein as the Continuous Model (CM); there, the full coupling between both rotational and translational interface DoFs is enforced; hence the name Continuous. Figure 5.6 depicts a schematic valid for all ANSYS FE models of the piping considered in the present chapter. A careful reader can note that the support structure depicted in Figure 5.1(a) was not included in the NS for two reasons: i) to impart the most severe earthquake in terms of PGA, amplitude and frequency to the piping system; ii) to avoid the complexity of a non-linear computation of the NS during RT. In this respect, the floor of the support structure that sustained the piping network was considered as a rigid floor. In fact, a seismic analysis of the supporting structure with the piping system exhibited that the maximum Root Mean Square (RMS) between relative movements of support points $S1$, $S2$, $S3$ and $S4$ with respect to the reference point R, see Figure 5.6, was about $0.83mm$. This value was assumed to be small compared to the RMS of the maximum relative displacement of piping system points, i.e. $50.87mm$ at point $P1$; see again Figure 5.6. As a result, the assumption of rigid floor was justified. Moreover, the input earthquake for experiments was chosen to be the most severe floor accelerogram in terms of amplitude and resonance frequency of the piping network among the ones at support points. Finally without inelastic support structure, the earthquake amplification at the floor level both at the SLV and SLC limit states was not reduced.

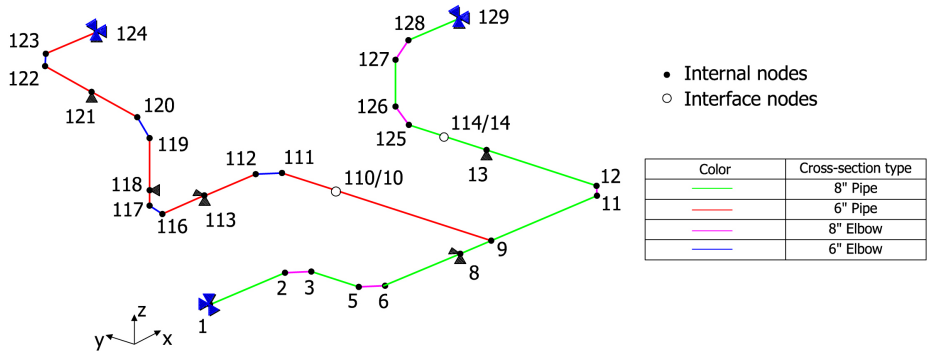

Figure 5.6: Schematic of ANSYS FE models of the piping system showing pipe sections and significant nodes.

With reference to the schematic of Figure 5.6, following coupling conditions were were set as internal constraint equations, respectively:

$$u_x^{10} = u_x^{110} \ , \ u_y^{10} = u_y^{110} = 0 \ , \ u_z^{10} = u_z^{110} = 0 \tag{5.9}$$

$$u_x^{14} = u_x^{114} \ , \ u_y^{14} = u_y^{114} = 0 \ , \ u_z^{14} = u_z^{114} = 0 \tag{5.10}$$

Modal analyses conducted on both the CM and RM proved the effectiveness of the coupling setting, which slightly affected the dynamic properties of the piping network. In particular in both cases, the first 10 modes were able to excite about 80% of the total mass of the piping system in the x direction, as reported in Table 5.3. For both models, Mode #1 and Mode #2 depicted in Figure 5.7 carried most of the modal mass. They were the basis for the calculation of the equivalent viscous damping according to a Rayleigh formulation. An additional comparison between RM and CM FE models was made based on the Modal Assurance Criterion (MAC), which is a score aimed at comparing two eigenvectors (Allemang, 2003). In detail, a MAC matrix can compare eigenvectors of two models and provides a unit value for perfect correlation and zero for orthogonal modes. It is defined as follows:

$$MAC() = \frac{(\phi_{CM}^T \phi_{RM})}{(\phi_{CM}^T \phi_{CM})(\phi_{RM}^T \phi_{RM})} \tag{5.11}$$

where ϕ_{CM} and ϕ_{RM} are eigenvectors of CM and RM, respectively. The relevant components of the MAC matrix are reported in Table 5.4. A careful reader can

	ANSYS CM		ANSYS RM	
Mode	Frequency [Hz]	Modal mass ration	Frequency [Hz]	Modal mass ration
1	6.0213	0.3235	5.8666	0.2413
2	6.5427	0.2546	6.4731	0.3359
3	7.1418	0.0005	7.0579	0.0000
4	8.2225	0.0050	7.4108	0.0060
5	9.7197	0.0584	9.5757	0.0518
6	12.0349	0.0578	11.9818	0.0771
7	13.0057	0.0357	12.4471	0.0276
8	15.1504	0.0001	14.8247	0.0000
9	17.8459	0.0795	15.3468	0.0089
10	18.5989	0.0175	17.4335	0.0593
	TOTAL	0.8327	TOTAL	0.8078

Table 5.3: First 10 eigenfrequencies and participation masses of the piping system model

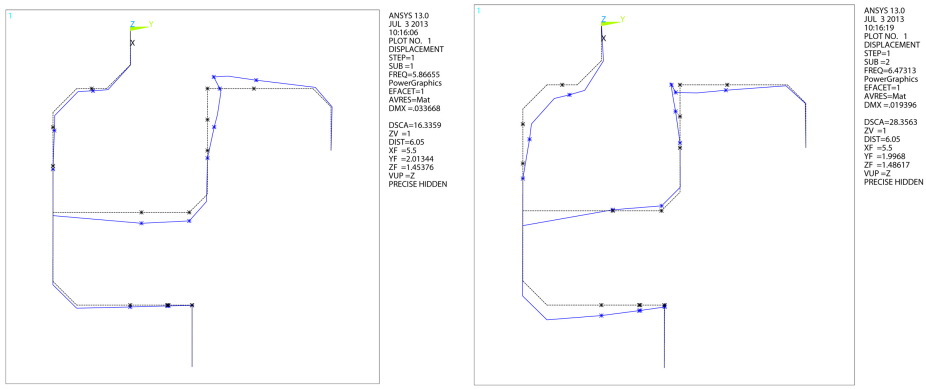

(a) (b)

Figure 5.7: **a** Mode #1 at 5.87Hz; **b** Mode #2 at 6.47Hz of the ANSYS RM.

		ANSYS RM									
		1	2	3	4	5	6	7	8	9	10
ANSYS CM	1	**0.94**	0.10	0.00	0.03	0.00	0.00	0.02	0.00	0.00	0.04
	2	0.26	**0.92**	0.00	0.03	0.00	0.03	0.02	0.00	0.01	0.02
	3	0.00	0.00	**0.92**	0.07	0.00	0.00	0.00	0.05	0.00	0.00
	4	0.01	0.01	0.01	**0.86**	0.00	0.02	0.08	0.00	0.00	0.01
	5	0.00	0.00	0.00	0.10	**0.93**	0.01	0.04	0.00	0.00	0.00
	6	0.00	0.02	0.00	0.00	0.00	**0.88**	0.00	0.00	0.02	0.00
	7	0.02	0.01	0.00	0.02	0.00	0.14	**0.88**	0.00	0.00	0.02
	8	0.00	0.00	0.06	0.00	0.00	0.00	0.00	**0.97**	0.00	0.00
	9	0.05	0.02	0.00	0.02	0.02	0.00	0.00	0.00	**0.01**	0.86
	10	0.00	0.02	0.00	0.01	0.00	0.03	0.01	0.03	0.66	**0.02**

Table 5.4: MAC matrix between ANSYS CM and RM models

observe that the two main modes of the piping system, i.e. Mode #1 and Mode #2, agree with a MAC value greater than 0.92. Further time history analyses were conducted on both the CM and the RM. Relevant differences were measured by the Normalized Energy Error (NEE) and the Normalized Root-Mean Square Error (NRMSE) defined as,

$$\text{NRMSE}(\mathbf{x}_{CM}, \mathbf{x}_{RM}) = \frac{\sqrt{\frac{1}{n}\sum_{i=1}^{n}(x_{RM,i} - x_{CM,i})^2}}{\max(\mathbf{x}_{CM}) - \min(\mathbf{x}_{CM})} \tag{5.12}$$

$$\text{NEE}(\mathbf{x}_{CM}, \mathbf{x}_{RM}) = \frac{\sum_{i=1}^{n} x_{RM,i}^2 - \sum_{i=1}^{n} x_{CM,i}^2}{\sum_{i=1}^{n} x_{CM,i}^2} \tag{5.13}$$

where, $\mathbf{x}_{CM}$ and $\mathbf{x}_{RM}$ are nodal displacement responses of CM and RM, respectively; n is the relevant length of samples. In detail, NEE involves the signal energy, and is significantly sensitive to amplitude differences and less sensitive to frequency mismatches. The NRMSE, on the other hand, shows high sensitiveness to frequency variation and is little affected by amplitude differences. Both

	Coupling DoF #1	Coupling DoF #2
NEE	0.085	1.548
NRMSE	0.099	0.214

Table 5.5: NRMSE and NEE between RM and CM

normalizations are such that the amplitude -PGA value- of the seismic input has no effects on both NEE and NRMSE in the linear range. With regard to Coupling DoFs #1 and #2 shown in Figure 5.5, Table 5.5 reports values of aforementioned errors. Both error values highlight a comparatively less accuracy on Coupling DoF #2. In fact, a preliminary seismic time history analysis of the CM exhibited that bending moments, which were closed to zero in coupling nodes, were higher in Coupling Node #2 than Coupling Node #1. Since these moments were neglected for substructuring purposes, Coupling DoF #2 was more affected by this approximation. Nonetheless, as shown in Tables 5.3 and 5.4, frequencies, modal masses and mode shapes were well preserved by the RM up to Mode #8. As a result, the proposed tailoring of the PS was able to reproduce the dynamic characteristics of the piping system.

5.3.2 ANSYS FE models of the piping system for RT

With regard to RT, a critical limitation was posed by hydraulic actuators. Owing to several factors, such as delay and hydraulic power deficiency, high frequency operations set limits of about $\pm 10mm$ to maximum strokes of actuators at about $6.00Hz$. Hence, it was not possible to run an RT on the piping system with high PGA values. Therefore, a modified numerical substructure was conceived by adding masses to several nodes of the ANSYS RM. Table 5.6 additional masses aimed at reducing the eigenfrequencies of the global emulated system. Note that changes to the NS were conceived towards the development of RT algorithms; they were not intended for improved performance of the piping system at serviceability and/or other limit states. The main eigenfrequencies of the ANSYS Modified Model (MM) of the piping system were reduced to about $1.00Hz$; they are summarized in Table 5.7. This modifications allowed to carry out RT on the piping system with low

Node	Mass [kg]
110	22000
111	20000
114	26000
115	18000
119	18000
126	22000
127	22000

Table 5.6: Additional nodal masses of the ANSYS MM.

Mode	Frequency [Hz]
1	0.7784
2	1.1004
3	1.1050
4	1.3918
5	1.5963
6	1.7897
7	2.5991
8	3.4125
9	5.0047
1	6.5750

Table 5.7: Modal frequencies of the ANSYS MM.

PGA earthquakes.

5.4 Model reduction techniques applied to the PS

Let us first establish the system of equations of motion of the piping system subjected to seismic loading where, for simplicity, linear models are assumed. Hence, the dynamic problem can be stated for both PDT and RT cases, respectively, as follows:

$$\left(\mathbf{M}^N + \mathbf{M}^P\right)\ddot{\mathbf{u}} + \mathbf{K}^N\mathbf{u} = \mathbf{r}^{PDT} + \mathbf{f} \tag{5.14}$$

$$\mathbf{M}^N\ddot{\mathbf{u}} + \mathbf{K}^N\mathbf{u} = \mathbf{r}^{RT} + \mathbf{f} \tag{5.15}$$

where, M and K stands for mass and stiffness matrices of the system, respectively; $\mathbf{u}$ and $\ddot{\mathbf{u}}$ are displacement and acceleration vectors; $\mathbf{f}$ and $\mathbf{r}$ are the external force vector and restoring force vector. For simplicity, damping contributions were neglected in these expressions. In detail, each matrix can be partitioned in pure Numerical-, pure Physical- and Boundary-DoFs, respectively, after Bursi (2008). For brevity, the following simplified notation holds: *N-DoFs*, *P-DoFs* and *B-DoFs*,

respectively. Thus,

$$\mathbf{u} = \left[\mathbf{u}^{N^T} \mathbf{u}^{B^T} \mathbf{u}^{P^T} \right] \tag{5.16}$$

Accordingly, a generic load vector **f** for a typical seismic input reads:

$$\mathbf{f} = \left[\mathbf{f}^{N^T} \mathbf{f}^{B^T} \mathbf{f}^{P^T} \right] = - \left(\mathbf{M}^N + \mathbf{M}^P \right) \mathbf{I} \ddot{u}_g \tag{5.17}$$

in which, **I** defines a Boolean vector that projects seismic inertial acceleration $\ddot{u}_g$ to desired DoFs. All matrices must be intended as expanded to the totality of the DoFs of the emulated system being considered. In detail, **M** and **K** read, respectively:

$$\mathbf{K}^N = \begin{bmatrix} \mathbf{K}^N_{NN} & \mathbf{K}^N_{NB} & \mathbf{0} \\ \mathbf{K}^N_{BN} & \mathbf{K}^N_{BB} & \mathbf{0} \\ \mathbf{0} & \mathbf{0} & \mathbf{0} \end{bmatrix} \mathbf{K}^P = \begin{bmatrix} \mathbf{0} & \mathbf{0} & \mathbf{0} \\ \mathbf{0} & \mathbf{K}^P_{BB} & \mathbf{K}^P_{BP} \\ \mathbf{0} & \mathbf{K}^P_{PB} & \mathbf{K}^P_{PP} \end{bmatrix} \tag{5.18}$$

$$\mathbf{M}^N = \begin{bmatrix} \mathbf{M}^N_{NN} & \mathbf{M}^N_{NB} & \mathbf{0} \\ \mathbf{M}^N_{BN} & \mathbf{M}^N_{BB} & \mathbf{0} \\ \mathbf{0} & \mathbf{0} & \mathbf{0} \end{bmatrix} \mathbf{M}^P = \begin{bmatrix} \mathbf{0} & \mathbf{0} & \mathbf{0} \\ \mathbf{0} & \mathbf{M}^P_{BB} & \mathbf{M}^P_{BP} \\ \mathbf{0} & \mathbf{M}^P_{PB} & \mathbf{M}^P_{PP} \end{bmatrix} \tag{5.19}$$

Since the restoring force vector **r** refers to the PS, it is restricted to *B*- and *P-DoFs*,

$$\mathbf{r} = \left[\mathbf{0}^{N^T} \mathbf{r}^{B^T} \mathbf{r}^{P^T} \right] \tag{5.20}$$

In particular, the restoring force vector **r** is peculiar of the testing strategy and for a linear regime reads:

$$\mathbf{r}^{PDT} = -\mathbf{K}^P \mathbf{u} \tag{5.21}$$

$$\mathbf{r}^{RT} = -\mathbf{K}^P \mathbf{u} - \mathbf{M}^P \ddot{\mathbf{u}} \tag{5.22}$$

In order to provide reduced matrices and compatible loading vectors, two reduction techniques were analysed and applied herein. They relied on,

$$\mathbf{u} = \left[\mathbf{u}^{N^T} \mathbf{u}^{B^T} \mathbf{u}^{P^T} \right]^T = \mathbf{T} \left[\mathbf{u}^{N^T} \mathbf{u}^{B^T} \mathbf{u}^{q^T} \right]^T = \mathbf{T}\tilde{\mathbf{u}} \tag{5.23}$$

where **T** is a reduction basis that keeps both *N-DoFs* and *B-DoFs* whilst discards remainder *P-DoFs*. In order to retain important properties of the PS, e.g., mode shapes of interest, further *q-DoFs* can be introduced. Resulting reduced matrices and vectors read:

$$\tilde{\mathbf{K}} = \mathbf{T}^T\mathbf{K}\mathbf{T} \ , \ \tilde{\mathbf{M}} = \mathbf{T}^T\mathbf{M}\mathbf{T} \ , \ \tilde{\mathbf{f}} = \mathbf{T}^T\mathbf{f} \tag{5.24}$$

where $\tilde{\mathbf{K}}$ $\tilde{\mathbf{M}}$ and $\tilde{\mathbf{f}}$ represent reduced stiffness matrix, mass matrix and force vector, respectively. From a hybrid simulation perspective, **T** establishes a kinematic relationship between displacements experienced by retained DoFs, i.e. *B-DoFs* and *q-DoFs*, and displacement experienced on discarded DoFs, i.e. *P-DoFs*. Based on Eq. (5.23), both Eqs. (5.21) and (5.22) can be condensed. Reduction strategies entail some general questions:

1. How can the minimum rank of an effective reduction basis be estimated?
2. Is there an optimal kinematic relationship, which provides an optimal reduction basis?
3. Which kinematic relationships actually hold for a PS and are they peculiar of the testing strategy?
4. Can a consistent hybrid simulation be performed when the kinematic relationships imposed by the testing procedure are far from those corresponding to the optimal reduction basis?

In order to answer to the above-mentioned questions, the Principal Component Analysis (PCA) was of valuable help (Chatterjee, 2000). The PCA is a numerical procedure aimed at projecting a set of possibly correlated vectors into a reduced set of linearly uncorrelated vectors, named Principal Components (PCs), which carry the most of the variance of the original vector set. In order to find out the PCs of a displacement response **X** of the PS, the Singular Value Decomposition (SVD) factorization was applied, i.e.,

$$\mathbf{X} = \mathbf{U}\mathbf{S}\mathbf{V}^T \tag{5.25}$$

where: each row of **X** corresponds to a time history at one node of the PS; each column corresponds to a snapshot of the system at a specific time; column vector

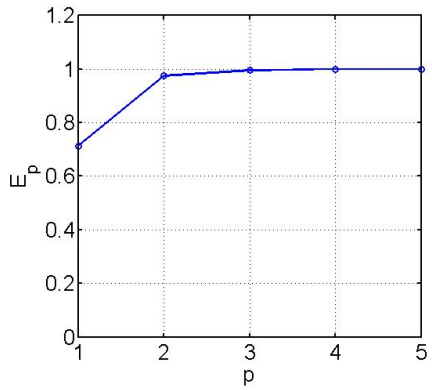

Figure 5.8: Cumulative distribution of data energy.

$\mathbf{u}_i$ of the orthonormal matrix **U** is the PC $i-th$ of **X**; column vector $\mathbf{v}_i$ of the orthonormal matrix **V** provides time modulation of corresponding PC $\mathbf{u}_i$; **S** is a rectangular matrix that contains singular values σ_i of each PC as main diagonal entries in decreasing order. The square of σ_i is the variance carried by **X** in the PC $\mathbf{u}_i$ according to its time modulation $\mathbf{v}_i$; it is proportional to the signal energy of **X** associated with each PC $\mathbf{u}_i$. The number of non-zero singular values equals the rank of the **X** matrix. Accordingly, the PCA was applied to the PS, to estimate the minimum rank of suitable reduction bases. In the present case, **X** contains discrete values and the PCA is equivalent to the Proper Orthogonal Decomposition (POD). In particular, **X** collected the displacement responses of the *B-DoFs* and of the *P-DoFs* calculated by means of a time history analysis of the RM subjected to selected earthquakes. Let $\sigma_1 > \sigma_2 > ... > \sigma_i$ be the decreasing singular values of the dynamic response; if we define $E = \sum_i \sigma_i$ as the total energy in the data, $E_p = \frac{\sum_{i=1}^{p} \sigma_i}{E}$ represents the normalized data energy carried by the first p modes. In this respect, Figure 5.8 shows calculated values of E_p up to the 5^{th} proper mode. It can be observed that almost the total energy of data was carried by two main modes, i.e. the PCs. On the basis of Eq. (5.25), the data set **X** was reconstructed by exploiting an increasing number p of modes; thus both NEEs and NRMSEs were calculated on Coupling DoFs #1 and #2, see Table 5.8 and 5.9, with respect to the RM solution.

A reader can observe that both errors drop after the 2^{nd} proper mode. As a result, the response path of the PS followed a two-dimensional state space path. In

	Number of proper modes retained				
Coupling DoF	1	2	3	4	5
#1	0.0721	0.0086	0.0013	0.0000	0.0000
#2	0.3162	0.0000	0.0000	0.0000	0.0000

Table 5.8: NEE of reconstructed displacement responses of coupling DoFs with respect to the RM solution.

	Number of proper modes retained				
Coupling DoF	1	2	3	4	5
#1	0.0353	0.0121	0.0047	0.0001	0.0000
#2	0.0962	0.0000	0.0000	0.0000	0.0000

Table 5.9: NRMSE of reconstructed displacement responses of Coupling DoFs #1 and #2 with respect to the RM solution.

addition, answers to the previously posed questions could be:

1. A kinematic relationship based on a two rank reduction basis can effectively reduce the PS.
2. An optimal reduction basis should embed the span of PCs. Nonetheless, actual kinematic assumption peculiar of each single testing procedure not necessarily fulfill this requirement, since they depend on the loading excitation.
3. In the case of a real-time interaction between PS and NS, the dynamic properties of the actual autonomous system are preserved in the laboratory; as a result, the SEREP reduction basis was applied to the RT case without adding any further *q-DoF* (OCallahan and Riemer, 1989).
4. Since the PS could experience only static deformations in the laboratory during PDT, the Craig-Bampton (CB) (Bampton, 1968) approach was selected; as a result, additional *q-DoFs*, which numerically accounted for non-negligible local dynamics, enriched the Guyan reduction basis (Guyan, 1965).

A preliminary investigation of reduction strategies was conducted in the linear regime. Therefore, both the SEREP and the CB reduction strategies were validated through numerical simulations on the RM of the elastic piping system. Both Krylov and PCA reduction bases were explored too. The transfer systems -hydraulic actuators- were characterized by an ideal unitary transfer function, i.e. in absence of delay, phase lags and amplitude distortions.

5.4.1 A modified version of the SEREP method applied to RT

In the RT technique, the PS behaves as a black-box and measured restoring forces can be defined as in Eq. (5.22). In this case, the SEREP technique was very effective for the reduction of earthquake forces of Eq. (5.17) to Coupling DoFs. In the ideal case, the coupled system is expected to behave as the emulated piping network, and therefore, modal properties should be preserved. As a consequence, a modified version of the SEREP method, called M-SEREP, was applied. In detail, the eigenvectors of the PS were reduced on a few significant eigenmodes of the global emulated system. In particular, let us split the mass normalized eigenvectors Φ of the global emulated system in retained Φ_R and truncated Φ_L eigenmodes -column wise- and relevant *N-DoFs*, *B-DoFs* and *P-DoFs* -row wise-:

$$\mathbf{\Phi} = \begin{bmatrix} \mathbf{\Phi}_R \mathbf{\Phi}_L \end{bmatrix} = \begin{bmatrix} \mathbf{\Phi}_{RN} \mathbf{\Phi}_{LN} \\ \mathbf{\Phi}_{RB} \mathbf{\Phi}_{LB} \\ \mathbf{\Phi}_{RP} \mathbf{\Phi}_{LP} \end{bmatrix} \tag{5.26}$$

The resulting transformation matrix $\mathbf{T}_{SE}$ reads:

$$\mathbf{T}_{SE} = \begin{bmatrix} \mathbf{I} \\ \mathbf{I} \\ \mathbf{\Phi}_{RP} \mathbf{\Phi}_{RB}^{-1} \end{bmatrix} \tag{5.27}$$

As a result, both *N-DoFs* and *B-DoFs* were preserved, whilst *P-DoFs* masses and stiffness were condensed to *B-DoFs*:

$$\mathbf{u} = \begin{bmatrix} \mathbf{u}^{N^T} \mathbf{u}^{B^T} \mathbf{u}^{P^T} \end{bmatrix}^T = \mathbf{T}_{SE} \begin{bmatrix} \mathbf{u}^{N^T} \mathbf{u}^{B^T} \end{bmatrix}^T \tag{5.28}$$

The choice of a specific reduced basis should primarily be based on the type of excitation to which the system is subjected. Accordingly, Mode #1 and Mode #2 depicted in Figure 5.7, carried most of the modal mass in x direction; thus they

	Coupling DoF #1	Coupling DoF #2
NEE	0.133	0.001
NRMSE	0.015	0.002

Table 5.10: M-SEREP method: NEE and NRMSE between RM and Reduced model

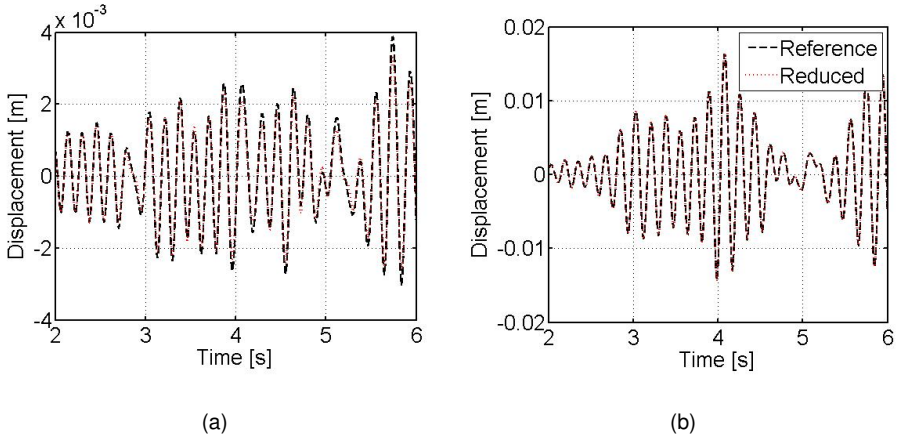

Figure 5.9: Comparison of displacement responses of the RM and M-SEREP reduced model at coupling DoFs **a** #1 and **b** #2.

were retained for this reduction. The inversion of $\mathbf{\Phi}_{RB}$ entailed a predetermined number of retained modes that must be equal to the number of *B-DoFs*. Hence, a modified RM was set, where the PS was replaced by its reduced counterpart. Relevant NEE and NRMSE errors calculated with respect to the RM on Coupling DoF responses are reported in Table 5.10. In addition, Figure 5.9 depicts the displacement response of the Coupling DoF #1 of both the RM and the reduced model. As one may note, the low values of both NEEs and NRMSEs reported in Table 5.10 as well as time histories of Figure 5.9, confirm a good agreement between responses; therefore, the M-SEREP reduction approach was effective.

5.4.2 Krylov and PCA reduction bases applied to RT

Since eigenvectors of the global system are considered, neither the distribution nor the time modulation of external loads affect the SEREP reduction basis. Given the span and the dimension of the optimal reduction basis, a minimum set of whatever combination of eigenvectors could not entail a satisfactory reduction. In fact, the reduction process discards part of input-output relations embedded in the transfer function of the system. The computation of Padé approximation of transfer functions via Krylov subspace techniques is one of the popular choices for the reduction of very high order systems. As a result, input-output relations are preserved. For a second-order undamped system, the Krylov subspace $\mathbf{\Phi}_{KR}$ is defined as follows (Craig, 1991):

$$\mathbf{\Phi}_{KR} = \text{span}\left(\mathbf{K}^{-1}\mathbf{f}\ ,\ (\mathbf{K}^{-1}\mathbf{M})\mathbf{K}^{-1}\mathbf{f}\ ,\ (\mathbf{K}^{-1}\mathbf{M})^2\mathbf{K}^{-1}\mathbf{f}\ ,\ \ldots\ ,\ (\mathbf{K}^{-1}\mathbf{M})^{q-1}\mathbf{K}^{-1}\mathbf{f}\right) \quad (5.29)$$

In particular, Taylor expansions at $s = 0$ of transfer functions of both the reduced and the reference systems match up to term q^{th} when the full span of Eq. (5.29) is retained (Srinivasan Puri, 2008). Since suitable reduction bases were restricted to vector pairs, the Krylov subspace considered for the reduction of the ANSYS RM reads,

$$\mathbf{\Phi}_{KR} = \left[(\mathbf{K}^{-1}\mathbf{M})^{p}\mathbf{K}^{-1}\mathbf{f}\ ,\ (\mathbf{K}^{-1}\mathbf{M})^{q}\mathbf{K}^{-1}\mathbf{f}\right] \quad (5.30)$$

where exponents $p,q \in \mathbb{N}$. Let us split the Krylov subspace span $\mathbf{\Phi}_{KR}$ according to *N-DoFs*, *B-DoFs* and *P-DoFs* :

$$\mathbf{\Phi}_{KR} = \begin{bmatrix} \mathbf{\Phi}_{KR,N} \\ \mathbf{\Phi}_{KR,B} \\ \mathbf{\Phi}_{KR,P} \end{bmatrix} \quad (5.31)$$

The resulting transformation matrix $\mathbf{T}_{KR}$ reads:

$$\mathbf{T}_{KR} = \begin{bmatrix} \mathbf{I} \\ \mathbf{I} \\ \mathbf{\Phi}_{KR,P}\mathbf{\Phi}_{KR,B}^{-1} \end{bmatrix} \quad (5.32)$$

Accordingly, both *N-DoFs* and *B-DoFs* were preserved, whilst *P-DoFs* masses and stiffness were condensed to *B-DoFs*.

$$\mathbf{u} = \begin{bmatrix} \mathbf{u}^{N^T} \mathbf{u}^{B^T} \mathbf{u}^{P^T} \end{bmatrix}^T = \mathbf{T}_{KR} \begin{bmatrix} \mathbf{u}^{N^T} \mathbf{u}^{B^T} \end{bmatrix}^T \tag{5.33}$$

In greater detail, exponents p and q of (5.30) where selected in order to minimize the NRMSE between displacement responses of reference and reduced models at Coupling DoFs #1 and #2. The entailing loss function reads:

$$\{\hat{p}, \hat{q}\} = \min_{p,q} \left(\text{NRMSE}\left(\mathbf{u}_x^{110}, \tilde{\mathbf{u}}_x^{110}\right) + \text{NRMSE}\left(\mathbf{u}_x^{114}, \tilde{\mathbf{u}}_x^{114}\right)\right) \tag{5.34}$$

The solution of the minimization problem led to $\hat{p} = 3$ and $\hat{q} = 94$. Nonetheless, both the spatial distribution and the time modulation characterize the applied load $\mathbf{f}$ and, therefore, the displacement responses of the system. Reduction bases that do not account for the latter could fail when resonance occurs. In order to circumvent such limitation, which affects both SEREP- and Krylov-based methods, PCs of the response of the reference system can be selected as effective reduction bases (Lülf, 2013). According to Figure 5.8, which shows the cumulative distribution of data energy of PCs, PC #1 and #2 were collected in the PCA-based subspace span.

$$\mathbf{\Phi}_{PCA} = \begin{bmatrix} \mathbf{u_1} , \mathbf{u_2} \end{bmatrix} \tag{5.35}$$

Since they carried the most of the variance of the dynamic response of the PS, they capture the state space path of the system being reduced. Let us split the PCA subspace span $\mathbf{\Phi}_{PCA}$ according to *N-DoFs*, *B-DoFs* and *P-DoFs*, i.e.

$$\mathbf{\Phi}_{PCA} = \begin{bmatrix} \mathbf{\Phi}_{PCA,N} \\ \mathbf{\Phi}_{PCA,B} \\ \mathbf{\Phi}_{PCA,P} \end{bmatrix} \tag{5.36}$$

The resulting transformation matrix $\mathbf{T}_{PCA}$ reads:

$$\mathbf{T}_{PCA} = \begin{bmatrix} \mathbf{I} \\ \mathbf{I} \\ \mathbf{\Phi}_{PCA,P} \mathbf{\Phi}_{PCA,B}^{-1} \end{bmatrix} \tag{5.37}$$

Accordingly, both *N-DoFs* and *B-DoFs* were preserved, whilst *P-DoFs* masses and stiffness were condensed to *B-DoFs*. Table 5.11 compares performances of M-SEREP, Krylov and PCA methods. Both NRMSEs and NEEs are calculated with

	NRMSE		NEE	
	Coupling DoF #1	Coupling DoF #2	Coupling DoF #1	Coupling DoF #2
M-SEREP	1,24E-02	1,32E-03	1,32E-01	5,46E-04
Krylov	1,22E-02	1,32E-03	1,23E-01	3,06E-04
PCA	1,05E-02	1,52E-03	9,99E-03	7,55E-05

Table 5.11: NEE and NRMSE between ANSYS RM and reduced models.

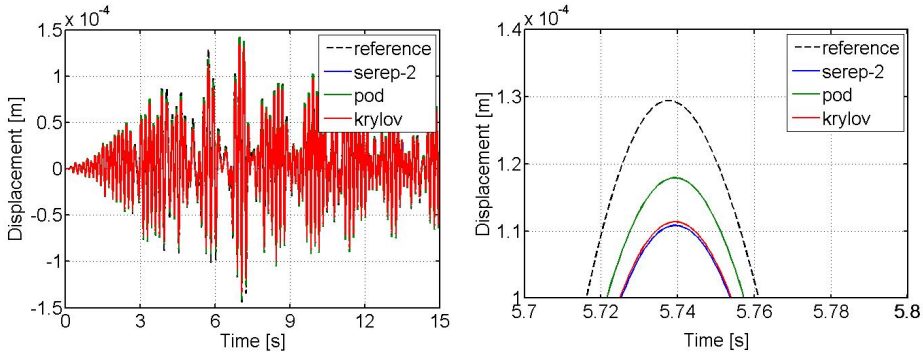

Figure 5.10: Comparison of displacement responses of reduced models at Coupling DoF #1.

respect to the Coupling DoF displacement response of the ANSYS RM. As can be appreciated in Table 5.11, errors on Coupling DoF #1, which are higher then those on Coupling DoF #2, clearly emphasize the performance ranking of proposed methods. The greater is the information flowing into the reduction basis, the better is the performance of the reduced model. Figure 5.10 compares displacement responses on Coupling DoF #1 obtained with all aforementioned reduction strategies. According to Figure 5.10(a), all proposed methods were capable of reproducing the dynamic response of the ANSYS RM. As can be appreciated, fitting performance at peaks confirmed error trends reported in Table 5.11.

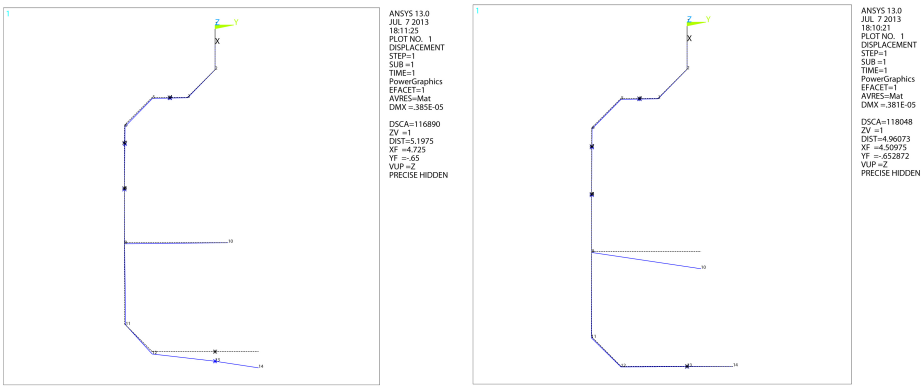

(a) (b)

Figure 5.11: **a** Constraint Mode #1; **b** Constraint Mode #2.

5.4.3 The Craig-Bampton reduction technique applied to PDT

In order to describe this technique and with reference to the PS, it is necessary to introduce the so-called constraint modes. These modes are static deformation shapes owing to unit displacements applied to boundary DoFs, one by one, whilst the other retained (Girard, 2010). According to their definition, these modes cope with the PDT technique; so, they were calculated through static analyses on the FE model of the PS. Figure 5.11 depicts the constraint modes of the PS for both Coupling DoFs #1 and #2. Since the dynamic response of the piping system was described by Modes #1 and #2 depicted in Figure 5.7, one can observe that a typical PDT cannot reproduce the response path of the PS. In fact, constraint modes shown in Figure 5.11 entail deformations concentrated toward cantilever pipe elements, whilst the remainder parts of the PS remains undeformed. Nonetheless, the portion of the dynamic response of the PS that cannot be excited during the PDT can be simulated numerically. At this point, the Craig-Bampton (CB) method (Bampton, 1968) comes on stage. Starting from the FE model of the PS, its reduced counterpart can be obtained assuming as basis both static and modal vec-

tors, i.e.

$$\mathbf{u} = \begin{bmatrix} \mathbf{u}^N \\ \mathbf{u}^B \\ \mathbf{u}^P \end{bmatrix} = \begin{bmatrix} \mathbf{I} & \mathbf{0} & \mathbf{0} \\ \mathbf{0} & \mathbf{I} & \mathbf{0} \\ \mathbf{0} & \mathbf{\Phi}_S & \mathbf{\Phi}_D \end{bmatrix} \begin{bmatrix} \mathbf{u}^N \\ \mathbf{u}^B \\ \mathbf{u}^q \end{bmatrix} = \mathbf{T}_{CB} \begin{bmatrix} \mathbf{u}^N \\ \mathbf{u}^B \\ \mathbf{u}^q \end{bmatrix} = \tilde{\mathbf{u}} \tag{5.38}$$

where, $\mathbf{T}_{CB}$ is the CB transformation matrix. With regard to the PS, the matrix $[\mathbf{I}\ ,\ \mathbf{\Phi}_S]^T$ contains the aforementioned constraint modes, whilst $[\mathbf{0}\ ,\ \mathbf{\Phi}_R]^T$ collects a certain number of fixed interface vibration modes. In detail, they correspond to eigenmodes of the substructure constrained at its *B-DoFs*. The number of constraint modes is fixed and equal to the number of *B-DoFs*, whilst, the number of fixed interface vibration modes is up to the user. If a proper selection of fixed interface vibration modes is made, a consistent reduced counterpart of the PS valid for both static and dynamic analyses can obtained. Moreover, looking at the block diagonal structure of the reduced stiffness matrix $\mathbf{K}_{CB}$ provided by Eq. (5.24), i.e.

$$\mathbf{r} = \begin{bmatrix} \mathbf{0} \\ \mathbf{r}^B \\ \mathbf{r}^q \end{bmatrix} = \begin{bmatrix} \mathbf{0} & \mathbf{0} & \mathbf{0} \\ \mathbf{0} & \tilde{\mathbf{K}}^P_{BB} & \mathbf{0} \\ \mathbf{0} & \mathbf{0} & \tilde{\mathbf{K}}^P_{qq} \end{bmatrix} = \begin{bmatrix} \mathbf{u}^N \\ \mathbf{u}^B \\ \mathbf{u}^q \end{bmatrix} \tag{5.39}$$

the restoring force contribution of constraint and fixed interface vibration modes, one notes that they are pleasantly uncoupled. Since the component $\mathbf{r}^B$ is measured during the PDT and the $\mathbf{r}^q$ can be easily calculated by the submatrix $\tilde{\mathbf{K}}^P_{qq}$, the CB method lends itself for an effective implementation of the PDT technique. In order to perform an optimal selection of reduction basis vectors, a sweep analysis was conducted on the number of retained fixed interface vibration modes; they were sorted in decreasing order with respect to their modal masses along the loading direction. For each selection of fixed interface vibration modes, a modified RM embedding the reduced counterpart of the PS was devised and both NEE and NRMSE errors were calculated with respect to the RM on the displacement responses of the Coupling DoFs #1 and #2; they are reported in Tables 5.12 and 5.13, respectively. On the basis of figures of Tables 5.12 and 5.13, only two Fixed Interface Vibration Modes #1 and #3 were enough to entail asymptotic values of both NRMSEs and NEEs; these modes are depicted in Figure 5.12 and allowed for a quite accurate reduction. The dynamic responses of the modified RM embedding

	Number of retained fixed interface vibration modes					
Coupling DoF	0	1	2	3	4	5
#1	0.848	0.012	0.012	0.011	0.011	0.011
#2	0.747	0.015	0.002	0.002	0.002	0.002

Table 5.12: CB method: NEEs on coupling DoFs resulting from the sweep analysis.

	Number of retained fixed interface vibration modes					
Coupling DoF	0	1	2	3	4	5
#1	0.105	0.006	0.003	0.003	0.003	0.003
#2	0.122	0.003	0.001	0.001	0.001	0.001

Table 5.13: CB method: NRMSEs on coupling DoFs resulting from the sweep analysis

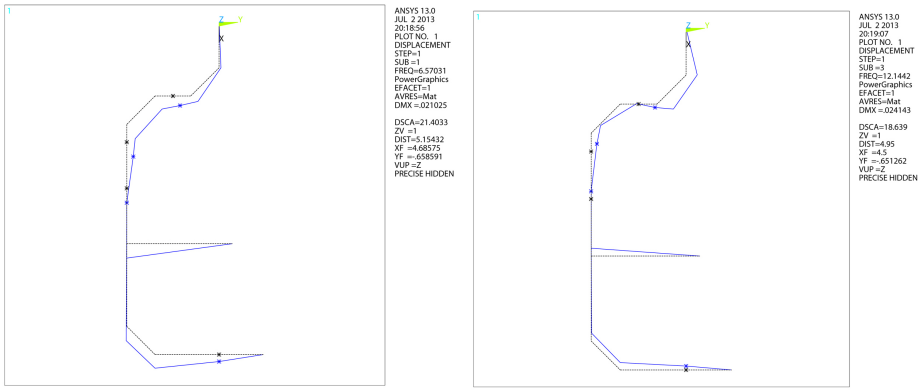

(a) (b)

Figure 5.12: Fixed Interface Vibration **a** Mode #1 at 6.57Hz and **b** Mode #3 at 12.44Hz of the PS.

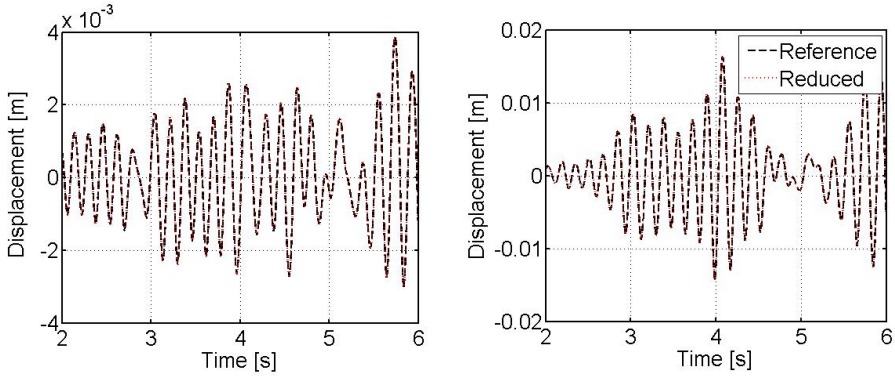

Figure 5.13: Comparison of displacement responses of the RM and CB reduced models at Coupling DoF **a** #1 and **b** #2.

the reduced PS with two retained fixed interface vibration modes and of the RM are compared in Figure 5.13. We can conclude that also the CB method allowed for an effective simulation of the piping system by means of PDT techniques.

5.5 Description of the experimental campaign

5.5.1 The experimental set-up

The experimental set-up was placed on the reaction floor of the Materials and Structural Testing laboratory (LPMS) of the University of Trento. The test specimen corresponded to the PS of the piping system of Figure 5.5; schematic of the specimen and set-up is depicted in Figure 5.14. In order to measure strains, displacements and rotations in different positions, the test specimen and in particular, elbows and the Tee joint, were instrumented with 22 strain gauges and 7 displacement transducers. Data were acquired by 4 Spider8 acquisition systems and by an MTS FT60 controller. Reza (2013) reports a comprehensive description of the acquisition set-up. In order to simulated realistic operating conditions, all pipes were filled with water at 32bar pressure.

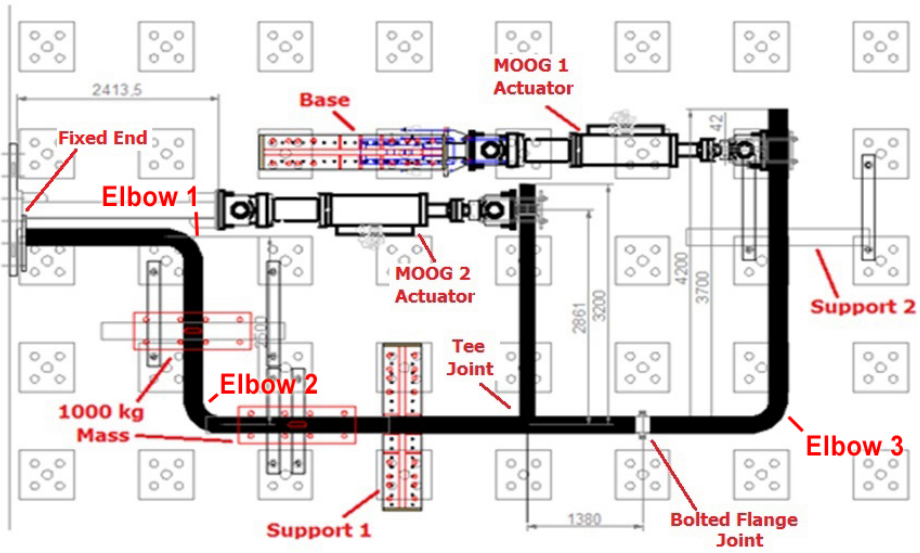

Figure 5.14: Top view of the experimental set-up of the PS for the purpose of hybrid simulation.

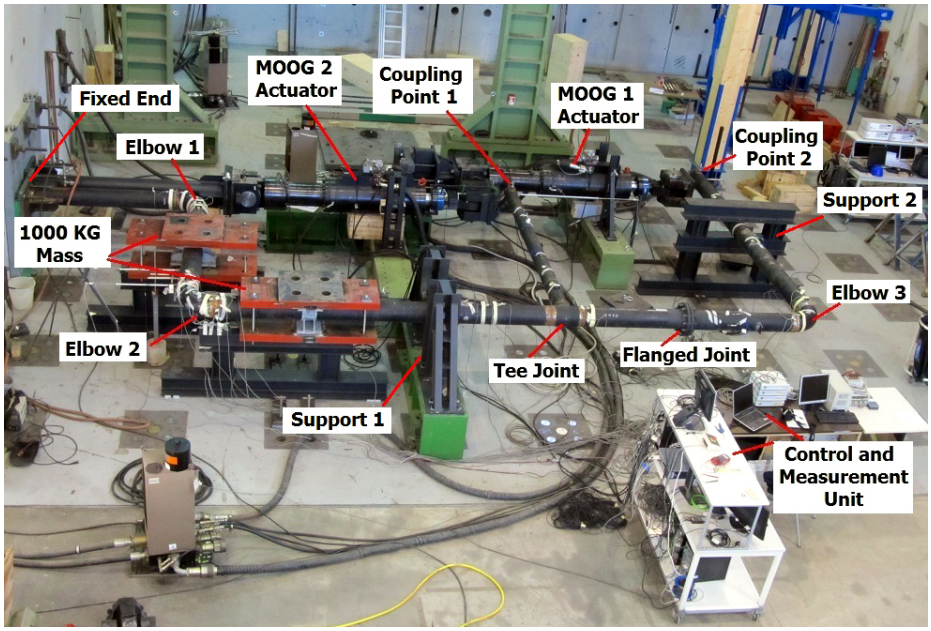

Figure 5.15: Actual experimental set-up for hybrid simulations.

5.5.2 The LSRT2 time integration algorithm

The robustness and the quality of a PDT or RT depend, among other factors, on the integration scheme employed to solve Eq. (5.14) or Eq. (5.15). Since the transfer system is generally affected by delay, distortion of the transfer function and noise, which may lead to instability, unconditionally stable integration methods are preferable, since they are more robust. Typically, real-time machines handling controllers impose a deterministic solving time. Consequently, nonlinear solver characterized by a fixed number of iterations are crucial. Among RT compatible algorithms, the method proposed by (Chen, 2008), the HHT-α implementation of (Rae-Young, 2007) and the equivalent force control method of (Wu, 2007) are the most widespread adopted strategies. Nonetheless in hybrid simulations, the numerical models of both NS and PS can be profitably used for dynamic identification, model-based control and/or model order reduction; in these conditions, a unique representation of the system is preferable. As a result, the most flexible and generic state space form represents a reasonable choice. Accordingly, time integration algorithms tailored to first order systems are deemed necessary. Moreover, they allow for the integration of coupled physics characterized by different time derivative orders, e.g. thermo-mechanical coupling. The LSRT2 algorithm presented hereinafter is conceived for first-order systems, and therefore, fulfills this requirement. In details, it embeds the favorable L-Stability property and is real-time compatible. Moreover, it allowed for time integrating a linear Numerical Substructure characterized by high frequency content with a feasible time step ($\approx 1 msec$). In this respect, the following state-space representation is introduced:

$$\bar{\mathbf{M}}\dot{\mathbf{y}}_n + \bar{\mathbf{K}}\mathbf{y}_n = \mathbf{g}_n \tag{5.40}$$

where,

$$\bar{\mathbf{K}} = \begin{bmatrix} \mathbf{0} & -\mathbf{I} \\ \tilde{\mathbf{K}}^N & \mathbf{0} \end{bmatrix} , \bar{\mathbf{M}} = \begin{bmatrix} \mathbf{I} & \mathbf{0} \\ \mathbf{0} & \tilde{\mathbf{M}}^N \end{bmatrix} , \mathbf{y}_n = \begin{bmatrix} \tilde{\mathbf{u}}_n \\ \tilde{\dot{\mathbf{u}}}_n \end{bmatrix} , \mathbf{g}_n = \begin{bmatrix} \mathbf{0} \\ \tilde{\mathbf{f}}_n + \tilde{\mathbf{r}}_n^{RT} \end{bmatrix} \tag{5.41}$$

$$\bar{\mathbf{K}} = \begin{bmatrix} \mathbf{0} & -\mathbf{I} \\ \tilde{\mathbf{K}}^N & \mathbf{0} \end{bmatrix} , \bar{\mathbf{M}} = \begin{bmatrix} \mathbf{I} & \mathbf{0} \\ \mathbf{0} & \tilde{\mathbf{M}}^N + \tilde{\mathbf{M}}^P \end{bmatrix} , \mathbf{y}_n = \begin{bmatrix} \tilde{\mathbf{u}}_n \\ \tilde{\dot{\mathbf{u}}}_n \end{bmatrix} , \mathbf{g}_n = \begin{bmatrix} \mathbf{0} \\ \tilde{\mathbf{f}}_n + \tilde{\mathbf{r}}_n^{PDT} \end{bmatrix} \tag{5.42}$$

where, **r** is the restoring force vector; Eqs. (5.41) and (5.42) refer to the RT and the PDT cases, respectively. To carry out both RTs and PDTs, the L-Stable Real-Time compatible algorithm with two stages (LSRT2) method developed by Bursi (2011) was employed. For a proper selection of relevant parameters, this monolithic algorithm results to be second order accurate and L-stable. The LSRT2 results to be more competitive than popular Runge-Kutta methods in terms of stability, accuracy and ease of implementation (Bursi, 2011). This method is unconditionally stable for uncoupled problems and entails a moderate computational cost for real-time performance. It can be summarized in algorithmic form as follows:

procedure LSRT-2(...)

for $n = 1 : 1 : step$ **do**

$\mathbf{k}_1 = (\mathbf{I} - \gamma \Delta t \mathbf{J})^{-1}(\bar{\mathbf{M}}^{-1}(\mathbf{g}_n - \bar{\mathbf{K}}\mathbf{y}_n))\Delta t$

$\mathbf{y}_{n+\alpha_2} = \mathbf{y}_n + \alpha_{21}\mathbf{k}_1$ ▷ 1^{st} stage actuator command

$\mathbf{k}_2 = (\mathbf{I} - \gamma \Delta t \mathbf{J})^{-1}(\bar{\mathbf{M}}^{-1}(\mathbf{g}_{n+\alpha_2} - \bar{\mathbf{K}}\mathbf{y}_{n+\alpha_2}) + \mathbf{J}\gamma_{21}\mathbf{k}_1)\Delta t$

$\mathbf{y}_{n+1} = \mathbf{y}_n + b_1\mathbf{k}_1 + b_2\mathbf{k}_2$ ▷ 2^{nd} stage actuator command

end for

end procedure

where Δt is the time step. According to the reported pseudo code, the displacement command $\mathbf{y}_{n+a_2}$ is sent to actuators at the end of the first stage; then, the restoring force is fed back to the algorithm through $\mathbf{g}_{n+a_2}$ at the second stage. Accordingly, the displacement command $\mathbf{y}_{n+1}$ is sent to actuators at the end of the second stage. In order to preserve A-Stability, the Jacobian matrix J was evaluated on the global piping system as follows:

$$\mathbf{J} = \begin{bmatrix} \mathbf{0} & \mathbf{I} \\ -(\tilde{\mathbf{M}}_N + \tilde{\mathbf{M}}_P)^{-}1(\tilde{\mathbf{K}}_N + \tilde{\mathbf{K}}_P) & -(\tilde{\mathbf{M}}_N + \tilde{\mathbf{M}}_P)^{-}1(\tilde{\mathbf{C}}_N + \tilde{\mathbf{C}}_P) \end{bmatrix} \tag{5.43}$$

In order to achieve L-stability, second order accuracy and to reduce algorithmic damping in the low frequency range, the following parameters are recommended for the LSRT2 method:

$$\gamma = 1 \pm \frac{\sqrt{2}}{2}\ ,\ \alpha_2 = \alpha_{21} = \frac{1}{2}\ ,\ \gamma_{21} = -\gamma\ ,\ b_1 = 0\ ,\ b_2 = 1 \tag{5.44}$$

Favourable dissipative properties of the LSRT2 are shown in Figure 5.16, where both the spectral radius ρ and equivalent algorithmic damping $\bar{\xi}$ are depicted. In

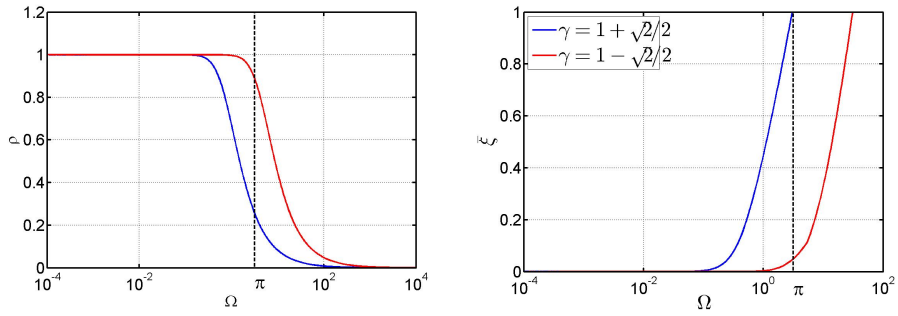

Figure 5.16: LSRT2 algorithm: **a** spectral radius ρ; and **b** algorithmic damping $\bar{\xi}$.

detail $\Omega = \omega\Delta t$ is the dimensionless frequency and $\Omega = \pi$ corresponds to the normalized Nyquist frequency. Since excitation of higher modes was not appreciated, simulations were conducted considering the less dissipative setting characterized by $\gamma = 1 - \sqrt{2}/2$.

5.5.3 Architecture of experimental implementations

In order to carry out hybrid simulations, linear matrices from both the ANSYS RM and the ANSYS MM were used to model the NS by means of the Matlab/Simulink code in the Host PC. The Host PC compiled the system of equations discretized in time by the LSRT2 algorithm, which was then sent to an xPC target - a real time operating system installed in a target PC- via a LAN connection. During experimental tests, integration algorithms solved Eq. (5.14) or (5.15) in the xPC target and estimated displacement commands for the PS. These displacement commands were written to the xPC target, which instantaneously copied these signals to an MTS controller through a SCRAMNET -a reflective memory between the Host PC and the controller-. The controller then commanded two MOOG actuators -capacity: 1000kN force, $\pm$250mm stroke- to move the Coupling DoFs #1 and #2 to desired positions. Again, the SCRAMNET memory instantaneously supplied corresponding restoring forces measured by load cells to the xPC target. The software scheme and the hardware equipment used for hybrid tests are depicted in Figure 5.17 In order to compensate actuator delays, the over prediction based method

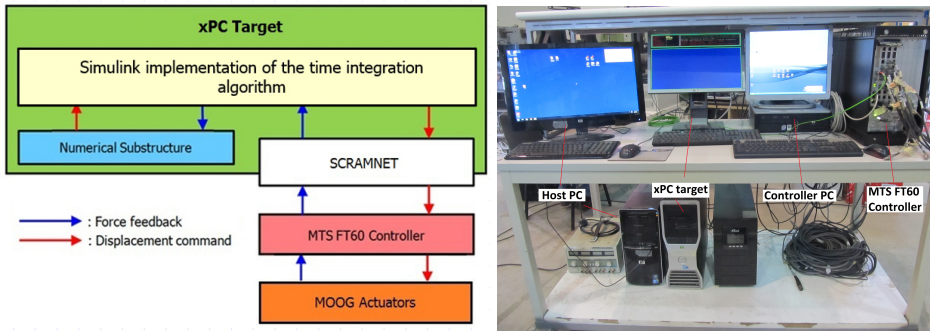

(a) (b)

Figure 5.17: **a** Architecture of the implementation and **b** hardware equipment.

developed by Wu (2013) was implemented with Simulink models of relevant algorithms. This newly developed compensation technique consists of an upper bound delay τ_c and optimal feedback. It ensures dynamic stability and achieves a nearly exact compensation for delay. The idea behind this over prediction technique is to assume an upper bound delay τ_c not less than the possible maximum delay τ and use it for prediction. The schematic of the over prediction technique and its validation on experimental signals are illustrated in Figure 5.18. The maximum delay of the transfer system was measured through experimental tests of the actuator control system and comparison of the input-output signals. In particular, τ_c was taken as 22ms. As can be appreciated in Figure 5.18(b), the optimal displacement -OPT- well agree with the actuator command -CMD-. As a consequence, the effective RT simulation of the modified piping system was allowed.

5.5.4 The test program

As reported in Table 5.14, a number of PDT and RT were carried out. RT were conducted with low PGA values and handled a similar structure owing to limitations underlined in Section 6. PDTs were performed with the CB reduction, whilst the M-SEREP reduction was adopted to perform RT. All PDTs were carried out at a 50 times extended earthquake time. Since rate dependent effects can practically be neglected for steel components (Tanaka, 2012), PDT is a suitable strategy for simulating their actual responses under dynamic loading. In all tests, earthquake

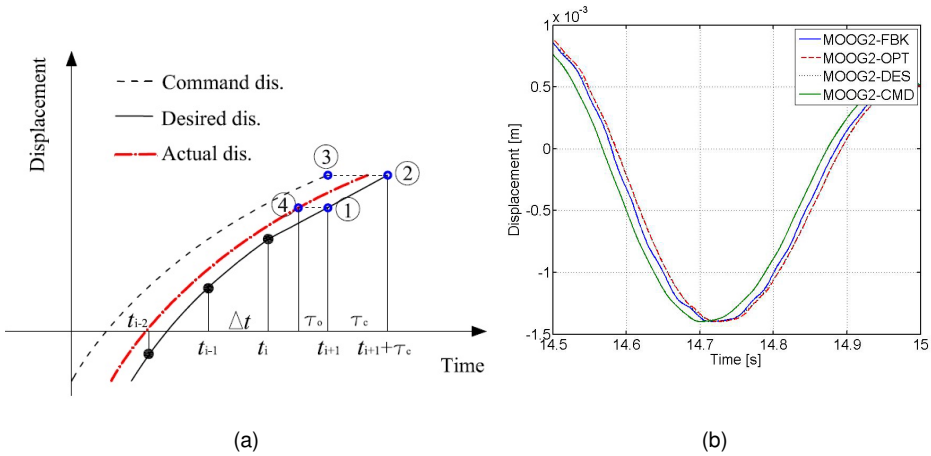

(a) (b)

Figure 5.18: **a** Schematics of the delay over prediction scheme and **b** experimental validation of the delay compensation strategy.

loading was applied in the horizontal x direction shown in Figure 5.5. Note that support motions were not required to be considered separately in hybrid simulations; in fact the system of Eqs. (5.14) and (5.15) allowed for relative movements between floor and piping network. All experimental results were compared to numerical simulations of ANSYS FE models. According to Table 5.14, the ANSYS MM was taken as reference for the RT case, whilst PDTs refer to the ANSYS RM.

Test type	Description	Red. method	PGA	FE model
RT	Elastic test, RT	M-SEREP	0.02g	ANSYS MM
PDT	Elastic test, ET	CB	0.04g	ANSYS RM
PDT	Operational limit state test, SLOT	CB	0.08g	ANSYS RM
PDT	Damage limit state test, SLDT	CB	0.11g	ANSYS RM
PDT	Safe life limit state test, SLVT	CB	0.42g	ANSYS RM
PDT	Collapse limit state test, SLCT	CB	0.60g	ANSYS RM

Table 5.14: Hybrid test program

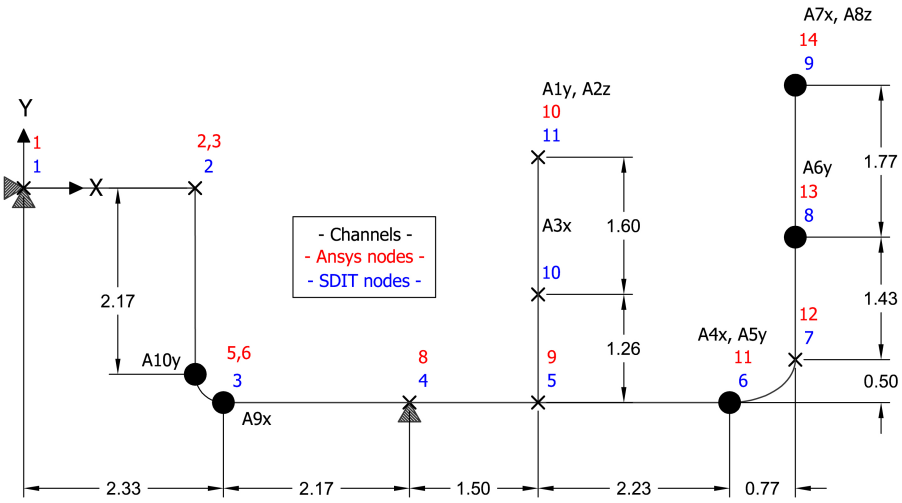

Figure 5.19: Acquisition set-up for the dynamic characterization of the PS.

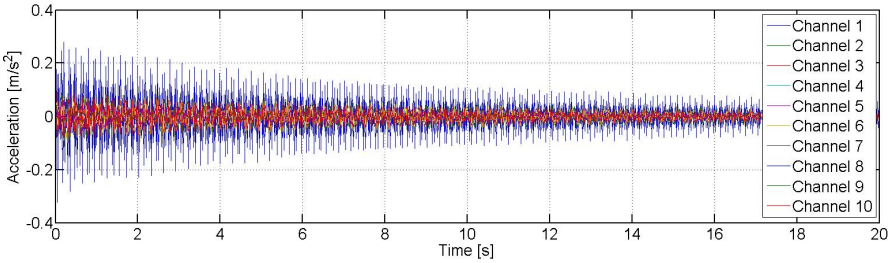

Figure 5.20: Free decay response of the PS subjected to hammer tests.

5.6 Dynamic identification of the PS

Identification Tests (IDTs) were performed on the PS to characterize both its modal properties and damping ratios. In greater detail, IDTs were carried out using 10 accelerometers and a National Instruments data acquisition system. Figure 5.19 depicts the experimental set-up for the dynamic identification of the PS. Free decay signals of the type depicted in Figure 5.20 were produced through hammer hits. A time domain identification strategy was selected. In detail, modal parameters were identified applying the Eigensystem Realization Algorithm (ERA) (Juang, 1984) implemented in the Structural Dynamic Identification (SDIT) toolbox (Ceravolo, 2009, 2013). They are summarized by Table 5.15 for both values of water

	Frequency [Hz]		Damping	
Mode	IDT 1bar	IDT 32bar	IDT 1bar	IDT 32bar
1	3.41	3.46	0.0059	0.0030
2	5.55	5.54	0.0120	0.0016
3	7.17	7.23	0.0018	0.0020
4	8.94	7.54	0.0193	0.0060
5	10.14	9.15	0.0120	0.0234
6	12.47	10.17	0.0149	0.0125
7	14.38	12.58	0.0058	0.0051
8	16.68	14.46	0.0024	0.0042

Table 5.15: Dynamic characterization of the PS: frequency and damping values for both the water pressure values.

pressure, i.e. 1bar and 32bar. As can be appreciated in Table 5.15, modal parameters of lower modes were not sensitive to water pressure variations. Figure 5.21 reports cluster and stabilization diagrams relevant to the 32bar water pressure case. According to the cluster diagram of Figure 5.21(a), the reference damping value assumed to conduct hybrid simulations was set to 0.005.

5.7 Main experimental results and validation of algorithms

All hybrid simulations listed in Table 5.14 were successfully carried out. A 0.5% damping found through the IDTs was used in the NS during tests. Experimental results exhibited a favorable performance of the piping system and its components under all limit state earthquakes. In fact, it was observed that, even under SLC, the whole piping system remained below its yield limits without any leakage, and only limited strains and rotations were found in different components. In all tests, maximum strain was found in Elbow #2, as can be noted in Figure 5.22; in greater detail, the maximum elbow flank strain at SLCT was about $950\mu m/m$, which was well below its yield strain of $2019\mu m/m$. Figure 5.23 presents acceleration time history of Coupling DoF #2 at SLCT. One can observe that the input earthquake at $5.88 m/s^2$ was significantly amplified during testing; in fact, the maximum acceleration was

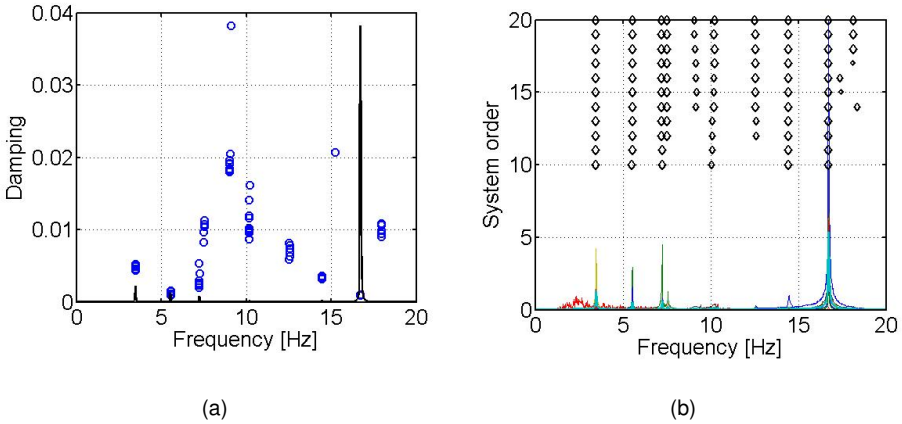

Figure 5.21: Dynamic characterization of the PS: **a** cluster diagram and **b** stabilization diagram relevant the 32bar water pressure case.

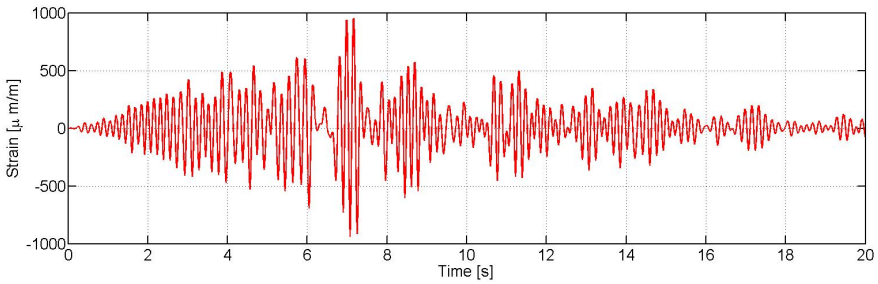

Figure 5.22: Strain history in Elbow #2 at SLCT.

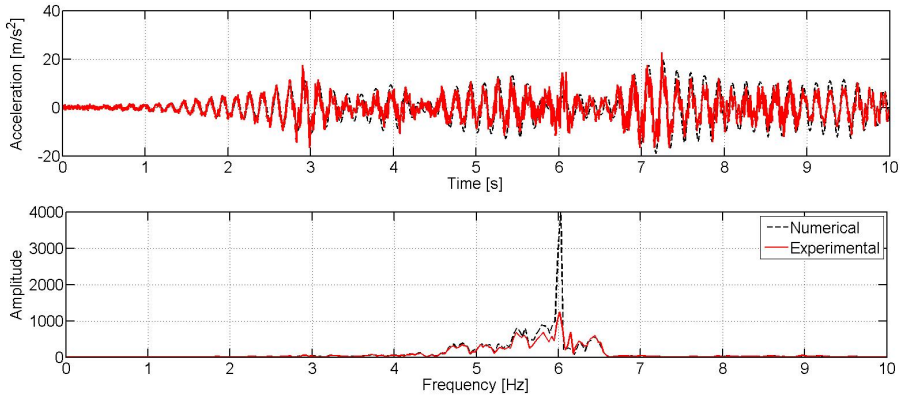

Figure 5.23: Acceleration response of Coupling DoF #2 for PDT at SLC.

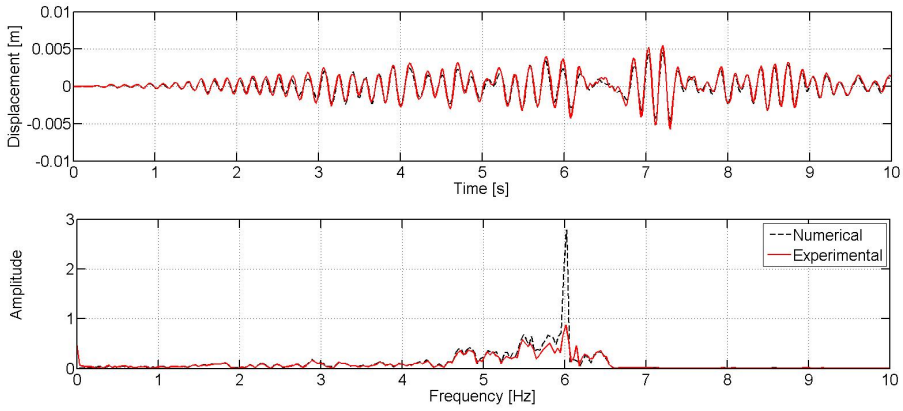

Figure 5.24: Displacement response of Coupling DoF #1 for PDT at SLC.

about three times that of the corresponding input. Moreover, relevant Fourier spectra illustrate that the dynamic response of the piping system was dominated by its lower modes corresponding to 5.87Hz -1st Mode- and 6.32Hz -2nd Mode-. Figures 5.24 and 5.25, which compare measured displacement responses to reference numerical solutions, prove the effectiveness of the proposed approach. With regard to RT, the piping system exhibited a favorable response. See in this respect, the acceleration time history of Coupling DoF #2 from RT presented in Figure 5.26. One may note that the input PGA was amplified about two times in this test. Moreover, relevant Fourier spectra show that the systems responses were dominated

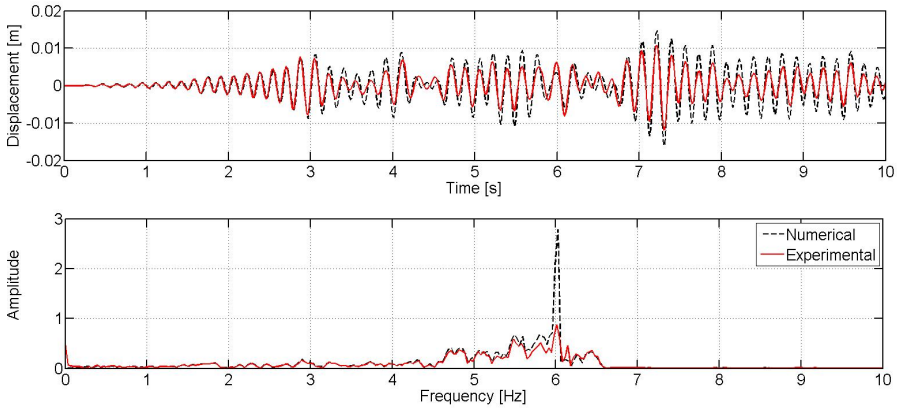

Figure 5.25: Displacement response of Coupling DoF #2 for PDT at SLC.

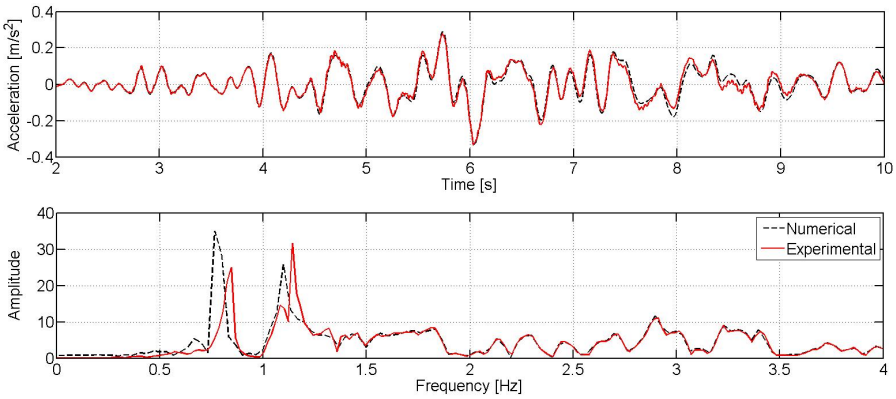

Figure 5.26: Acceleration response of Coupling DoF #2 for RT.

by its lower modes corresponding to frequencies 0.78Hz and 1.10Hz. In addition, the LSRT2 integrator proved to be effective for RT; as depicted in Figures 5.27 and 5.28, it entailed experimental responses in agreement with relevant numerical simulations. Because the PS responded in the linear range, both NEE and NRMSE errors were quantified also for these cases. Relevant estimates can be found in Table 5.16 and Table 5.17 for PDT and RT, respectively. Given the different approximations involved, NRMSE error values indicated a favorable agreement between numerical and experimental results. As expected and because of signal energy involved, NEE errors were found to be comparatively greater. Thus, effectiveness of

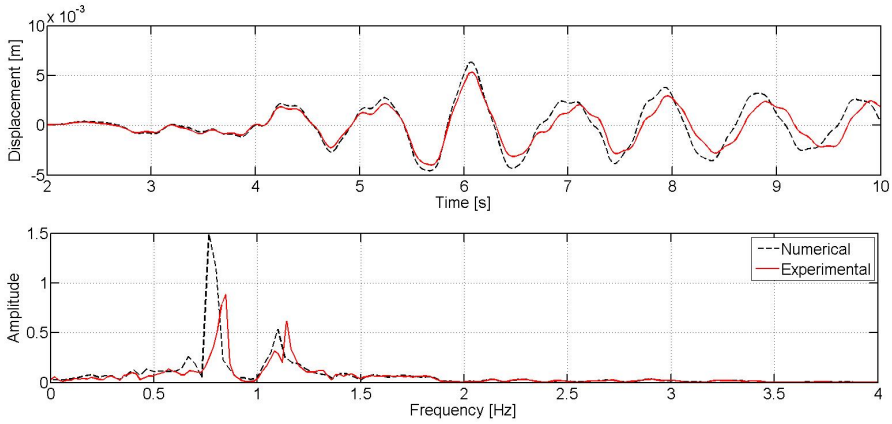

Figure 5.27: Displacement response of Coupling DoF #1 for RT.

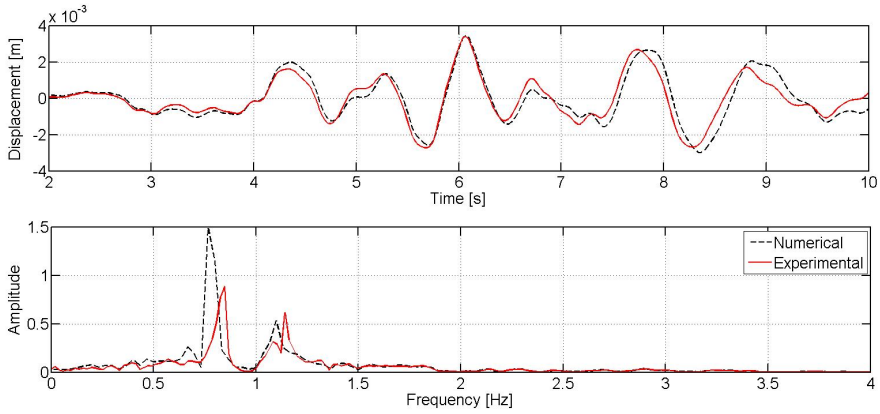

Figure 5.28: Displacement response of Coupling DoF #2 for RT.

	Coupling DoF #1	Coupling DoF #2
NEE	0.236	0.635
NRMSE	0.038	0.066

Table 5.16: NEE and NRMSE between experimental and numerical responses in the PDT case at SLCT

	Coupling DoF #1	Coupling DoF #2
NEE	0.494	0.614
NRMSE	0.083	0.239

Table 5.17: NEEs and NRMSEs between experimental and numerical responses in the RT case

both the CB and M-SEREP reduction techniques were experimentally justified as was predicted analytically. Moreover, a favorable performance of the piping system was found, which always remained in the linear regime without any leakage; thus the over-conservativeness of relevant design standards was confirmed (Touboul, 2006; Otani and Shiratori, 2011; Paolacci, 2013; Paolacci F., 2011). In addition, the choice of reduction bases derived from a linear FE model of the piping system was supported.

5.8 Conclusions

A novel hybrid simulation approach for seismic performance evaluation of industrial piping systems based on model reduction techniques was presented. In this respect, a deep insight into the dynamic response of an emulated global system was provided. In particular the PCA was applied to the displacement responses of the PS of ANSYS RM of the piping system. The clear understanding of reduction basis requirements paved the way for the implementation of a number of model reduction techniques aimed at extending the applicability range of hybrid simulation techniques beyond its traditional scope. In detail, the M-SEREP method was applied to the RT, whilst the well-known CB method was tailored to the PDT case. Since applied techniques do not account for distribution and time modulation of external loading, input-output relations of the system being reduced were neglected. Therefore, two additional strategies were investigated from a numerical viewpoint only. In greater detail, Krylov and PCA bases were applied to the PS in the RT case; entailing approximation errors emphasized their improved performances compared to the applied M-SEREP method. Numerical and experimental validations of the proposed approaches were presented in terms of two error

measures capable of emphasizing both energy and frequency aspects involved in approximations. As a result, both the RT and the PDT techniques were successfully applied to the suggested case study. In order to comply with experimental limitations of the facility, a modified NS was considered for RTs. With regard to time integration, the LSRT2 algorithm tailored to Hamiltonian system was adopted in the experimental campaign. The relevant state-space form naturally favor the exploitation of a more general framework where numerical integration, model reduction, system identification and control techniques can more easily interact. The favorable performance of the piping system, which always remained in the linear regime without any leakage, corroborated the choice of reduction bases derived from linear time-invariant FE models. Hence, the reduction techniques involved in hybrid simulations presented in this study were justified.

CHAPTER 6

MODIFIED GENERALIZED-α BASED PARTITIONED TIME INTEGRATION ALGORITHMS FOR HYBRID SYSTEMS

6.1 Introduction

Todays state-of-the-art servo-hydraulic control systems run at sampling times Δt of the order of $1 msec$ and below. With regard to the continuous PDT method, this means that new displacement values are required at very short and deterministic time intervals for the signal generation of actuator commands. On the other hand, the numerical integration of the equation of motion can be very time consuming in the case of complex NSs. Hence, the computational driver and the control system run at different time rates (Schellenberg, 2009). In order to achieve greater computational efficiency, one must be able to solve numerical and physical subdomains, separately, with different time steps and then couple their solutions together. Therefore, parallel partitioned time integration algorithms, which allow for the concurrent solution of involved subdomains, represent a suitable approach. Since numerical models of both NSs and PSs can be profitably used for dynamic identification, model-based control and model order reduction, a unique representation of the system is preferable. As a result, the most flexible state space form is a reasonable choice. From this perspective, three partitioned time integration schemes tailored to first order systems were developed for the purpose of hybrid simulation They were based on a Modified version of the Generalized-α (MG-α) method proposed by Jansen et al. (2000). First, the monolithic MG-α algorithm was introduced for the uncoupled case. Its stability, accuracy and spectral properties were investigated from both the analytical and the numerical side. A careful

description of both the GC-MG-α and the PM-MG-α time integration procedures followed. The former, which consists of a staggered scheme, was proposed as starting procedure of the latter, which is a not self-starting parallel scheme, within the same implementation. Then, as an alternative approach, the parallel partitioned GCbis-MG-α method was introduced. Features of both strategies were analyzed on numerical case studies. Finally, experimental validations were reported and main conclusions were drawn.

6.2 The monolithic MG-α time integration algorithm

Since proposed time integration algorithms are tailored to first order systems, the following reference semi-discretized equation of motion is introduced and refers to linear mechanical systems:

$$\mathbf{M}\dot{\mathbf{y}} + \mathbf{K}\mathbf{y} = \mathbf{F}(t) \tag{6.1}$$

with,

$$\mathbf{M} = \begin{bmatrix} \mathbf{I} & \mathbf{0} \\ \mathbf{0} & \mathbf{m} \end{bmatrix} \quad \mathbf{K} = \begin{bmatrix} \mathbf{0} & -\mathbf{I} \\ \mathbf{k} & \mathbf{c} \end{bmatrix} \quad \mathbf{y} = \begin{bmatrix} \mathbf{x} \\ \dot{\mathbf{x}} \end{bmatrix} \quad \mathbf{F}(t) = \begin{bmatrix} \mathbf{0} \\ \mathbf{f}(t) \end{bmatrix} \tag{6.2}$$

In detail, **k**, **c** and **m** stand for stiffness, damping and mass matrices, respectively; **x** and $\dot{\mathbf{x}}$ are displacement and velocity state components, and $\mathbf{f}(t)$ is the external load. Eq. (6.2) can be easily generalized to the case of nonlinear restoring forces,

$$\mathbf{M}\dot{\mathbf{y}} + \mathbf{R}(\mathbf{y}) = \mathbf{F}(t) \tag{6.3}$$

with,

$$\mathbf{R}(\mathbf{y}) = \begin{bmatrix} -\dot{\mathbf{x}} \\ \mathbf{r}(\mathbf{x}, \dot{\mathbf{x}}) \end{bmatrix} \tag{6.4}$$

For the sake of simplicity, the implementations described herein refer to the linear case.

6.2.1 Time integration procedure

The Generalized-α method was developed by Chung and Hulbert (1993) for second order systems. It was extended to first order systems by Jansen et al. (2000). According to (6.1), the discretized equation of motion reads,

$$\mathbf{M}\dot{\mathbf{y}}_{n+\alpha_m} + \mathbf{K}\mathbf{y}_{n+\alpha_f} = \mathbf{F}_{n+\alpha_f} \tag{6.5}$$

where,

$$\dot{\mathbf{y}}_{n+\alpha_m} = \dot{\mathbf{y}}_n + \alpha_m \left(\dot{\mathbf{y}}_{n+1} - \dot{\mathbf{y}}_n\right) \tag{6.6}$$

$$\mathbf{y}_{n+\alpha_f} = \mathbf{y}_n + \alpha_f \left(\mathbf{y}_{n+1} - \mathbf{y}_n\right) \tag{6.7}$$

$$\mathbf{f}_{n+\alpha_f} = \mathbf{f}_n + \alpha_f \left(\mathbf{f}_{n+1} - \mathbf{f}_n\right) \tag{6.8}$$

and,

$$\mathbf{y}_{n+1} = \mathbf{y}_n + \Delta_t(1-\gamma)\dot{\mathbf{y}}_n + \Delta_t\gamma\dot{\mathbf{y}}_{n+1} \tag{6.9}$$

where Δt is the integration time step, whilst parameters α_m, α_f and γ are functions of the infinity spectral radius ρ_∞ parameter. In greater detail, they read:

$$\alpha_m = \frac{1}{2} \cdot \frac{3-\rho_\infty}{1+\rho_\infty} \tag{6.10}$$

$$\alpha_f = \frac{1}{1+\rho_\infty} \tag{6.11}$$

$$\gamma = \frac{1}{2} + \alpha_m - \alpha_f \tag{6.12}$$

The resulting multistep method is second order accurate. With regard to the linear problem, if ρ_∞ is chosen to be zero the method is said to annihilate the high frequencies; conversely if ρ_∞ is chosen to be unitary, the method is equivalent to the trapezoidal rule and high frequencies as well as the others are preserved. In order to force the balance equation at the end of the time step, the so called velocity-like state variables $\mathbf{v}_n$ entered in Eq. (6.9) in place of state derivatives,

$$\mathbf{y}_{n+1} = \mathbf{y}_n + \mathbf{v}_n\Delta t\,(1-\gamma) + \mathbf{v}_{n+1}\Delta t\gamma \tag{6.13}$$

The aforementioned velocity-like state variables were defined by the following recurrence relation (Erlicher et al., 2002; Bruls, 2008):

$$\alpha_m\mathbf{v}_{n+1} + (1-\alpha_m)\mathbf{v}_n = \alpha_f\dot{\mathbf{y}}_{n+1} + (1-\alpha_f)\dot{\mathbf{y}}_n \tag{6.14}$$

With regard to linear systems defined by Eq. (6.1), the implementation of the MG-α is reported in algorithmic form:

procedure MG-α(...)

$\tilde{\mathbf{M}} = \mathbf{M} + \mathbf{K}\gamma\Delta t\dfrac{\alpha_f}{\alpha_m}$

$\dot{\mathbf{y}}_0 = \mathbf{M}^{-}1(\mathbf{F}_0 - \mathbf{K}\mathbf{y}_0)$

$\mathbf{v}_0 = \dot{\mathbf{y}}_0$

for $n = 1 : 1 : step$ **do**

$\tilde{\mathbf{y}}_{n+1} = \mathbf{y}_n + \mathbf{v}_n\Delta t\dfrac{\alpha_m - \gamma}{\alpha_m} + \dot{\mathbf{y}}_n\gamma\Delta t\dfrac{1-\alpha_f}{\alpha_m}$

$\dot{\mathbf{y}}_{n+1} = \tilde{\mathbf{M}}^{-1}(\mathbf{F}_{n+1} - \mathbf{K}\tilde{\mathbf{y}}_{n+1})$

$\mathbf{y}_{n+1} = \tilde{\mathbf{y}}_{n+1} + \dot{\mathbf{y}}_{n+1}\gamma\Delta t\dfrac{\alpha_f}{\alpha_m}$

end for

end procedure

Finally, a suitable non iterative implementation of the MG-α method tailored to nonlinear systems defined by Eq. (6.3) is reported in algorithmic form:

procedure MG-α(...)

$\tilde{\mathbf{M}} = \mathbf{M} + \left.\dfrac{\partial\mathbf{R}}{\partial\mathbf{y}}\right|\mathbf{y}_0\gamma\Delta t\dfrac{\alpha_f}{\alpha_m}$

$\dot{\mathbf{y}}_0 = \mathbf{M}^{-}1(\mathbf{F}_0 - \mathbf{R}(\mathbf{y}_0))$

$\mathbf{v}_0 = \dot{\mathbf{y}}_0$

for $n = 1 : 1 : step$ **do**

$\tilde{\mathbf{y}}_{n+1} = \mathbf{y}_n + \mathbf{v}_n\Delta t\dfrac{\alpha_m - \gamma}{\alpha_m} + \dot{\mathbf{y}}_n\gamma\Delta t\dfrac{1-\alpha_f}{\alpha_m}$

$\dot{\mathbf{y}}_{n+1} = \tilde{\mathbf{M}}^{-1}(\mathbf{F}_{n+1} - \mathbf{R}(\tilde{\mathbf{y}}_{n+1}))$

$\mathbf{y}_{n+1} = \tilde{\mathbf{y}}_{n+1} + \dot{\mathbf{y}}_{n+1}\gamma\Delta t\dfrac{\alpha_f}{\alpha_m}$

end for

end procedure

The proposed implementation considers only one predictor-corrector stage. The tangent operator $\tilde{\mathbf{M}}$ is based on a priori estimations of tangent stiffness of all involved subsystems, regardless they are physical or numerical. This is crucial to ensure the A-stability. Since online estimations of physical tangent stiffness components can hinder the stability of the overall process, the tangent operator $\tilde{\mathbf{M}}$ is fixed.

6.2.2 Convergence analysis

The following Initial Value Problem (IVP) was considered to analyze both accuracy and stability properties of the MG-α method:

$$\omega^2 x + \ddot{x} = 0 \tag{6.15}$$

$$x(0) = 1; \tag{6.16}$$

Eq. (6.15) refers to a second order undamped oscillator characterized by a frequency equal to ω. The analytical solution of the IVP defined by (6.15) (6.16) reads,

$$x(t) = cos(wt) \tag{6.17}$$

A symbolic representation of the resulting transition matrix **A** was formulated by means of the Mathematica software,

$$\begin{bmatrix} \mathbf{y}_{n+m} \\ \mathbf{v}_{n+m} \end{bmatrix} = \begin{bmatrix} \mathbf{A}_{11} & \mathbf{A}_{12} \\ \mathbf{A}_{21} & \mathbf{A}_{22} \end{bmatrix}^m \begin{bmatrix} \mathbf{y}_n \\ \mathbf{v}_n \end{bmatrix} \tag{6.18}$$

The extended state vector of the four-by-four transition matrix **A** introduced by (6.18) collected state variables **y** and velocity like quantities **v**. Limit eigenvalues of **A** for $\Delta t \to 0$ read,

$$\lambda_1 = 1\ ,\ \lambda_2 = 1\ ,\ \lambda_3 = 3 + \frac{8}{-3+\rho_\infty}\ ,\ \lambda_4 = 3 + \frac{8}{-3+\rho_\infty} \tag{6.19}$$

Since ρ_∞ is comprised between 0 and 1, all of them fall within the unit circle. Thus, the method is said to be *zero stable*. The characteristic polynomial $p(x)$ of the transition matrix **A** is introduced to analyze the *accuracy* of the MG-α method, i.e.

$$\begin{aligned} p(x) = [(-3+\rho_\infty)^2(1+\rho_\infty)^2 + 4\Omega^2]x^4 + ... \\ -[8((-3+\rho_\infty)(-1+\rho_\infty)(1+\rho_\infty)^2 - 2\rho_\infty\Omega^2)]x^3 + ... \\ +[2((1+\rho_\infty)^2(11+\rho_\infty(-26+11\rho_\infty)) + 12\rho_\infty^2\Omega^2)]x^2 + ... \\ +[8(-1+\rho_\infty(2+\rho_\infty(4+\rho_\infty(-2-3\rho_\infty+2\Omega^2))))]x + ... \\ +[(-1+2\rho_\infty+3\rho_\infty^2)^2 + 4\rho_\infty^4\Omega^2] \end{aligned} \tag{6.20}$$

where $\Omega = \Delta t\omega$ is the dimensionless frequency of the S-DoF system. Since the matrix $\mathbf{A}$ is a solution of its characteristic polynomial $p(x)$, the following recurrence relation holds for all state variables:

$$\begin{aligned}
&[(-3+\rho_\infty)^2(1+\rho_\infty)^2+4\Omega^2]\mathbf{y}_{n+4}+\ldots\\
-&[8((-3+\rho_\infty)(-1+\rho_\infty)(1+\rho_\infty)^2-2\rho_\infty\Omega^2)]\mathbf{y}_{n+3}+\ldots\\
+&[2((1+\rho_\infty)^2(11+\rho_\infty(-26+11\rho_\infty))+12\rho_\infty^2\Omega^2)]\mathbf{y}_{n+2}+\ldots\\
+&[8(-1+\rho_\infty(2+\rho_\infty(4+\rho_\infty(-2-3\rho_\infty+2\Omega^2))))]\mathbf{y}_{n+1}+\ldots\\
+&[(-1+2\rho_\infty+3\rho_\infty^2)^2+4\rho_\infty^4\Omega^2]\mathbf{y}_n=\mathbf{0};
\end{aligned} \tag{6.21}$$

The Local Truncation Error (LTE) can be calculated as the residual of (6.21), when each state component $\mathbf{y}_{n+m}$ is replaced by the Taylor expansion of the exact analytical solution of the IVP $\mathbf{y}(t_{n+m})$. As a result,

$$\begin{aligned}
LTE = \Delta t^6\frac{2}{3}\frac{d^4y(t_n)}{dt^4}(64+\rho_\infty(81+\rho_\infty(24+\rho_\infty)))\omega^2+\\
\Delta t^5\frac{8}{3}\frac{d^3y(t_n)}{dt^3}(1+\rho_\infty)(16+\rho_\infty(11+\rho_\infty))\omega^2+\\
\Delta t^4\frac{8}{3}(1+\rho_\infty)^2(\frac{d^4y(t_n)}{dt^4}(11-(-4+\rho_\infty)\rho_\infty)+3\frac{d^2y(t_n)}{dt^2}(4+\rho_\infty)\omega^2)+\\
\Delta t^3 16(1+\rho_\infty)^3(\frac{d^3y(t_n)}{dt^3}+\frac{dy(t_n)}{dt}\omega^2)+\\
\Delta t^2 4(1+\rho_\infty)^4(\frac{d^2y(t_n)}{dt^2}+\omega^2y(t_n))
\end{aligned} \tag{6.22}$$

As can be appreciated in (6.22), coefficients of Δt^2 and Δt^3 simplify since they satisfy the IVP differential equation; see Eq. (6.15) in this respect. The resulting LTE is $O(\Delta t^3)$. As a consequence, the Global Error (GE) is $O(\Delta t^2)$. In greater detail, the GE reads,

$$e_n = |\mathbf{y}(t_n) - \mathbf{y}_n| \tag{6.23}$$

where, y_n is the approximated solution of the IVP problem obtained with the numerical integration method and $y(t_n)$ is the corresponding exact solution. Trends of GEs at $t_n = 0.5s$ versus time integration steps were estimated on the IVP defined by Eqs. (6.15) and (6.16) with $\omega = 6$. The reference solution $y(t_n)$ was approximated with the trapezoidal rule algorithm considering a $\Delta t = 1e-4s$. Then, the MG-α

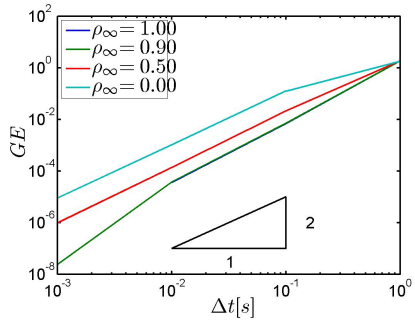

Figure 6.1: MG-α method: GE.

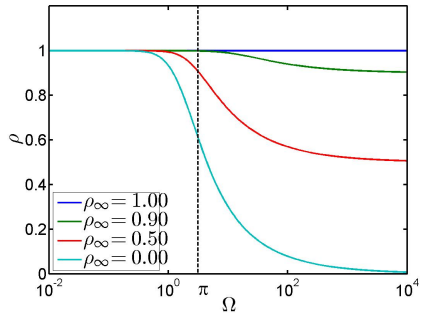

Figure 6.2: MG-α method: spectral radius.

method was applied assuming increasing time steps, i.e. Δt = $1, 1e-1, 1e-2$ and $1e-3s$. Figure 6.1 depicts GE trends with respect to time step lengths in the log-log plane. As can be appreciated in Figure 6.1, numerical simulations confirmed analytical results expressed by (6.22). Thus, the MG-α method is second order accurate regardless the value of ρ_∞ parameter. Eigenvalues of the transition matrix **A** were calculated for increasing dimensionless frequencies Ω and different ρ_∞ parameters, i.e. ρ_∞ = 0.0, 0.5, 0.9 and 1.0. Figure 6.2 reports obtained spectral radius trends. With regard to Figure 6.2, $\Omega = \pi$ corresponds to the Nyquist frequency. As can be appreciated in the same figure, spectral radii ρ tend to ρ_∞ values as far as the dimensionless frequency Ω goes to ∞; therefore, the MG-α method is L-stable when $\rho_\infty < 1.00$. Given $\lambda_{1,2}$ the eigenfrequency pair of the transition matrix **A** corresponding to physical frequencies of the system, i.e. $\pm\omega$, modal characteristics $\bar{\Omega}$ and $\bar{\xi}$ of the discretized system can be calculated according to the following

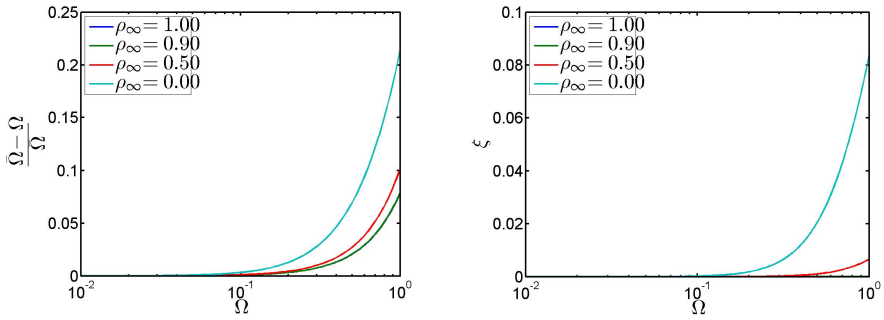

(a) (b)

Figure 6.3: MG-α method: **a** frequency error; and **b** algorithmic damping.

equation:

$$\lambda_{1,2} = C + \imath D = e^{-\bar{\Omega}(\bar{\xi} \pm \imath)} \tag{6.24}$$

where, discretized frequency $\bar{\Omega}$ and damping $\bar{\xi}$ read,

$$\bar{\Omega} = \arctan(\frac{D}{C}) \tag{6.25}$$

$$\bar{\xi} = -\frac{\ln(C^2 + D^2)}{2\bar{\Omega}} \tag{6.26}$$

Figure 6.3 shows trends of both quantities for increasing values of Ω. As can be appreciated in Figure 6.3, lower values of ρ_∞ entail greater frequency errors $(\bar{\Omega} - \Omega)/\bar{\Omega}$ and increasing algorithmic damping $\bar{\xi}$. With regard to the latter feature, the resulting user controlled algorithmic damping allows for damping out spurious higher modes typical of FE discretisation, which can hinder the stability of the integration procedure.

6.3 The partitioned staggered GC-MG-α time integration algorithm

A partitioned implementation of the MG-α is presented. The coupling scheme is derived from the GC method (Combescure, 2002), which was conceived to couple different Newmark integrators (Newmark, 1959). The resulting staggered procedure is not prone to parallel implementation and, thus, it is not valid for continuous

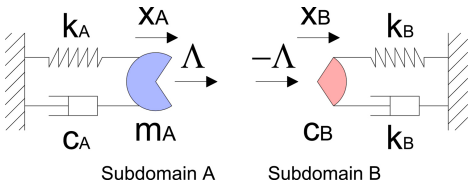

Figure 6.4: Reference split-mass S-DoF system

PDT implementations. Nonetheless it was implemented as starting procedure for the PM-MG-α method. For the sake of clarity, matrices involved in following calculations refer to the S-DoF split-mass system of Figure 6.4. According to Figure 6.4, coupled equations of motion read,

$$\mathbf{M}^A\dot{\mathbf{y}}^A + \mathbf{K}^A\mathbf{y}^A + \mathbf{L}^{A\,T}\lambda = \mathbf{F}^A(t) \tag{6.27}$$

$$\mathbf{M}^B\dot{\mathbf{y}}^B + \mathbf{K}^B\mathbf{y}^B + \mathbf{L}^{B\,T}\lambda = \mathbf{F}^B(t) \tag{6.28}$$

$$\mathbf{L}^A\mathbf{Y} + \mathbf{L}^B\mathbf{Y} = \mathbf{0} \tag{6.29}$$

where $\mathbf{L}^A$ and $\mathbf{L}^B$ are Boolean matrices that map interface forces λ over local Subdomains A and B, respectively. According to the state space formulation of Eq. (6.2) and to Figure 6.4, matrices read,

$$\mathbf{M}^A = \begin{bmatrix} 1 & 0 \\ 0 & m^A \end{bmatrix} \quad \mathbf{K}^A = \begin{bmatrix} 0 & -1 \\ k^A & c^A \end{bmatrix} \quad \mathbf{y}^A = \begin{bmatrix} x^A \\ \dot{x}^A \end{bmatrix} \quad \mathbf{F}^A(t) = \begin{bmatrix} 0 \\ f^A(t) \end{bmatrix} \quad \mathbf{L}^{A\,T} = \begin{bmatrix} 0 \\ \mathbf{I}^{A\,T} \end{bmatrix} \tag{6.30}$$

$$\mathbf{M}^B = \begin{bmatrix} 1 & 0 \\ 0 & m^B \end{bmatrix} \quad \mathbf{K}^B = \begin{bmatrix} 0 & -1 \\ k^B & c^B \end{bmatrix} \quad \mathbf{y}^B = \begin{bmatrix} x^B \\ \dot{x}^B \end{bmatrix} \quad \mathbf{F}^B(t) = \begin{bmatrix} 0 \\ f^B(t) \end{bmatrix} \quad \mathbf{L}^{B\,T} = \begin{bmatrix} 0 \\ \mathbf{I}^{B\,T} \end{bmatrix} \tag{6.31}$$

where $\mathbf{I}^{A\,T}$ and $\mathbf{I}^{B\,T}$ are equal to 1 and -1 respectively. According to the Boolean matrices $\mathbf{L}^A$ and $\mathbf{L}^B$ reported in Eqs. (6.30) and (6.31), the proposed method

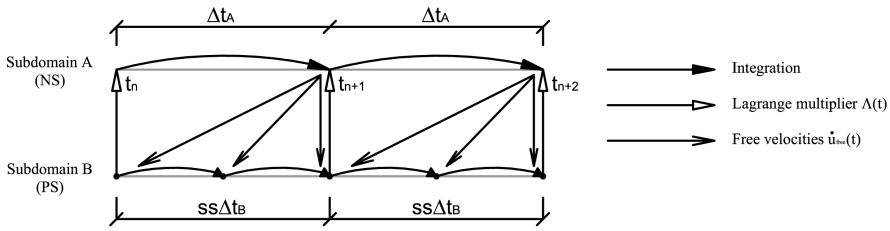

Figure 6.5: Task sequence of the GC-MG-α method.

enforces the continuity of velocities at subdomain interfaces. The task sequence of the GC method was inherited as it is. It is depicted in Figure 6.5. According to Figure 6.5, a coarse time step Δt_A was applied to Subdomain *A*, whilst the fine time Δt_B to Subdomain *B*. MG-α schemes were adopted to solve the *free problems* on each subdomain. Coupling operators were derived accordingly. With regard to hybrid simulation, Subdomain *B* always refers to the PS, where displacement commands are generated at the controller rate. Conversely, Subdomain *A* refers to the NS, which needs more computational resources and thus larger solving times.

6.3.1 Time integration procedure

The time integration procedure is summarized herein. For the sake of clarity, it refers to the S-DoF split-mass system depicted in Figure 6.4 and relevant matrices reported in both Eqs. (6.30) (6.31). In order to squeeze the notation, $\tilde{\mathbf{M}}^A$ and $\tilde{\mathbf{M}}^B$ matrices are introduced:

$$\tilde{\mathbf{M}}^A = \mathbf{M}^A + \mathbf{K}^A \gamma^A \Delta t^A \left(\frac{\alpha_f^A}{\alpha_m^A} \right) \tag{6.32}$$

$$\tilde{\mathbf{M}}^B = \mathbf{M}^B + \mathbf{K}^B \gamma^B \Delta t^B \left(\frac{\alpha_f^B}{\alpha_m^B} \right) \tag{6.33}$$

First, the *free problem* is Subdomain *A* is solved advancing from t_n to t_{n+1}.

$$\tilde{\mathbf{y}}_{n+1}^{A,free} = \mathbf{y}_n^A + \mathbf{v}_n^A \Delta t^A \left(\frac{\alpha_m^A - \gamma^A}{\alpha_m^A} \right) + \dot{\mathbf{y}}_n^A \Delta t^A \gamma^A \left(\frac{1 - \alpha_f^A}{\alpha_m^A} \right) \tag{6.34}$$

$$\dot{\mathbf{y}}_{n+1}^{A,free} = \tilde{\mathbf{M}}^{A^{-1}} \left(\mathbf{F}_{n+1}^A - \mathbf{K}^A \tilde{\mathbf{y}}_{n+1}^{A,free} \right) \tag{6.35}$$

$$\mathbf{y}_{n+1}^{A,free} = \tilde{\mathbf{y}}_{n+1}^{A,free} + \dot{\mathbf{y}}_{n+1}^{A,free} \gamma_A \Delta t_A \left(\frac{\alpha_f^A}{\alpha_m^A} \right) \tag{6.36}$$

Then, free-body solutions $\mathbf{y}_n^{A,free}$ and $\mathbf{y}_{n+1}^{A,free}$ are interpolated over the fine time step grid:

$$\mathbf{y}_{n+\frac{j}{ss}}^{A,free} = \mathbf{y}_n^{A,free} \left(1 - \frac{j}{ss} \right) + \mathbf{y}_{n+1}^{A,free} \left(\frac{j}{ss} \right) \tag{6.37}$$

$$\dot{\mathbf{y}}_{n+\frac{j}{ss}}^{A,free} = \dot{\mathbf{y}}_n^{A,free} \left(1 - \frac{j}{ss} \right) + \dot{\mathbf{y}}_{n+1}^{A,free} \left(\frac{j}{ss} \right) \tag{6.38}$$

The residual $\mathbf{s}$ of the balance equation of the Subdomain A at interpolated times is calculated; thus,

$$\mathbf{s}_{n+\frac{j}{ss}} = \mathbf{L}^A \left(\mathbf{F}^A_{n+\frac{j}{ss}} - \mathbf{M}^A \dot{\mathbf{y}}^{A,free}_{n+\frac{j}{ss}} - \mathbf{K}^A \mathbf{y}^{A,free}_{n+\frac{j}{ss}} \right) \tag{6.39}$$

Such residual is applied as interface load for the calculation of the *free problem* on Subdomain B.

$$\tilde{\mathbf{y}}_{n+\frac{j}{ss}}^{B,free} = \mathbf{y}^B_{\frac{j-1}{ss}} + \mathbf{v}^B_{\frac{j-1}{ss}} \Delta t^B \left(\frac{\alpha_m^B - \gamma^B}{\alpha_m^B} \right) + \dot{\mathbf{y}}^B_{\frac{j-1}{ss}} \gamma^B \Delta t^B \left(\frac{1 - \alpha_f^B}{\alpha_m^B} \right) \tag{6.40}$$

$$\dot{\mathbf{y}}_{n+\frac{j}{ss}}^{B,free} = \tilde{\mathbf{M}}^{B^{-1}} \left(\mathbf{F}^B_{n+\frac{j}{ss}} - \mathbf{K}^B \tilde{\mathbf{y}}^{B,free}_{n+\frac{j}{ss}} - \mathbf{L}^{B^T} \mathbf{s}_{n+\frac{j}{ss}} \right) \tag{6.41}$$

$$\mathbf{y}_{n+\frac{j}{ss}}^{B,free} = \tilde{\mathbf{y}}_{n+\frac{j}{ss}}^{B,free} + \dot{\mathbf{y}}_{n+\frac{j}{ss}}^{B,free} \gamma^B \Delta t^B \left(\frac{\alpha_f^B}{\alpha_m^B} \right) \tag{6.42}$$

Numerical simulations proved that the residual $\mathbf{s}$ evaluated by (6.39) and applied in (6.40) is crucial to preserve the second order accuracy in the case without sub-cycling, i.e. $ss = 1$. At the end of each fine time step the *link problem* is solved as follows:

$$\mathbf{\Lambda}_{n+\frac{j}{ss}} = -\mathbf{H}^{-1} \left(\mathbf{L}^A \mathbf{y}^{A,free}_{n+\frac{j}{ss}} + \mathbf{L}^B \mathbf{y}^{B,free}_{n+\frac{j}{ss}} \right) \tag{6.43}$$

where $\mathbf{H}$ is the Steklov-Poincaré operator, which reads:

$$\mathbf{H} = \gamma^A \Delta t^A \left(\frac{\alpha_f^A}{\alpha_m^A} \right) \mathbf{L}^A \tilde{\mathbf{M}}^{A^{-1}} \mathbf{L}^{A^T} + \gamma^B \Delta t^B \left(\frac{\alpha_f^B}{\alpha_m^B} \right) \mathbf{L}^B \tilde{\mathbf{M}}^{B^{-1}} \mathbf{L}^{B^T} \tag{6.44}$$

Global state and velocity-like quantities are calculated on Subdomain B,

$$\dot{\mathbf{y}}^{B,link}_{n+\frac{j}{ss}} = \tilde{\mathbf{M}}^{B^{-1}} \mathbf{L}^{B^T} \mathbf{\Lambda}_{n+\frac{j}{ss}} \tag{6.45}$$

$$\dot{\mathbf{y}}^{B}_{n+\frac{j}{ss}} = \dot{\mathbf{y}}^{B,free}_{n+\frac{j}{ss}} + \dot{\mathbf{y}}^{B,link}_{n+\frac{j}{ss}} \tag{6.46}$$

$$\mathbf{y}^{B}_{n+\frac{j}{ss}} = \mathbf{y}^{B,free}_{n+\frac{j}{ss}} + \dot{\mathbf{y}}^{B,link}_{n+\frac{j}{ss}} \gamma^B \Delta t^B \left(\frac{\alpha_f^B}{\alpha_m^B} \right) \tag{6.47}$$

$$\mathbf{v}^{B}_{n+\frac{j}{ss}} = \dot{\mathbf{y}}^{B}_{n+\frac{j}{ss}} \left(\frac{\alpha_f^B}{\alpha_m^B} \right) + \dot{\mathbf{y}}^{B}_{n+\frac{j-1}{ss}} \left(\frac{1-\alpha_f^B}{\alpha_m^B} \right) - \mathbf{v}^{B}_{n+\frac{j-1}{ss}} \left(\frac{1-\alpha_m^B}{\alpha_m^B} \right) \tag{6.48}$$

Eqs. (6.37) to (6.48) loop until the end of the subcycling, i.e. $j = ss$. Finally, the solution of the *link problem* is solved on Subdomain A and global quantities are calculated. Hence,

$$\dot{\mathbf{y}}^{A,link}_{n+1} = \tilde{\mathbf{M}}^{A^{-1}} \mathbf{L}^{A^T} \mathbf{\Lambda}_{n+1} \tag{6.49}$$

$$\dot{\mathbf{y}}^{A}_{n+1} = \dot{\mathbf{y}}^{A,free}_{n+1} + \dot{\mathbf{y}}^{A,link}_{n+1} \tag{6.50}$$

$$\mathbf{y}^{A}_{n+1} = \mathbf{y}^{A,free}_{n+1} + \dot{\mathbf{y}}^{A,link}_{n+1} \gamma^A \Delta t^A \left(\frac{\alpha_f^A}{\alpha_m^A} \right) \tag{6.51}$$

$$\mathbf{v}^{A}_{n+1} = \dot{\mathbf{y}}^{A}_{n+1} \left(\frac{\alpha_f^A}{\alpha_m^A} \right) + \dot{\mathbf{y}}^{A}_{n} \left(\frac{1-\alpha_f^A}{\alpha_m^A} \right) - \mathbf{v}^{A}_{n} \left(\frac{1-\alpha_m^A}{\alpha_m^A} \right) \tag{6.52}$$

The proposed algorithm is not prone to parallel implementations. In fact, in order to solve Eqs. (6.62) to (6.73), which loop on Subdomain B from t_n to t_{n+1}, the *free problem* solution of Subdomain A at t_{n+1} is needed. Nonetheless, the proposed GC-MG-α method is a suitable initialization procedure for the parallel PM-MG-α time integration algorithm, which is presented in the next section. In fact, the GC-MG-α method is self starting. Velocity like quantities, initial state and its derivative

can be expressed as combination of initial displacements, velocities and accelerations, i.e. $\mathbf{x}_0$, $\dot{\mathbf{x}}_0$ and $\ddot{\mathbf{x}}_0$, respectively:

$$\ddot{\mathbf{x}}_0 = \mathbf{m}^{-1}(\mathbf{f}_0 - \mathbf{k}\mathbf{x}_0 - \mathbf{c}\dot{\mathbf{x}}_0) \tag{6.53}$$

$$\mathbf{y}_0 = \begin{bmatrix} \mathbf{x}_0 \\ \dot{\mathbf{x}}_0 \end{bmatrix} \tag{6.54}$$

$$\mathbf{v}_0 = \dot{\mathbf{y}}_0 = \begin{bmatrix} \dot{\mathbf{x}}_0 \\ \ddot{\mathbf{x}}_0 \end{bmatrix} \tag{6.55}$$

Such approximation does not affect accuracy and stability characteristics of original coupling schemes.

6.3.2 Accuracy analysis

The order of accuracy of the GC-MG-α method was estimated by means of numerical simulations on the split-mass S-DoF system of Figure 6.4. Linear parameters of both subdomains reads,

$$k^A = 0.53\ ,\ c^A = 0\ ,\ m^A = 0.47\ ,\ k^B = 0.47\ ,\ c^B = 0\ ,\ m^B = 0.53 \tag{6.56}$$

No external loads were considered and a unit displacement was assumed as initial condition. The trapezoidal rule solution calculated with a $\Delta t = 1e-4s$ time step was considered as reference. The GE was evaluated according to Eq. (6.23) at $t_n = 0.5s$ for decreasing time step values, i.e. $\Delta t_A = 1e-2, 1e-3, 1e-4$ and $1e-5s$. Figure 6.6 depicts obtained trends for different values of ρ_∞ parameters with and without subcycling. According to trends depicted in Figure 6.6, the GC-MG-α method is second order accurate in the case without subcycling and first order accurate in the case with subcycling. Therefore, original accuracy characteristics of the GC method are preserved.

6.4 The partitioned parallel PM-MG-α time integration algorithm

A partitioned time integration scheme based on the MG-α is presented. The coupling scheme is derived from the PM method (Pegon and Magonette, 2002;

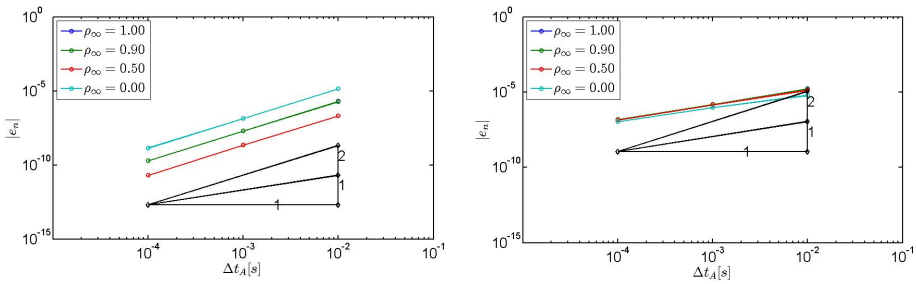

(a) (b)

Figure 6.6: GC-MG-α: GE trends with **a** *ss* = 1 and **b** *ss* = 10, i.e. without and with subcycling, respectively.

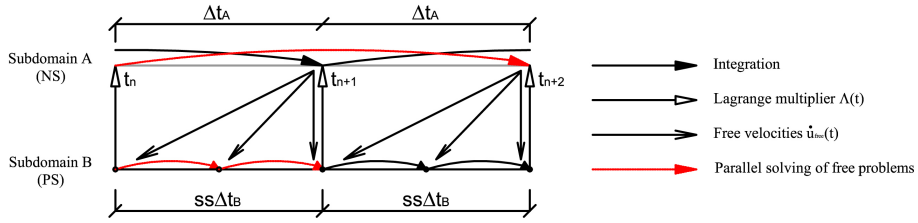

Figure 6.7: Task sequence of the PM-MG-α method.

Bonelli et al., 2008), which was conceived for Newmark integrators (Newmark, 1959) and then extended to Generalized-α schemes by Bursi (2010). As a consequence, it is prone to parallel implementations, where free solutions on both subdomains advance simultaneously. Matrices involved in following calculations are the same reported for the GC-MG-α method and refer to the same S-DoF split-mass system of Figure 6.4. According to Boolean matrices reported in Eqs. (6.35) and (6.36), the proposed method enforces the continuity of interface velocities. The task sequence of the PM-method was completely inherited. It is depicted in Figure 6.7. A coarse time step Δt_A was applied to Subdomain *A*, whilst the fine time step Δt_B to Subdomain *B*. MG-α schemes were adopted to solve the *free problems* on each subdomain. Coupling operators were derived accordingly. With regard to hybrid simulation, Subdomain *B* always refers to the PS, where displacement commands are generated at the controller rate. Conversely, Subdomain *A* refers to the NS, which needs more computational resources and thus larger solving times.

6.4.1 Time integration procedure

The time integration procedure is summarized herein. For the sake of clarity, it refers to the S-DoF split-mass system depicted in Figure 6.4 and relevant matrices reported in Eqs. (6.35) (6.36). In order to squeeze the notation, $\tilde{\mathbf{M}}^A$ and $\tilde{\mathbf{M}}^B$ matrices are introduced:

$$\tilde{\mathbf{M}}^A = \mathbf{M}^A + \mathbf{K}^A \gamma^A 2\Delta t^A \left(\frac{\alpha_f^A}{\alpha_m^A} \right) \tag{6.57}$$

$$\tilde{\mathbf{M}}^B = \mathbf{M}^B + \mathbf{K}^B \gamma^B \Delta t^B \left(\frac{\alpha_f^B}{\alpha_m^B} \right) \tag{6.58}$$

First, the *free problem* is Subdomain A is solved advancing from t_n to t_{n+1}.

$$\tilde{\mathbf{y}}_{n+2}^{A,free} = \mathbf{y}_n^A + \mathbf{v}_n^A 2\Delta t^A \left(\frac{\alpha_m^A - \gamma^A}{\alpha_m^A} \right) + \dot{\mathbf{y}}_n^A 2\Delta t^A \gamma^A \left(\frac{1 - \alpha_f^A}{\alpha_m^A} \right) \tag{6.59}$$

$$\dot{\mathbf{y}}_{n+2}^{A,free} = \tilde{\mathbf{M}}^{A^{-1}} \left(\mathbf{F}_{n+2}^A - \mathbf{K}^A \tilde{\mathbf{y}}_{n+2}^{A,free} \right) \tag{6.60}$$

$$\mathbf{y}_{n+2}^{A,free} = \tilde{\mathbf{y}}_{n+2}^{A,free} + \dot{\mathbf{y}}_{n+2}^{A,free} \gamma_A 2\Delta t_A \left(\frac{\alpha_f^A}{\alpha_m^A} \right) \tag{6.61}$$

According to (6.59) (6.60) and (6.61), a time step equal to $2\Delta t_A$ is exploited in Subdomain A in order to anticipate information on the Subdomain B at the beginning of a new time step. At the same time, available free-body solutions $\mathbf{y}_n^{A,free}$ and $\mathbf{y}_{n+1}^{A,free}$ are interpolated over the fine time step grid:

$$\mathbf{y}_{n+\frac{j}{ss}}^{A,free} = \mathbf{y}_n^{A,free} \left(1 - \frac{j}{ss} \right) + \mathbf{y}_{n+1}^{A,free} \left(\frac{j}{ss} \right) \tag{6.62}$$

$$\dot{\mathbf{y}}_{n+\frac{j}{ss}}^{A,free} = \dot{\mathbf{y}}_n^{A,free} \left(1 - \frac{j}{ss} \right) + \dot{\mathbf{y}}_{n+1}^{A,free} \left(\frac{j}{ss} \right) \tag{6.63}$$

Then, the residual $\mathbf{s}$ on the balance equation of Subdomain A is calculated at interpolated times.

$$\mathbf{s}_{n+\frac{j}{ss}} = \mathbf{L}^A \left(\mathbf{F}_{n+\frac{j}{ss}}^A - \mathbf{M}^A \dot{\mathbf{y}}_{n+\frac{j}{ss}}^{A,free} - \mathbf{K}^A \mathbf{y}_{n+\frac{j}{ss}}^{A,free} \right) \tag{6.64}$$

Such residual is applied as interface load for the solution of the *free problem* on Subdomain B.

$$\tilde{\mathbf{y}}^{B,free}_{n+\frac{j}{ss}} = \mathbf{y}^{B}_{\frac{j-1}{ss}} + \mathbf{v}^{B}_{\frac{j-1}{ss}} \Delta t^{B} \left(\frac{\alpha_m^B - \gamma^B}{\alpha_m^B} \right) + \dot{\mathbf{y}}^{B}_{\frac{j-1}{ss}} \gamma^B \Delta t^B \left(\frac{1-\alpha_f^B}{\alpha_m^B} \right) \tag{6.65}$$

$$\dot{\mathbf{y}}^{B,free}_{n+\frac{j}{ss}} = \tilde{\mathbf{M}}^{B^{-1}} \left(\mathbf{F}^{B}_{n+\frac{j}{ss}} - \mathbf{K}^{B} \tilde{\mathbf{y}}^{B,free}_{n+\frac{j}{ss}} - \mathbf{L}^{B^T} \mathbf{s}_{n+\frac{j}{ss}} \right) \tag{6.66}$$

$$\mathbf{y}^{B,free}_{n+\frac{j}{ss}} = \tilde{\mathbf{y}}^{B,free}_{n+\frac{j}{ss}} + \dot{\mathbf{y}}^{B,free}_{n+\frac{j}{ss}} \gamma^B \Delta t^B \left(\frac{\alpha_f^B}{\alpha_m^B} \right) \tag{6.67}$$

Numerical simulations proved that the residual $\mathbf{s}$ evaluated by Eq. (6.64) and applied in Eq. (6.65) is crucial to preserve the second order of accuracy in the case without subcycling, i.e. $ss = 1$. At the end of each fine time step the *link problem* is solved as follows:

$$\mathbf{\Lambda}_{n+\frac{j}{ss}} = -\mathbf{H}^{-1} \left(\mathbf{L}^{A} \mathbf{y}^{A,free}_{n+\frac{j}{ss}} + \mathbf{L}^{B} \mathbf{y}^{B,free}_{n+\frac{j}{ss}} \right) \tag{6.68}$$

where $\mathbf{H}$ is the Steklov-Poincaré operator, which reads:

$$\mathbf{H} = \gamma^A 2 \Delta t^A \left(\frac{\alpha_f^A}{\alpha_m^A} \right) \mathbf{L}^{A} \tilde{\mathbf{M}}^{A^{-1}} \mathbf{L}^{A^T} + \gamma^B \Delta t^B \left(\frac{\alpha_f^B}{\alpha_m^B} \right) \mathbf{L}^{B} \tilde{\mathbf{M}}^{B^{-1}} \mathbf{L}^{B^T} \tag{6.69}$$

Therefore, the *link problem* is solved on Subdomain B, and total state and velocity like quantities are calculated,

$$\dot{\mathbf{y}}^{B,link}_{n+\frac{j}{ss}} = \tilde{\mathbf{M}}^{B^{-1}} \mathbf{L}^{B^T} \mathbf{\Lambda}_{n+\frac{j}{ss}} \tag{6.70}$$

$$\dot{\mathbf{y}}^{B}_{n+\frac{j}{ss}} = \dot{\mathbf{y}}^{B,free}_{n+\frac{j}{ss}} + \dot{\mathbf{y}}^{B,link}_{n+\frac{j}{ss}} \tag{6.71}$$

$$\mathbf{y}^{B}_{n+\frac{j}{ss}} = \mathbf{y}^{B,free}_{n+\frac{j}{ss}} + \dot{\mathbf{y}}^{B,link}_{n+\frac{j}{ss}} \gamma^B \Delta t^B \left(\frac{\alpha_f^B}{\alpha_m^B} \right) \tag{6.72}$$

$$\mathbf{v}^{B}_{n+\frac{j}{ss}} = \dot{\mathbf{y}}^{B}_{n+\frac{j}{ss}} \left(\frac{\alpha_f^B}{\alpha_m^B} \right) + \dot{\mathbf{y}}^{B}_{n+\frac{j-1}{ss}} \left(\frac{1-\alpha_f^B}{\alpha_m^B} \right) - \mathbf{v}^{B}_{n+\frac{j-1}{ss}} \left(\frac{1-\alpha_m^B}{\alpha_m^B} \right) \tag{6.73}$$

Eqs. (6.62) to (6.73) loop until the end of subcycling, i.e. $j = ss$. Then, the solution of the *link problem* on Subdomain A is calculated.

$$\dot{\mathbf{y}}_{n+1}^{A,link} = \tilde{\mathbf{M}}^{A^{-1}} \mathbf{L}^{A^T} \mathbf{\Lambda}_{n+1} \tag{6.74}$$

$$\dot{\mathbf{y}}_{n+1}^{A} = \dot{\mathbf{y}}_{n+1}^{A,free} + \dot{\mathbf{y}}_{n+1}^{A,link} \tag{6.75}$$

$$\mathbf{y}_{n+1}^{A} = \mathbf{y}_{n+1}^{A,free} + \dot{\mathbf{y}}_{n+1}^{A,link} \gamma^A 2\Delta t^A \left(\frac{\alpha_f^A}{\alpha_m^A} \right) \tag{6.76}$$

$$\mathbf{v}_{n+1}^{A} = \dot{\mathbf{y}}_{n+1}^{A} \left(\frac{\alpha_f^A}{\alpha_m^A} \right) + \dot{\mathbf{y}}_{n-1}^{A} \left(\frac{1-\alpha_f^A}{\alpha_m^A} \right) - \mathbf{v}_{n-1}^{A} \left(\frac{1-\alpha_m^A}{\alpha_m^A} \right) \tag{6.77}$$

The proposed algorithm is prone to parallel implementations. In fact, Eqs. (6.62) to (6.73) loop over j from 1 to ss on Subdomain B while the *free problem* solution advance of from t_n to t_{n+2} on Subdmain A. Since the *free problem* solution on Subdomain A at t_1 is needed to advance from t_0 to t_1 on Subdomain B, the PM-MG-α method is not self starting. As a consequence, the GC-MG-α method was implemented as starting procedure. In greater detail, it provide the first three steps solution on both subdomains. It is evident that the proposed PM-MG-α method nicely suites the requirements of hybrid simulation. The PM-MG-α method entails interface energy dissipation owing to PM coupling scheme. Nonetheless, it generates smooth actuator commands since the *link problem* is solved at each fine time step.

6.4.2 Accuracy analysis

The order of accuracy of the GC-MG-α method was estimated by means of numerical simulations on the split-mass S-DoF system of Figure 6.4. Linear parameters of both subdomains reads,

$$k^A = 0.53 \ , \ c^A = 0 \ , \ m^A = 0.47 \ , \ k^B = 0.47 \ , \ c^B = 0 \ , \ m^B = 0.53 \tag{6.78}$$

No external loads were considered and a unit displacement was assumed as initial condition. The trapezoidal rule solution calculated with a $\Delta t = 1e-4s$ time step

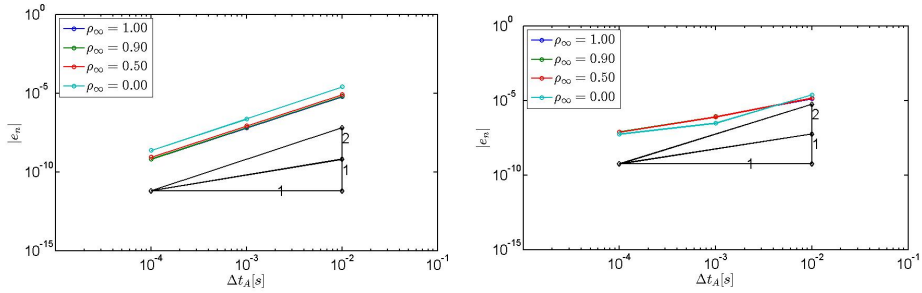

Figure 6.8: PM-MG-α: GE trends with **a** *ss* = 1 and **b** *ss* = 10, i.e. without and with subcycling, respectively.

was considered as reference. The GE was evaluated according to Eq. (6.23) at t_n = 0.5*s* for decreasing time step values, i.e. $\Delta t = 1e-2, 1e-3, 1e-4$ and $1e-5s$. Figure 6.8 depicts obtained trends for different values of ρ_∞ parameters with and without subcycling. According to trends depicted in Figure 6.8 the initialization procedure do not affect the order of accuracy of the proposed method. In fact, accuracy properties of the PM method are preserved.

6.5 The partitioned parallel GCbis-MG-α time integration algorithm

An alternative parallel partitioned time integration scheme based on the MG-α was developed. The coupling scheme of the GCbis method proposed by Mahjoubi (2010) was adopted, which was conceived for Newmark integrators (Newmark, 1959). As a consequence, it is prone to parallel implementations, where *free problems* advance simultaneously on both subdomains. For the sake of simplicity, the following equations refer to the same S-DoF split-mass system of Figure 6.4. According to Boolean matrices reported in (6.35) and (6.36), the proposed method enforces the continuity of interface velocities. The task sequence of the GCbis-method was completely inherited and is depicted in Figure 6.9. A coarse time step Δt_A was applied to Subdomain *A*, whilst a fine time Δt_B to Subdomain *B*. MG-α schemes were adopted to solve the *free problems* on each subdomain. Coupling operators were derived accordingly. Since the *link problem* is solved at coarse time steps, interpolated *free quantities* of Subdomain *A* are not needed to ad-

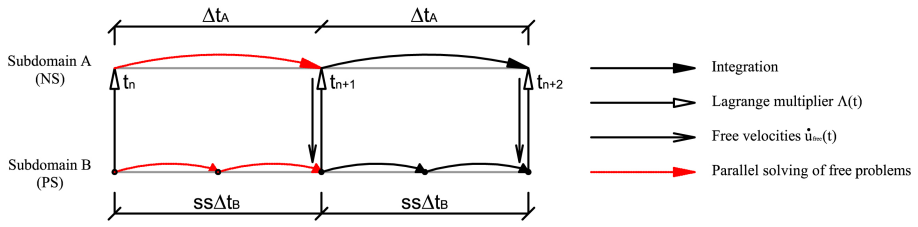

Figure 6.9: Task sequence of the GCbis-MG-α method

vance in the solution on Subdomain *B*. With regard to hybrid simulation, Subdomain *B* always refers to the PS, where displacement commands are generated at the controller rate. Conversely, Subdomain *A* refers to the NS, which needs more computational resources and thus larger solving times.

6.5.1 Time integration procedure

To pave the way of the algorithmic implementation of the GCbis-MG-α method, the following compact notation is introduced.

$$\mathbb{M}\mathbb{Y}_{n+1} = \mathbb{F}_{n+1} - \mathbb{N}\mathbb{Y}_n \tag{6.79}$$

where:

$$\mathbb{M} = \begin{bmatrix} \mathbf{K} & \mathbf{M} & \mathbf{0} \\ \mathbf{I} & -\mathbf{I}\gamma\Delta t\left(\frac{\alpha_f}{\alpha_m}\right) & \mathbf{0} \\ \mathbf{0} & -\mathbf{I}\alpha_f & \mathbf{I}\alpha_m \end{bmatrix} \mathbb{N} = \begin{bmatrix} \mathbf{0} & \mathbf{0} & \mathbf{0} \\ \mathbf{I} & -\mathbf{I}\gamma\Delta t\left(\frac{1-\alpha_f}{\alpha_m}\right) & -\mathbf{I}\Delta t\left(\frac{\alpha_m-\gamma}{\alpha_m}\right) \\ \mathbf{0} & \mathbf{I}(\alpha_f-1) & \mathbf{I}(1-\alpha_m) \end{bmatrix} \tag{6.80}$$

$$\mathbb{Y}_n = \begin{bmatrix} \mathbf{y}_n \\ \dot{\mathbf{y}}_n \\ \mathbf{v}_n \end{bmatrix} \mathbb{F}_{n+1} = \begin{bmatrix} \mathbf{F}_{n+1} \\ \mathbf{0} \\ \mathbf{0} \end{bmatrix} \tag{6.81}$$

Accordingly, discretized coupled equations of motion read,

$$\mathbb{M}^A\mathbb{Y}^A_{ss} + \mathbb{L}^A\mathbf{\Lambda}_{ss} = \mathbb{F}^A_{ss} - \mathbb{N}^A\mathbb{Y}^A_0 \tag{6.82}$$

$$\mathbb{M}^B\mathbb{Y}^B_j + \mathbb{L}^B\mathbf{\Lambda}_j = \mathbb{F}^B_j - \mathbb{N}^B\mathbb{Y}^B_{j-1} \tag{6.83}$$

$$\mathbb{B}^A \mathbb{Y}^A_{ss} + \mathbb{B}^B \mathbb{Y}^B_{ss} = \mathbf{0} \tag{6.84}$$

where $j \in [1, 2, ..., ss]$, whilst matrices $\mathbb{L}^{(\bullet)}$ and $\mathbb{B}^{(\bullet)}$ recall the notation of the GCbis method (Mahjoubi, 2010):

$$\mathbb{L}^{(\bullet)} = \mathbb{B}^{(\bullet)^T} = \begin{bmatrix} \mathbf{L}^{(\bullet)^T} \\ \mathbf{0} \\ \mathbf{0} \end{bmatrix} \tag{6.85}$$

Balance and coupling equations can be rearranged in matrix form as,

$$\begin{bmatrix} \mathbb{M}^B & & & & & \left(\frac{1}{ss}\right)\mathbb{L}^B \\ \mathbb{N}^B & \mathbb{M}_B & & & & \left(\frac{2}{ss}\right)\mathbb{L}^B \\ & \ddots & \ddots & & & \vdots \\ & & \mathbb{N}^B & \mathbb{M}_B & & \mathbb{L}^B \\ & & & & \mathbb{M}^A & \mathbb{L}^A \\ & & & \mathbb{B}^B & \mathbb{B}^A & \mathbf{0} \end{bmatrix} \begin{bmatrix} \mathbb{Y}^B_1 \\ \mathbb{Y}^B_2 \\ \vdots \\ \mathbb{Y}^B_{ss} \\ \mathbb{Y}^A_{ss} \\ \mathbf{\Lambda}_{ss} \end{bmatrix} = \begin{bmatrix} \mathbb{F}^B_1 - \mathbb{N}^B \mathbb{Y}^B_0 - \left(1 - \frac{1}{ss}\right)\mathbb{L}^B \mathbf{\Lambda}_0 \\ \mathbb{F}^B_2 - \left(1 - \frac{2}{ss}\right)\mathbb{L}^B \mathbf{\Lambda}_0 \\ \vdots \\ \mathbb{F}^B_{ss} \\ \mathbb{F}^A_{ss} - \mathbb{N}^A \mathbb{Y}^A_0 \\ \mathbf{0} \end{bmatrix} \tag{6.86}$$

Eq (6.86) can be solved using a bordered system approach. Subdomain matrix blocks can be clubbed together and the system expressed as:

$$\begin{bmatrix} \mathrm{M} & \mathrm{L} \\ \mathrm{B} & 0 \end{bmatrix} \begin{bmatrix} \mathrm{Y} \\ \Lambda_{ss} \end{bmatrix} = \begin{bmatrix} \mathrm{F} \\ 0 \end{bmatrix} \tag{6.87}$$

Since the global solution is the sum of *free* and *link* quantities,

$$\mathrm{Y} = \mathrm{Y}^{free} + \mathrm{Y}^{link} \tag{6.88}$$

where:

$$\mathrm{Y}^{free} = \mathrm{M}^{-1}\mathrm{F} \tag{6.89}$$

$$\mathrm{Y}^{link} = \mathrm{M}^{-1}\mathrm{L}\Lambda_{ss} \tag{6.90}$$

the second row of Eq. (6.87) can be split as follows:

$$\mathrm{BY}^{free} + \mathrm{BY}^{link} = 0 \tag{6.91}$$

Accordingly, Lagrange multipliers Λ_{ss}, can be easily expressed through the Steklov-Poincaré operator H, which is the dual Shur complement of the block matrix of Eq. (6.87). In greater detail,

$$\mathrm{H}\Lambda_{ss} = \mathrm{BY}^{free} \tag{6.92}$$

$$\mathrm{H} = -\mathrm{BM}^{-1}\mathrm{L} \tag{6.93}$$

Since *free problems* are solved concurrently, the proposed algorithm is prone to parallel implementation, and thus, it complies with hybrid simulation requirements. The size of the Steklov-Poincaré operator H of the GCbis-MG-α is proportional to the number of substeps. Nonetheless, it is computed once at the beginning of the procedure. Moreover, the algorithm is self starting. As result, initial velocity like quantities, state vector and its derivative can be estimated according to the GC method, see Eqs. (6.53), (6.54) and (6.55) in this respect. Initial Lagrange multipliers λ_0 must be provided as well and can be estimated as follows:

$$\lambda_0 = \mathbf{l}^A(\mathbf{f}_0^A - \mathbf{k}^A\mathbf{x}_0^A - \mathbf{c}^A\dot{\mathbf{x}}_0^A - \mathbf{m}^A\ddot{\mathbf{x}}_0^A) \tag{6.94}$$

According to the GCbis method, the GCbis-MG-α method does not entail interface energy dissipation. Nonetheless, particular care must be devoted to the subcycling setting in order to avoid discontinuous actuator commands. Since the *link problem* is solved at coarse time steps excessive jumps can hinder the PDT.

6.5.2 Accuracy analysis

The order of accuracy of the GCbis-MG-α method was estimated by means of numerical simulations on the split-mass S-DoF system of Figure 6.4. Linear parameters of both subdomains read,

$$k^A = 0.53\ ,\ c^A = 0\ ,\ m^A = 0.47\ ,\ k^B = 0.47\ ,\ c^B = 0\ ,\ m^B = 0.53 \tag{6.95}$$

No external loads were considered and a unit displacement was assumed as initial condition. The trapezoidal rule solution calculated with a $\Delta t = 1e-4s$ time step

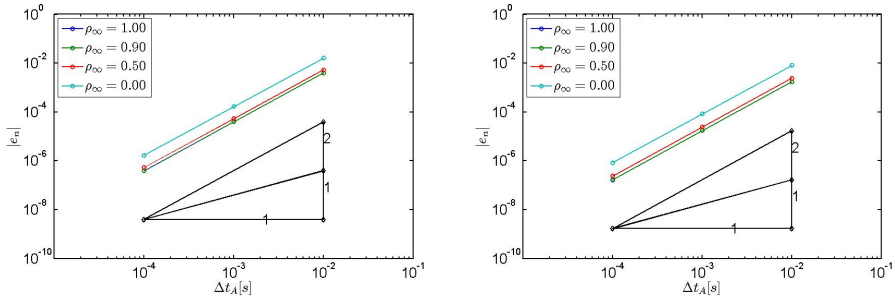

(a) (b)

Figure 6.10: GCbis-MG-α: GE trends with **a** *ss* = 1 and **b** *ss* = 10, i.e. without and with subcycling, respectively.

was considered as reference. The GTE was evaluated according to Eq. (6.23) at t_n = 0.5*s*. It was estimated for decreasing time step values, i.e. $\Delta t = 1e-2, 1e-3, 1e-4$ and $1e-5s$. Figure 6.10 depicts obtained trends for different values of ρ_∞ parameters with and without subcycling. Accordingly, the GCbis-MG-α method is second order accurate regardless the subcycling setting.

6.6 Numerical validations of proposed MG-α based partitioned time integration algorithms

In order to validate proposed partitioned time integration schemes, two benchmark case studies were analyzed. In greater detail, a 30-DoFs 2D plane structure was considered to check implementations and compare accuracy performance in terms of GEs. Then, a 3-DoFs split-mass stiff system was conceived to validate the favorable user controlled algorithmic damping feature.

6.6.1 30-DoFs benchmark 2D plane system

In order to validate implementations of all proposed partitioned time integration schemes, a parametric benchmark system of the type depicted in Figure 6.11 was developed in the Matlab environment. Given the number of strips and the Partitioning Layout (PL), the developed algorithm provides matrices of both global and partitioned systems. All plane elements were characterized by same characteristics. In particular, a single 0.001*m* thick 0.2*m* side *PLANE182* square element

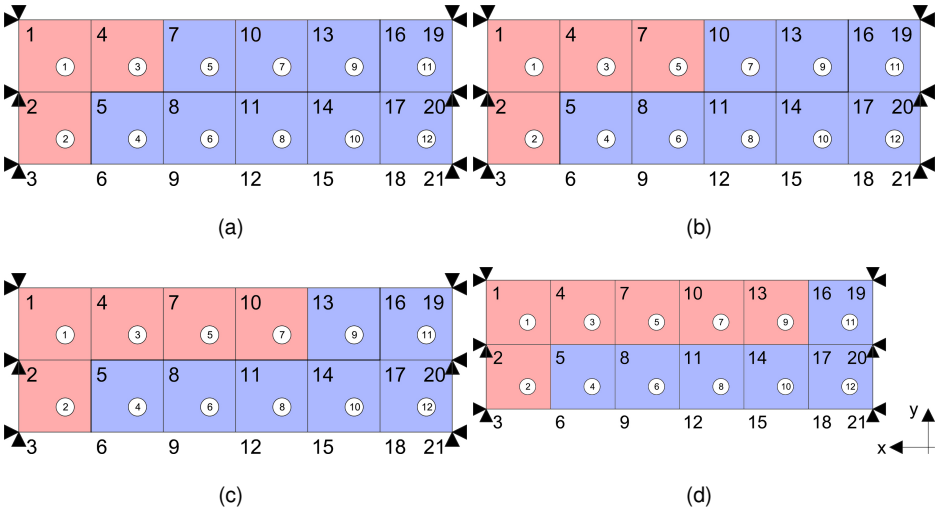

Figure 6.11: 30-DoFs 2D plane structure with PL: **a** #1; **b** #2; **c** #3 and; **d** #4.

was imported from ANSYS and considered as reference block. A Young modulus $E = 2e9GPa$, a density $\rho_d = 5000kg/m^3$ and a Poisson ratio $\nu = 0.3$ were assumed. Figure 6.11 depicts the obtained 30-DoFs benchmark 2D plane system with different PLs. As can be appreciated in Figure 6.11, the 2D plane structure was characterized by six vertical strips of two elements each one. Rotational DoFs were neglected. PLs entailed an increasing number of interface DoFs. Table 6.1 summarized modal characteristics of the 2D plane structure. According to the maximum eigenfrequency of the system that is reported in Table 6.1, a $\Delta t_A = 1e-5s$ was assumed as coarse time step. External loads were neglected and a unit displacement was applied along the x direction at Node #4 as initial condition. The reference solution was obtained applying the trapezoidal rule with a time step $\Delta_t = 1e-6s$. Since the proposed benchmark case study was aimed at validating matrix assembling procedures and energy preserving features, a $\rho_\infty = 1.00$ was assumed for all simulations. Algorithmic performances were compared in terms of GEs on displacement responses at Node #5 along the x direction at $t_n = 0.01s$. Table 6.1 summarized obtained results. As can be appreciated in Table 6.2, with regard to the case without subcycling, i.e. $ss = 1$, the GCbis-MG-α and the GC-MG-α methods entailed same GEs. Moreover, such errors were not sensitive to the PL.

Mode	Frequency [Hz]	Mode	Frequency [Hz]	Mode	Frequency [Hz]
1	129	11	971	21	1469
2	269	12	971	22	1661
3	282	13	988	23	1717
4	481	14	1074	24	1729
5	555	15	1117	25	1836
6	615	16	1163	26	1866
7	730	17	1234	27	1918
8	811	18	1300	28	1986
9	845	19	1356	29	2000
10	917	20	1394	30	2079

Table 6.1: Modal frequencies of the benchmark plane system.

		GE [m]		
Subcycling	PL	GCbis-MG-α	GC-MG-α	PM-MG-α
1	#4	0.0012278	0.0012278	0.00017134
1	#3	0.0012278	0.0012278	0.00066305
1	#2	0.0012278	0.0012278	0.00055381
1	#1	0.0012278	0.0012278	0.00038507
10	#4	0.0012571	0.0154940	0.0095934
10	#3	0.0011780	0.0124330	0.0097588
10	#2	0.0012169	0.0085877	0.0079391
10	#1	0.0008354	0.0089781	0.0064601

Table 6.2: GEs of displacement responses at Node #5 along the x direction calculated at $t_n = 0.01s$.

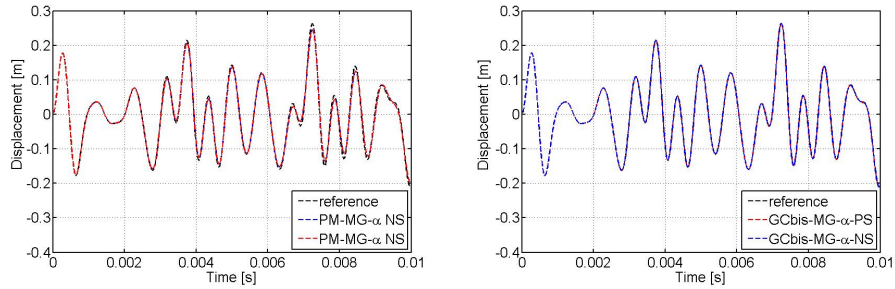

(a) (b)

Figure 6.12: Displacement responses at Node #4 in *x* direction calculated with the **a** PM-MG-α and the **b** GCbis-MG-α method

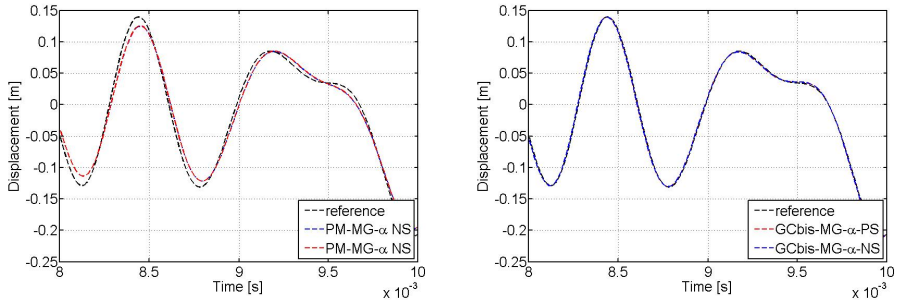

(a) (b)

Figure 6.13: Zoom on displacement responses at Node #4 in *x* direction calculated with the: **a** PM-MG-α and; the **b** GCbis-MG-α method.

Since it preserves the second order accuracy, the GCbis-MG-α is the more performing in the case with subcycling. According to PLs depicted in Figure 6.11, all proposed methods showed increasing GEs with respect to the number of interface DoFs. Figure 6.12 depicts displacement responses obtained with the GCbis-MG-α and the PM-MG-α methods with *ss* = 5. Both algorithms well reproduced reference solutions. As can be appreciated in Figure 6.13, which depict zooms on last 0.002s of same time histories, reduced peaks were observed when the PM-MG-α method was applied. In fact, dissipated energy at the interface occurred when the PM-G-α method was applied.

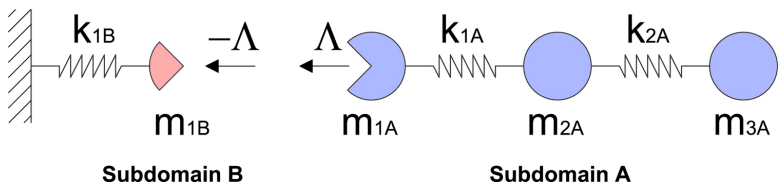

Figure 6.14: Benchmark split-mass 3-DoFs stiff system.

6.6.2 3-DoFs benchmark chain-like stiff system

In order to emphasize the favorable user-controlled algorithmic damping features of the proposed methods, numerical simulations on a 3-DoFs chain-like stiff system depicted in Figure 6.14 were carried out. Matrices of both subdomains read:

$$\mathbf{k}^A = \begin{bmatrix} k_2 & -k_2 & 0 \\ -k_2 & k_2+k_3 & -k_3 \\ 0 & -k_3 & k_3 \end{bmatrix} \quad \mathbf{m}^A = \begin{bmatrix} m_1/2 & 0 & 0 \\ 0 & m_2 & 0 \\ 0 & 0 & m_3 \end{bmatrix} \quad \mathbf{f}^A = \begin{bmatrix} m_1/2 \\ m_2 \\ m_3 \end{bmatrix} \quad \mathbf{l}^{A\,T} = \begin{bmatrix} 1 \\ 0 \\ 0 \end{bmatrix} \tag{6.96}$$

$$\mathbf{m}^B = \begin{bmatrix} m_1/2 \end{bmatrix} \quad \mathbf{k}^B = \begin{bmatrix} k_1 \end{bmatrix} \quad \mathbf{f}^B = \begin{bmatrix} m_1/2 \end{bmatrix} \quad \mathbf{l}^{A\,T} = \begin{bmatrix} -1 \end{bmatrix} \tag{6.97}$$

where the following masses $m_1 = 1944$, $m_2 = 828$ and $m_3 = 20kg$ and stiffnesses $k_1 = k2 = k_3 = 1e6N/m$, were considered. The resulting 3-DoFs chain-like system was characterized by eigenfrequencies at 2.85, 6.91 and 36.02Hz. Since the present benchmark test focused on user-controlled damping features, a time step $\Delta t_A = 0.01s$ was selected. Accordingly, the higher frequency at 36.02Hz was close to the resulting Nyquist frequency of 50Hz. Moreover, no subcycling was applied. Simulations were performed assuming $\rho_\infty = 1.00$ and $\rho_\infty = 0.00$. In order to excite the stiff mode, free decay responses were simulated applying a unitary initial displacement at DoF #3. Figure 6.15 depicts displacement responses obtained with the GC-bis-MG-α method. As can be appreciated in Figure 6.15, the stiff mode at 36.02Hz was preserved in the case of $\rho_\infty = 1.00$. Conversely, the same mode was quickly damped out with ρ_∞ set to zero. All presented partitioned schemes produced consistent results.

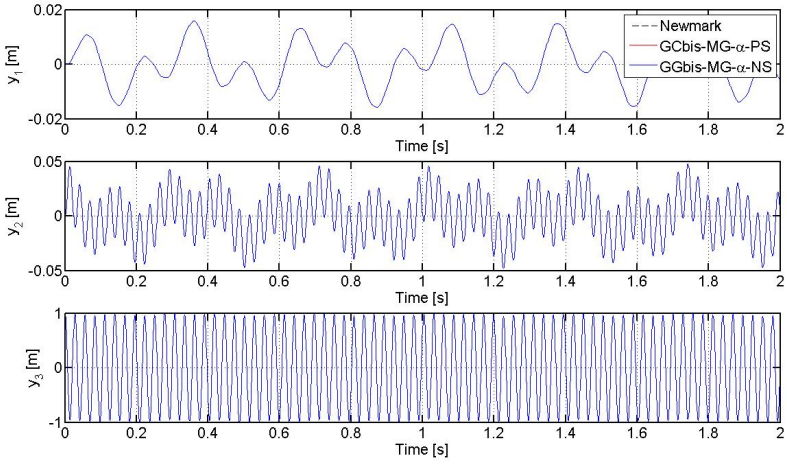

(a)

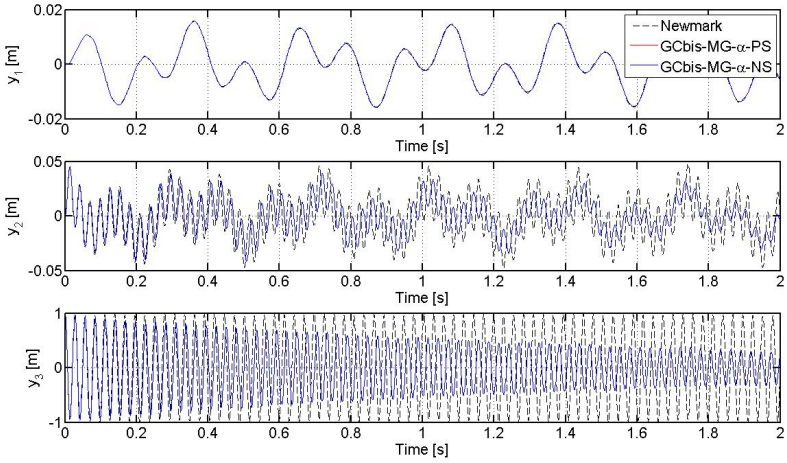

(b)

Figure 6.15: Displacement responses calculated with the GCbis-MG-α method with: **a** ρ_∞ = 1.0; and **b** ρ_∞ = 0.0.

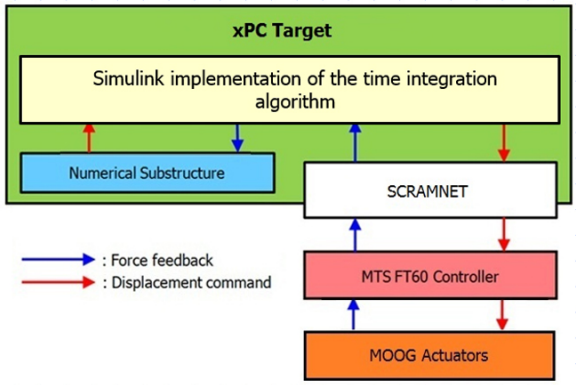

Figure 6.16: Architecture of experimental implementations of the proposed time integration algorithms for the purpose of hybrid simulation.

6.7 Experimental validations of proposed schemes

In order to validate experimental implementations of proposed time integration schemes, hybrid simulations were conducted at the laboratory of Structures and Materials of the University of Trento. The same experimental equipment of the *INDUSE* experimental campaign was adopted. Therefore, the architecture of the implementation of the monolithic LSRT-2 algorithm described in Chapter 5 was exploited. For the sake of clarity, the block diagram of Figure 6.16 reports the aforementioned architecture. According to the block diagram of Figure 6.16, all algorithms as well as NSs were implemented in the *Simulink environment*. Resulting models were converted to *C* code for *xPC-Target* through the *Simulink Coder* software. Figure 6.17 reports a screenshoot of the Simulink implementation of the GCbis-MG-α method. As can be appreciated in Figure 6.17, *Data stores* blocks store state vectors and Lagrange multipliers, whilst *rate transition* blocks interface integrators of PSs and NSs, which advance at different time steps. In order to allow for the concurrent solution of both *free problems*, the *multitask data sore* option was set to *none*. Such setting was crucial to exploit parallel computation resources. According to the continuous PDT method, the time integrator of the PS provides displacement commands to actuators at the controller rate. The experimental validation of the proposed implementation relevant to the GCbis-MG-α method was conducted on a 4-DoFs chain like stiff system. In greater detail, a pair of cantilever

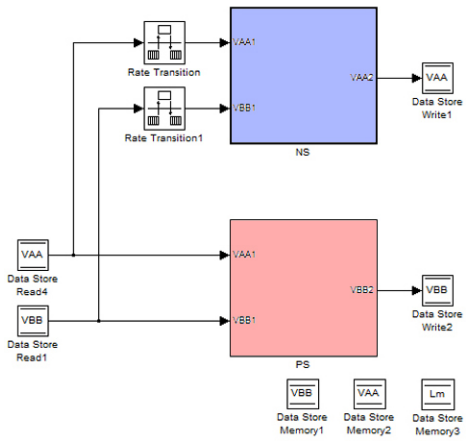

Figure 6.17: Simulink implementation of the GCbis-MG-α algorithm.

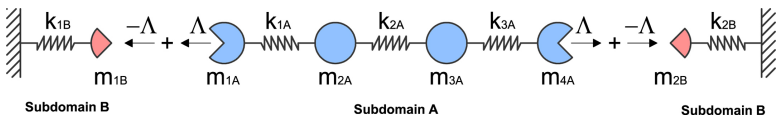

Figure 6.18: Split-mass 4-DoFs chain like system for the experimental validation of the GCbis-MG-α method.

beams clamped at the base was considered as 2-DoFs PS, whilst the remainder part of the system was numerically simulated. The experimental implementation of the PM-MG-α method was validated during the *INDUSE* experimental campaign discussed in Chapter 5. As a consequence, the same piping system was considered as benchmark case study. In both cases, linear NSs were considered. Nonetheless, the proposed implementations can be easily extended to nonlinear NSs.

6.7.1 Experimental validation of the GCbis-MG-α method

A 4-DoFs chain-like stiff system was conceived to validate the GCbis-MG-α method. In greater detail, two cantilever beams clamped at the base were considered as PSs. Figure 6.18 reports the entire emulated system. Two physical cantilever beams clamped at the base replaced extreme springs. Figure 6.19 depicts both front and side views of the resulting experimental set-up. Reference linear solutions were provided by the trapezoidal rule. The following matrices were

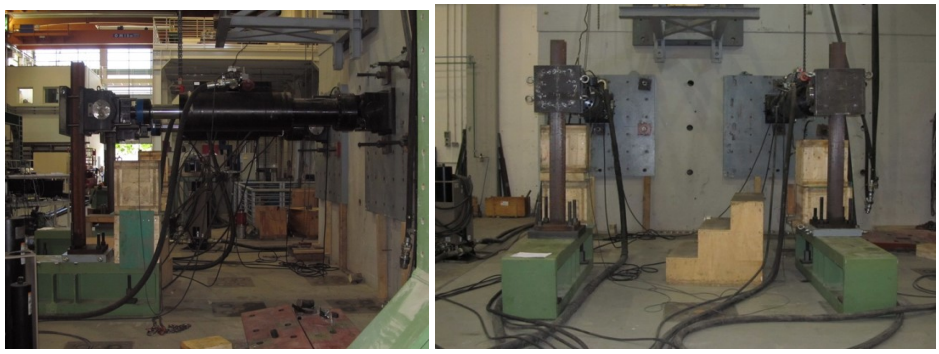

(a) (b)

Figure 6.19: Experimental set-up of the PS: **a** side; and **b** front views.

assumed:

$$\mathbf{k}^A = \begin{bmatrix} k_1 & -k_1 & 0 & 0 \\ -k_1 & 2k_1 & -k_1 & 0 \\ 0 & -k_1 & 2k_1 & -k_1 \\ 0 & 0 & -k_1 & k_1 \end{bmatrix} \quad \mathbf{m}^A = \begin{bmatrix} m_1/2 & 0 & 0 & 0 \\ 0 & m_2 & 0 & 0 \\ 0 & 0 & m_3 & 0 \\ 0 & 0 & 0 & m_4/2 \end{bmatrix} \quad \mathbf{f}^A = \begin{bmatrix} m_1/2 \\ m_2 \\ m_3 \\ m_4/2 \end{bmatrix} \quad \mathbf{l}^{A\,T} = \begin{bmatrix} 1 & 0 \\ 0 & 0 \\ 0 & 0 \\ 0 & 1 \end{bmatrix} \tag{6.98}$$

$$\mathbf{m}^B = \begin{bmatrix} m_1/2 & 0 \\ 0 & m4/2 \end{bmatrix} \quad \mathbf{k}^B = \begin{bmatrix} k1 & 0 \\ 0 & k1 \end{bmatrix} \quad \mathbf{f}^B = \begin{bmatrix} m_1/2 \\ m_4/2 \end{bmatrix} \quad \mathbf{l}^{B\,T} = \begin{bmatrix} -1 & 0 \\ 0 & -1 \end{bmatrix} \tag{6.99}$$

where masses m_1, m_2 and m_4 were set to 2000kg whilst m_3 was set to 5kg. Moreover, the stiffness parameter $k_1 = 4e6N/m$, corresponded to the flexural stiffness of one physical column measured at the actuator level. The resulting linear model of the emulated 4-DoFs chain-like stiff system was characterized by 5.27, 8.99, 12.03 and 201.44Hz eigenfrequencies. No viscous damping was applied. Hybrid simulations were conducted replacing linear restoring forces of Subdomain *B* with their physical counterparts. A coarse time step $\Delta t_A = 1/1024s$ was selected for the NS. A Nyquist frequency of 512Hz, which was comparable to that of the stiff mode at 201.44Hz, resulted from this setting. Since the time scale λ was set to 128 and the controller rate was $1024Hz$, the subcycling parameter *ss* was set to 128. In order to excite the stiff mode, a unit initial displacement was applied to DoF

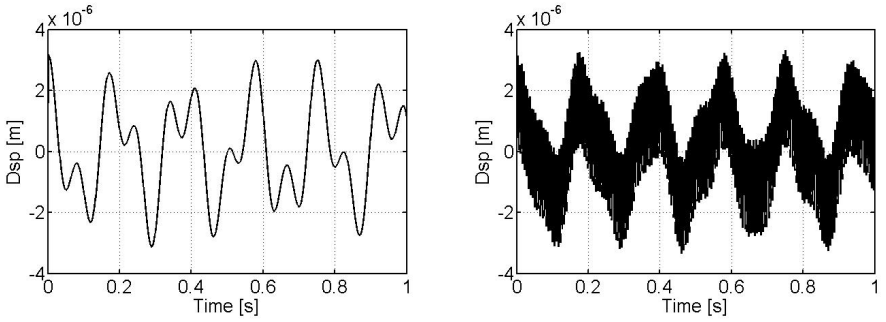

(a) (b)

Figure 6.20: Simulated *Link* displacement histories of the 4-DoFs chan-like stiff system at DoFs **a** #1 and **b** #4. The GCbis-MG-α method was applied with the subcycling setting foreseen for the experimental validation.

#3. Since the GCbis-MG-α handles the *link* problem at coarse time step, a numerical simulation of the experimental validation test was set and time histories of both *link* solutions were checked. Figure 6.20 reports time histories of *link* displacement histories relevant to both physical DoFs. As can be appreciated, the proposed coupling scheme did not entail excessive jumps on actuator commands. In fact, *link* displacements always remained very small. As a consequence, this subcycling setting was successfully implemented for the purpose of continuous PDT. Furthermore, Figure 6.21 compares experimental displacement responses of the hybrid system to the reference linear solution. Both simulations well agree with reference solutions on DoF #1 where the response of the stiff mode was negligible. With regard to displacement responses of DoF #3, the stiff mode was preserved in the case of ρ_∞ = 1.00. Eventually, it was damped out after few cycles in the case of ρ_∞ = 0.50.

6.7.2 Experimental validation of the PM-MG-α method

Since the experimental implementation of the PM-MG-α method was validated during the INDUSE experimental campaign, the same piping system was considered as benchmark case study. The structural system is carefully described in

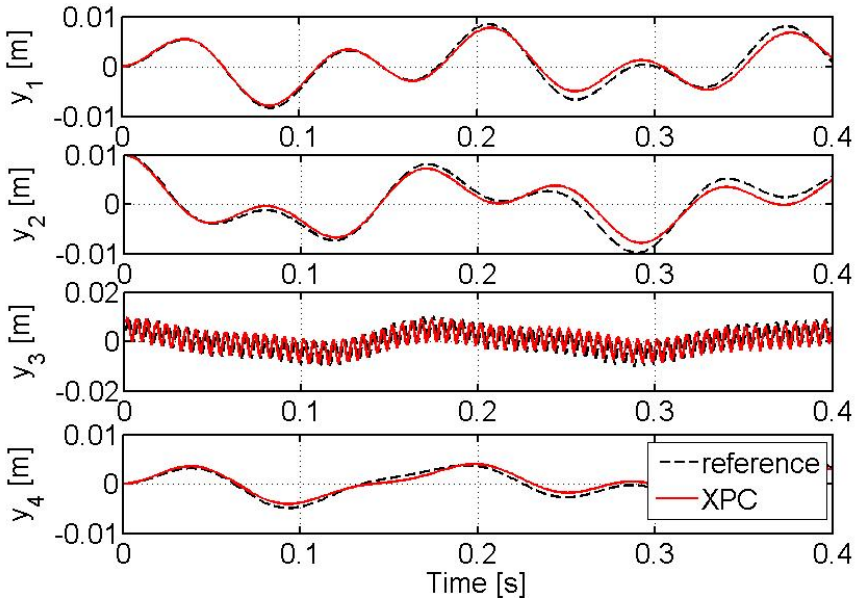

(a)

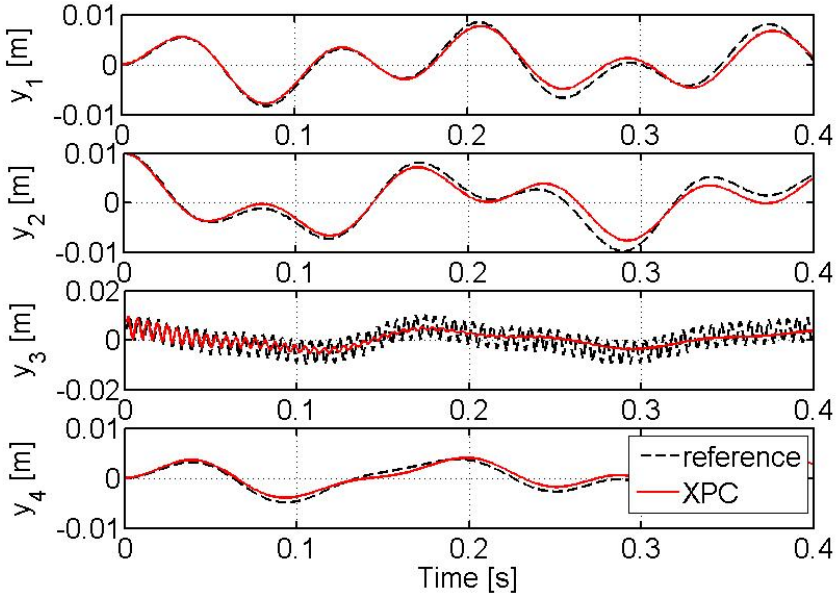

(b)

Figure 6.21: Displacement histories of the 4-DoFs chan-like stiff system obtained with the GCbis-MG-α method with: **a** ρ_∞ = 1.00; and **b** ρ_∞ = 0.50.

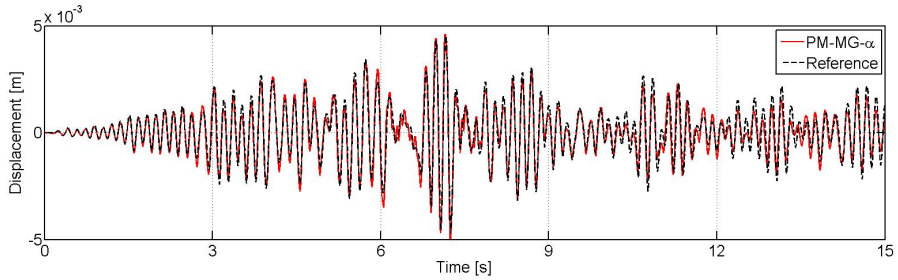

Figure 6.22: Displacement history at the Coupling DoF #1 of the piping system obtained with the PM-MG-α method with ρ_∞ = 1.00.

Chapter 5 as well as the experimental set-up. In greater detail, the piping subjected to PDTs and characterized by lower eigenmodes at about 5Hz was considered. Mass and load matrices of the PS were obtained applying the Craig-Bampton approach. The Collapse Limit State accelerogram at the piping system level was selected as seismic input. Since the response of the PS remained in the linear range, the *INDUSE* piping system was a suitable benchmark case study. A coarse time step Δt_A of $1/1024s$ was selected for the NS. Since the time scale λ was set to 64 and the controller rate was $1024Hz$, the subcycling parameter *ss* was set to 64. The GC-MG-α was implemented as initialization procedure. Figure 6.22 shows the comparison between the displacement response of the emulated system measured at Coupling DoF #1, see Chapter 5 in this respect, and the reference linear solution. As can be appreciated from Figure 6.22, displacement histories well agreed and the experimental implementation of the PM-MG-α was validated.

6.8 Conclusions

Partitioned multi-time integration schemes represent a suitable approach for the implementation of continuous PDT, where the computational driver and the control system run at different time rates. In fact, they allow for the parallel solution of involved subdomains, i.e. PSs and NSs, with different time steps. From this perspective, three partitioned time integration schemes were developed for the purpose of hybrid simulation. Since numerical models of both NSs and PSs can be profitably used for dynamic identification, model-based control and model order reduction, the most flexible state space form was selected. First, the monolithic MG-α algo-

rithm was introduced for the uncoupled case. Stability, accuracy and spectral properties were investigated from both the analytical and the numerical side. A careful description of both the GC-MG-α and the PM-MG-α time integration procedures followed. The former, which consists on a staggered scheme, was proposed as starting procedure of the latter, which is a not self-starting parallel scheme, within the same implementation. Then, the parallel partitioned GCbis-MG-α method was introduced as an alternative approach. Features of both strategies were analyzed on numerical case studies. In greater detail, the PM-MG-α method exhibited second order accuracy without subcycling and first order accuracy with subcycling, whilst the GCbis-MG-α method was endowed with second order accuracy regardless subcycling setting. In the case with ρ_∞ = 1.00, i.e. no algorithmic damping, the PM-MG-α method still entails interface energy dissipation, whilst the GCbis-MG-α is always conservative. Moreover, the self starting feature of the GCbis-MG-α method simplifies implementations on controllers. Nonetheless, the GCbis-MG-α method handles *link problems* at coarse time steps. As a result, in order to avoid non smooth actuator commands at fine time steps, particular care must be devoted to the subcycling setting . Finally, experimental validations of both approaches were presented and properties inherited from parent algorithms were confirmed for the purpose of hybrid simulation.

CHAPTER 7

SUMMARY, CONCLUSIONS AND FUTURE PERSPECTIVES

7.1 Summary

As anticipated, the performed research activity focused on three main objectives: i) modeling of tunable nonlinear Numerical Substructures (NSs) for the purpose of the hybrid simulation of the Rio Torto Bridge, where a consistent degradation of all piers, i.e. physical and numerical, was needed; ii) the implementation of hybrid simulations of an industrial piping system characterized by a twisted and branched Physical Substructure (PS) with a reduced number of actuators; iii) the development of hybrid compatible partitioned time integration algorithms tailored to first order systems and prone to parallel implementations for continuous Pseudo-Dynamic Testing (PDT). Accordingly, summaries of relevant research activities follow.

With regard to the Rio Torto case study, the fiber-based OpenSEES Reference Model (RM) model was implemented as reference for the testing campaign. Deck, piers and relevant Friction Pendulum Bearing (FPB) isolator pairs were considered as macro elements for substructuring purposes. First, an ANSYS Reference Model (RM) of the bridge was implemented to provide linear mass and stiffness matrices of the system. Then, its internal constraint setting was analyzed and small simplifications were introduced. The resulting ANSYS Simplified Model (SM) facilitated the substructuring of piers as Single-Degree-of-Freedom (S-DoF) elements preserving global modal characteristics. Reduced S-DoF piers were extended to the nonlinear range by means of modified Bouc-Wen springs (Smyth et al., 1999). OpenSEES FPB isolator elements were replaced by S-DoF state space models ca-

pable of reproducing their characteristic bilinear hysteretic loop (Mostaghel, 1999). Tailored NSs were successfully implemented for the purpose of the hybrid simulation of the Rio Torto Bridge at the ELSA facility of the Joint Research Centre of Ispra (VA), Italy. In detail, 1:2.5 scale mock-up models of Piers #9 and #11 together with relevant FPB isolation devices were coupled to the remainder part of the bridge implemented in the CAST3M FE code. The partitioned method developed by Pegon and Magonette (2002) allowed for the implementation of the continuous PDT method. Moreover, a tool for the identification of parameters of OpenSEES FE models was implemented in the Matlab environment. As a result, after each test, physical piers were characterized in terms of damage. The OpenSEES RM model of the Rio Torto Bridge was updated accordingly and taken as reference for the updating of reduced S-DoF piers, i.e. NSs., for subsequent tests.

With reference to the industrial piping system case study, two FE models were implemented: the ANSYS Continuous Model (CM) and the ANSYS Reference Model (RM); they embedded continuous and actual coupling conditions between PS and NS, respectively. Simplified straight elbow elements were devised and implemented in both AMSYS models. In order to apply HSDS to the piping system with a pair hydraulic actuators despite the geometric complexity of the specimen, reduced matrices of the PS were deemed necessary. In order to characterized reduction basis requirements, the Principal Component Analysis (PCA) was applied to the displacement response of the PS of the ANSYS RM; and both span and minimum rank of any effective reduction basis were defined. Accordingly, a Modified version of the System Equivalent Reduction and Expansion Process (M-SEREP) method was tailored to the PS in the RT case, whilst the well-known Craig-Bampton (CB) method was applied to the PDT case. Krylov and PCA bases were investigated from a numerical perspective only. Therefore, both PDTs and RTs were successfully implemented at the Laboratory of Structures and Materials of the University of Trento. In particular, the LSRT2 time integration algorithm (Bursi, 2011) tailored to Hamiltonian system was adopted in the experimental campaign. The delay compensation strategy proposed by Wu (2013) and based on the over prediction of the actuator command was selected.

With reference to the development of hybrid compatible partitioned time inte-

gration algorithms, the monolithic Modified Generalized-α (MG-α) algorithm was selected as basic scheme for the uncoupled case. Partitioned implementations were derived from well-know coupling scheme based on the Finite Element Tearing Interconnecting (FETI) approach (Gravouil, 2001; Pegon and Magonette, 2002; Mahjoubi, 2010). First convergence and spectral properties of the MG-α method were analyzed. Then, both the GC-MG-α and the PM-MG-α partitioned time integration procedures were presented. The former, which consists of a staggered scheme, was proposed as starting procedure of the latter, which is a no self starting parallel scheme, within the same implementation. Then, the parallel partitioned GCbis-MG-α method was introduced as an alternative approach. Performances of all developed partitioned time integration algorithms were analyzed on numerical case studies. In detail, a 3-DoFs chain-like stiff system emphasized the favorable user-controlled algorithmic damping features. Then, a 30-DoFs plane structure with variable partitioning was conceived to shed light on interface energy dissipation. Finally, experimental validation tests were conducted at the Laboratory of Structures and Material of the University of Trento.

7.2 Conclusions

Before stressing general conclusions, results of all performed studies are briefly summarized herein.

The assessment of the seismic performances of the Rio Torto Bridge was conceived within the RETRO transnational activity funded by the SERIES research project. In greater detail, a comprehensive set of hybrid simulations covered both as-built and retrofitted conditions. Since computational resources denied the implementation of NSs based on fiber elements, the nonlinear dynamic substructuring of the OpenSEES RM of the Rio Torto Bridge was devised. A novel testing procedure aimed at simulating a consistent degradation among physical and numerical piers was applied to the Rio Torto Bridge. It was based on off-line sessions of model identification of PSs and updating of NSs. As a result, a consistent degradation of physical and numerical piers was successfully simulated. Characterizations of physical piers highlighted an appreciable degradation of stiffness and strength characteristics after non isolated tests. In particular, crack spread and failure of transverse beams characterized the Ultimate Limit State (ULS) dam-

age patterns. Accordingly, modal frequencies of the non isolated bridge showed decreasing trends as far as damage was accumulating within both physical and numerical piers. Since the characterization of FPB isolators highlighted friction coefficients higher than design values, i.e. μ = 7% $>$ 4%, most significant tests were conducted considering numerical FPB isolators. Pier responses remained in the linear range at both limit states; and the effectiveness of the proposed retrofitting was confirmed. Further hybrid simulations were conducted with physical piers and FPB isolators. Reduced vertical forces were applied to physical FPB isolators to compensate excessive friction coefficients. Entailing results confirmed responses obtained with only numerical FPB isolators.

In the case of simple structural topologies, i.e., shear type frames, inverted pendulum systems, chain like systems, etc., few actuators handling the totality of physical DoFs can efficiently reproduce the response path of tested specimens; and the system of equations of motion can be solved through suitable time integrators. Nonetheless, this approach is not suitable for dealing with complex PSs subjected to distributed inertia forces, where a plenty of physical DoFs come on stage; and this is the case of typical piping networks. The need for assessing dynamic responses of typical industrial piping systems subjected to seismic loading motivated the author to apply model reduction techniques to experimental dynamic substructuring. In this respect, a deep insight into the dynamic response of an emulated global system from a specimen perspective was provided applying the PCA. The clear understanding of reduction basis requirements paved the way for the implementation of a number of model reduction techniques aimed at extending the applicability range of both RT and PDT techniques, beyond their traditional scope. As a result, hybrid simulations of the piping system were successfully implemented with a reduced number of actuators. The favorable performance of the piping system, which always remained in the linear regime without any leakage, corroborated the choice of reduction bases derived from linear time-invariant FE models. Hence, reduction techniques proposed in this study for the purpose of hybrid simulation were justified.

Parallel partitioned schemes represent a valuable approach to handle the computational driver and the control system at different time rates. Since they allow for

the parallel analysis of involved subdomains, the continuous PDT method can be easily implemented in a rigorous manner from the system dynamics perspective. In fact, inherent subcycling capabilities allow for squeezing the available solving time according to the complexity of the NS; and any interpolation/extrapolation of actuator commands is completely avoided. As far as numerical models of both NSs and PSs can be profitably used for dynamic identification, model-based control and model order reduction, the most flexible state space form is a reasonable choice. Moreover, the L-Stability feature is preferable in the case of stiff system typical of FE discretisation. Accordingly, the MG-α, which embeds both of suggested features, was selected as basic monolithic scheme, and three partitioned time integration schemes were developed. Since the parallel feature is crucial for the implementation of hybrid simulations, the GC-MG-α and the PM-MG-α partitioned time integrators were combined within the same implementation. The former, acted as initialization procedure for the latter. The GCbis-MG-α was proposed as alternative approach. All proposed schemes are second order accurate without subcycling; nevertheless, only the GC-bis-α method preserves the second order accuracy with subcycling. In the case without algorithmic damping, i.e. ρ_∞ = 1.00, the PM-MG-α method still entails interface energy dissipation, whilst the GCbis-MG-α is energy preserving. Moreover, the self starting feature of the GCbis-MG-α method entails simpler implementations. Accordingly, the GCbis-α seems to be more appealing for the purpose of hybrid simulation. Both proposed approached were successfully validated through experimental case studies. Since the GCbis-α handles the *link* problem at coarse time steps, particular care was devoted to the selection of a proper subcycling setting.

As testified by discussed results, dynamic substructuring played a significant role on both physical and numerical sides. With regard to the Rio Torto case study, it allowed for the implementation of reduced nonlinear NSs complying with available computational resources and prone to fast updating sessions. With respect to the piping network case study, it paved the way for a rational implementation of hybrid simulations despite the complex geometry of the PS. In both the two cases negligible local dynamics were identified and discarded. A rigorous approach based on the PCA was given to investigate minimum requirements of optimized simplified

models. Model updating techniques enhanced their inherent flexibility. In this view, effective error measures are crucial for the sake of comparison of entailing approximation errors. In the present work both NEEs and NRMSEs were extensively applied to validate all approximated models. From the time integration perspective, proposed parallel partitioned schemes contributed to relax computational limitations that are still strict in the case of cumbersome NSs. Since they rely on the FETI approach, it is interesting to note that they also fall in the category of domain decomposition methods. Summarizing, HSDS can benefit of proposed methodological approaches and algorithms that extend its scope beyond traditional limits.

7.3 Future perspectives

State space hysteretic models were implemented for the purpose of nonlinear dynamic substructuring of the OpenSEES RM of the Rio Torto Bridge. In greater detail, the reduction process pursued a kinematic matching between substructured components and their reference counterparts. A possible application of online model updating techniques to NSs will be investigated in the case of realistic structural systems. In the author knowledge, few attempts were done and they were restricted to benchmark case studies (Kwon and Kammula, 2013; Yang, 2012).

A number of model reduction bases was investigated for the purpose of the hybrid simulation of an industrial piping system. Nevertheless, techniques applied in PDTs and RTs did not account for the distribution and the time modulation of external loads. As a result, input-output relations of the system being reduced were lost in the reduction process. Improved performance can be achieved by reduction bases accounting for such information. Krylov (Srinivasan Puri, 2008) and PCA (Lülf, 2013) subspaces, which were investigated from the numerical side only, provided promising results and deserve further studies. Balanced truncation methods represent a further suitable approach; in fact, they retain both reachability and observability states providing error bounds on output responses (Gugercin and Antoulas, 2004). Future research studies will shed light on these methods from the hybrid simulation perspective. The enhancement of the proposed approach to nonlinear PSs deserve further investigations from both the numerical and the experimental perspectives.

Work is still in progress to provide analytical proofs of convergence and spec-

tral properties of presented partitioned schemes. Further validations based on nonlinear systems will be provided as well. When more than two subdomains are connected to the same node, the uniqueness of the constraint equation set is lost. In order to force positive definite Poincaré-Steklov operators of proposed algorithms, localized Lagrange multipliers (Park et al., 2000) represent a tempting approach. In fact they prevent redundant constraint equations. As far as a domain decomposition method based on continuity of the primary variable suffers from stability issues, a continuity constraint on the time derivative of the primary variable is the best choice (Nakshatrala et al., 2008). Since analyzed Initial Value Problems (IVPs) involved second order Ordinary Differential Equations (ODEs) where both primal quantities -displacements- and their derivatives -velocities- filled the state vector, constraint equations were set on state vectors. In order to generalize proposed implementations to first order ODEs, e.g. heat equation, coupling operators will be tailored to state vector rates. Finally, to avoid storage of state derivatives, constraint equations expressed in terms of velocity like quantities will be investigated.

BIBLIOGRAPHY

ABAQUS. Theory manual, abaqus, version 6.3, 2003.

Corritore D. Derisi R. Di Sarno L. Mohamad A. Paolacci F. Yenidogan C. Alessandri, S. Numerical simulation of the seismic response of the rio-torto viaduct for psd test campaign. retro project. Technical report, 2013.

R.J. Allemang. The modal assurance criterion–twenty years of use and abuse. *Journal of Sound and Vibration*, 37(8):14–23, 2003. URL `http://www.sandv.com/downloads/0308alle.pdf`.

ANSYS. Release 11.0 documentation for ansys, 2007.

Craig J.R. Bampton, M.C. Coupling of substructures for dynamic analyses. *AIAA Journal*, 6(7):1313–1319, 1968.

A Bonelli, OS Bursi, L He, G Magonette, and P Pegon. Convergence analysis of a parallel interfield method for heterogeneous simulations with dynamic substructuring. *International journal for numerical methods in engineering*, 75(7):800–825, 2008. URL `http://onlinelibrary.wiley.com/doi/10.1002/nme.2285/pdf`.

Arnold M. Bruls, O. The Generalized-α Scheme as a Linear Multistep Integrator: Toward a General Mechatronic Simulator. *Journal of Computational and Nonlinear Dynamics*, 3(4):041007, 2008. ISSN 15551423. doi: $10.1115/1.2960475$. URL `http://computationalnonlinear.asmedigitalcollection.asme.org/article.aspx?articleid=1395094`.

Ceravolo R. Erlicher S. Zanotti Fragonara L. Bursi, O.S. Identification of the hysteretic behaviour of a partial-strength steel-concrete moment-resisting frame

structure subject to pseudodynamic tests. *Earthquake Engineering & Structural Dynamics*, 41(14):1883–1903, 2012. ISSN 00988847. doi: 10.1002/eqe.2163. URL http://doi.wiley.com/10.1002/eqe.2163.

He L. Bonelli A. Pegon P. Bursi, O.S. Novel generalized-α methods for interfield parallel integration of heterogeneous structural dynamic systems. *Journal of Computational and Applied Mathematics*, 234(7):2250–2258, August 2010. ISSN 03770427. doi: 10.1016/j.cam.2009.08.082. URL http://linkinghub.elsevier.com/retrieve/pii/S0377042709005615.

Jia C. Vulcan L. Neild S.A. Wagg D.J. Bursi, O.S. Rosenbrock-based algorithms and subcycling strategies for real-time nonlinear substructure testing. *Earthquake Engineering & Structural Dynamics*, 40(1):1–19, 2011. URL http://onlinelibrary.wiley.com/doi/10.1002/eqe.1017/pdf.

O S Bursi, A. Gonzalez-Buelga, L Vulcan, S A Neild, and D J Wagg. Novel coupling Rosenbrock-based algorithms for real-time dynamic substructure testing. *Earthquake Engineering & Structural Dynamics*, 37(3):339–360, 2008. ISSN 00988847. doi: 10.1002/eqe.757. URL http://doi.wiley.com/10.1002/eqe.757.

O. S. Bursi, Z. Wang, C. Jia, and B. Wu. Monolithic and partitioned time integration methods for real-time heterogeneous simulations. *Computational Mechanics*, 2012. ISSN 0178-7675. doi: 10.1007/s00466-012-0800-0. URL http://link.springer.com/10.1007/s00466-012-0800-0.

Wagg D. Bursi, O.S. *Modern testing techniques for structural systems*. Springer, 2008. ISBN 978-3-211-09444-0. URL http://link.springer.com/book/10.1007/978-3-211-09445-7.

Cast3M. Un logiciel de simulation numérique, 2003. URL http://www-cast3m.cea.fr/.

Abbiati G. Ceravolo, R. Sdit release 3.1 user's manual. structural identification toolbox for matlab. Technical report, Polytechnic of Turin, Turin,Italy, 2009.

Abbiati G. Ceravolo, R. Time Domain Identification of Structures: Comparative Analysis of Output-Only Methods. *Journal of Engineering Mechanics*, 139(4): 537–544, April 2013. ISSN 0733-9399. doi: 10.1061/(ASCE)EM.1943-7889.0000503. URL http://ascelibrary.org/doi/abs/10.1061/%28ASCE%29EM.1943-7889.0000503.

Rosario Ceravolo, Silvano Erlicher, and Luca Zanotti Fragonara. Comparison of restoring force models for the identification of structures with hysteresis and degradation. *Journal of Sound and Vibration*, 332(26):6982–6999, December 2013. ISSN 0022460X. doi: 10.1016/j.jsv.2013.08.019. URL http://linkinghub.elsevier.com/retrieve/pii/S0022460X13006846.

A. Chatterjee. An introduction to the proper orthogonal decomposition. *Current science*, 78(7):808–817, 2000. URL http://www.currentscience.ac.in/Downloads/article_id_078_07_0808_0817_0.pdf.

Eleni N Chatzi and Andrew W Smyth. The unscented kalman filter and particle filter methods for nonlinear structural system identification with non-collocated heterogeneous sensing. *Structural control and health monitoring*, 16(1):99–123, 2009.

Ricles J.M. Chen, C. Development of direct integration algorithms for structural dynamics using discrete control theory. *Journal of Engineering Mechanics*, 134 (8):676–683, 2008.

J Chung and GM Hulbert. A time integration algorithm for structural dynamics with improved numerical dissipation: the generalized-α method. *Journal of applied mechanics*, 60(2):371–375, 1993.

Gravouil A. Combescure, A. A numerical scheme to couple subdomains with different time-steps for predominantly linear transient analysis. 191:1129–1157, 2002. URL http://www.sciencedirect.com/science/article/pii/S0045782501001906.

Su T. Craig, R. Krylov model reduction algorithm for undamped structural dynamics systems. *Journal of guidance, control, and dynamics*, 14(6):1311–1313, 1991. URL http://arc.aiaa.org/doi/abs/10.2514/3.20789?journalCode=jgcd.

Di Sarno L. Della Corte G. Paolacci F. Marioni A. De Risi, R. and F. Taucer. Seismic analysis and retrofitting of an existing rc highway bridge part ii: Analysis of the isolated bridge. In *Proceedings of the 14th Italian National Conference on Earthquake Engineering*, Bari, Italy, 2011.

Nie J. DeGrassi, G. and C. Hofmayer. Seismic analysis of large-scale piping systems for the jnes-nupec ultimate strength piping test program, u.s. nrc. nureg/cr-6983, bnl-nureg-81548-2008. Technical report, 2008. URL http://pbadupws.nrc.gov/docs/ML0903/ML090330722.pdf.

EN13480-3. Metallic industrial piping - part 3: Design and calculation, 2002.

S. Erlicher, L. Bonaventura, and O. S. Bursi. The analysis of the Generalized-α method for non-linear dynamic problems. *Computational Mechanics*, 28(2):83–104, March 2002. ISSN 01787675. doi: $10.1007/s00466\text{-}001\text{-}0273\text{-}z$. URL http://www.springerlink.com/openurl.asp?genre=article&id=doi:10.1007/s00466-001-0273-z.

EUROCODE-8. Design of structures for earthquake resistance, part 2: Bridges, 2004.

Verderame G. M. Manfredi G. Fabbrocino, G. Experimental behaviour of anchored smooth rebars in old type reinforced concrete buildings. *Engineering Structures*, 27(10):1575–1585, 2005. URL http://www.sciencedirect.com/science/article/pii/S0141029605001938.

M.N. Fardis. Seismic engineering research infrastructures for european synergies, series project, grant number: 227887, 2009-2013. Technical report, European Laboratory for Structural Assessment (ELSA), 2009. URL http://www.series.upatras.gr/.

Charbel Farhat and Francois-Xavier Roux. A method of finite element tearing and interconnecting and its parallel solution algorithm. *International Journal for Numerical Methods in Engineering*, 32(6):1205–1227, 1991. ISSN 1097-0207. doi: $10.1002/\mathrm{nme}.1620320604$. URL http://dx.doi.org/10.1002/nme.1620320604.

Charbel Farhat, Po-Shu Chen, and Jan Mandel. A scalable lagrange multiplier based domain decomposition method for time-dependent problems. *International Journal for Numerical Methods in Engineering*, 38(22):3831–3853, 1995. ISSN 1097-0207. doi: $10.1002/\mathrm{nme}.1620382207$. URL `http://dx.doi.org/10.1002/nme.1620382207`.

Roy N. Girard, A. *Structural dynamics in industry*, volume 7. John Wiley & Sons, 2010. ISBN 978-1-84821-004-2.

Combescure A. Gravouil, A. *International Journal for Numerical Methods in Engineering*, 50(1):199–225, 2001. URL `http://onlinelibrary.wiley.com/doi/10.1002/1097-0207(20010110)50:1%3C199::AID-NME132%3E3.0.CO;2-A/abstract`.

Serkan Gugercin and Athanasios C Antoulas. A survey of model reduction by balanced truncation and some new results. *International Journal of Control*, 77 (8):748–766, 2004.

Robert J Guyan. Reduction of stiffness and mass matrices. *AIAA journal*, 3(2): 380–380, 1965.

M Javad Hashemi and Gilberto Mosqueda. Innovative substructuring technique for hybrid simulation of multistory buildings through collapse. *Earthquake Engineering & Structural Dynamics*, pages n/a–n/a, 2014. ISSN 00988847. doi: $10.1002/\mathrm{eqe}.2427$. URL `http://doi.wiley.com/10.1002/eqe.2427`.

M Javad Hashemi, Armin Masroor, and Gilberto Mosqueda. Implementation of online model updating in hybrid simulation. *Earthquake Engineering & Structural Dynamics*, 43(3):395–412, 2014.

T Ichinose, Y Kanayama, Y Inoue, and JE Bolander Jr. Size effect on bond strength of deformed bars. *Construction and building materials*, 18(7): 549–558, 2004. URL `http://www.sciencedirect.com/science/article/pii/S0950061804000455#`.

Kenneth E Jansen, Christian H Whiting, and Gregory M Hulbert. A generalized-α method for integrating the filtered navier–stokes equations with a stabilized

finite element method. *Computer Methods in Applied Mechanics and Engineering*, 190(3):305–319, 2000. URL http://www.sciencedirect.com/science/article/pii/S0045782500002036.

Pappa R. S. Juang, J. N. An eigensystem realisation algorithm (era) for modal parameter identification and modal reduction. *NASA/JPL Workshop on Identification and Control of Flexible Space Structures*, 8(5):620–627, 1984.

D.C. Kent and R. Park. Flexural members with confined concrete. *Journal of the Structural Division, Proceedings of the American Society of Civil Engineers*, ST7 (97):1969–1990, 1971.

Gaëtan Kerschen, Keith Worden, Alexander F. Vakakis, and Jean-Claude Golinval. Past, present and future of nonlinear system identification in structural dynamics. *Mechanical Systems and Signal Processing*, 20(3):505–592, April 2006. ISSN 08883270. doi: 10.1016/j.ymssp.2005.04.008. URL http://linkinghub.elsevier.com/retrieve/pii/S0888327005000828.

D. De Klerk, D. J. Rixen, and S. N. Voormeeren. General Framework for Dynamic Substructuring: History, Review and Classification of Techniques. *AIAA Journal*, 46(5):1169–1181, May 2008. ISSN 0001-1452. doi: 10.2514/1.33274. URL http://arc.aiaa.org/doi/abs/10.2514/1.33274.

Elisabeth Krausmann, Ana Maria Cruz, and Bastien Affeltranger. The impact of the 12 may 2008 wenchuan earthquake on industrial facilities. *Journal of Loss Prevention in the Process Industries*, 23(2):242–248, 2010.

Oh-sung Kwon and Viswanath Kammula. Model updating method for substructure pseudo-dynamic hybrid simulation. *Earthquake Engineering Structural Dynamics*, 2013. doi: 10.1002/eqe. URL http://onlinelibrary.wiley.com/doi/10.1002/eqe.2307/full.

Giuseppe Lomiento, Noemi Bonessio, and Gianmario Benzoni. Friction Model for Sliding Bearings under Seismic Excitation. *Journal of Earthquake Engineering*, 17(8):1162–1191, November 2013. ISSN 1363-2469. doi: 10.1080/13632469.2013.814611. URL http://www.tandfonline.com/doi/abs/10.1080/13632469.2013.814611.

Tran D. Ohayon R. Lülf, F. A. Reduced bases for nonlinear structural dynamic systems: A comparative study. *Journal of Sound Vibration*, 332:3897–3921, 2013. URL http://www.sciencedirect.com/science/article/pii/S0022460X13001272.

Najib Mahjoubi. *Methode generale de couplage de schema dintegration multi-echelles en temps en dynamique des structures*. PhD thesis, Institut National des Sciences Appliquées de Lyon, 2010.

Pinto E. Menegotto M. Method of analysis for cyclically loaded reinforced concrete plane frames including changes in geometry and non-elastic behavior of elements under combined normal force and bending. In *IABSE Symposium*, Lisbon, Portugal, 1973.

Naser Mostaghel. Analytical Description of Pinching, Degrading Hysteretic Systems. *Journal of Engineering Mechanics*, 125(2):216–224, February 1999. ISSN 0733-9399. doi: 10.1061/(ASCE)0733-9399(1999)125:2(216). URL http://ascelibrary.org/doi/abs/10.1061/%28ASCE%290733-9399%281999%29125%3A2%28216%29.

J.E. Mottershead and M.I. Friswell. Model updating in structural dynamics: A survey. *Journal of Sound and Vibration*, 167(2):347–375, 1993. ISSN 0022460X. doi: 10.1006/jsvi.1993.1340. URL http://linkinghub.elsevier.com/retrieve/pii/S0022460X83713404.

John E. Mottershead, Michael Link, and Michael I. Friswell. The sensitivity method in finite element model updating: A tutorial. *Mechanical Systems and Signal Processing*, 25(7):2275–2296, 2011. ISSN 08883270. doi: 10.1016/j.ymssp.2010.10.012. URL http://linkinghub.elsevier.com/retrieve/pii/S0888327010003316.

K. B. Nakshatrala, K. D. Hjelmstad, and D. A. Tortorelli. A feti-based domain decomposition technique for time-dependent first-order systems based on a dae approach. *International Journal for Numerical Methods in Engineering*, 75(12):1385–1415, 2008. ISSN 1097-0207. doi: 10.1002/nme.2303. URL http://dx.doi.org/10.1002/nme.2303.

N.M. Newmark. A method of computation for structural dynamics. *Journal of the Engineering Mechanics Division*, (3):67–94, 1959.

NTC-2008. D.m. 14-01-2008: Norme tecniche per le costruzioni, 2008.

Avitabile P. OCallahan, J.C. and R. Riemer. System equivalent reduction expansion process (serep). In *Proceedings of the 6th International Modal Analysis Conference*, pages 129–37, Las Vegas, 1989.

Nakamura I. Takada H. Otani, A. and M. Shiratori. Consideration on seismic design margin of elbow in piping. In *Proceedings of the ASME 2011 Pressure Vessels 237 and Piping Division Conference, PVP2011, July 17-21*, Baltimore, Maryland, USA, 2011.

F Paolacci and R Giannini. An experimental and numerical investigation on the cyclic response of a portal frame pier belonging to an old reinforced concrete viaduct. *Earthquake Engineering & Structural Dynamics*, 41(6):1109–1127, May 2012. ISSN 00988847. doi: $10.1002/\mathrm{eqe}.1175$. URL `http://doi.wiley.com/10.1002/eqe.1175`.

F Paolacci, R Giannini, and M De Angelis. Seismic response mitigation of chemical plant components by passive control techniques. *Journal of Loss Prevention in the Process Industries*, 26(5):924–935, 2013.

Reza Md. S. Bursi O.S. Gresnigt A.M. Kumar A. Paolacci, F. Main issues on the seismic design of industrial piping systems and components. In *ASME 2013 Pressure Vessels and Piping Conference*. American Society of Mechanical Engineers, 2013.

M.S. Bursi O.S. Paolacci F., Reza. Seismic design criteria of refinery piping systems. In *COMPDYN 2011 - III ECCOMAS Thematic Conference on Computational Methods in Structural Dynamics and Earthquake Engineering, 26-28 May*, Corfu, Greece, 2011.

K. C. Park, C. a. Felippa, and U. a. Gumaste. A localized version of the method of Lagrange multipliers and its applications. *Computational Mechanics*, 24(6):

476–490, January 2000. ISSN 0178-7675. doi: 10.1007/s004660050007. URL http://link.springer.com/10.1007/s004660050007.

P. Pegon and G. Magonette. Continuous psd testing with non-linear substructuring: Presentation of a stable parallel inter-field procedure - tr 1.02.167. Technical report, European Laboratory for Structural Assessment (ELSA), Joint Research Centre of Ispra (VA), Italy, 2002.

P. Pegon and G. Magonette. Continuous psd testing with non-linear substructuring: Using the operator splitting technique to avoid iterative procedures - tr spi.05.30. Technical report, European Laboratory for Structural Assessment (ELSA), Joint Research Centre of Ispra (VA), Italy, 2005.

Mancini G. Pinto, P.E. Seismic assessment and retrofit of existing bridges. reluis project. Technical report, 2009. URL http://www.reluis.it.

a. Prakash and K. D. Hjelmstad. A FETI-based multi-time-step coupling method for Newmark schemes in structural dynamics. *International Journal for Numerical Methods in Engineering*, 61(13):2183–2204, December 2004. ISSN 0029-5981. doi: 10.1002/nme.1136. URL http://doi.wiley.com/10.1002/nme.1136.

Calvi G.M. Kowalsky M.J. Priestley, M.J.N. *Displacement-Based Seismic Design of Structures*. IUSS PRESS, Pavia, Italy, 2007. ISBN 88-6198-000-6.

M. J. Nigel Priestley, Ravindra Verma, and Yan Xiao. Seismic Shear Strength of Reinforced Concrete Columns. *Journal of Structural Engineering*, 120(8):2310–2329, August 1994. ISSN 0733-9445. doi: 10.1061/(ASCE)0733-9445(1994)120:8(2310). URL http://ascelibrary.org/doi/abs/10.1061/%28ASCE%290733-9445%281994%29120%3A8%282310%29.

Shing B.P. Stauffer E. Thoen B. Rae-Young, J. Performance of a real-time pseudodynamic test system considering nonlinear structural response. *Earthquake Engineering & Structural Dynamics*, 36(12):1785–1809, 2007. URL http://onlinelibrary.wiley.com/doi/10.1002/eqe.722/abstract.

MS. Reza. *Seismic safety evaluation of industrial piping systems and components*

under serviceability and ultimate limit state conditions. PhD thesis, University of Trento, Trento,Italy, 2013.

Daniel J. Rixen and Paul L.C. van der Valk. An Impulse Based Substructuring approach for impact analysis and load case simulations. *Journal of Sound and Vibration*, 332(26):7174–7190, December 2013. ISSN 0022460X. doi: 10.1016/j.jsv.2013.08.004. URL http://linkinghub.elsevier.com/retrieve/pii/S0022460X13006615.

Andreas H Schellenberg. *Advanced Implementation of Hybrid Simulation*. PhD thesis, University of California, Berkeley, 2009.

A. W. Smyth, S. F. Masri, A. G. Chassiakos, and T. K. Caughey. On-line parametric identification of mdof nonlinear hysteretic systems. *Journal of Engineering Mechanics*, 125(2):133–142, February 1999. ISSN 0733-9399. doi: 10.1061/(ASCE)0733-9399(1999)125:2(133). URL http://ascelibrary.org/doi/abs/10.1061/%28ASCE%290733-9399%281999%29125%3A2%28133%29.

Wei Song and Shirley Dyke. Development of a cyber-physical experimental platform for real-time dynamic model updating. *Mechanical Systems and Signal Processing*, 37(1-2):388–402, May 2013. ISSN 08883270. doi: 10.1016/j.ymssp.2012.12.007. URL http://linkinghub.elsevier.com/retrieve/pii/S0888327013000046.

R. Srinivasan Puri. *Krylov Subspace Based Direct Projection Techniques for Low Frequency, Fully Coupled, Structural Acoustic Analysis and Optimization*. PhD thesis, Oxford Brookes University, Oxford,England, 2008.

Y. Tanaka. Study on analogy between dynamic load and displacement-controlled load. *International Journal of Pressure Vessels and Piping*, 90: 37–45, 2012. URL http://www.sciencedirect.com/science/article/pii/S0308016111001426.

Vesna Terzic and Bozidar Stojadinovic. Hybrid Simulation of Bridge Response to Three-Dimensional Earthquake Excitation Followed by Truck Load. *Journal of Structural Engineering*, (1):A4014010, July 2013. ISSN 0733-9445. doi: 10.

1061/(ASCE)ST.1943-541X.0000913. URL http://ascelibrary.org/doi/abs/10.1061/%28ASCE%29ST.1943-541X.0000913.

Blay N. Sollogoub P. Chapuliot S. Touboul, F. Enhanced seismic criteria for piping. *Nuclear engineering and design*, 236(1):1–9, 2006. URL http://www.sciencedirect.com/science/article/pii/S002954930500244X.

Karamanos S.A. Gresnigt A.M. Varelis, G.E. Pipe elbows under strong cyclic loading. *Journal of Pressure Vessel Technology*, 135(1):011207, 2013. URL http://pressurevesseltech.asmedigitalcollection.asme.org/article.aspx?articleid=1678512.

Collins M.P. Vecchio, F.J. Predicting the response of reinforced concrete beams subjected to shear using modified compression field theory. *ACI Structural Journal*, 85(3):258–268, 1988. URL http://www.concrete.org/Publications/ACIMaterialsJournal/ACIJournalSearch.aspx?m=details&ID=2515.

S.N. Voormeeren and D.J. Rixen. A family of substructure decoupling techniques based on a dual assembly approach. *Mechanical Systems and Signal Processing*, 27:379–396, February 2012. ISSN 08883270. doi: 10.1016/j.ymssp.2011.07.028. URL http://linkinghub.elsevier.com/retrieve/pii/S0888327011003177.

Wang Q. Shing B.P. Jinping O. Wu, B. Equivalent force control method for generalized real-time substructure testing with implicit integration. *Earthquake engineering & structural dynamics*, 36(9):1127–1149, 2007. URL http://onlinelibrary.wiley.com/doi/10.1002/eqe.674/abstract.

Wang Z. Bursi O.S. Wu, B. Actuator dynamics compensation based on upper bound delay for real-time hybrid simulation. *Earthquake Engineering & Structural Dynamics*, 42(12):1749–1765, 2013. URL http://onlinelibrary.wiley.com/doi/10.1002/eqe.2296/full.

Tsai K. Elnashai A.S. Hsieh T. Yang, Y. An online optimization method for bridge dynamic hybrid simulations. *Simulation Modelling Practice and Theory*, 28:42–54, 2012. ISSN 1569190X. doi: 10.1016/j.simpat.2012.06.002. URL http://linkinghub.elsevier.com/retrieve/pii/S1569190X12000871.